DISSERTATION

# DYNAMICS OF LOW-DENSITY ULTRACOLD PLASMAS IN EXTERNALLY APPLIED ELECTRIC AND MAGNETIC FIELDS

Submitted by

Truman M. Wilson

Department of Physics

In partial fulfillment of the requirements

For the Degree of Doctor of Philosophy

Colorado State University

Fort Collins, Colorado

Fall 2013

Doctoral Committee:

Advisor: Jacob Roberts

David Krueger
Stephen Lundeen
Azer Yalin

ABSTRACT

DYNAMICS OF LOW-DENSITY ULTRACOLD PLASMAS IN EXTERNALLY APPLIED ELECTRIC AND MAGNETIC FIELDS

The experiments described in this thesis were focused on the influence of external electric and magnetic fields and electron evaporation on the evolution of ultracold plasmas (UCPs). The UCPs were created from the photoionization of $^{85}$Rb which was first captured in a magneto-optical trap (MOT) and then magnetically trapped and transferred by a set of magnetic coils attached to a motorized translation stage to a region of the vacuum chamber with a set of electrodes. The first experiment studied the response of the UCP to sharp electric field pulses, which included 2 cycles of a sine wave pulse. These experiments showed a resonant response to the 2 cycles of rf that was density dependent, but was not a collision based mechanism. Instead, the response was caused by a rapid energy transfer to individual electrons through the collective motion of the electron cloud in the UCP. This density-dependent response allowed us to develop a technique for measuring the expansion rate of the UCPs in our system. It was also observed in second set of experiments that electron evaporation from the UCP had a significant effect on the amount of energy that was transferred to the ions to drive the UCP expansion. Model calculations show that we should expect electron evaporation to have a more significant influence on the UCP expansion rate at the relatively low densities of the UCPs that we create compared to other experiments. By modeling electron evaporation during expansion, our data are consistent with evaporation reducing the electron temperature significantly, which lowers the overall UCP expansion rate. In addition to these studies, we also performed an experiment in which it was observed that in the presence of a magnetic field there was a significant increase in the initial UCP expansion rate coupled with a deceleration of the ion expansion at later times in the UCP evolution. Our observations to date are consistent with the magnetic field influencing electron screening and UCP formation. By restricting the electrons motion in the direction transverse to the magnetic field lines to circular orbits around the magnetic field lines, the electrons cannot move appropriately to screen the internal radial electric fields produced by the excess of ions. Studies of this effect are currently under way. Future

studies include direct measurements of the electron temperature and collision rates between the components of the UCP as we move towards trapping the UCP in a Penning trap.

ACKNOWLEDGEMENTS

The work presented in this thesis would not have been possible without the support of many of the individuals that I am fortunate to know. First, I would like to thank my advisor Professor Jacob Roberts. He has been an excellent mentor and granted me the opportunity to work on an exciting research project where I obtained many skills which I know will serve me well in the future. Working for him allowed me to grow as a scientist over the last six years. I would not be where I am today without his guidance. I would also like to thank Wei-Ting Chen who worked as a graduate student on the ultracold plasma project with me since its inception. Working together, we were able to a build a new experimental apparatus that was nothing more than an empty lab table when we started. We worked well together to perform the experiments present in this thesis, and I thank him for all of his help. I would also like to thank the many undergraduate research assistants for all of their contributions to the experiment. Finally, I would like to thank my wonderful wife Becky. Without her love and support, I would be lost.

TABLE OF CONTENTS

# Chapter 1

# Introduction to Ultracold Plasma Physics

Since the creation of ultracold plasma (UCP) systems [1] from the photoionization of ultracold atoms, there has been a wide range of experiments that explore a rich assortment of plasma phenomena in these systems. Ultracold plasmas occupy a unique position in plasma parameter space (which is typically defined by plasma temperature and density) that makes it possible to study "exotic" plasma systems (e.g. astrophysical plasmas) using a small-scale apparatus in a laboratory environment. One of the most interesting features of UCP systems is that they are created with both components (ion and electron) near the strong-coupling regime [2], where the Coulomb potential energy of nearest-neighbor particles is on the order of the kinetic energy of the particles in the system. In this regime, strong particle correlations can develop, which can lead to phase transitions to liquid- and solid-like states in plasma systems [2–4]. Also, as plasma systems approach the strong-coupling regime, many typical assumptions about the plasma behavior break down. This leads to a deviation from predicted calculations of plasma properties such as the collision [5] and recombination rates [6, 7].

Plasma systems exist over many orders of magnitude in both temperature and density as seen in Figure 1.1 [8]. Plasmas are mainly defined by the collective behavior exhibited by a system of charges, and therefore exist in many types of systems ranging from exotic astrophysical systems such as the cores of Jupiter and the sun, to more common systems to the human experience such as lightning and fire. Although these systems can all be defined as plasmas, their behavior can be very different depending on where they lie on Figure 1.1. Of particular importance to ultracold plasma systems is the change in behavior at the crossover to the strong-coupling regime, represented by the $\Gamma = 1$ line in Figure 1.1. It is near this line in temperature and density space that particle correlations begin to develop that can significantly alter how the plasma behaves. By studying these changes in UCP systems, we can gain insight into the properties of other systems that exist around the same value of the strong coupling parameter, $\Gamma$. It is important and convenient to measure these properties in UCP systems, as the cores of Jupiter and the sun are technologically inaccessible by direct probes. Also, other laboratory systems that can achieve such a degree of

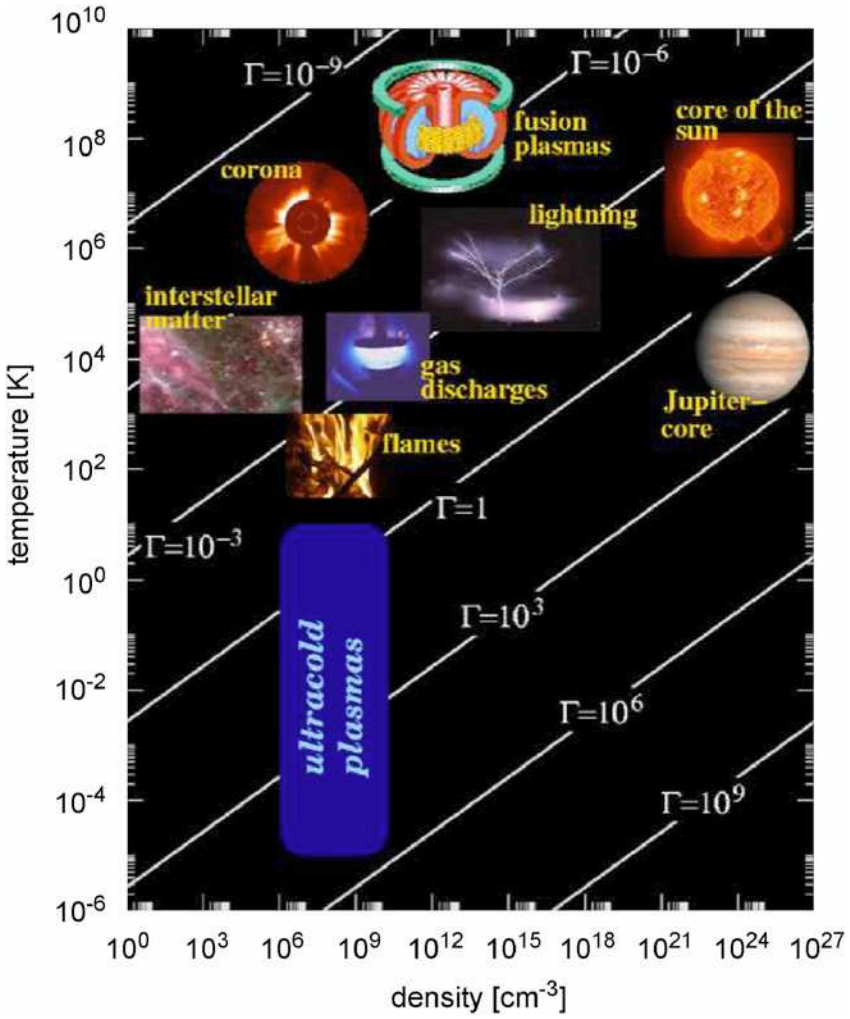


Figure 1.1: A plot of where various plasma systems lie in density and (ion) temperature space in relation to ultracold plasma systems. This source of this figure can be found in [8]. The diagonal lines show constant values of the strong-coupling parameter, which is defined by $\Gamma = e^2/4\pi\epsilon_0 a k_B T$, where $e$ is elementary charge, $\epsilon_0$ is the permittivity of free space, $k_B$ is Boltzmann's constant, $T$ is the temperature of the particles, and $a$ is the Wigner-Seitz radius given by $a = (3/4\pi n)^{1/3}$ (where $n$ is the density). The location of ultracold plasmas in this diagram shows the theoretical value for the strong-coupling parameter that can be obtained based on the initial conditions. However, various heating effects after the initial creation of the UCP limit the value of the strong-coupling parameter that can be studied once the UCP formation process is complete. These heating effects are discussed in the text.

strong-coupling in both the electron and ion components tend to be much more complicated than UCP systems.

Ultracold plasmas are highly reproducible, table-top systems that provide a convenient way to study a wide range of plasma phenomena in a laboratory environment. The UCPs are produced using well known techniques for the production of ultracold atoms [9] followed by either direct photoionization [1] or by excitation to highly excited Rydberg states, which then spontaneously evolve into a UCP [10]. The UCPs that are produced have a relatively small physical extent, which ranges from a few hundred $\mu$m to greater than 1 mm. This allows for the construction of small scale assemblies to produce the various electric and magnetic fields that can be used to manipulate and probe the UCP. The low temperature of the UCPs also allows for the magnetization of the constituent particles of the UCP at relatively low magnetic fields. UCPs also have a density distribution which is not homogeneous, which alters the collective mode behavior [11] and the response of the UCP to externally applied rf fields [12–15].

Aside from the interesting physics associated with many plasma systems that are near the strong-coupling regime as stated above, UCPs have the potential to be used to model the physics of globular star cluster formation [16]. Models of globular star cluster dynamics can be very complicated, with assumptions that can be difficult to verify experimentally since the evolution of actual star clusters happens on cosmic timescales. So, observations of star clusters only provide a snapshot of the evolution and do not provide significant insight on dynamic processes. UCP systems provide a small-scale system for experimentally testing some of the models of globular cluster evolution. Since the Coulomb forces that govern the interaction between particles in a plasma also vary as $1/r^2$ as does the force of gravity, a simple change in the gravitational constant in the models for cluster dynamics can allow for a comparison of these models to UCP systems. Many of the dynamic processes in UCP systems have analogous process in globular star clusters. Of particular interest is the three-body recombination process, which for UCP systems produces highly excited Rydberg atoms with a free electron that carries away the excess energy. In globular star clusters, this process results in the formation of binary star systems with a third star carrying away the excess energy. Also of interest is the evaporation of high kinetic energy stars out of the

cluster. In UCP systems, electrons continually escape from the UCP through collisional processes that allow them to overcome the Coulomb potential provided by the excess of ions in the UCP.

Ultracold plasma systems have the potential to give us insight into processes that are important for experiments concerning the production of anti-hydrogen from recombination processes involving confined anti-protons and positrons in the same region of space [17]. The production of anti-hydrogen via this method relies on three-body recombination processes which can dominate the dynamics of UCP systems in a certain parameter range [18, 19]. To trap the anti-protons and positrons in the same region of space, a nested Penning trap configuration involving a set of electrodes to confine the particles axially along with a strong axial magnetic field to confine the particles radially is used [17]. This type of configuration has been used to trap UCPs in [20], but was found to allow particles to escape along certain paths out of the trap (a solvable problem addressed in our apparatus). By using these types of traps for UCP systems, we can test the physics of trap loading, particle dynamics, and recombination physics that can be useful for anti-hydrogen experiments without the need for expensive equipment to produce the constituent anti-matter particles.

Ultracold plasma experiments will also be used to test the results of theoretical predictions for plasma dynamics that can be difficult to model. These difficulties in modeling plasma dynamics arise from the many different timescales that need to be considered for the different processes that take place in the UCP if the ion and electron trajectories are tracked classically. In particular, the formation of bound-states through recombination processes produce problems in numerical evaluation because the electron motion requires timesteps that are too small to be practical (fs or less). These bound electrons are typically in highly-excited Rydberg states which still interact in a non-negligible way with the other UCP particles. Solutions to this modeling problem involve designating a spherical radius around each ion where electrons that penetrate this radius are treated quantum-mechanically rather than classically [21]. At this point it is unknown how well this type of modeling describes the collision dynamics and the establishment of thermal equilibrium in ultracold plasma systems. We hope to be able to study these effects in our UCPs which will allow us to better understand how to model UCP systems efficiently.

To perform the UCP experiments that are presented in this thesis, we constructed a novel apparatus that separates the region in the vacuum system where the ultracold atoms are laser-cooled and collected from the region where the UCP experiments are performed. We did this

to allow for the independent optimization of each of the two regions. In the plasma region, we constructed a set of cylindrically symmetric electrodes which can provide a potential that will allow us to create the nested Penning trap configuration that will simultaneously trap electrons and ions in the same region of space. This trap will allow us to explore long-timescale plasma processes (such as electron-ion thermalization) that are longer than the natural lifetime of the UCPs that are allowed to expand freely. However, trapped UCPs are not the focus of this thesis. Instead, we found that our apparatus was also well-suited for studying UCP physics at lower densities than were typical for other experiments.

The experiments performed for this thesis focus on UCP diagnostic techniques and evolution dynamics in freely expanding, low-density UCPs that will be necessary to understand fundamental UCP physics as well as dynamics of loading the Penning trap for future experiments. The first experiment characterized a collisionless, resonant response of the UCPs created in our system to short bursts of externally applied rf electric fields. This response allowed us to determine the peak density of the UCP at a chosen time in the UCP evolution, further allowing us to measure the UCP expansion rate. The second experiment focuses on the influence of electron evaporative cooling on the expansion rate of the UCPs in our system, where a significant decrease in the UCP expansion rate was observed compared to a full conversion of the initial ionization energy to expansion energy. Finally, I will discuss the influence of a relatively weak, uniform magnetic field on the early time expansion behavior in our UCPs, where an increase in the expansion rate was observed in the presence of a magnetic field. These experiments will be outlined at the end of this chapter and be discussed in detail in the later chapters of this thesis. To better understand the context of these experiments, I will briefly outline the important aspects of UCP physics in this chapter and discuss some of the previous experiments that have been performed that have increased our understanding of UCP systems.

## 1.1 Ultracold Plasma Formation and Evolution

The formation of ultracold plasmas from photo-ionized ultracold atoms was first reported by Killian *et al.* in 1999 [1], and has become a common method for producing two-component plasmas in a state that is near the strongly coupled regime. These plasmas can also be produced by exciting

ultracold atoms or molecules to a highly excited Rydberg state, which then spontaneously evolve into a plasma through collisional processes [22]. Ionization through Rydberg atoms can have its advantages, as this formation process starting with correlated Rydberg atoms from a "Rydberg blockade" forms more highly ordered initial plasma distributions [23]. However, for our experiments, direct photo-ionization will provide greater control over the initial electron energy and will allow for us to explore UCP phenomena over a wide range of initial ionization energies.

Ultracold plasma evolution can generally be split into two parts: formation and expansion. An example electron signal as measured by the micro-channel plate detector (MCP, see Chapter 3) can be seen in Figure 1.2, where the two parts of the plasma evolution are highlighted. The electron signal from our MCP is proportional to the rate of electron escape from the UCP. During the formation stage (I), the ultracold atoms are photoionized by an intense laser pulse, freeing the electrons. To conserve both energy and momentum during the process, the electrons will carry away nearly all of the excess photon energy above the ionization threshold (see Chapter 3). The ions will have a temperature that is close to that of the original ultracold atom distribution, which is typically less than 1 mK. Since one electron is created for every ion, the UCP is initially neutral throughout all space, which provides no means of confinement for the electrons in the UCP in the absence of external electric and magnetic fields. So, electrons will begin to escape until there is an imbalance of ions and electrons that creates a space charge that is large enough to confine the remaining electrons. This initial escape is typically referred to as the "prompt peak", and can be seen in Figure 1.2.

In the work in [1], it was shown that for a given set of plasma parameters, a minimum number of ions is needed in order to trap at least one electron with energy equal to the initial ionization energy. This number is known as the threshold number and will be a useful concept for calibrating our MCP signal and electric field environment as shown in Chapter 3. The threshold ion number was shown in [1] to be an equivalent to the requirement that the one-dimensional rms size of the plasma, $\sigma$, be greater than the Debye screening length, $\lambda_D$. The requirement that the scale size of the plasma is greater than $\lambda_D$ is also what usually distinguishes a plasma system from a system being just a collection of charged particles.

As the UCP evolves (II), the potential well created by the excess of ions can become greater than the initial ionization energy, which then requires electrons to have higher energy than their

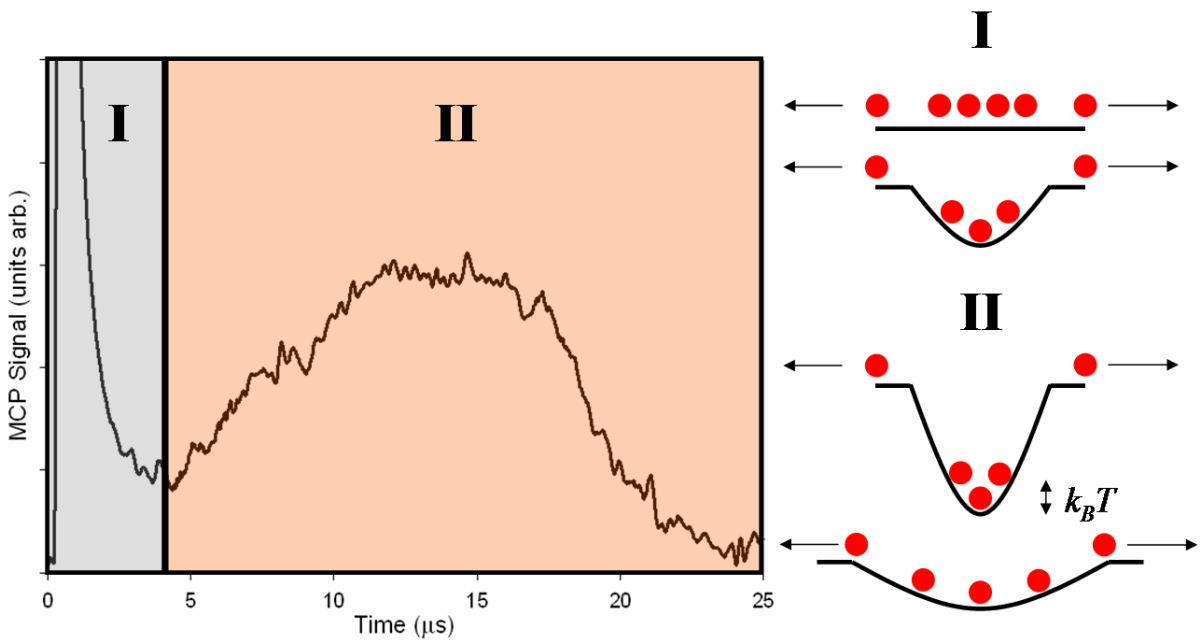


Figure 1.2: A diagram of the UCP formation process. The left graph shows a detector signal that is proportional to the rate of electron escape from the UCP, which is split into two parts: the UCP formation (I) and expansion (II). The right diagram shows the evolution of the potential well during these two stages with the red circles representing electrons. During formation (I), the UCP is initially neutral. The finite energy of the electrons will send some of the electrons out of the UCP, resulting in the development of an excess of positive charge, creating a potential well. As the UCP evolves (II), the electron thermalize [24] and the high energy electrons escape. This creates a potential well that is greater than the average temperature of the electrons. As the UCP expands, this potential well decreases along with the UCP electron temperature.

initial formation energy in order to escape the UCP. The electrons begin to thermalize [24], which creates an energy distribution where the highest energy electrons are able to escape the UCP. This lowers the overall temperature of the electrons until potential well created by the ions can be many times $k_B T_e$.

During the expansion stage, the electrons that are trapped by the excess of ions can be treated as a confined gas that exerts a thermal pressure on the ions, driving them outward. A more computationally useful understanding of the expansion is to note that the greater temperature of the electrons compared to the ions will cause the electron density to decrease in space slightly relative to the ions. This decrease in the electron density produces electric fields that confine the electrons, but anti-confine the ions. So, these electric fields will drive the ion expansion, with higher electron temperatures leading to faster expansion. As the UCP increases in size, the potential well naturally becomes shallower, allowing more electrons to escape as seen in Figure 1.2. This expansion into free space will cause the UCP to "fall apart", which means that UCPs created outside of a trap created by externally applied fields will have a finite lifetime. This lifetime ranges from ∼20-120 $\mu$s for the UCPs created in our system.

## 1.2 Strong Coupling in Plasmas

One of the most interesting features of UCP systems is the ability to create the UCP with both components at energies and densities that would nominally make them very strongly-coupled. In the next section, I will discuss the various heating effects which limit the amount of strong-coupling that can take place in UCP systems upon formation. At this point, I will define strong-coupling parameter, $\Gamma$, which is the ratio of the nearest-neighbor Coulomb potential energy to the average kinetic energy of the particles in the plasma, as given by[2],

$$\Gamma = \frac{e^2}{4\pi\epsilon_0 a k_B T} \tag{1.1}$$

where $e$ is elementary charge, $\epsilon_0$ is the permittivity of free space, $k_B$ is Boltzmann's constant, $T$ is the temperature of the particles, and $a$ is the Wigner-Seitz given by $a = (3/4\pi n)^{1/3}$, where $n$ is the density. A plasma system is generally considered to be in the strong-coupling regime for $\Gamma \geq 1$. However, the influence of strong-coupling physics is still expected for $\Gamma$ less than but near to 1.

Strongly-coupled plasmas appear in a variety of astrophysical systems including the core of Jupiter [25, 26], the core of the sun [27], the surface of white dwarf stars [28], and dusty (complex) plasmas [29] as well as other laboratory systems [27, 30, 31]. Typical plasma systems have $\Gamma \ll 1$ owing to either a low density (interstellar medium) or a high temperature (lightning, Tokamak fusion plasmas). In ultracold plasma systems, precise control over the initial state of the system allows for the creation of UCPs with low initial energy. This can produce values of the strong-coupling parameter near 1 even for relatively low densities plasmas.

As the strong-coupling parameter increases, stronger particle correlations begin to develop. These strong correlations can lead to phase transitions where the particles in the plasma exhibit the behavior of liquids and solids [2]. If the strong-coupling parameter reaches high enough values, the particles in the plasma can become highly ordered enough to form a lattice. This transition is known as Wigner crystallization. For one-component plasmas (i.e. plasmas with just ions or just electrons, but not both), Wigner-crystallization has been demonstrated by laser-cooling Beryllium ions in a Penning trap [3]. For two-component plasmas, laser cooling is predicted to be capable of producing strongly-coupled ions that will undergo Wigner-crystallization [4]. However, even in this case the electron component is expected to remain weakly-coupled. Wigner-crystallization of a two-component plasma has not been demonstrated experimentally.

As plasmas approach the strong-coupling regime, many theoretical descriptions of plasma behavior are expected to breakdown. This is particularly important in UCP systems when discussing collision rates between particles and three-body recombination processes which are discussed further in Chapter 2. For the calculations of the collision rates, the Coulomb logarithm $\ln(\Lambda)$ (where $\Lambda$ is the ratio of the distance of closest approach between colliding particles to the collision cut-off distance, the Debye length) can actually become negative. A negative Coulomb logarithm is nonsensical, and indicates a breakdown of the plasma theory. Also, a negative Coulomb logarithm would suggest that there is less than one electron per Debye length cubed. This indicates that any theoretical picture of screening has to break down as any scattering with less than one particle per screening length is nonsensical. So, it will be necessary to re-evaluate some of the standard plasma physics theory using more sophisticated models.

Although there are many heating mechanisms that limit the strong-coupling parameter that will be discussed in the next section, there should still be effects from strong-coupling physics

present even if $\Gamma < 1$. These effects would likely be present in the collision rates and three-body recombination rates of the UCP system. These rates have not been measured explicitly in UCP systems. Also, our recent measurements of the effects of electron evaporation on the UCP expansion rate (see Chapter 5) indicate that it may be possible to achieve higher values of $\Gamma$ than predicted for other UCP conditions [19]. These measurements will lead to a new line of investigation where we will study the effectiveness of forced evaporative cooling to achieve even higher values of the electron strong-coupling parameter.

## 1.3 Limits to the Strong Coupling Parameter

While the ion component of the strong coupling parameter can evolve to have strong coupling parameters $\Gamma_i > 1$ [32], there still exist many heating effects which limit the amount of strong-coupling that can be achieved when creating ultracold plasmas for both the ion and electron components. While these heating effects may be mitigated by studying UCPs at low-density as we do for our experiments, it is useful to review the limitations to strong-coupling in UCP systems so that we may better understand how to overcome these difficulties. These heating effects include three-body recombination [18, 19], disorder-induced heating [33], threshold lowering [34], and Debye screening [35] (which doesn't cause heating but does reduce the correlation energy of the ions). In fact, experimental and theoretical studies of ultracold plasmas have shown that under typical conditions in experiments elsewhere that the electron strong-coupling parameter will be limited to values of $\Gamma_e \sim 0.2$ [18, 19], which makes finding ways to circumvent these heating mechanisms very important for pushing UCPs further into the strong-coupling regime. A summary of the effects discussed in this section can be found in Table 1.1 at the end of this section.

It is important to note that disorder-induced heating and threshold lowering only contribute heat to the UCP during formation. Also, for the low-density UCPs that we create using our system, three-body recombination heating is significantly reduced compared to other UCP experiments. Later in this thesis, I will show that evaporative cooling of the electron component will be enhanced at lower UCP density (Chapter 5). Therefore, forced evaporative cooling schemes should be more effective for the UCPs created in our system. Thus, there are reasons to be optimistic about the possibility of producing UCPs with $\Gamma_e$ closer to the strong coupling limit than in other UCP experiments.

### 1.3.1 Three-Body Recombination

One of primary heating mechanisms that limits the strong-coupling of the electrons in UCP systems is three-body recombination [18, 19, 36]. In this process, a collision occurs between two electrons and an ion that binds one of the electrons to the ion in a highly-excited Rydberg state. To conserve energy and momentum, the other electron will carry away the excess binding energy from the collision. This excess energy will eventually be thermalized via collisions among the electrons in the UCP, which raises the temperature of the remaining electrons. In many experiments, the heating from three-body recombination is detectable through an increase in the expansion rate of the UCPs at low temperatures. The strong scaling in temperature of the recombination process limits the strong coupling to $\Gamma_e \sim 0.2$ for the experiments in [18], consistent with theoretical predictions [19].

The temperature scaling of the recombination process is predicted to go as $T_e^{-9/2}$, and can be deduced from the following argument [37]. We will first consider an electron-ion pair, with a "distance of closest approach" defined by $b = e^2/(4\pi\epsilon_0 k_B T_e)$, where $T_e$ is the temperature of the electrons in the plasma. The collision frequency of such an electron-ion pair is given by $nv_e b^2$, where $n$ is the density of the ions and electrons and $v_e$ is the characteristic velocity of the electrons which is proportional to $\sqrt{T}$. To determine the scaling of the three-body recombination rate, we must multiply this collision frequency by probability that a second electron will be close enough to participate in the collision and carry the excess binding energy away. This probability is given by $nb^3$, where in a weakly-coupled plasma (where this scaling is expected to be valid) $nb^3 \ll 1$. This gives a three-body recombination rate that is proportional to $n^2 v_e b^5$, and thus scales as $n^2 T_e^{-9/2}$.

The classical three-body recombination rate is given by [8],

$$K_{TBR}^{tot} \sim 3.8 \times 10^{-9} \cdot T_e^{-9/2} n_e^2 \quad \mathrm{s}^{-1} \tag{1.2}$$

where $n_e$ is in units of /cm$^3$ and $T_e$ is in units of K. A useful formulation of this rate is to take the inverse value, which gives the three-body recombination time. The recombination time gives an estimate of how long it takes for an ion to undergo a recombination event. By calculating this time for our range of conditions, it will allow us to determine whether or not we expect three-body recombination to add a significant amount of heat to the UCP. At electron temperatures greater than 10 K for the UCPs in our system, the three-body recombination time can be longer than 150

$\mu$s, which is longer than the UCP lifetime for all of our experimental conditions. However, because of the strong temperature scaling, this heating from three-body recombination can cause an increase in the UCP expansion rate at our lowest initial ionization energies as discussed in Chapter 4.

Since the $T^{-9/2}$ scaling of the three-body recombination rate suggests a divergence at very low temperatures, this scaling can not hold for temperatures that approach $T = 0$ K without producing an infinite recombination rate. A simple thought experiment would say that since translational motion of the particles ceases at $T = 0$, that collisional processes would not be able to take place, thus the three-body recombination rate is expected to be reduced. For high-density, low-temperature plasmas, the scaling rate of three-body recombination is predicted to be reduced to $T^{-1}$ [6]. However, in this treatment, the value of $\Lambda$ in the Coulomb logarithm was assumed to be much greater than 1, which is not always the case in ultracold plasma systems. Molecular dynamics simulations of the effects of strong-coupling on the three-body recombination rate have shown that the three-body recombination rate is expected to fall off exponentially in the strong coupling parameter [7]. Instead of a $T^{-9/2}$ scaling, the rate was found to scale as $\Gamma_e^{9/2}\exp(-\lambda_0\Gamma_e)$, where $\lambda_0$ is a constant that was determined from the results of the simulation. At this point, the limitation of the strong coupling parameter for electrons [18, 19] has not allowed for measurements of the three-body recombination rate to be performed to test this scaling. Measurements performed in [38] have attempted to confirm the $T^{-9/2}$ scaling for plasmas with electrons below the strong-coupling limit. However, a better characterization of the electron temperature will be necessary to confirm this trend. A possible technique for characterizing the electron temperature at chosen times in the UCP evolution will be discussed in Chapter 8.

The design of our experimental apparatus allows for the capability of applying strong magnetic fields to the UCP as part of the Penning trap configuration. Therefore, it is useful to consider the effects of strong magnetic fields on the three-body recombination rate. For a highly magnetized plasma, the Larmor radius of the particles is much less than the classical distance of closest approach between the particles. In this case, the plasma particles are strongly confined to motion along the magnetic field lines, and perpendicular translation is severely restricted. The effect of this degree of magnetization is to reduce the three-body recombination rate in the plasma by an order of magnitude as compared to the unmagnetized case [37]. In this case, it was predicted that the scaling of the three-body recombination rate with density and electron temperature was the same

as in the unmagnetized case. However, these results have not been experimentally verified in UCP systems.

### 1.3.2 Disorder-Induced Heating

One of the most significant processes that limits the strong-coupling of UCPs early in their lifetime is what is known as disorder-induced heating [33]. This heating process occurs during the formation of the UCP, and is far more important heating mechanism for the ions in the UCP. Even though UCPs can be created with initial temperatures and densities that would correspond to high values of the strong-coupling parameter for both the ions and electrons, the ultracold gas from which they are ionized is spatially uncorrelated. So, even if the plasma particles were at zero temperature initially (corresponding to infinite $\Gamma$), the Coulomb potential energy that results from the initial disordered state will convert to kinetic energy as the plasma particles move away from each other to lower the potential energy, resulting in finite temperatures. The density of the plasma then sets a lower limit on the achievable temperature of $k_B T \sim e^2/4\pi\epsilon_0 a$ [39], where $a = (3/4\pi n)^{1/3}$ is the Wigner-Seitz radius. This means that the disorder-induced heating limit to the strong coupling parameter is $\Gamma \sim 1$ in the absence of other effects. For the electrons, both evaporative cooling and cooling during expansion can reduce the effect of disorder-induced heating on the electron component. The ions have limited ability to cool during the UCP evolution and are thus affected more by this process.

Various methods have been proposed to mitigate the effects of disorder induced heating. As discussed previously, using a dense gas of Rydberg atoms can result in a "Rydberg blockade", where strong Rydberg-Rydberg interactions prevent atoms that are near an excited Rydberg atom to become excited, which allows for the development of spatial correlations [23]. The Rydberg atoms will then spontaneously ionize, carrying over this correlation to the UCP. Another method for producing highly correlated plasmas is to use a second stage ionization [40]. In this method, the plasma is created as usual from a single ionization, after which the disorder-induced heating stage takes place, leading to higher correlations but also higher temperatures. At this point, the plasma ions are ionized a second time. Since the previous ionization stage resulted in higher correlation, there is a much smaller effect owing to disorder-induced heating in the second stage ionization. Also, since the charge is suddenly doubled, it quadruples the value of the strong-coupling parameter while

introducing little heat. Other proposals suggest that the effect of disorder-induced heating could be reversed into a cooling process with a properly prepared initial state of atoms in an optical lattice [41]. However, this would be difficult in practice since even minor defects in the optical lattice would produce a large amount of correlation heating.

For our system, we have initial peak UCP densities in a range $\sim 10^7$-$10^8$ /cm$^3$, which results in correlation temperatures of $< 1$ K. For the electron component, this will be much less than the initial ionization energy in most cases, which makes this effect negligible. For the ion component, this will decrease the values of $\Gamma_i$ from their initial values substantially. However, it is expected that as the plasma evolves that $\Gamma_i$ will increase, producing ions in the strong-coupling regime [32]. Our future experiments (Chapter 8) will focus mainly on the strong-coupling parameter of the electrons, $\Gamma_e$.

### 1.3.3 Threshold Lowering

Another contributor to the heating of the electron component of the UCP at early times is the threshold lowering effect [34]. This effect results from the interaction of nearest neighbor ions on the ionization potential of unionized atoms. The potential from the neighboring particles can be summed together on the line between them as $U(r) \propto -1/r - 1/(2a + r)$, where $a$ is the separation between the two particles (generally considered to be the Wigner-Seitz radius). The calculations in [34] considered an initial distribution of atoms in a perfect lattice for the purposes of this calculation. It was shown that the effect of threshold lowering can be significant for low initial ionization energies, and will set a minimum achievable temperature for electron components in UCPs that is dependent on the density as $k_B T_{e\,\min} = 7e^2/4\pi\epsilon_0 a$. For the plasma conditions achievable in our system, this effect will be on the order of a few Kelvin for the electron component of our UCPs.

The low-density UCPs produced by our system will have negligible effects from three-body recombination under most conditions. This makes our system suitable for studying these effects so that we can make comparisons to the theoretical predictions of the minimum achievable electron temperatures under our UCP conditions. This type of measurement will require a way to measure the electron temperature shortly after the UCP formation, which will be discussed in Chapter 8.

### 1.3.4 Electron Shielding

Recent investigations of the effect of electron screening on the ion-ion potential energy have shown that electron shielding can reduce the ion-ion interactions, lowering the amount of strong-coupling for the ions [35]. The experiments and calculations from this work focus on times very early in the formation of the UCP ($< 1$ $\mu$s). For very cold electrons, the Debye screening length can become comparable to the inter-ion spacing in the plasma. Under these conditions, the interpretation of the strong coupling parameter for the ions can become imprecise, as effects from the electron-ion and electron-electron coupling can play a role on the ion-ion coupling. For these conditions, the authors in [35] calculated the total electrostatic potential energy of the UCP to evaluate the strong-coupling of the system. Although screening can reduce the amount of disorder-induced heating that is observed in UCP systems (making $\Gamma$ larger), the authors in [35] found that the effect of electron screening was to reduce the total coupling of the system by the same amount so that $\Gamma \sim 1$. In the absence of external heating of the electrons or an initially ordered spatial distribution, this screening will fundamentally limit the amount of coupling that can be achieved for the ions in UCPs.

### 1.3.5 Electron Cooling through Evaporation

Each of the heating mechanisms discussed in this section except three-body recombination occur during the formation process of the UCP and not during the subsequent UCP evolution. Although these processes limit the lowest achievable initial temperatures, this energy can be removed from the UCP post-formation through electron evaporation. Thus, electron evaporative cooling is a process that increases the degree of electron strong-coupling in spite of these initial heating mechanisms. At lower densities, the effect of electron evaporation is predicted to increase (Chapter 5) and the effect of three-body recombination is predicted to decrease. Although the three-body recombination process is continuous, as long as sufficient cooling can be obtained via electron evaporation, lower temperatures and thus stronger electron coupling should be able to be obtained in our lower-density systems.

Table 1.1: A table summarizing the various mechanisms that can effect the ion and electron strong-coupling parameters in UCP systems. This table includes which component of the UCP is affected by each process, how each process scales with the UCP density and temperature, and when the effect is most relevant during the UCP evolution.

| **Effect** | **UCP Component Affected** | **Scaling** | **Duration** |
|---|---|---|---|
| Three-Body Recombination | Electron | Increased Heating as $n^2/T_e^{9/2}$ | Full Evolution |
| Disorder-Induced Heating | Ion and Electron | Increased Heating as $n^{1/3}$ | UCP Formation |
| Threshold Lowering | Electron | Increased Heating as $n^{1/3}$ | UCP Formation |
| Electron Screening | Ion | Lower Ion Coupling at Lower $T_e$ | Post Formation |
| Electron Evaporation | Electron | Increased Cooling at Lower Density | Post Formation |

## 1.4 Thesis Summary

Before proceeding further into this thesis, I wish to provide a brief overview of the topics covered in each chapter for convenience to the reader.

### 1.4.1 Chapter 2: Fundamental Plasma Physics Theory

Before discussing the specifics of the experiments that I perform for the work in this thesis, it is useful to provide an overview of a background in the relevant fundamental plasma physics. This overview will help put the experiments from this thesis into the proper context and helps to provide estimates of the plasma properties that we wish to measure or have relevance for the assumptions of how our UCPs behave. An important aspect of this fundamental theory review is to show that some of the calculations from standard treatments of plasmas break down when the plasma approaches the strongly-coupled regime. This is due in part to the fact that the Coulomb logarithm, $\ln(\Lambda)$, can become negative in this regime. This translates directly to a non-physical picture for collisions in plasmas. I will also discuss some of the models for dynamics in plasmas which allows for the prediction of the expansion of UCPs in various regimes. All of the topics discussed in this chapter will be referenced in the chapters that follow, and are important concepts for understanding the physics of the experiments performed for this thesis.

### 1.4.2 Chapter 3: Ultracold Plasma Apparatus

In this chapter, I will discuss a novel apparatus that was built to study UCP physics here at Colorado State University. The main feature of this new apparatus is separation of the MOT region, where we collect and cool ultracold atoms, from the plasma physics region, where we photoionize these ultracold atoms. The design of this apparatus is based off of BEC apparatus designs from experiments at JILA in Boulder, Colorado [42]. The purpose of the separation of the two regions is to independently optimize the MOT loading and plasma regions of the vacuum chamber. To transfer the atoms between regions, we can load the atoms from the MOT into a magnetic quadrupole trap. This trap is created by the same coils that create the magnetic field required for the MOT and are attached to a motorized translation stage.

In the plasma region, we have a set of seven cylindrically symmetric electrodes which were designed to produce electric potentials in a Penning trap configuration to axially confine both components of the plasma. These electrodes would block optical access to the MOT if they were placed in the same region, which would disrupt the collection of ultracold atoms needed for the experiments. Outside of the vacuum chamber, we were able to wrap various configurations of magnetic coils which we use for our experiments. To characterize the UCP, we use an extracted electron signal to detect the rate of electron escape on a micro-channel plate detector. This chapter will detail all of the design considerations that went into the construction of this apparatus as well as calculations and measurements that detail the system performance.

### 1.4.3 Chapter 4: UCP Response to Short Bursts of RF

As discussed in Chapter 2, a fundamental class of responses of UCPs to externally applied rf fields is the plasma oscillation. Although these responses occur in a variety of ways, the key feature of the plasma oscillation is that it typically depends on only the density of the constituent particles of the plasma. These means that driving a plasma oscillation on resonance can be a useful tool for determining the density of UCPs.

The technique developed to measure the density of the UCPs in our system uses two cycles of rf to drive a plasma oscillation at a chosen point in the UCP evolution. Through the course of our investigations, we were able to determine that the rf drove a collisionless oscillation of the UCP electron cloud where the electron cloud moved collectively in response to the rf. By modeling this

response for finite size, non-uniform density plasmas, we were able to determine the expected peak density (and through this the rms size) of a UCP based on the measured resonant frequency and the imbalance of electrons and ions in the UCP. This technique for measuring the density in our UCPs was essential, as other methods that have been developed using continuous rf have limited applicability for our system since the collisionless motion dominates the rf response signals [14, 18]. Also, measuring the density at specific points in the UCP evolution allows for us to measure the expansion rate and to make expansion rate comparisons over a range of UCP conditions. This will allow us to make comparisons to model calculations and serves as our main measurement technique for all of the UCP experiments discussed in this thesis.

### 1.4.4 Chapter 5: Electron Evaporative Cooling in UCP Systems

One of the main goals of many UCP experiments is to achieve more strongly-coupled plasmas, with many experiments focusing on the ion component of the UCP. Early experimental and theoretical work has shown that electron component of the UCP is limited by three-body recombination processes to $\Gamma_e \sim 0.2$ [18, 19]. This limit to the strong-coupling parameter for the electrons occurs even when the ions are able to evolve into the strongly-coupled regime [32]. However, the parameter range under which these models were evaluated have negligible loss of energy from the UCP through evaporative cooling.

In this chapter, I will discuss a model that we developed that shows that for our relatively low density UCPs, that electron evaporative cooling should have a significant effect on the amount of energy that is available to drive the UCP expansion compared with other experiments. Measurements of the expansion of our UCPs showed that the expansion energy was indeed reduced by a significant amount. By inputting our electron evaporation data into our evaporative cooling model, we were able to predict the electron temperature evolution of the UCP. These calculations showed that it may be possible for the electron strong-coupling parameter, $\Gamma_e$, to exceed the 0.2 theoretical limit in [18, 19] before there is a significant three-body recombination rate to heat the electrons. Subtle heating effects may still be present, and will require the development of a direct temperature measurement technique in our systems. However, these measurements show that electron evaporative cooling can be significant in our system, and should lead to future experiments where we forcibly cool the electrons using evaporation.

### 1.4.5 Chapter 6: Early Time UCP Expansion in a Uniform Magnetic Field

For many UCP experiments that we wish to perform, we will create the UCP in the presence of a magnetic field that is axially symmetric to our electrodes assembly. The presence of the magnetic field can help extract the electrons from the plasma region to our detector in some situations and also will work to radially confine the electrons and ions in the Penning trap configuration. So, determining the effects of the magnetic field on the formation and evolution of the UCP will be important for separating the effects of the presence of a magnetic field from other effects that we might wish to study.

Our measurements of the UCP expansion rate at early times show that in the presence of a relatively weak magnetic field ($\sim$10 G, much weaker than the $\sim$1000 G fields that will be used in the Penning trap), that there is a dramatic increase in the UCP expansion rate compared to the magnetic field free case. To gain an understanding of the underlying mechanism to this increased expansion, we developed a model of UCP formation that determines the steady state distribution of electrons after the UCP forms if the electrons' motion is strictly confined to the magnetic field lines. For these calculations, we found that the electrons would move to screen the electric field in the axial direction, but would leave the radial field unscreened. This unscreened field would increase the ion expansion in the radial direction. Investigations into this effect are still under way, and the preliminary results of this line of investigation will be presented in this chapter.

### 1.4.6 Chapter 7: Two-Photon Light-Assisted Collisions in an $^{85}$Rb MOT

The experiments described in Chapter 7 detail measurements that were made before the construction of our UCP apparatus during my early tenure as a graduate student. In these measurements, we applied additional light resonant on the $5P_{3/2} - 5D_{5/2}$ transition to an $^{85}$Rb MOT. The original goal of this work was to excite to auto-ionizing states of Rb through this excitation as a possible method for creating a UCP without the need for a dye-laser system to directly photo-ionize the atoms. This type of auto-ionizing state had been observed in previous work using different transitions in Rb. Instead, we observed a large loss rate consistent with two-body, light-assisted collisions that did not have enough energy to produce Rb ions. The second excitation in the MOT put long-range Rb molecules in a long-lived excited state that carried the molecule towards close internuclear separation. The subsequent decay of the molecule to a lower excited state put the

atom pair on a molecular curve that accelerated the atoms to speeds that ejected them from the MOT. The loss mechanism will be important for any experiments that involve transitions to this type of excited state.

### 1.4.7 Chapter 8: Future Work

The discussion in Chapter 8 will focus on the experiments that have been planned for the next few years of work on this project. The first goal is to finish the investigation of the increased expansion rate that is observed for UCPs formed in the presence of a magnetic field, discussed in Chapter 6. After this, the next planned experiment focuses on the response of the electron cloud to two sharp electric field pulses as discussed in Chapter 4. These measurements showed a damped, oscillating response to the electric field impulses. The goal of this experiment is to characterize this damping behavior, and to attempt to relate the damping time constant to electron-ion 90 degree deflection times.

The next experiment will involve the development of a local temperature probe that can measure the temperature of the electrons at a specified point in the UCP evolution. The goal is to have an independent measure of the electron temperature that does not rely on the overall UCP expansion rate. Preliminary techniques to measure the temperature using ramps between electric field levels have been attempted, but require a better characterization of the electric field environment to produce consistent results. The development of a temperature probe will allow us to compare the results of this measurement to those of the temperature profile obtained from our expansion measurements. We wish to confirm that the electron strong coupling parameter, $\Gamma_e$, does indeed exceed the 0.2 limit [18, 19]. We also wish to test whether forced evaporative cooling on the electrons can be effective in lowering the electron temperature.

After the development of these techniques for characterizing the UCP, we will begin experiments trapping the UCP in a Penning trap. The goal of these experiments will be to measure long timescale plasma processes such as the electron-ion thermalization rate and ion-ion collision rates, which are very slow compared to the lifetime of the UCP outside of the trap. Also, we will be able to study the physics associated with loading the Penning trap, and develop techniques to characterize and optimize the loading of the Penning trap.

These are just examples of the proposed measurements for this system, and a detailed description of these, among other experiments, will be given in Chapter 8.

## Conclusion

To summarize, ultracold plasma (UCP) systems can be used to study a wide range of plasma phenomena near the strongly-coupled regime. These systems can be used to test plasma theoretical model predictions. They can be used to find breakdowns in classical plasma physics theory as assumptions used in those theoretical calculations are no longer valid at the very low electron temperatures in UCP systems. UCPs systems can also be used to make experimental comparisons to wide variety of more sophisticated plasma physics theories that take strong-coupling physics into account. Also, these systems will provide a valuable tool that can be used to make comparisons to analogous astrophysical systems. These systems help us understand not only certain astrophysical plasmas such as the core of Jupiter and the core of the sun, but also can used to model the dynamics of globular clusters. Also, the measurements made on recombination processes in UCP systems can be useful for understanding the formation of anti-hydrogen in nested Penning traps.

The experiments in this thesis focus on techniques that allow us to characterize the state of the UCP systems that we create. The first experiment that we performed involved the UCP response to short bursts of externally applied rf fields which allowed us to determine the density of the UCP as a function of time. From these expansion rates, we were able to make comparisons to theoretical models of the UCP expansion to determine the effect of electron evaporative cooling and externally applied magnetic fields to the UCP expansion. Understanding these mechanisms will allow us to make future attempts at pushing the electron component of the UCP closer to the strong-coupling limit. Also, future experiments will involve loading the UCP in a nested Penning trap configuration, which will allow us to study relatively long timescale UCP processes.

## References for Chapter 1


[1] T. C. Killian, S. Kulin, S. D. Bergeson, L. A. Orozco, C. Orzel, and S. L. Rolston, Phys. Rev. Lett. **83**, 4776 (1999).

[2] S. Ichimaru, Rev. Mod. Phys. **54**, 1017 (1982).

[3] J. J. Bollinger, J. M. Kriesel, T. B. Mitchell, L. B. King, M. J. Jensen, W. M. Itano, and D. H. E. Dubin, J. Phys. B: At. Mol. Opt. Phys. **36**, 499-510 (2003).

[4] T. Pohl, T. Pattard, and J.M. Rost, Phys. Rev. Lett. **92**, 155003 (2004).

[5] F. Anderegg, D. H. E. Dubin, T. M. O'Neil, and C. F. Driscoll, Phys. Rev. Lett. **102**, 185001 (2009).

[6] Y. Hahn, Phys. Lett. A **231**, 82 (1997).

[7] A. V. Lankin and G. E. Norman, J. Phys. A: Math. Theor. **42**, 214042 (2009).

[8] T.C. Killian, T. Pattard, T. Pohl, J.M. Rost, Phys. Reports **449**, 77-130 (2007).

[9] H. J. Metcalf and P. van der Straten, *Laser Cooling and Trapping* (Springer-Verlag, New York, 1999).

[10] M. P. Robinson, B. L. Tolra, M. W. Noel, T. F. Gallagher, and P. Pillet, Phys. Rev. Lett. **85**, 4466 (2000).

[11] R. S. Fletcher, X. L. Zhang, and S. L. Rolston, Phys. Rev. Lett. **96**, 105003 (2006).

[12] S. D. Bergesonand R. L. Spencer, Phys. Rev. E **67**, 026414 (2003).

[13] A. Lyubonko, T. Pohl, and J. M. Rost, New J. Phys. **14**, 053039 (2012).

[14] K. A. Twedt and S. L. Rolston, Phys. Rev. Lett. **108**, 065003 (2012).

[15] T. M. Wilson, W. T. Chen, and J. L Roberts, Phys. Rev. A **87**, 013410 (2013).

[16] D. Comparat, T. Vogt, N. Zahzam, M. Mudrich and P. Pillet, Mon. Not. R. Astron. Soc. **361**, 1227-1242 (2005).

[17] G. Gabrielse, S.L. Rolston, L. Haarsma, and W. Kells, Phys. Lett. A **129**, 38 (1988).

[18] S. Kulin, T. C. Killian, S. D. Bergeson, and S. L. Rolston, Phys. Rev. Lett. **85**, 318 (2000).

[19] F. Robicheaux, and J. D. Hanson, Phys. Rev. Lett. **88**, 055002 (2002).

[20] J. H. Choi, B. Knuffman, X. H. Zhang, A. P. Povilus, and G. Raithel, Phys. Rev. Lett. **100**, 175002 (2008).

[21] Private communication with M. S. Murillo, Los Alamos National Laboratory.

[22] J. P. Morrison, C. J. Rennick, and E. R. Grant, Phys. Rev. A **79**, 062706 (2009).

[23] M. Robert-de-Saint-Vincent, C. S. Hofmann, H. Schempp, G. Gunter, S. Whitlock, and M. Weidemüller, Phys. Rev. Lett. **110**, 045004 (2013).

[24] L. Spitzer, Jr., *Physics of Fully Ionized Gases* (Dover, New York, 1962).

[25] E. E. Salpeter, Ap. J. **181**, L83 (1973).

[26] H. C. Graboske, J. B. Pollack, A. S. Grossman, and R. J. Olness, Ap. J. **199**, 265 (1975).

[27] S. Ichimaru, Rev. Mod. Phys. **65**, 255 (1993).

[28] E. E. Salpeter and H. M. van Horn, Ap. J. **155**, 183 (1969).

[29] M. Bonitz, C. Henning, and D. Block, Rep. Prog. Phys. **73**, 066501 (2010).

[30] R. W. Lee *et al*, J. Opt. Soc. Am. B **20**, 770 (2003).

[31] M. Koenig *et al*, Plasma Phys. Control. Fusion **47**, B441?B449 (2005).

[32] T. Pohl, T. Pattard, and J. M. Rost, Phys. Rev. Lett. **94**, 205003 (2005).

[33] A. Denning, S. D. Bergeson, and F. Robicheaux, Phys. Rev. A **80**, 033415 (2009).

[34] Y. Hahn, Phys. Rev. E **64**, 046409 (2001).

[35] M. Lyon, S. D. Bergeson, and M. S. Murillo, Phys. Rev. E **87**, 033101 (2013).

[36] P. Gupta, S. Laha, C. E. Simien, H. Gao, J. Castro, T. C. Killian, and T. Pohl, Phys. Rev. Lett. **99**, 075005 (2007).

[37] M. E. Glinsky and T. M. O'Neil, Phys. Fluids B **3**, 1279 (1991).

[38] R. S. Fletcher, X. L. Zhang, and S. L. Rolston, Phys. Rev. Lett. **99**, 145001 (2007).

[39] S. G. Kuzmin and T. M. ONeil, Phys. Plasmas **9**, 3743 (2002).

[40] N. Rock, A. Wilkins, M. Lyon, and S. D. Bergeson, DAMOP 2012 Meeting, K1.00095

[41] T. Pohl, T. Pattard, and J. M. Rost, J. Phys. B: At. Mol. Opt. Phys. **37**, L183 (2004).

[42] H. J. Lewandowski, D. M. Harber, D. L. Whitaker, and E. A. Cornell, J. Low Temp. Phys. **132**, 309 (2003).

# Chapter 2

# Overview of Relevant Plasma Physics Theory

While plasma physics covers a broad range of phenomena for a wide variety of plasma systems, to better understand ultracold plasma (UCP) systems, we can draw upon several concepts that are discussed in many introductory plasma physics textbooks. Although the usual assumptions made in formulating the most common 'textbook' treatments of the topics discussed in this chapter will not be valid for certain parameter ranges in UCP systems, these concepts will allow us to discuss our experiments in terms that are familiar to someone with knowledge of basic plasma systems. In fact, this breakdown of the assumptions made for basic plasma systems is one of the reasons that UCP systems are interesting to study.

In this chapter, I will discuss collective effects (such as Debye screening and plasma oscillations), collisional processes, and give a brief overview of some of the models of plasma dynamics (which help us understand how to model the expansion of UCPs). In the later chapters discussing our UCP experiments, I will refer back to concepts discussed in this chapter to in order to better frame the discussion of our experiments. This chapter is intended only to be an overview, and when appropriate, more sophisticated modeling and calculations that concern the specific experiments discussed in this thesis will be discussed in the chapters corresponding to those experiments. Although the concepts discussed here are not explicitly measured in the work presented in this thesis, it will be necessary to understand these concepts in order to interpret the overall behavior of the UCPs created in our system.

## 2.1 Debye Shielding

A fundamental property of plasmas is the ability of the constituent particles to move in order to screen out electric fields inside the plasma. This screening occurs over a fundamental length scale that is known commonly as the Debye screening length, $\lambda_D$, which is dependent, as most plasma properties are, on the temperature and density of the particles in the plasma. For ultracold plasma systems, the screening length sets the minimum size for forming a UCP [1], where the rms size of the UCP must be greater than the Debye screening length upon formation.

To determine the Debye screening length for a certain set of UCP conditions, we can consider the standard textbook treatment of Debye screening, in which a test particle with positive charge $q_T$ is placed slowly in a neutral, uniform distribution of ions and electrons in thermal equilibrium [2, 3]. When the test particle is inserted into the plasma, charges of like sign will be repelled and charges of opposite sign will be attracted. However, since the ions are much more massive than the plasma electrons, we will consider the ions to be immobile for simplicity. Since we are considering a slow perturbation upon insertion of the test particle, the density of the plasma particles in relation to the test particle can be written from the Boltzmann relation as [3],

$$n_e(r) = n_{e0} \exp\left(\frac{e\Phi(r)}{k_B T_e}\right) \tag{2.1}$$

where $e$ is elementary charge (positive), $k_B$ is Boltzmann's constant, $\Phi$ is the potential, and the test particle is considered to be centered on the origin. Before the test particle is inserted, $\Phi(r) = 0$ and the density is uniform over all space. So, using this relation, we can write down Poisson's equation with the test particle inserted as,

$$\begin{aligned} \nabla^2\Phi(r) &= -\frac{\rho(r)}{\epsilon_0} \\ &= -\frac{1}{\epsilon_0}\left(q_T\delta(r) - en_{e0}\exp\left(\frac{e\Phi(r)}{k_B T_e}\right) + en_{i0}\right) \end{aligned} \tag{2.2}$$

If we consider the perturbation from the test particle to be small, then we can assume that $e\Phi \ll k_B T$ [2, 3]. So, we can expand the exponential term to be $\sim (1+e\Phi/k_B T)$. Since the initial electron and ion densities are equal, Equation 2.2 reduces to,

$$\nabla^2\Phi(r) = -\frac{1}{\epsilon_0}\left(q_T\delta(r) - \frac{n_{e0}e^2\Phi(r)}{k_b T_e}\right) \tag{2.3}$$

We can rearrange the terms to get,

$$\nabla^2\Phi(r) - \frac{n_{e0}e^2}{\epsilon_0 k_B T_e}\Phi(r) = -\frac{q_T}{\epsilon_0}\delta(r) \tag{2.4}$$

Here, we can define the Debye screening length to be,

$$\lambda_D = \sqrt{\frac{\epsilon_0 k_B T}{n_{e0}e^2}} \tag{2.5}$$

so that,

$$\nabla^2\Phi(r) - \frac{1}{\lambda_D^2}\Phi(r) = -\frac{q_T}{\epsilon_0}\delta(r) \tag{2.6}$$

With the assumption that $\Phi(\infty) = 0$ and that the potential becomes the standard Coulomb potential as $r \to 0$, this differential equation can be solved to be,

$$\Phi(r) = \frac{q_T}{4\pi\epsilon_0 r}\exp\left(-\frac{r}{\lambda_D}\right) \tag{2.7}$$

So, we can see from Equation 2.7 that the normal Coulomb potential from the test charge is screened out exponentially on a length scale determined by the Debye screening length. For an externally applied electric field, the existence of a plasma mode accounts for the screening for applied electric fields at frequencies that are much less than the plasma frequency (the plasma frequency is defined in Section 2.2) [4].

While the Debye screening length provides a reference scale length for plasma systems, the assumptions made in this derivation are not always valid for UCP systems. For instance, the assumption of a Maxwell-Boltzmann distribution for the electrons will not be true of UCPs with sufficiently high initial ionization energies. Also, for collisionless plasmas, a paradox arises. As electrons accelerate towards a positive test charge, the density of the electrons should actually decrease in order to conserve particle flux [3]. This results in what is known as anti-shielding, where the test charge actually has more positive charge from the plasma around it. However, more sophisticated modeling of dynamic screening, in which electrons can become trapped in adiabatically produced potential wells around the test particle, produce shielding in collisionless plasmas where anti-shielding was predicted from less sophisticated models [5, 6].

For the UCPs produced in our system, we have densities that range from $\sim 10^7$-$10^8$ /cm$^3$ and initial ionization energies ranging from $\Delta E/k_B = 10 - 400$ K. If we take the temperature of the UCP electrons to be $2\Delta E/3k_B$, then an estimate for the Debye screening length for our system ranges from $\lambda \sim 20 - 350$ $\mu$m. These lengths are all less than the $\sim$1 mm spatial extent of the system, $\sigma$ (where the density in spherical coordinates is given by $n(r) = n_0 \exp(-r^2/2\sigma^2)$). So, for many of our UCP conditions, we expect any external electric fields to be well screened in the center of the plasma as well as fields owing to variations in the ion and electron density far away from the center of the plasma. Although UCPs do not have a uniform density distribution as assumed in

this calculation, for very short screening lengths compared to the size of the UCP, this derivation should be a reasonable approximation for the screening length around a point using the local value of the UCP density.

## 2.2 Plasma Oscillations

One fundamental response to perturbations of the charge distributions in plasma systems is the plasma oscillation. As charge is moved, either through forces from external electric fields or thermal fluctuations, the unscreened charge creates an electric field and restoring force on the perturbed charges to oppose the displacement. To understand the nature of this response to charge density perturbations in a simple and computationally tractable system, we can examine restoring force on an uniform density, infinite, two-component plasma where the charge densities for the positive and negative charges are offset from each other by a distance, $\Delta x$. This is a standard textbook treatment of plasma oscillations [2, 3].

A diagram of the physical situation under consideration for this calculation can be seen in Figure 2.1. Here, we consider two infinite, uniform density charge distributions consisting of positively charged ions and electrons with density distributions of $n_{i/e} = n_0$. Initially, the plasma is neutral everywhere until a perturbation is introduced that offsets a slab of the electron distribution from the ion distribution by a distance $\Delta x$. When this offset occurs, two regions of space develop where the charge distribution is no longer neutral, creating two infinite slabs of charge at $\rho = \pm e n_0$ respectively. These two slabs will create an electric field that is non-zero between them with a field outside that remains at zero (this is because for infinite slabs of charge, the field does not fall off with distance and therefore the positive and negative slabs neutralize the field on the outside). To calculate the field produced by the offset of the charge distributions, we can uses Gauss' law with the appropriate choice of a Gaussian surface. In this case, it is convenient to use a cylindrical pill box, with end caps of surface area, $A$, as seen in Figure 2.1. Gauss' law is given by,

$$\oint_S \vec{E} \cdot d\vec{A} = \frac{Q_{enc}}{\epsilon_0} \tag{2.8}$$

Here, the amount of charge enclosed in our Gaussian surface is given by $Q_{enc} = e n_0 A \Delta x$. Our choice of Gaussian surface aligns the electric field perpendicular to the face of the end cap of our

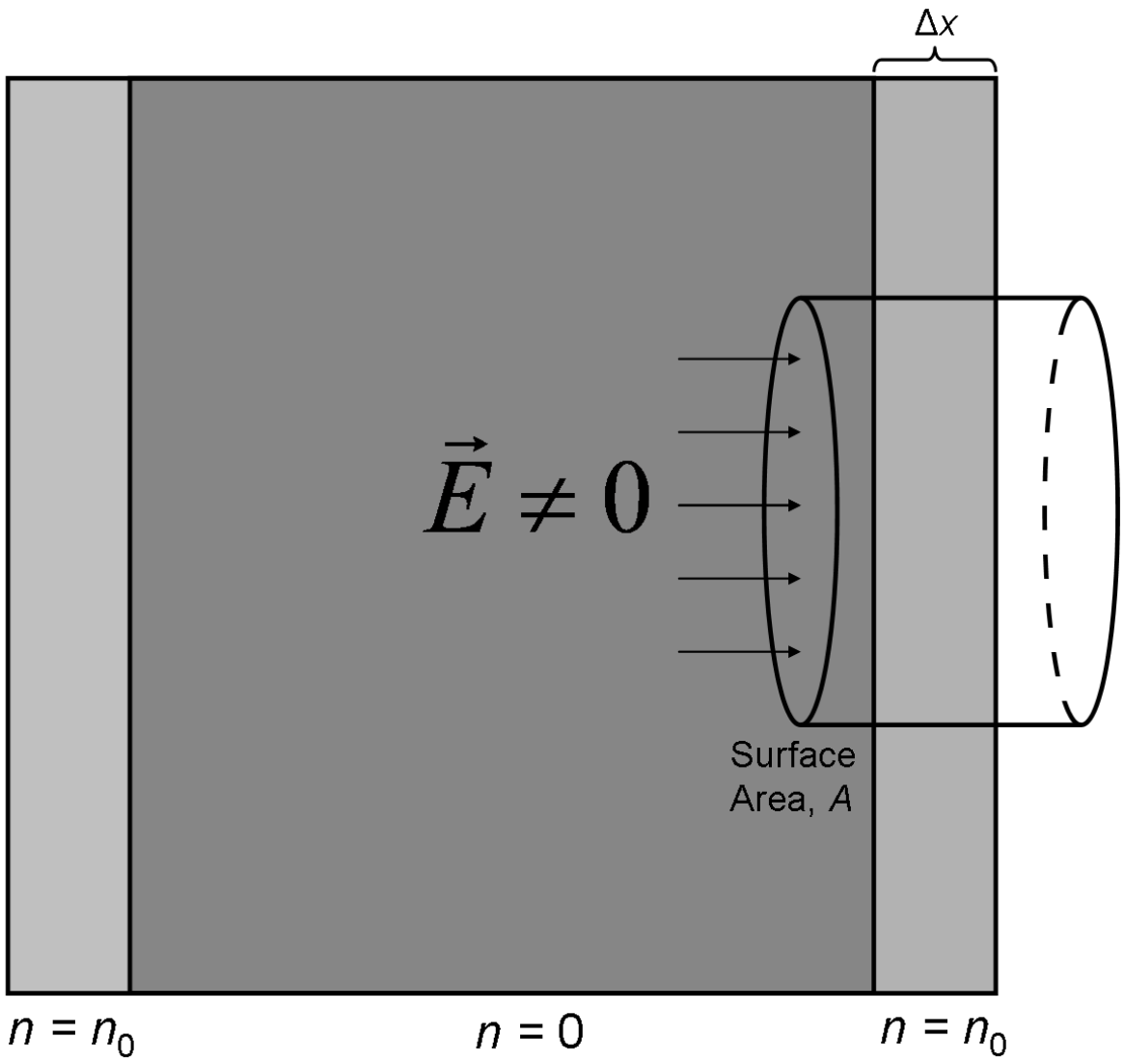


Figure 2.1: A standard textbook treatment of plasma oscillations using infinite slabs of positive and negative charge [2, 3]. When the slabs are offset from each other by a distance $\Delta x$, it creates region in space where the charge is no longer neutralized, creating a non-zero electric field. To calculate the electric field, we can use Gauss' law with a cylindrical pill box with end caps of surface area, $A$, used as the surface for the calculations. The electric field produces a restoring force on the slab of charge that will create simple harmonic motion at the plasma frequency, $f_p$.

pill box, so,

$$\oint_S \vec{E} \cdot d\vec{A} = |\vec{E}|A = \frac{en_0 A\Delta x}{\epsilon_0} \tag{2.9}$$

So,

$$|\vec{E}| = \frac{en_0\Delta x}{\epsilon_0} \tag{2.10}$$

Since the ions are much more massive than the electrons, we can consider them to be stationary and calculate the restoring force on the electron component of the plasma. So, from Equation 2.10, we can calculate the restoring force on the electrons to be

$$F = m_e\frac{d^2\Delta x}{dt^2} = -\frac{e^2 n_0}{\epsilon_0}\Delta x \tag{2.11}$$

Putting this in a more familiar form, we obtain,

$$\frac{d^2\Delta x}{dt^2} = -\frac{e^2 n_0}{m_e\epsilon_0}\Delta x = -\omega_p^2\Delta x \tag{2.12}$$

where $\omega_p = \sqrt{e^2 n_0/m_e\epsilon_0}$ is defined as the angular plasma frequency for the electrons (the plasma frequency of oscillation is defined as $2\pi f_p = \omega_p$). It should be noted that this derivation for the plasma frequency is for "cold" electrons, meaning that the thermal motion of the electrons is ignored. This assumption is generally true for UCP systems. The plasma frequency for the ions (or any other species of particles in the plasma) can be found by substituting the ion mass and density into the formula for the plasma frequency. For two-component systems, the actual plasma frequency is found by summing the frequency of the component species in quadrature. However, since the ion mass is much greater than the electron mass, the plasma frequency is approximately equal to the plasma frequency of the electrons alone.

We can note that the plasma frequency for the electrons depends only on one variable, the electron density, $n_0$. So, exploiting this relationship by driving the plasma with external AC electric fields can be useful as a probe for determine the density of plasma systems as will be shown in this thesis. Dependence on only the density allows us to determine a simple relationship for the plasma frequency as a function of density given by [2],

$$f_p = \frac{\omega_p}{2\pi} \sim 8980\sqrt{n_0} \quad \text{Hz} \tag{2.13}$$

where $n_0$ is in units of $\mathrm{cm}^{-3}$.

Since this plasma frequency was derived from a uniform, infinite plasma, this situation will not apply directly to UCP systems. However, it will serve as a good reference for the models of the UCP response to externally applied rf fields. Also, there are many other types of plasma resonances, collective modes, and plasma waves that can be excited for UCP systems when subjected to external fields [7–10]. These resonances provide great insight into the fundamentals of UCP physics [7, 8] and can be used as probes to determine the UCP density [9, 10] with progress towards electron temperature measurements [7]. Additional details on plasma oscillations in UCPs are given in Chapter 4 of this thesis.

## 2.3 Coulomb Collisions

When studying relaxation to equilibrium in plasmas, the primary mechanism for establishing thermal equilibrium is through coulomb collisions between the constituent particles of the plasma. These collisions are of particular interest in ultracold plasma systems when considering temperature equilibration and its effects on modeling the plasma system. For UCP systems, the electrons and ions are created out of thermal equilibrium with respect to each other and the electron-ion equilibration process is much longer than the natural lifetime of the UCP as it expands and falls apart. For the electrons themselves, these timescales can range from very short to very long in comparison to the lifetime of the UCP depending on the initial ionization energy of the UCP owing to the $T^{3/2}$ scaling of the of the equilibration timescale as will be shown in this section.

The most important aspect of Coulomb collisions as opposed to other types of binary collisions is the long range nature of the Coulomb force. This means that collisions between particles that are very far apart (which produce only small deflections in the particle trajectories) are the most important contribution in the collision process. When calculating the total collision cross section for charged particle collisions, there is a divergence at low collision angles (high impact parameter) that complicates the calculations for these collision processes [2, 3, 11] because the geometric pair-number increases more rapidly than the $1/r$ potential falls off. These low angle collisions at high impact parameter can not be ignored, as it turns out that they are the much more likely to produce large changes to the momentum of particles in a cumulative fashion than a single large collision.

However for plasmas, Debye screening will work to eliminate fields that are outside of a Debye length from the particles involved in the collision, which sets an upper limit to the possible impact parameters (lower limit for the collision angle) for possible Coulomb collisions at a Debye length. This will allow us to calculate the collision rates and equilibration timescales for the constituent particles in a plasma.

### 2.3.1 Collision Timescales Between Plasma Particles

Collision processes in plasma systems play a very important role in non-equilibrium dynamics and work to transfer energy and establish thermal equilibrium among the constituent particles of the system. Upon formation of the UCP, the electrons and ions are not in thermal equilibrium with each other and do not individually start out in a Maxwell-Boltzmann distributions. As the UCP evolves, the particles in the UCP will work towards establishing a quasi-equilibrium. The electrons being far more mobile particles in the system will be able to establish an equilibrium distribution among themselves (although still not quite Maxwell-Boltzmann because of the finite potential well depth provided by the ions) while transferring energy to the ions as the UCP expands.

When discussing collisions in our ultracold plasma systems, it is convenient to consider the possible types of collisions between particles and their associated timescales. While these collision timescales are not directly measured for the UCPs in our system, they do serve as a means of estimating whether or not the charge distributions can be treated as being in thermal equilibrium. The timescales most important for our system involve either electron-electron interactions or electron-ion interactions. For electron-electron interactions, the first important timescale is a determination of how long it takes for a particle with $3/2k_BT$ of kinetic energy to undergo $3/2k_BT$ of energy changing collisions and is known as the electron self-equilibration time given by [11],

$$t_{se} = \frac{0.266\, T_e^{3/2}}{n_e \ln(\Lambda)} \quad \text{sec} \tag{2.14}$$

where $n_e$ is in units of $\text{cm}^{-3}$ and $T_e$ is in units of K. The logarithmic term in the denominator is the Coulomb logarithm and is defined as $\ln(\Lambda) = \ln\left(12\pi n_e \lambda_D^3\right)$ where $\lambda_D$ is the Debye screening length. The temperature term, $T_e$, represents the average kinetic energy associated with a distribution of electrons that will thermalize to a temperature $T_e$ since the distribution of electrons is not initially in thermal equilibrium by definition. The self equilibration timescale can be seen to scale as

approximately $T_e^{3/2}/n_e$, since the $\ln(\Lambda)$ is a slowly varying function of the density and temperature. This means that higher energy, lower density electrons take a longer time to thermalize.

The second electron-electron interaction timescale of interest is the electron equipartition time, which defines the cross-dimensional thermal relaxation time. This timescale is of particular importance when discussing the collisional redistribution of externally imparted energy from applied rf in our UCP systems, which is discussed further in Chapter 4. The electron-electron equipartition time is given by [11],

$$t_{eq} = \frac{5.87\, T_e^{3/2}}{\sqrt{229.5}\, n_e \ln(\Lambda)} \quad \text{sec} \tag{2.15}$$

where again $n_e$ is in units of $\text{cm}^{-3}$. It can be seen here that $t_{eq}$ and $t_{se}$ have the same scaling in temperature and density, but differ in the value of their pre-factors. The ratio of the two times, $t_{eq}/t_{se}$ is found to be $\sim$1.46.

For our UCP systems, these timescales can range from 10s of ns to 10s of $\mu$s when calculated using the average density and estimated temperature, which will allow us to study the physics of these ultracold plasmas in a regime where collisions are important and in a regime where we can treat the UCP as a collisionless fluid. However, UCPs have a non-uniform density and start with a uniform electron energy distribution. This complicates the exact meaning of these collision timescales, and are used as only estimates until accurate measurements can be made to compare to these calculations. More sophisticated modeling of collisions in UCP systems has shown that reaching an energy distribution that is close to Maxwellian at the highest part of the energy distribution can take several times longer than these calculated collision timescales [12]. Also, since the collision timescales for the electrons are functions of the Coulomb logarithm, $\ln(\Lambda)$, these theoretical predictions for the collision timescales are expected to break down when the electron component of the UCP approaches the strong-coupling limit. This is because the value of $\ln(\Lambda)$ can actually become negative in this regime, making the collision timescales determined from Equations 2.14 and 2.15 nonsensical.

While electron self-collisions can occur on a short timescale relative to the UCP natural lifetime and work towards creating a thermal electron distribution upon ionization, the ions themselves begin with a thermal distribution that is approximately equal to that of the original ultracold atom distribution. However, the ions quickly heat to temperatures of $\sim$1 K owing to disorder-induced

heating (see Chapter 1). Since the dominant ion motion is due to expansion, ion-ion collisions are generally neglected in UCP systems. However, the ions do have collisional interactions with the electrons that are most important for randomizing the electron motion. This can cause a damping of the electron motion when driven by an external rf field as discussed in Chapter 4.

To determine the timescale of electron-ion collisions, we define the time we are interested in as the amount of time it takes to have a net 90 degree deflection from an electron's original trajectory resulting from collisions [2, 11]. As discussed previously, small angle collisions play a dominant role in collisional processes in plasmas, so from this assumption, the mean free path of an electron for a net 90 degree change from its original trajectory owing to small angle collisions is given by [2, 11],

$$\lambda_m = \frac{(12\pi\epsilon_0 k_B T_e)^2}{8\pi n_e e^4 \ln(\Lambda)} \tag{2.16}$$

We can divide $\lambda_m$ by the mean thermal velocity of an electron given by $v_T = \sqrt{3k_B T/m_e}$ to determine the 90 degree collision time as given by [2, 11],

$$t_{90} = \frac{2\pi\epsilon_0^2\sqrt{m_e}\,(3k_B T)^{3/2}}{10^6 n_e e^4 \ln(\Lambda)} \quad \text{sec} \tag{2.17}$$

where $n_e$ is in units of $\text{cm}^{-3}$. Again, it can be noted that $t_{90}$ scales as $T_e^{3/2}/n_e$ with an additional, slowly varying Coulomb logarithm term, $\ln(\Lambda)$. The electron-ion collision timescale is on the order of the electron-electron collisional timescales and falls in between $t_{se}$ and $t_{eq}$. An example of the collision timescales over a range of temperatures and densities relative to our UCP experiments can be seen in Table 2.1.

Although these calculations can provide estimates of the collisional timescales in UCP systems, the UCPs created in our system have a non-uniform density distribution which differs from the standard "textbook" assumptions used when calculating the collision timescales. This could result in significant modifications to the predicted collision rates. Also, when the UCP approaches the strong coupling regime, these calculations are expected to break down as mentioned above. Aside from the breakdown of the Coulomb logarithm term, the collision rate in a one-component plasma has been shown to be enhanced by strong correlations [13]. This occurs because higher correlation leads to better screening of the repulsive Coulomb potential between like charges, allowing collisions to occur at closer range. This scaling can actually be quite strong, as the collision rate was observed to scale exponentially with the strong coupling parameter for $\Gamma > 1$. For two component ultracold

Table 2.1: A table of the electron self-equilibration time, $t_{se}$, in units of $\mu$s over a range of temperature and density conditions which are relevant to our UCP experiments. To find the electron equipartition time, $t_{eq}$, and the 90 degree deflection time, $t_{90}$, the values in this table can be divided by 0.69 and 1.39 respectively.

| $n_e(\mathrm{cm}^{-3})$ \ $T_e(\mathrm{K})$ | 1 | 10 | 25 | 50 | 100 | 200 |
|---|---|---|---|---|---|---|
| $5\times10^6$ | 0.03 | 0.33 | 1.02 | 2.48 | 6.17 | 15.6 |
| $1\times10^7$ | 0.02 | 0.17 | 0.54 | 1.3 | 3.22 | 8.08 |
| $5\times10^7$ | 0.01 | 0.04 | 0.12 | 0.29 | 0.71 | 1.77 |
| $1\times10^8$ | 0.01 | 0.02 | 0.07 | 0.15 | 0.37 | 0.92 |

plasma systems, this process becomes more complicated, as the electron component of the UCP screens out the potential from the ions, reducing their correlation energy [14]. Such a scaling of the collision rates with the strong coupling parameter has not been calculated for UCP systems. To start, the scaling of the collision rate for UCP outside the strongly-coupled regime has yet to be measured, which will be necessary in order to observe any type of collisional enhancement owing to strong coupling.

## 2.4 Models of Plasma Dynamics

Plasma dynamics can be modeled in many different ways, and as with any model, one needs to consider the situation in order to determine what level of sophistication is needed to understand the relevant physics of the system. In this section, I will outline several methods for modeling plasma dynamics and discuss the applicability of each method. These methods include dynamic particle simulations, models of the evolution of phase space distributions, and fluid models among others. For UCP systems, each of these methods have been implemented in order to model the dynamics of UCP systems under a variety of conditions.

The simplest model setup, yet potentially the most computationally intensive, is the dynamic particle simulation [15]. In this method, individual particles can be tracked along with their interactions with each other. Because of the $1/r^2$ dependence of the Coulomb force, this method can be troublesome in a variety of different ways. First, the Coulomb force is long range, meaning that interactions between many particle pairs must be taken into account when modeling the plasma dynamics. Also, at short range, numerical instabilities can develop if particles approach too close

to each other during any particular time step. Therefore, these types of simulations can require very short time steps and also suffer greatly from $N^2$ type computation times. To model long timescale processes, these simulations can take many *months* to complete, and therefore are most useful when studying short timescale processes. However, modifications have been made using a mean field approximation to calculate the force on the electrons in a Monte Carlo simulation, which allowed for a model of longer timescale expansion dynamics in [12]. In general, these types of particle simulation methods are useful for modeling plasma dynamics that lead to electron escape.

Another method for modeling plasmas is by tracking the phase-space distributions of the ions and electrons as they evolve in time. The evolution of the phase space distribution for a spherically-symmetric plasma is governed by the Vlasov equation, which in three dimensions is given by [3],

$$\frac{\partial f(\vec{v},\vec{r},t)}{\partial t} + \vec{v}\cdot\frac{\partial f(\vec{v},\vec{r},t)}{\partial \vec{r}} + \frac{\partial}{\partial \vec{v}}\cdot(\vec{a}f) = 0 \tag{2.18}$$

where $f(\vec{v},\vec{r},t)$ is the phase space distribution of the ions or electrons in velocity and position space as a function of time and $\vec{a}$ is the acceleration of the particles in the plasma as governed by the Lorentz force. It should be noted that the Vlasov equation assumes a collisionless plasma which is generally not valid for most ultracold plasma systems. However, collisions cannot produce a net energy transfer in a spherically symmetric system because any transfer of energy owing to collisions is balanced by transfer back in the opposite direction. This allows for these solutions to be used to model the evolution of UCP systems. This method for modeling plasmas has been particularly useful for UCP systems as an exact solution of the Vlasov equation has been found for spherically symmetric, quasi-neutral, two-component plasmas in one [16] and three dimensions [17]. These models show a self-similar expansion that is driven by the thermal pressure of the electrons. This model is useful as it relates the expansion of the UCP to the initial electron temperature [18], which predicts that the rms size of the UCP changes as,

$$\sigma(t) = \sqrt{\sigma(0)^2 + \frac{k_B T_e}{m_i}\,t^2} \tag{2.19}$$

where $\sigma$ is the rms size of the plasma across one spatial dimension, $T_e$ is the temperature of the electrons, and $m_i$ is the mass of the ions. Expansion in ultracold plasmas has been shown to match the predictions of the Vlasov model in [19, 20]. Comparisons of expansion to this model have also allowed for the study of processes that alter the electron temperature at early times, such as

three-body recombination [18] and evaporative cooling (Chapter 5). This modeling has been useful for ultracold plasma physics because it produces results that can be directly compared to UCP expansion data without the need to run computationally intensive simulations.

Another model of plasma expansion treats the two components of the plasma as interacting fluids [12]. This model of the plasma expansion tracks the expansion of the ions as energy is transferred from the electrons. More details of this model are presented in Chapter 5, as we make modifications to this model to take into account the effect of electron evaporation on the electron temperature and ion expansion energy. Modifications to this model have also been made to account for the plasma expansion in two dimensions [21], which account for the expansion dynamics of plasmas that are no longer spherically symmetric.

## Conclusion

In this chapter, I have outlined several important fundamental concepts for plasma physics experiments as they relate to ultracold plasma systems. While many of these textbook phenomena are not directly applicable to UCP systems, they serve as a both a reference for understanding fundamental concepts in these systems as well as a starting point for a more sophisticated modeling approach. Many of these concepts will be discussed throughout this thesis in reference to our experimental parameters. Additional details on more sophisticated models that relate directly to UCP systems will be given in the relevant chapters concerning those topics.

## References for Chapter 2


[1] T. C. Killian, S. Kulin, S. D. Bergeson, L. A. Orozco, C. Orzel, and S. L. Rolston, Phys. Rev. Lett. **83**, 4776 (1999).

[2] D. A. Gurnett and A Bhattacharjee, *Introduction to Plasma Physics* (Cambridge University Press, 2005)

[3] P. M. Bellan, *Fundamentals of Plasma Physics* (Cambridge University Press, New York, 2006).

[4] A. V. Latyshev and A. A. Yushkanov, Theor. Math. Phys. **147**, 854 (2006).

[5] C. Hansen and J. Fajans, Phys. Rev. Lett. **74**, 4209 (1995).

[6] C. Hansen, A. B. Reimann, and J. Fajans, Phys. Plasmas **3**, 1820 (1996).

[7] R. S. Fletcher, X. L. Zhang, and S. L. Rolston, Phys. Rev. Lett. **96**, 105003 (2006).

[8] X. L. Zhang, R. S. Fletcher, and S. L. Rolston, Phys. Rev. Lett. **101**, 195002 (2008).

[9] S. Kulin, T. C. Killian, S. D. Bergeson, and S. L. Rolston, Phys. Rev. Lett. **85**, 318 (2000).

[10] K. A. Twedt and S. L. Rolston, Phys. Rev. Lett. **108**, 065003 (2012).

[11] L. Spitzer, Jr., *Physics of Fully Ionized Gases* (Dover, New York, 1962).

[12] F. Robicheaux and J. D. Hanson, Phys. Plasmas **10**, 2217 (2003).

[13] F. Anderegg, D. H. E. Dubin, T. M. O'Neil, and C. F. Driscoll, Phys. Rev. Lett. **102**, 185001 (2009).

[14] M. Lyon, S. D. Bergeson, and M. S. Murillo, Phys. Rev. E **87**, 033101 (2013).

[15] S. G. Kuzmin and T. M. O'Neil, Phys. Rev. Lett. **88**, 065003 (2002).

[16] A.V. Baitin and K. M. Kuzanyan, J. Plasma Phys. **59**, 83 (1998).

[17] D. S. Dorozhkina and V. E. Semenov, Phys. Rev. Lett. **81**, 2691 (2000).

[18] P. Gupta, S. Laha, C. E. Simien, H. Gao, J. Castro, T. C. Killian, and T. Pohl, Phys. Rev. Lett. **99**, 075005 (2007).

[19] S. Laha, P. Gupta, C. E. Simien, H. Gao, J. Castro, T. Pohl, and T. C. Killian, Phys. Rev. Lett. **99**, 155001 (2007).

[20] J. P. Morrison, C. J. Rennick, and E. R. Grant, Phys. Rev. A **79**, 062706 (2009).

[21] E. A. Cummings, J. E. Daily, D. S. Durfee, and S. D. Bergeson, Phys, Plasmas **12**, 123501 (2005).

# Chapter 3

# Ultracold Plasma Apparatus

In the previous chapters, I discussed the formation of ultracold neutral plasmas (UCPs) from photoionized ultracold atoms [1] as well as the details of some of the physics of strongly-coupled plasmas [2]. I also presented some of the background details on the physics of plasmas that are confined in a Penning trap configuration [3]. The Penning trap will allow for the study of long timescale plasma processes relative to the natural lifetime of UCPs such as the electron-ion thermalization rates and ion-ion collision rates [4]. I also presented much of the background physics that will be needed to understand the experiments presented in this thesis [5, 6].

To design an apparatus to perform experiments using UCPs, one must consider each step of the experiment separately and find the means to integrate each subsystem together. The main consideration for this apparatus was the creation of a Penning trap for a two-component UCP, which requires a particular configuration of electrodes and magnetic field environment in the UCP formation region. This electrode configuration would limit the optical access needed to cool and trap the ultracold atoms in the magneto-optical trap (MOT). Therefore it was necessary to separate the MOT region from the UCP region and transfer the ultracold atoms between the two using a magnetic quadrupole trap mounted to a motorized translation stage [7].

In this chapter, I will discuss each of the subsystems of this experimental setup and all of their components in detail. I will discuss the design considerations and equipment needed for the vacuum system, the lasers required for magneto-optical trapping and photoionization, the design of the magnetic trap and electrode assembly, and the charge detection system. The equipment used in this experiment is a combination of commercially available scientific equipment and equipment that was designed and constructed here at Colorado State University. The in-house designs will be detailed in this chapter as a reference for future users of this experimental apparatus.

## 3.1 Design of the Apparatus

The design of our ultracold plasma apparatus, seen in Figure 3.1, differed from those seen in typical UCP experiments and required special considerations in order to accommodate the complex electrical environment that was necessary for our planned experiments. The Penning trap electrode

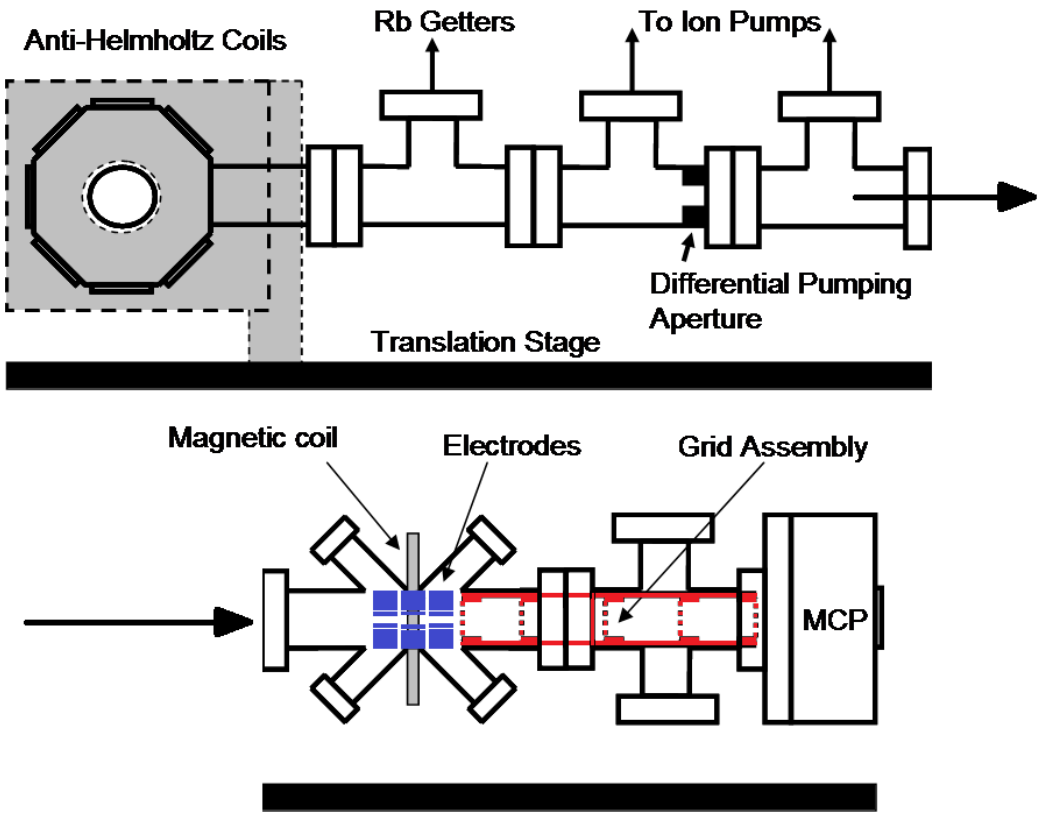


Figure 3.1: A diagram of the vacuum chamber used for the experiments described in this thesis. The diagram is split into two sections for clarity. The top and bottom sections of the diagram are connected at the arrows. MCP stands for micro-channel plate detector and is discussed in detail in Section 3.6. The electrodes assembly is highlighted in blue and the grids assembly is highlighted in red.

configuration that is used in the experiments detailed in this thesis consists of seven cylindrical copper electrodes which are described in detail in Section 3.4.1. This set of electrodes would eliminate the optical access needed to produce a MOT if the ultracold atom production and UCP creation took place in the same region of space as in other UCP experiments [1]. To eliminate this problem, we separated the MOT region from the plasma region in space, and optimized each region individually to produce the proper environment for both creating the MOT and for creating UCPs. The MOT and UCP regions are separated by a distance of $\sim$73 cm. To transfer the ultracold atoms produced by the MOT to the UCP region, we used a set of anti-Helmholtz coils attached to a linear translation stage to magnetically trap the atoms from the MOT. These are the same magnetic coils that are used to provide the anti-Helmholtz field for the MOT. The two regions are separated further by a differential pumping aperture, with an ion-pump on each side of the aperture to pump down each region of the vacuum chamber. The vacuum chamber has several additional areas in the chamber with electrical feed-throughs that provide the voltages that are used on the electrode and grid assemblies.

The optimal design of the vacuum chamber was to arrange most of the vacuum components along a straight line so that we could transfer the atoms using a linear translation stage. The anti-Helmholtz coils that provided the magnetic field to create the magnetic trap had to be mounted with one of the coils above the chamber and the other coil below the chamber. This means that there could not be any mount supporting the vacuum chamber that was directly below the chamber, otherwise the path of the anti-Helmholtz coils would be obstructed. To prevent this problem, we designed a set of mounts that can support the full weight of the vacuum chamber from the side by using clamps that reached in between the anti-Helmholtz coils to hold the chamber. These mounts also had the added feature of being able to finely adjust the height of the vacuum chamber on both ends, which helped with the alignment of the atom transfer which will be discussed later. An additional support mount was placed below the micro-channel plate detector which was outside the range of the translation stage motion.

The anti-Helmholtz coil mounts also had a special design that was necessary for the production of our MOT. As seen in Figure 3.1, the coil mount is in an "L" shape, keeping the mount far from the center of the coils. We did this so that there would be room for the mirrors that were necessary to input the MOT beams into the vacuum chamber. The coils themselves require a relatively large

amount of current for magnetic trapping (120 A) and through repeated runs of the experiment, will dissipate a large amount of energy through resistive heating. This heating could eventually lead to a breakdown in performance, as the resistance of the coils will increase as they are heated. So, we designed the anti-Helmholtz coils so that they could be water-cooled during the operation of the experiment. The wire used for the coils was kapton-insulated, square copper tubing. The normal application of this type of tubing is in refrigeration systems and works perfectly for our purposes. The wire is hollow, which allows us to flow water through the center of the wire to keep it cool during the operation of the experiment. Also, since the wire is square, it lays nicely inside of the coil forms and stacks in successive layers as we wrapped the coils.

The rest of the apparatus will be explained in detail throughout the following sections of this chapter. The details presented in this chapter are necessary for fully understanding the experiments presented in Chapters $4-6$.

## 3.2 Laser Cooling and Magneto-Optical Trapping

The development of laser cooling and trapping techniques has provided useful tools in a wide variety of atomic physics experiments [8]. In the experiments discussed in this thesis, we use these techniques in order to produce the ultracold atom source needed to create plasmas at very low initial temperatures. The most used version of laser cooling, Doppler cooling, takes advantage of the momentum transfer properties of atom-photon scattering and the Doppler shift. These properties create a damping force on atoms in motion that slow atoms moving toward a laser beam. With the addition of a magnetic field, this force can also be position dependent, creating the conditions needed to cool and trap a sample of ultracold atoms.

For our experiments, we chose to use $^{85}$Rb because of the convenient laser transitions associated with laser cooling. $^{85}$Rb has a transition from the $5S_{1/2}$ ground state to the $5P_{3/2}$ excited state at 780 nm [9]. This wavelength can be produced by diode lasers that are used commercially for many applications, so they are cheap and readily available. Also, $^{85}$Rb has a nearly closed cooling transition that requires little repump light. In addition, our experiments require a two-photon ionization of the Rb atoms in order to produce ultracold plasmas. This can be done with the addition of light at 479 nm from a pulsed dye laser to ionize atoms by exciting electrons from the $5P_{3/2}$ state to the continuum [10].

### 3.2.1 The Force Exerted on an Atom by Laser Light and Doppler Cooling

To understand how atoms can be cooled by laser light, we can study the interaction of an atom with photons from a laser beam. For a two level atom with one optically active electron, the photon scattering rate from a laser with intensity $I$ is given by [8],

$$\gamma_p = 2\pi\Gamma \frac{I/2I_{sat}}{(1 + I/I_{sat} + (2\Delta/\Gamma)^2)} \tag{3.1}$$

where $\Gamma$ is the natural linewidth of the transition in Hz ($\sim$6 MHz for the cooling transition in Rb), $I_{sat}$ is the saturation intensity ($\sim$1.6 mW/cm$^2$ for Rb for circularly polarized light and fully spin-polarized atoms [9]), and $\Delta$ is the laser frequency detuning from the natural transition. When the atom absorbs a photon from the laser light, it will receive a momentum kick of $\hbar k$ in the direction of laser propagation. When a photon is spontaneously emitted, it will leave in a random direction, giving the atom a momentum kick in a random direction. The momentum kick from spontaneous emission will average out to zero over many photon emissions, so the average force on an atom in a laser light field is,

$$F = \hbar k \gamma_p = 2\pi\Gamma\hbar k \frac{I/2I_{sat}}{(1 + I/I_{sat} + (2\Delta/\Gamma)^2)} \tag{3.2}$$

where $k$ is the wave number of the photon from the laser light.

In principle, the laser light can both slow down and speed up an atom by scattering photons, meaning that considerations need to be taken in order to ensure that the atom is cooled when impinged upon by laser light. To do this, the Doppler effect is used with the fact that $\gamma_p$ falls off as the laser is detuned from resonance. Figure 3.2 shows the photon scattering rate as a function of laser detuning for a two-level atom. If the laser is detuned to the red of resonance, then the photon scattering rate is decreased from its peak. However, if the atom is moving opposite the propagation direction of the laser beam, then the frequency of laser light in the reference frame of the atom is blue-shifted, increasing the photon scattering rate. Moving in the same direction as the laser propagation, the light is red-shifted, decreasing the photon scattering rate. If we counter propagate two red-detuned lasers, then we ensure that the atom will scatter more photons from the beam that it is moving towards, slowing the atom if it travels in either direction. This is known as an optical molasses, and provides a velocity dependent damping force on atoms in the light field. We can use Equation 3.2 to determine the net cooling force on an atom with velocity $v$ in the

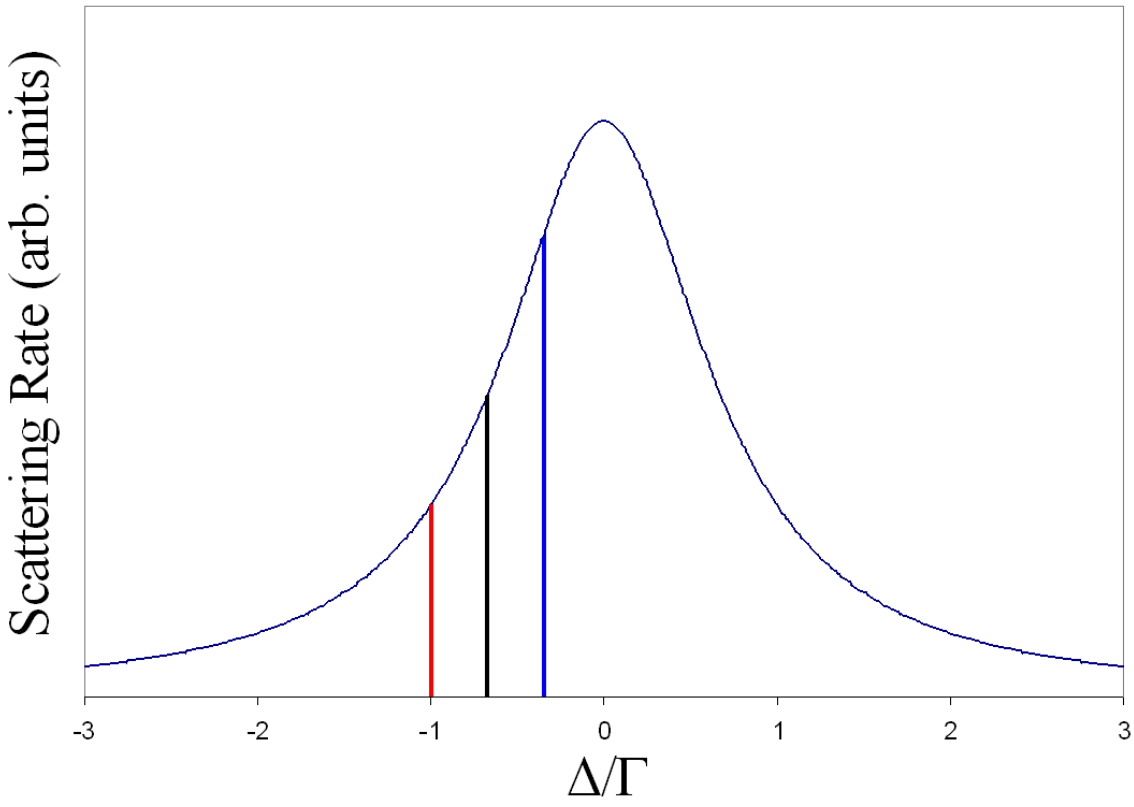


Figure 3.2: A plot of the photon scattering rate, $\gamma_p$ as a function of laser detuning. If the laser is red-detuned, an atom at rest will have a photon scattering rate shown by the black line. If it is moving opposite the propagation direction of the laser, the frequency will be blue-shifted, and the atom will have a higher scattering rate represented by the blue line. If the atom is moving in the same direction as the laser propagation, the frequency will be red-shifted, and the atom will have a lower scattering rate represented by the red line. In this configuration, we set the laser detuning so that the atom is more likely to scatter photons that slow it down.

counter-propagating laser field as,

$$F = \frac{\hbar k \gamma}{2} \left( \frac{I/I_{sat}}{(1 + I/I_{sat} + 4\left(\frac{\delta - kv}{\gamma}\right)^2} - \frac{I/I_{sat}}{(1 + I/I_{sat} + 4\left(\frac{\delta + kv}{\gamma}\right)^2} \right) \tag{3.3}$$

where $\gamma = 2\pi\Gamma$ and $\delta = 2\pi\Delta$. This function has a peak in the absolute velocity, meaning that high enough velocity atoms will feel little force. This sets a limit to the velocity of atoms that can be effectively Doppler cooled.

### 3.2.2 Creating a Magneto-Optical Trap

To create an atom trap, an optical molasses is not sufficient. While the optical molasses provides a damping force, it is not position dependent. So, even though atoms are slowed, they will eventually drift out of the cooling region. To create a position dependent force, we can add a linearly varying magnetic field to the optical molasses, creating a magneto-optical trap [11]. The simplest configuration to consider is the 1-D magneto-optical trap seen in Figure 3.3. Here, we consider a two-level system in which the excited state magnetic sublevels at $m_J = \pm 1, 0$ can be separated in energy owing to the Zeeman effect. The energy levels for the $m_J = \pm 1$ states will decrease in energy on opposite sides of the trap. These energy levels correspond to transitions from either a $\sigma^+$ or $\sigma^-$ laser beam. In this configuration, we counter-propagate red-detuned $\sigma^+$ and $\sigma^-$ beams in the trapping region. We can choose the propagation direction of the $\sigma^\pm$ beams so that atoms will preferentially scatter photons from the beam that will move it back towards the center of the trap. This creates a force on the atoms that depends on position, which is necessary for creating a trap at a particular location in space.

This concept can be extended to three dimensions, as seen in Figure 3.4. We use three orthogonal laser beams, which are retro-reflected back along their original path, creating a cooling force which will oppose atomic motion in every direction. The beams pass through a $\lambda/4$ wave plate before being retro-reflected, which reverses the handedness of the circularly polarized light. The magnetic field is provided by a set of magnetic coils in an anti-Helmholtz configuration. For our experiment, the $^{85}$Rb atoms are cooled using light at 780 nm to excite the $5S_{1/2}$ $F = 3$ to $5P_{3/2}$ $F = 4$ transition as seen in Figure 3.4. This transition is not completely closed, as off-resonant transitions to the $F = 3$ excited state can decay to the optically "dark" $F = 2$ ground state. So, our

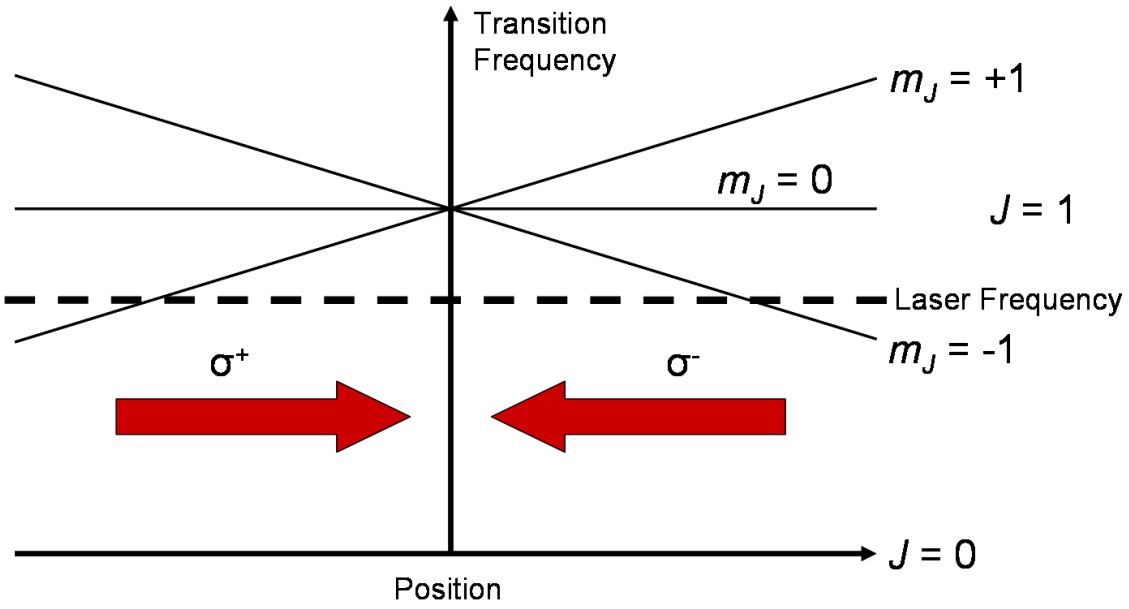


Figure 3.3: The energy levels for a 1-D magneto-optical trap as a function of position. Here we counter-propagate laser beams of opposite circular polarization that are red-detuned from the $m_J = 0$ transition. As an atom travels away from the center of the trap, it gets closer to resonance with the counter-propagating beam, pushing it back toward the center of the trap.

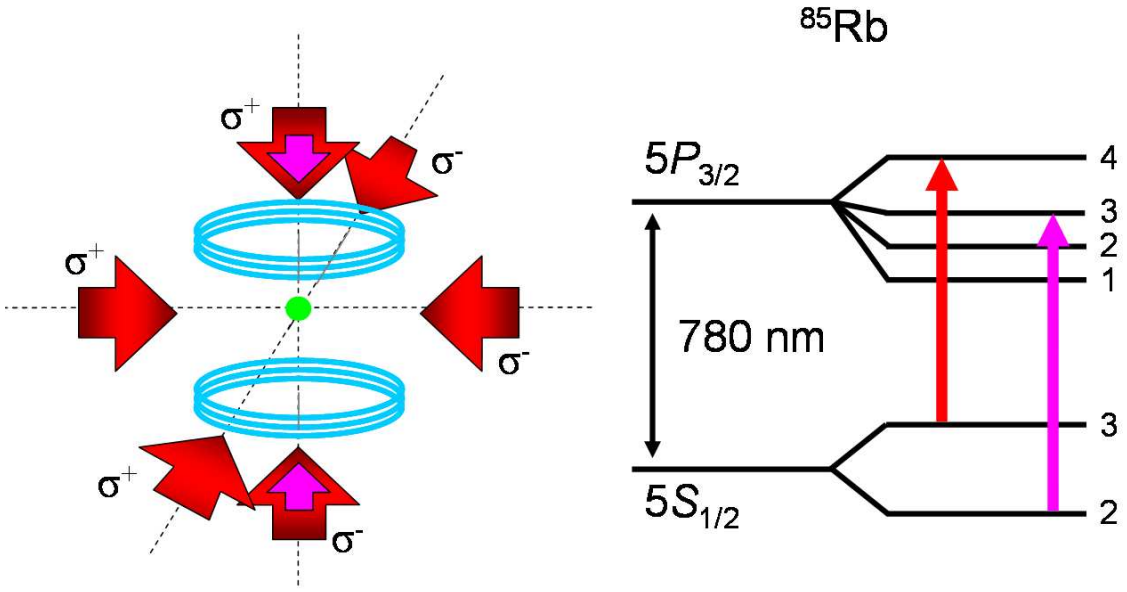


Figure 3.4: A diagram of the magneto-optical trap setup for our system with the relevant energy levels for $^{85}$Rb. The red line shows the main cooling transition between the $F = 3$ ground state and the $F = 4$ excited state. The $F = 3$ and $F = 4$ levels of the excited state are separated in frequency by ∼120 MHz, which leaves a non-vanishing probability for an off-resonant transition to the $F = 3$ excited state. Transitions to this state can decay to the $F = 2$ ground state, which requires a hyperfine repump, shown by the pink line, to get the atom back onto the main cooling transition.

system requires hyperfine repump light to get atoms back onto the cooling transition. The beams used to create the MOT have a ∼3 cm diameter and single-beam peak intensities of 11 mW/cm$^3$. The hyperfine repump light has beam diameters of ∼2 cm and peak intensities of 3 mW/cm$^3$

### 3.2.3 Diode Laser System

The lasers used for creating the MOT in our system are 780 nm, external cavity diode lasers (ECDL). The diode lasers used in our system are ADL-78901TX lasers produced by Roithner LaserTechnik. These lasers are inexpensive and readily available as they are mass produced for many commercial applications. For use in scientific experiments, we build our own laser housing system which provides a means for frequency control and temperature stabilization of the lasers. These lasers provide $> 70$ mW of total power, and can be tuned over a $10 - 14$ nm span of total wavelength, centered around 785 nm.

The diode lasers are housed in a Thorlabs LT230P-B collimation tube which allows us to minimize the output divergence of the beam. The beam is astigmatic, and can be corrected by using a prism pair after the output of the laser housing. To control the frequency of the laser, we use a Littrow configuration in which a diffraction grating after the output of the laser feeds back the $m = -1$ order diffraction spot through the laser. This increases the net gain of the laser at the wavelength associated with this diffraction. We can control the angle of the diffraction grating by using a piezo-electric transducer (PZT) which is attached to mount of the diffraction grating.

To tune the laser to the desired frequency, we use Doppler-free saturated absorption spectroscopy [12], which allows us to calibrate the PZT voltage that sets the angle of the diffraction grating to the transitions to the different hyperfine levels of the excited states as seen in Figure 3.5. In this saturated absorption set-up, we send two low-intensity beams through a Rb vapor cell, after which we measure the individual beam power on a pair of photo-diodes. When the beam is near resonance, the vapor absorbs light from the beam which lowers the beam power that is measured by the photo-diodes. A high-intensity beam is counter-propagated with one of the low-intensity beams that will saturate the transitions between the hyperfine states, which reduces the decrease in beam power on that low-intensity beam. The signal from the two photodiodes are subtracted, which shows peaks associated with the transitions between the hyperfine states as seen in Figure 3.5.

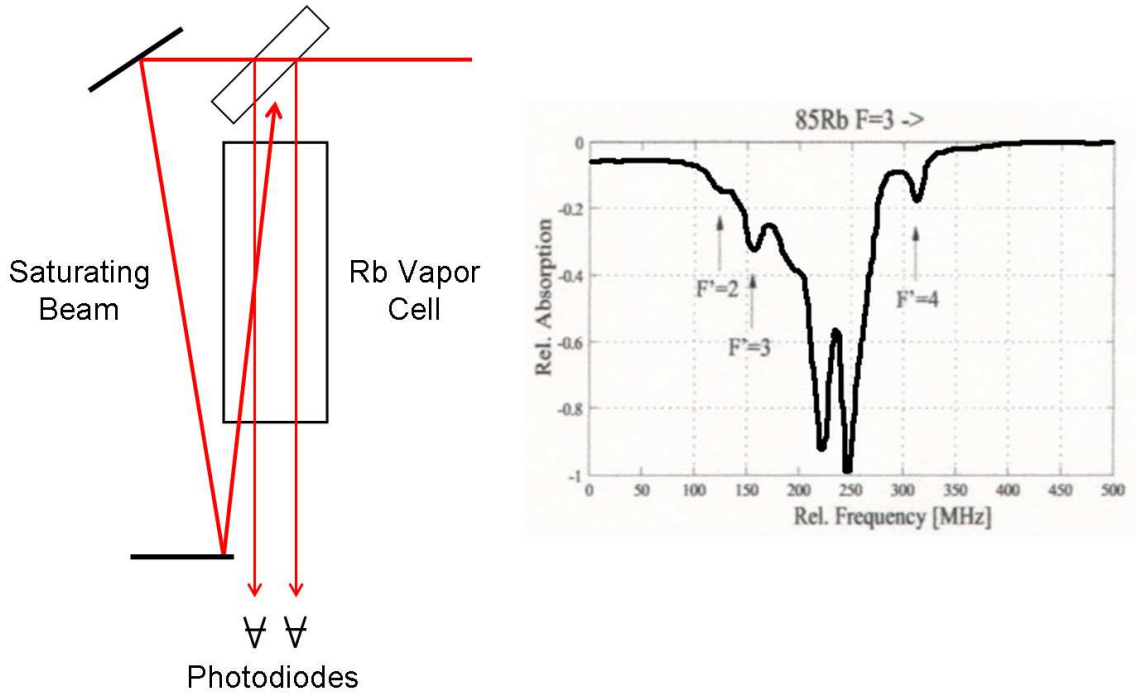


Figure 3.5: A diagram of the saturated absorption setup (left) for our system with the subtracted signal for $^{85}$Rb $5S_{1/2}$ $F = 3$ to $F = F'$ transition (right). The two larger peaks in the saturated absorption signal correspond to the crossover peaks, where saturating beam and the probe beam are resonant with two different hyperfine transitions because they are Doppler shifted into resonance with different velocity classes of atoms for their respective hyperfine transition. This occurs halfway between the relevant hyperfine transitions. The saturated absorption figure was taken from [13].

To lock the laser to a particular frequency, we use a Dichroic-Atomic-Vapor Laser Lock (DAVLL) system [14]. The DAVLL uses a Rb vapor cell in an approximately uniform magnetic field. The magnetic field induces Zeeman shifts which separate the frequencies of transitions driven by $\sigma^+$ and $\sigma^-$ light. The shifts produce Doppler absorption signals for $\sigma^+$ and $\sigma^-$ that are separated in frequency. We send a beam through the DAVLL cell that has both $\sigma^+$ and $\sigma^-$ components. After the cell, we can separate the two components of light using a $\lambda/4$ waveplate and a polarizing beam-splitting cube. We can then subtract the Doppler absorption signals of the two components from each other. This produces a signal that has a large linear slope which can be calibrated with the saturated absorption setup, and locked using a side-lock servo circuit.

To produce a stable laser mode, there are several requirements. First, we require precision laser current controllers. For this, we use ILX Lightwave model LDX-3525 precision current sources. This current source has the ability to produce a stable output current for our diode lasers at the 0.1% level. Also, we are able to further lock the laser current to the desired laser mode by modulating the current through the front panel of the current controller using a servo circuit. The servo circuit locks to our DAVLL signal, and sends a signal to the current controller to keep the laser mode at the correct frequency. The second requirement for stable laser operation is laser temperature stability on the 5 mK level. To maintain a consistent temperature, we require external control in which a temperature sensitive resistor is place in thermal contact with the laser mount inside the housing. This resistor provides the error signal in a temperature control servo circuit, which controls the current through a thermo-electric cooler that regulates the temperature of the laser. Stable laser operation also requires sufficient vibrational and electrical isolation. Mechanical and electrical kicks to the laser can cause the laser to lose its frequency lock on a regular basis, making experiments difficult to perform. Vibrational stability was obtained by placing thin sorbothane pads between the laser housing and the optical table. Electrical isolation is a bit more difficult as ground loops that may be introduced onto the electrical circuits controlling the laser can be difficult to counteract. This is typically combated by using highly conductive grounding strap to ensure that the lasers maintain a proper ground reference.

The laser housings that we use for our experiment are based on two different designs that both have advantages and disadvantages that need to be considered when deciding which type of housing to use. They are both based on the ECDL design described above, but one is designed in a compact

fashion to minimize the table "footprint" of the laser and the other was a larger design for maximum temperature stability. The smaller design does reduce the laser "footprint" by a factor of ∼2, but has had considerable temperature stability issues in the past. This is mainly due to the laboratory environment not maintaining a stable temperature throughout the course of the day, where we can see temperature shifts on the order of 10 degrees Fahrenheit. The temperature servo circuits for the laser are slow by design given the large thermal mass of the base of the lasers (generally a block of aluminum). Although this is designed to try and help maintain laser temperature stability, the small "footprint" design is sensitive to temperature swings in the laboratory, thus reducing the overall laser mode stability. The larger design was more suited to the requirements of our experiment, because we are not lacking in table space to the point where the smaller design becomes necessary. However, at this point we have greatly improved the temperature stability of the lab through the addition of a commercial air conditioning unit, making the replacement of the smaller laser design unnecessary.

### 3.2.4 Absorption Imaging

To characterize the atoms in the MOT and in the photoionization region of the vacuum chamber, we use absorption imaging which allows us to determine the MOT atom number, spatial extent, and temperature [15]. These techniques are standard in many ultracold atom experiments, and are only used in these experiments to initially characterize the MOT and magnetic trap loading, and to help us locate the position of the magnetically trapped atoms on the plasma side of the vacuum chamber. So, I will discuss these techniques only briefly here.

For a low-intensity ($I << I_{sat}$), resonant laser beam traveling through a cloud of atoms, the intensity of the laser beam as function of distance traveled through the cloud is governed by,

$$\frac{dI}{dz} = -n\sigma I \tag{3.4}$$

where $n$ is the density of atoms, $\sigma_0$ is the absorption cross section ($3\lambda^2/2\pi$ for circularly polarized light and fully spin-polarized atoms) and $I$ is the intensity of the laser at a given position in the atom cloud. We can integrate this equation over the direction of laser propagation to find the optical depth of the atom cloud to be $OD = ln(I/I_0)$, which in turn is proportional to the number of atoms in a given column of the atom cloud. Here $I$ is the measured intensity of a resonant,

low-intensity probe beam traveling through the cloud of atoms, and $I_0$ is the intensity of the beam without the atoms present. By measuring the optical depth spatial profile, we can determine the rms size of the cloud and the total number of atoms trapped in our MOT given by,

$$N = \frac{2\pi\sigma_x\sigma_y}{\sigma_0} OD_{peak} \tag{3.5}$$

where $\sigma_x$ and $\sigma_y$ are the rms sizes for the 2 spatial dimensions, and $OD_{peak}$ is the peak optical depth. These parameters can be obtained from an absorption image to calculate the total number of atoms in the MOT. For our system, we used linear polarization for our images. This has the effect of reducing the overall absorption cross section $\sigma_0$ by a factor of 2. These same techniques can also be used to characterize the atoms in the magnetic trap, which is discussed in the next section.

## 3.3 Magnetic Trapping and Transfer of the Ultracold Atoms

Since the UCP formation region and the MOT region are separated in space, we used a magnetic quadrupole trap mounted to a motorized translation stage to transfer ultracold atoms from the MOT region to the UCP formation region. This technique was first used in Bose-Einstein condensate (BEC) experiments at JILA in Boulder, Co [7]. To create the magnetic trap, we used a pair of multi-turn magnetic coils in an anti-Helmholtz (AH) configuration using hollow copper wire. The copper wire was water cooled by flowing water through the wire cavity to prevent overheating during the magnetic trapping

The trap itself is formed through the interaction of the magnetic field from the AH coil configuration with the magnetic dipole moment, $\mu$, of the valence electron in the $5S_{1/2}$ $F = 2$ ground state of $^{85}$Rb. The interaction energy of the electrons magnetic dipole and the quadrupole field is given by,

$$U = -\vec{\mu} \cdot \vec{B} \tag{3.6}$$

where $B$ is the externally applied field from the magnetic trap. The magnetic dipoles from the electrons will adiabatically follow the external magnetic field as long as the square of the larmor precession frequency, $\omega_L^2$, is much greater than the time rate of change of the larmor frequency,

$d\omega_L/dt$ as it travels through the magnetic field. This is easily satisfied for ultracold atoms except at a very small region around the center of the trap where $B = 0$. As long as this approximation holds true, then the interaction energy becomes [7],

$$U = -|\vec{\mu_B}| \cdot |\vec{B}| g_F m_F \tag{3.7}$$

where $g_F = -1/3$ is the $g$-factor for the $F = 2$ ground state in $^{85}$Rb and $m_F$ is the magnetic sublevel. This provides an interaction energy that will allow the trapping of atoms in particular magnetic states in the magnetic trap.

### 3.3.1 Calculating the Ideal Anti-Helmholtz Size and Spacing

To find the ideal magnetic field strength for creating a magnetic trap with an anti-Helmholtz configuration, I can start by calculating the magnetic field for a single magnetic coil of $N$ turns at an arbitrary point in space by direct integration of the Biot-Savart equation:

$$\vec{B} = \frac{\mu_0 N I}{4\pi} \int \frac{\vec{dl} \times \vec{r}}{r^3} \tag{3.8}$$

Here $\mu_0$ is the permeability of free space, $I$ is the current in the coil, and $\vec{r}$ is the position in space relative to the current element that we are integrating. To find the ideal trapping conditions, it is best to normalize the spatial coordinates with respect to the radius of the magnetic coil, $b$, to allow easy calculations for a variety of coil configurations. I'll define the following parameter,

$$B_0 = \frac{\mu_0 N I}{4\pi b} \tag{3.9}$$

Since there is cylindrical symmetry, I can solve Equation 3.8 in component form for a single coil of wire so that,

$$\frac{B_\rho}{B_0} = (\zeta - \zeta_0) \int_0^{2\pi} \frac{cos(\phi) d\phi}{(\eta^2 - 2\eta cos(\phi) + (\zeta - \zeta_0)^2 + 1)^{3/2}} \tag{3.10}$$

$$\frac{B_z}{B_0} = \int_0^{2\pi} \frac{(1 - \eta cos(\phi)) d\phi}{(\eta^2 - 2\eta cos(\phi) + (\zeta - \zeta_0)^2 + 1)^{3/2}} \tag{3.11}$$

where $\zeta = z/b$, $\zeta_0$ is half of the normalized coil separation (in terms of the coil radius), and $\eta = \rho/b$. Equations 3.8 and 3.9 can be calculated explicitly for a pair of coils located at $\pm\zeta_0$ in the configuration seen in Figure 3.4. The fields for the AH pair were then calculated numerically at

multiple positions in space and the magnitude of the field was fit to the approximate function:

$$\frac{B}{B_0} = \frac{Ab}{B_0}\sqrt{\eta^2 + 4\zeta^2} \tag{3.12}$$

where $A$ is the magnetic field gradient at the center of the trap in the radial direction. This shows that the magnitude of the magnetic field increases as you leave the center of the coils, creating a trap near the center of the coils as seen from Equation 3.7. The integration of Equations 3.10 and 3.11 allows us to calculate the field gradient, $A$, for an arbitrary coil size and spacing. Figure 3.6 shows the value of $A$ for a range of AH-coil sizes and separations. The strength of the magnetic trap is proportional to the value of the field gradient, and Figure 3.6 shows that in order to maximize the field gradient for a fixed current, the coil separation should be minimized over the range of experimentally accessible parameters.

The potential energy of an atom in the magnetic trap is given by,

$$U = \mu A g_F m_F \sqrt{\rho^2 + 4z^2} + mgz \tag{3.13}$$

The field gradient for trapping must be chosen so that the strength of the magnetic trap is enough to overcome the gravitational force acting on the atom (Note: the coil geometry is such that the direction of gravity is along the $z$-axis of the coils). To determine this, we can calculate the force of gravity in units of the magnetic field gradient in the $z$-direction. We can set $\rho = 0$ so that,

$$U = 2\mu A g_F m_F |z| + mgz \tag{3.14}$$

When $z < 0$, the forces from the magnetic trap and gravity oppose each other, giving a threshold value for the field gradient for magnetic trapping as given by

$$A_{min} = \frac{mg}{2\mu g_F m_F} \tag{3.15}$$

Since hyperfine state changing collisions limit the magnetic trap lifetime in the upper $F = 3$ ground state in $^{85}$Rb, we choose the $F = 2$ ground state to trap the atoms. The $m_F$ = -1,-2 magnetic sublevels are trappable since they create a minimum in the value of the magnetic field. Equation 3.15 gives a value for the minimum field gradient of 11 and 22 G/cm for the $m_F = -1$,-2 states respectively. For the coils to have clearance over the entire vacuum chamber, they need to be spaced by at least 5 inches. From Fig 3.6, for a spacing of 5 inches, the maximum field gradient is for coils

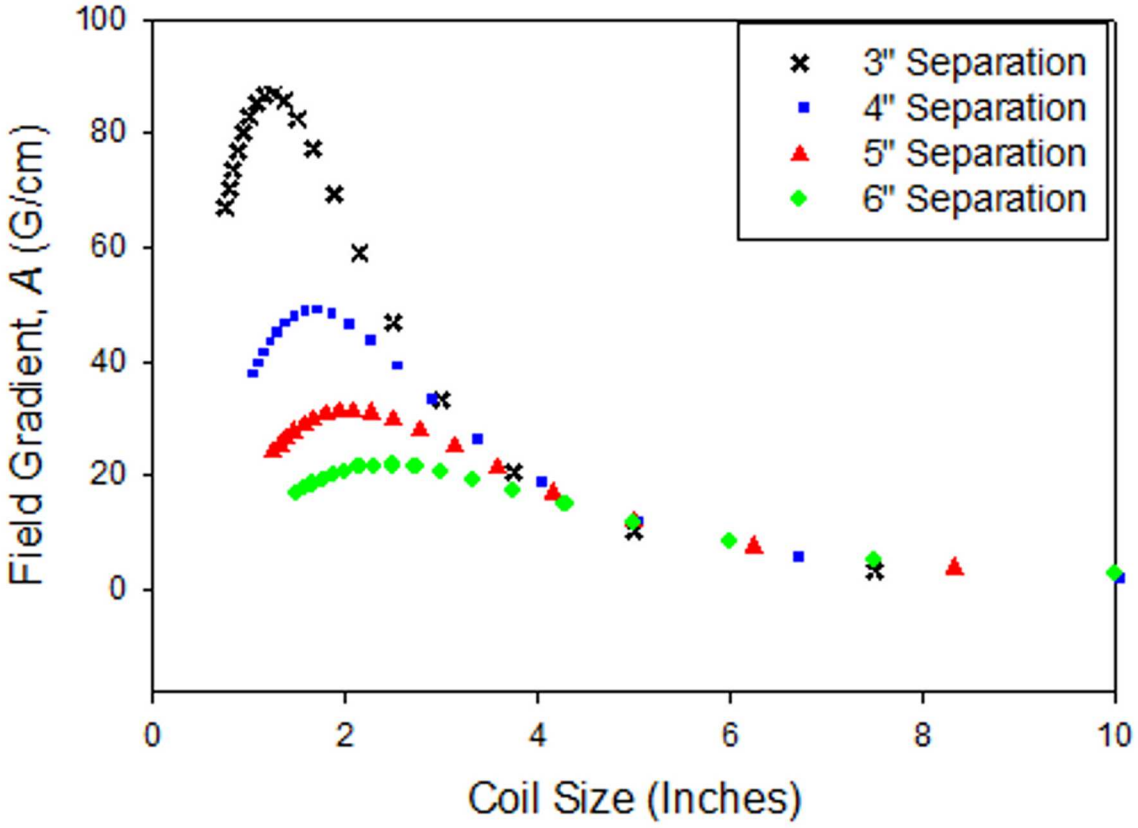


Figure 3.6: The magnetic field gradient as a function of the coil radius for various coil separations for $N = 30$ turns and 120 amps. The peak in the field gradient allows for the determination of the proper coil radius for a given separation. For our system, the separation needs to be 5 inches to sufficiently clear the vacuum system. This shows that we needed to make the coils with a 2 inch radius. The units for the coil separation and coil radius are in inches because the equipment in the machine shop used to create the coils uses British imperial units.

with a 2 inch radius. For $N = 30$ turns and a current of 120 Amps, this gives a field gradient of 33 G/cm, which is sufficient for trapping both $m_F = -1$,-2 states in the $F = 2$ ground state of $^{85}$Rb.

### 3.3.2 Loading the Magnetic Trap

The magnetic trap is loaded from the MOT by increasing the current through the same AH-coils that create the magnetic field for the MOT. The loading of the magnetic trap consisted of the following steps. After the atoms are cooled into the MOT, we used a compression stage to increase the density of the atoms in the MOT. To do this, the trapping laser is detuned from its original 10 MHz detuning used for loading the MOT to 45 MHz and the hyperfine repump laser is attenuated by 30 dB to decrease the radiation pressure from photon rescattering, allowing the atom cloud to compress. The compression stage lasts for 5 ms, after which the ultracold atoms are optically pumped to $F$=2 ground state by turning off the hyperfine repump light for 2 ms before the main trapping light is turned off (see Figure 3.4). Additional optical pumping into trappable $m_F$ states is not required as ∼40% of the MOT atoms are already in trappable states. Optical pumping would increase the number of atoms trapped but would require a significant amount of experimental implementation for little gain. After the atoms are pumped into the $F = 2$ ground state, all of the laser light is turned off and the atoms begin to fall under gravity. The AH-coils are then ramped up to 120 A, "catching" the falling atoms in the magnetic trap. Control of the timing of this sequence is important for optimizing the load into the magnetic trap. Ramping the current to 120 A too slowly will cause the atoms to fall out of the trap before it can be formed. The rate at which current can be provided to the coils will be limited by the coil inductance.

To control the current of the magnetic trap, I designed a circuit to regulate the voltage and current settings of an Agilent 6682A power supply. In principle, voltage and current can be computer controlled through GPIB, however the current and voltage can not be changed between levels in less than 50 ms by this method. Also, the inductance of the AH coils will work to prevent changes in the current, further slowing down the current ramp speed. For efficient magnetic trapping, the ramp time will have to be much faster than this, on the order of a couple of ms.

To change the current level faster, I designed a servo circuit to regulate the current through the AH-coils by controlling the gate voltage on a set of 12 field-effect transistors (FET) as seen in Figure 3.7. The servo circuit allows us to keep the current setting on the Agilent power supply

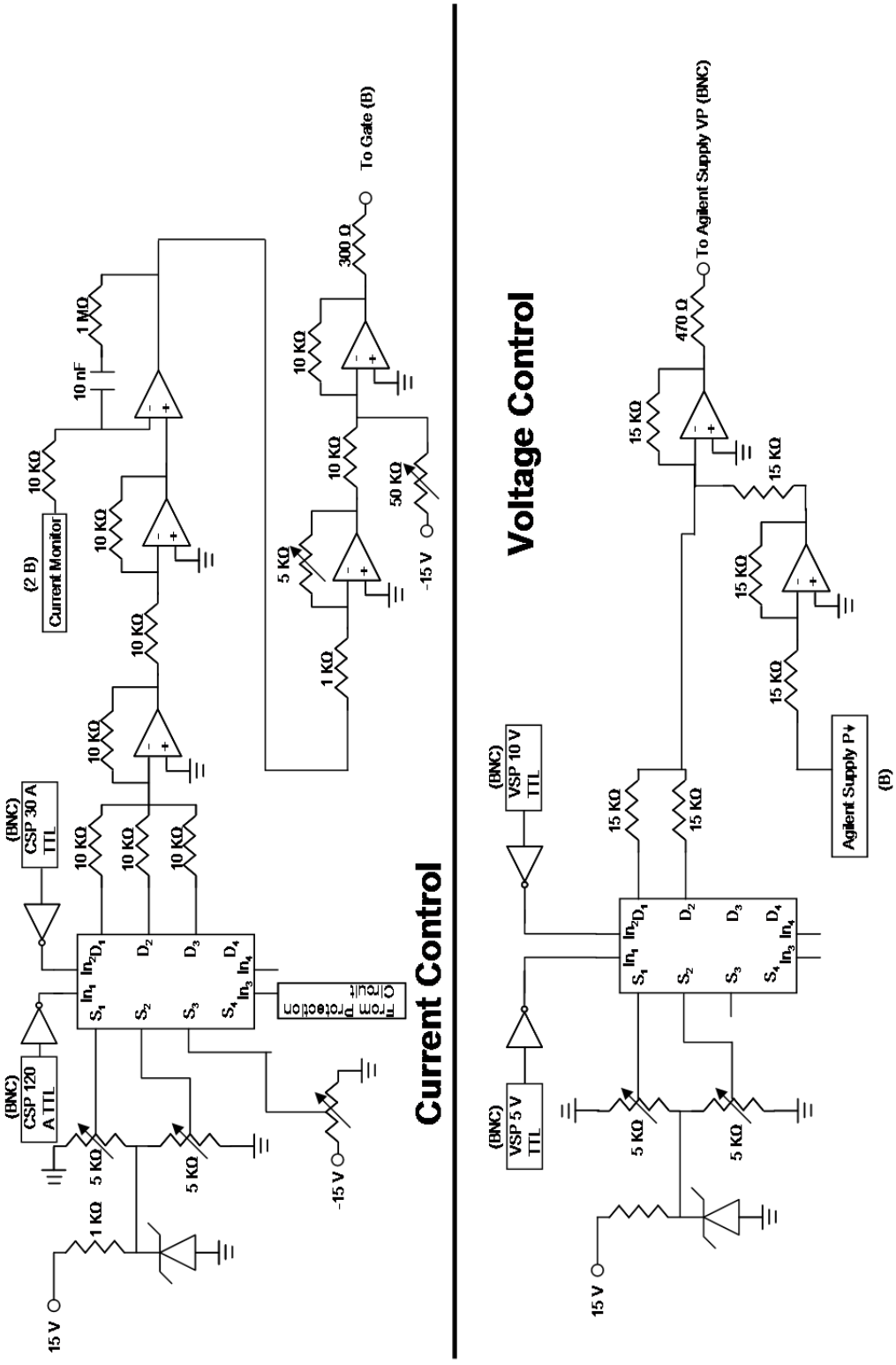


Figure 3.7: Current and voltage control circuit for the anti-Helmholtz coils

at the maximum current to be used during the experimental sequence, to avoid problems with the switching time. The inductance of the AH-coils was the main limiting factor to switching the magnitude of the current on the ms timescale. The voltage across an inductor is proportional to $LdI/dt$. To increase $dI/dt$, the servo circuit was designed to increase the voltage across the AH-coils and the FETs to 10 V, which is higher than the 1.2 V (30 A) needed for the MOT and the 4.5 V (120 A) needed for magnetic trap. During this stage, the servo decreases the gate voltage across the FETs to maintain the current needed for the MOT. To switch the current levels, the FET gate voltage is increased to close the FETs completely. At this point, nearly all of the voltage is across the coils, increasing $dI/dt$ to achieve a switching time of $\sim$2 ms. This rate of switching is sufficient for magnetic trapping, and is what we use for the work in this thesis.

One of the best ways to quickly determine the loading of the magnetic trap is to recapture the trapped atoms in the MOT. We start by loading the magnetic trap from the MOT. When the MOT laser light is turned off, any untrapped atoms will fall out of the MOT region under the effect of gravity. In just 200 ms, the untrapped atoms can fall nearly 20 cm, which is much greater than the spatial extent of the trap region. At this time the current through the AH-coils can be ramped down to the original MOT level (30 A) and the MOT laser light can be turned back on. The atoms that remain in the magnetic trap will be quickly recaptured by the MOT. By measuring the fluorescence of the MOT on a photodiode before and after the recapture, the fraction of the atoms trapped in the magnetic trap can be determined. If the $m_F$ levels for the atoms are completely randomized upon turning on the magnetic trap, I expect to trap $\sim$40% of the MOT atoms in the magnetic trap. However, the polarization of the MOT beams can provide some optical pumping which can improve the loading into the magnetic trap above 40%. This has limited effectiveness because the polarization of the MOT beams in the trapping region is not well characterized. Optimizing the polarization of the beams in the MOT region is difficult because the optical thickness of the MOT can affect the polarization of the retro-reflected beams.

Another property of the magnetic trap that we can determine by doing a recapture measurement is the lifetime of the atoms in the magnetic trap. Owing to collisions with room-temperature atoms in the background vapor, atoms will be lost from the trap. To measure the lifetime, we simply hold the atoms in the magnetic trap for varying lengths of time before performing the MOT recapture. The lifetime of the magnetic trap depends mostly on the quality of the vacuum and generally

increases the longer the system has been run since the last vacuum chamber bake-out. The lifetime will also depend on the vapor pressure of the background Rb that we get from running our Rb getters. For our system, the lifetime of the magnetic trap is typically between $2-4$ s. The lifetime of the magnetic trap is one of the limiting factors in the transfer efficiency of atoms to the plasma region. Other limiting factors will be discussed in section 3.3.3.

Another way to measure the loading of atoms into the magnetic trap is by using absorption imaging (Section 3.2.4). In this case, we find out not only how many atoms are loaded into the magnetic trap, but also the quality of the loading into the trap, which is determined by the density and temperature of the atoms in the trap. These two quantities will be related by the following expression,

$$n(\vec{r}) = n_0 exp\left(\frac{-U(\vec{r})}{k_B T}\right) \tag{3.16}$$

where $n_0$ is the peak density, $U$ is the magnetic trap potential energy as given by Equation 3.13, $k_B$ is Boltzmann's constant and $T$ is the temperature of the trapped atoms. Inefficient loading into the magnetic trap can cause an increase in the temperature of the trapped atoms, which lowers the overall density.

To measure the peak density, we measure the peak optical density using absorption imaging as seen in Figure 3.8. To do this, we pass a resonant, low-intensity beam through the cloud of atoms and image the beam on a CCD camera. The CCD camera we use for our absorption imaging is a Flea 2 model FL2-20S4M-C from Point Grey Research. The Flea 2 camera has a 1624×1224 pixel array with a 4.4 $\mu$m pixel size. Peak OD measurements can yield values as large as -1, with characteristic spatial extent of $\sim 0.8-1$ mm (a rms width across one spatial direction). This results in peak densities that can be as high as $10^{10}$ atoms/cm$^3$ and as many as $2.5 \times 10^7$ total atoms in the trap. One can note that magnetic trapping strength in the axial direction is twice as strong as in the radial direction. Figure 3.8 shows that this results in an asymmetric atom distribution with a ratio of $\sim 2/1$ when imaged in the MOT side of the vacuum chamber.

The temperature of the atoms in the magnetic trap can be measured by releasing the atoms from the trap and measuring the rate of expansion of the atom cloud using absorption imaging. This is not a measurement that was performed very often since measurements of the peak OD provided the information about the magnetic trap loading that we wish to know. However, the

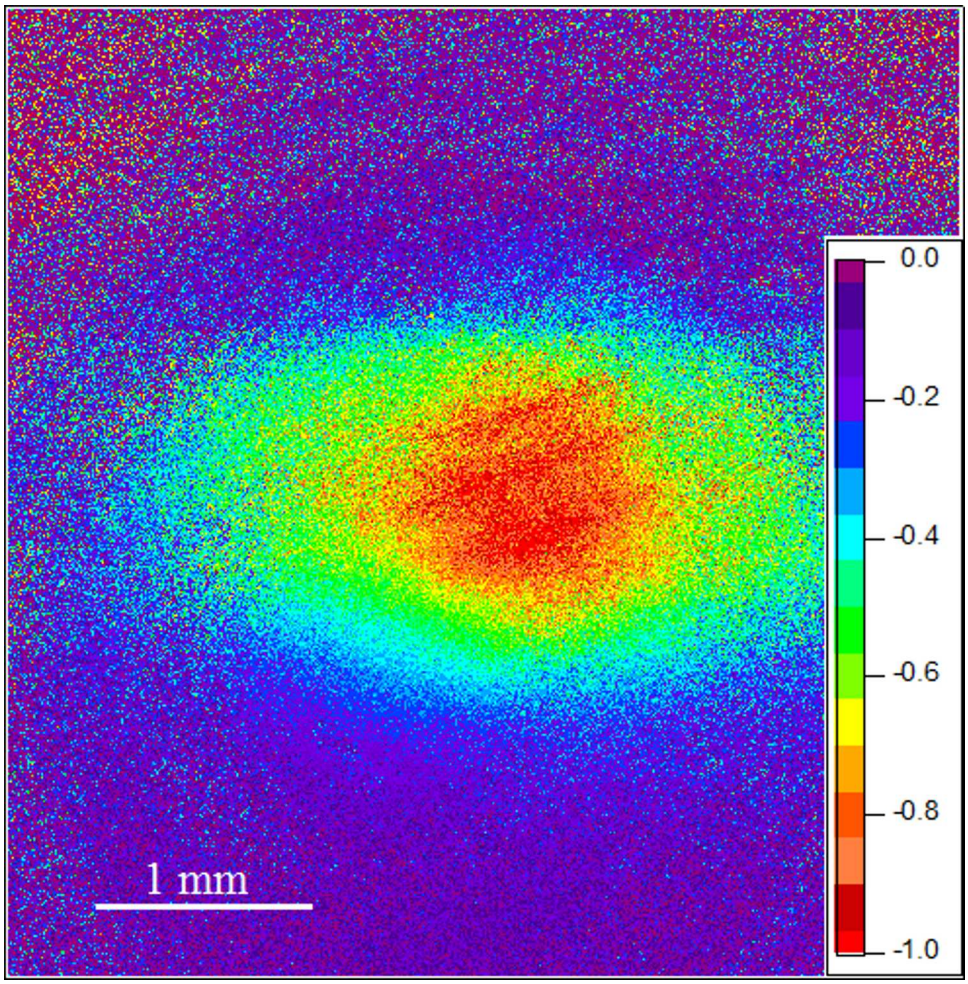


Figure 3.8: An absorption image of the magnetically trapped atoms in the MOT region of the vacuum chamber. To produce the image, the atoms are trapped in the magnetic trap for ∼200 ms to allow the untrapped atoms from the MOT to fall away. The atoms are then released from the trap, repumped to the $F = 3$ ground state and imaged using an optical probe beam tuned to the $5S_{1/2}$ $F = 3$ to $5P_{3/2}$ $F = 4$ transition. The color coded scale on the side of the image shows the optical depth (OD) image. There are $\sim 25 \times 10^6$ atoms in this image.

temperature of the magnetic trap will allow us to calculate some useful quantities that we will need in the discussion of the atom transfer in the next section.

The image of the atoms in the magnetic trap allows us to determine the rms size in each dimension. Upon their release from the magnetic trap, the atoms will freely expand. By measuring the rms size over multiple images over a range of times, we can find the temperature by fitting the rms size as a function of time to the following form,

$$\sigma(t) = \sqrt{\sigma(0)^2 + \frac{k_B T}{m} t^2} \tag{3.17}$$

For our system, the temperature of the atoms in the magnetic trap is typically $\sim$100 $\mu$K, which shows that there is not substantial heating during the loading of the magnetic trap.

### 3.3.3 Computer Control of the Translation Stage

The movement of the translation stage to transfer the atoms from the MOT region of the vacuum chamber to the plasma region requires precise control of the stage's position, velocity, and acceleration. The translation stage apparatus was sold by InPosition Technologies. The stage itself is attached to a large screw drive that moves the stage horizontally along the track when the screw is turned. The screw drive is turned by an external high-torque, Gemini GV6K servo-controlled motor which is capable positioning the translation stage with $\mu$m precision at speeds as high as 5 m/s. In practice, we operate the translation stage at a peak speed of 0.76 m/s, with a peak acceleration of 1.27 m/s$^2$ and peak deceleration of 0.63 m/s$^2$. Of great importance is the servo-tuning parameters of this motor, which take the weight load of the translation stage into account in order to properly accelerate the stage with the correct amount of torque. Improperly setting the servo parameters can cause servo oscillation and catastrophic damage to the system, so it is important that one sets the servo to correct parameters for the load that is attached to it.

The translation stage motor settings are controlled by the Motion Planner program, which was provided by manufacturer. This program provides the means to control the stage's movements as well as allowing the tuning of the servo parameters, which is necessary for proper control of the stage. The servo has proportional, integral, and differential gain control of the motor, and these gains serve as the tuning parameters for the translation stage and motor system. The servo tuner is a sub program of Motion Planner that allows for the tracking of the motion profile (stage position

vs. time) of small movements of the stage as a function of the servo tuning parameters. To set the servo parameters, we try to match the desired motion profiles as well as possible while adjusting the servo parameters. When the motion profiles are matched for small stage motions, we can begin to increase the acceleration and velocity of the stage to the operating conditions of the experiment.

During the experiment, the stage is controlled by loading pre-programmed motions to the motors on-board memory using Motion Planner. The stage movement is then controlled by TTL logic pulses (see Section 3.7) that set the timing of when the motor is turned on/off as well as sending commands to move the stage on its pre-programmed motions. It is important to keep the motor turned off when not in use as it outputs electrical noise that can be picked up by other experimental equipment in the laboratory. In the event of a power outage or system crash, the programmed motions will be cleared and the servo tuning parameters will be reset. It is important to set these parameters to the proper values before operating the stage. Please consult the Motion Planner Crash Guide which is attached to the inside of the Plasma Experiment Lab Book #1.

### 3.3.4 Transferring Atoms to the Plasma Region

After loading the magnetic trap, the atoms are then transferred to the plasma region by translating the AH-coils on a motorized linear translation stage. There are many factors that limit the transfer efficiency such as the magnetic trap lifetime and atom clipping on the differential pumping aperture (DPA) and electrode assembly. In this section, I will calculate the expected effect of the various transfer limitations as well as present measurements of how the system actually worked.

The plasma and MOT sides of the vacuum chamber are separated in space by $\sim$73 cm. The MOT side of the vacuum chamber requires a steady supply of background Rb vapor in order to load the MOT. This background limits the magnetic trap lifetime. So, to minimize this effect throughout the entire transfer of the atoms, we placed a 6 mm diameter aperture between the two regions and differentially pumped with an ion pump on both sides of the aperture as seen in Figure 3.1. This differential pumping allows us to maintain a higher vacuum quality on the plasma side of the vacuum chamber while maintaining a background of Rb vapor in the MOT side. One of the drawbacks of the differential pumping aperture is that the magnetically trapped atoms have a chance to be clipped at the aperture and lost during transfer. So, lining up the translation stage and

vacuum chamber to have the magnetically trapped atoms pass through the center of the aperture will be essential (and difficult).

We can estimate the amount of atoms that will pass through the aperture by integrating Equation 3.16 over the size of the aperture for a 100 $\mu$K distribution. The atoms in the $m_F = -2$ are more tightly confined than those in the $m_F = -1$ owing to the higher magnetic moment. So, for a 6 mm aperture, more than 95 % of the atoms in the $m_F = -2$ should pass through the aperture compared to ∼65 % for the $m_F = -1$ state. Atoms in both states should be in the trap in roughly equal amounts, so ∼80 % of the trapped atoms should pass through the aperture. Combined with a ∼3s trap lifetime, a 2s travel time, and a 1s settling time, we should be able to transfer ∼30 % of the trapped atoms to the plasma region of the vacuum chamber.

In practice, alignment of the magnetically trapped atoms with the aperture and the electrode assembly is difficult. To maximize the transfer of atoms to the plasma region, we first must successfully transfer atoms through the DPA. The best way to measure whether or not the atoms make it through the DPA is by using the MOT recapture method discussed in the previous section. Using this method, we transferred the magnetically trapped atoms to an arbitrary distance from the location of the MOT using the translation stage and then back to the location of the MOT for recapture. We compared the recapture fraction that we measure for this translation to that of no translation for the same amount of time in the magnetic trap. If there is no obstruction in the path of the atoms in the magnetic trap, then the measured recapture fraction should be the same in the two situations. To start, we measured the recapture fraction as a function of the distance from the initial MOT position until we found the drop in our recapture fraction at the DPA. The DPA is fixed in its location inside the vacuum chamber. So, to improve the transfer efficiency through the DPA, we must change the position of the center of the magnetic trap. To do this, we can change the vertical and horizontal position of the AH coils by small increments until the recapture that we measure when translating the atoms past the DPA is maximized.

Transfer through the DPA is not the only concern when getting atoms down to the plasma region of the vacuum chamber. We also must align the translation of the atoms with the center of the electrodes assembly. To check the transfer efficiency, the same recapture technique can be used. Again, the alignment will not start out being perfect. When transferring atoms by 73 cm, even a slight angular misalignment of the vacuum chamber with respect to the translation stage

will cause transfer inefficiencies. Such was the case for our system. However, for alignment with the electrodes, changing the location of the AH coils will prove difficult, as this may introduce new problems with transferring through the DPA. To deal with this problem, we added a pair of shim coils perpendicular to the motion of the track outside of the vacuum chamber near the electrodes (the alignment of the shim coil axis was horizontal (Figure 3.9), not vertical as we have a different way of adjusting that direction which will be discussed shortly). The effect of the shim coils is to change the location of the center of the magnetic trap when it gets close to the electrodes region. Changing the center of the trap will allow us to push the atoms closer to the center of the axis of the electrodes which will allow us to increase our transfer efficiency from the horizontal alignment.

Once we are able to get some degree of atom transfer into the electrodes region, we can fine tune the alignment by using absorption imaging. The first thing that we align is the vertical position of the atoms with respect to the electrodes. We can use a probe beam for imaging that has a size that is initially larger than the space provided by the center electrode (the beam comes in at 45 degrees with respect to this electrode, Figure 3.1). This will allow us to see an oval shaped shadow of the electrodes in our images of the beam. If the probe beam is aligned horizontally through the chamber, then the widest part of the beam that makes it through the chamber will be center position in the vertical direction. To align the atoms, we must physically move the vacuum chamber in the vertical direction using a special vacuum chamber mount. This mount is placed near the electrodes and changes the position of the electrodes without having a significant effect on the vertical position of the DPA.

Once the vertical alignment is optimized, the alignment of both horizontal directions needs to be optimized. Parallel to the translation stage motion, the distance of the track motion into the electrodes region can be easily changed. However, seeing an image of the atoms in the center of the imaging beam does not necessarily mean that the atoms are located in the center of the electrode assembly as seen in Figure 3.9. To check the alignment, we use absorption images of the atoms through both ports on the plasma side of the vacuum chamber, providing images at right angles with respect to each other. If the atoms are not visible in both images, then the alignment is not correct. We can adjust the atoms horizontal position perpendicular to the translation stage motion by using the transfer magnetic shim coils to move the center of the trap in the plasma region. We

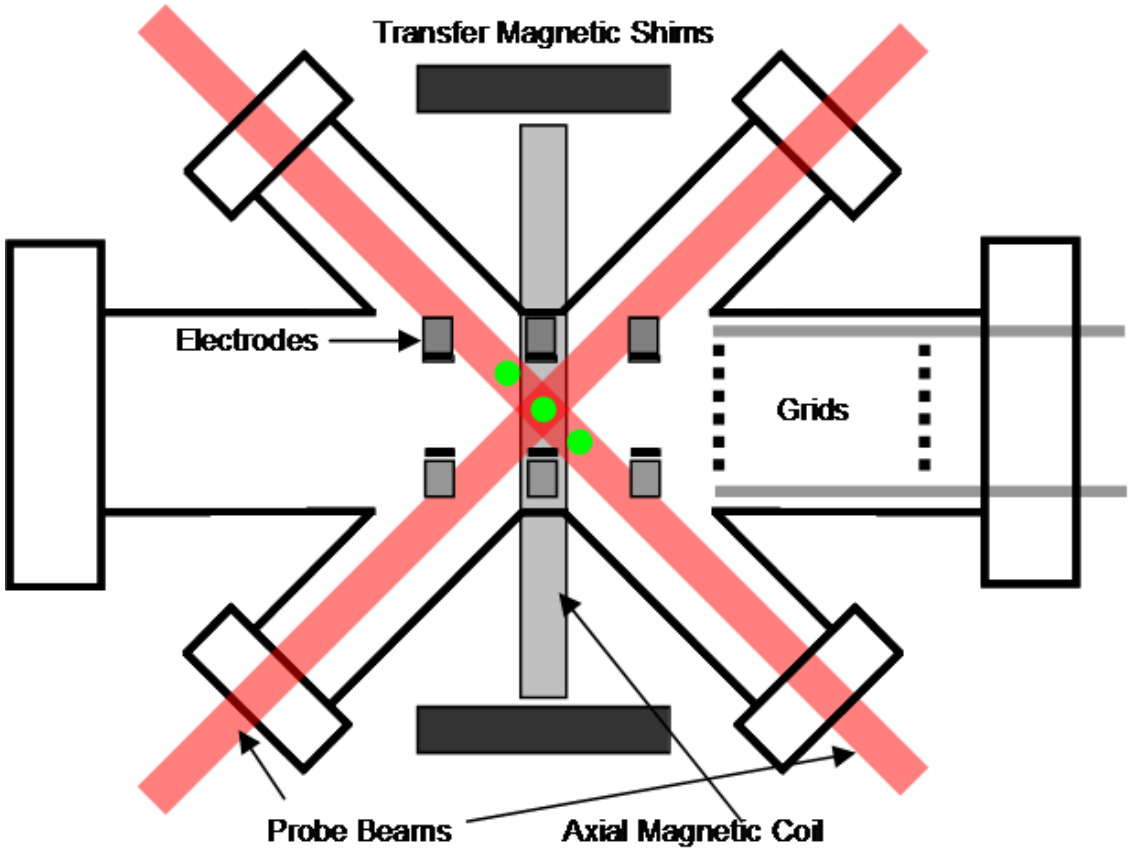


Figure 3.9: A diagram of our alignment technique to get the magnetically trapped atoms to the center of the electrode region. The green circles show the possible locations of the atoms when they can be seen in the center of the images from one of the probe beams. If the atoms are not visible in the image from the other probe beam coming in at a right angle with respect to the other beam, then the atoms are not aligned in the center of the electrodes region. To push the atoms to the proper position on axis, we can apply a magnetic field from the transfer shim coils until the image of the atoms is visible in the center of both beams.

can do this in combination with the final position of the translation stage to move the atoms until they are centered on both probe beam absorption images.

For our system, we transfer around 25% of the atoms to the plasma region. This is close to the 30% ideal transfer efficiency that was calculated based on our magnetic trap parameters. Perfect alignment is very difficult, so taking a small loss of atoms from clipping is expected, and the steps described in this section were used to minimize this loss of atoms.

## 3.4 Electric and Magnetic Field Environments

The main purpose behind the design of our ultracold plasma apparatus is to eventually trap both components of the plasma in a Penning trap configuration [3]. This required a region separate from the MOT where the ultracold atoms are cooled and trapped to produce the proper field environment. The electric fields were produced by a set of cylindrically symmetric copper electrodes which were placed inside the vacuum chamber mounted in a grounded aluminum housing as seen in Figure 3.10. The magnetic fields were produced by sets of wire coils which were wrapped to the outside of the vacuum chamber. This configuration is used in our current setup for the experiments discussed in this thesis.

### 3.4.1 Electrodes and Extraction Grids Assembly

The Penning trap configuration uses a combination of electric and magnetic fields in order to produce a trapping geometry for charged particles with opposite signs in the same region of space [3]. Charged particles cannot be trapped by electrostatic potentials alone. The potential from a configuration of electrodes will satisfy Laplace's equation in the absence of free charges, given by,

$$\nabla^2 \Phi(\vec{r}) = 0 \tag{3.18}$$

where $\Phi(\vec{r})$ is the electrostatic potential. This relationship implies that there are no minimums or maximums of the potential throughout space, only saddle points, which will only allow for points of unstable equilibrium. If we consider a cylindrical geometry of electrodes, the addition of a strong, uniform magnetic field in the axial direction can provide confinement for charged particles in the radial direction by taking advantage of the Lorentz force on charged particles. The trajectory of any charged particle traveling in the radial direction will confined to a circular orbit of radius $mv_r/eB$.

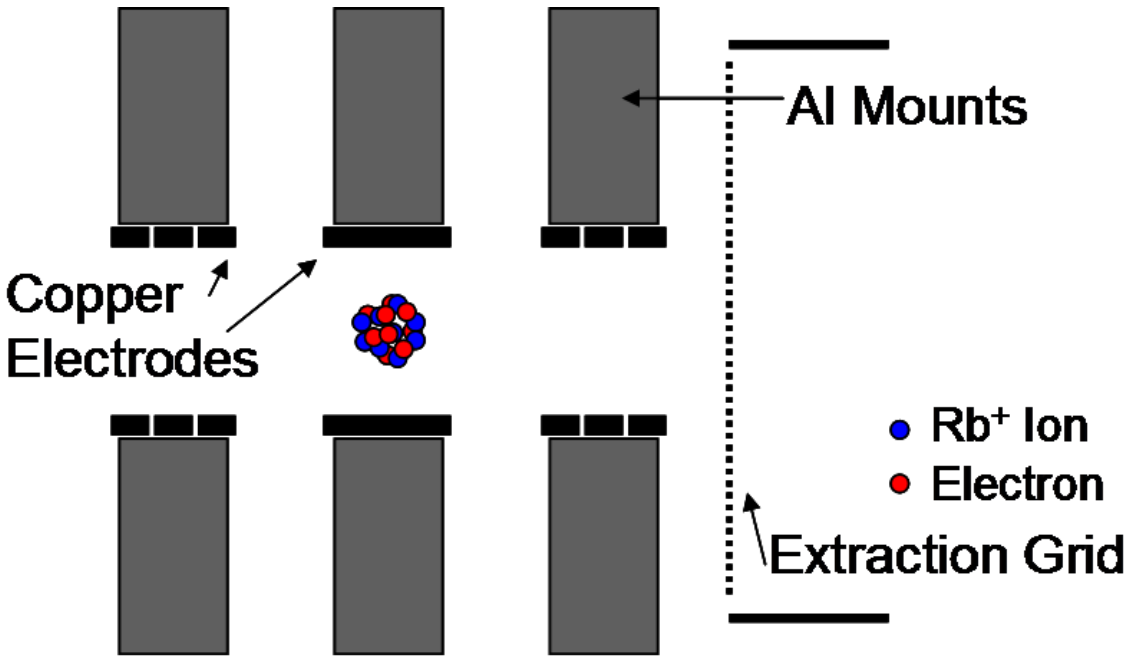


Figure 3.10: A diagram of a cross-section of the electrode assembly. The electrode assembly consists of 7 cylindrically symmetric copper rings, with 3 aluminum mounts. The electrodes are each individually wired to apply a separate potential on each ring if needed. The aluminum mounts are grounded to the vacuum chamber. The electrodes are electrically isolated from each other and the aluminum mounts by small strips of kapton. Outside of the electrode assembly is an aluminum wire mesh grid which is set to high voltage to extract the electrons towards the detector.

For $T_i = 1$ K, $T_e = 10$ K, and $B = 0.1$ T, the Larmor radius for the ions and electron is 124 $\mu$m and 1 $\mu$m respectively. This is smaller than our $\sim$850 $\mu$m rms size for the UCP in the radial direction. This leaves only the axial direction in need of electrostatic confinement.

The ideal electrostatic potential for our Penning trap configuration can be seen in Figure 3.11. Here the ions and electrons of the UCP would be confined to the same region of space. The UCP is created in a region with a flat central potential where the UCP ions and electrons will be most of the time. On the edge of the trapping region, there are wall potentials for both the ions and electrons separately to keep the particles from escaping the center region. Producing such an ideal potential is difficult, but shows us the properties of an axial potential that are needed in order to confine oppositely charged particles in the same region of space. This type of potential is also required in experiments involving the production of anti-Hydrogen [16], where anti-protons and positrons need to be trapped in the same region of space. However, our experiments will have the advantage of being able to directly acquire the particles to be trapped in the trapping region.

To produce a potential with these qualities, I designed a system of 7 electrodes made from copper rings seen in Figure 3.10. The electrodes have an outer diameter of 0.5 inches and an inner diameter of 0.42 inches. The electrodes have an axial extent of 0.2 and 0.07 inches for the center and outside electrodes respectively. The housings for each set of electrodes are spaced by 0.75 inches. The availability of this number of electrodes provides a way to manipulate the electric field environment to a great degree. We can calculate the electric field and potentials owing to this set of electrodes as well as charged particle trajectories in the system by using a commercial program, SIMION. This program allows us to easily manipulate the applied voltages on each on the electrodes to produce the desired on-axis potential. The potential produced by the SIMION calculations is shown in Figure 3.11. In principle, tuning the electrodes carefully can produce an even "flatter" electric field region than is shown in Figure 3.11. Based on our calculations and experimental observations using this electrode design, we have produced a second generation design of the electrodes assembly that should offer more control of the electric field environment in the central region of the electrodes.

In addition to the ability to create a Penning trap, our electrodes and grids assembly also needs to be able to extract the electrons out of the plasma region towards our micro-channel plate detector (MCP) for detection of our UCP signals. Since we are unable to image the ions of the UCPs as in

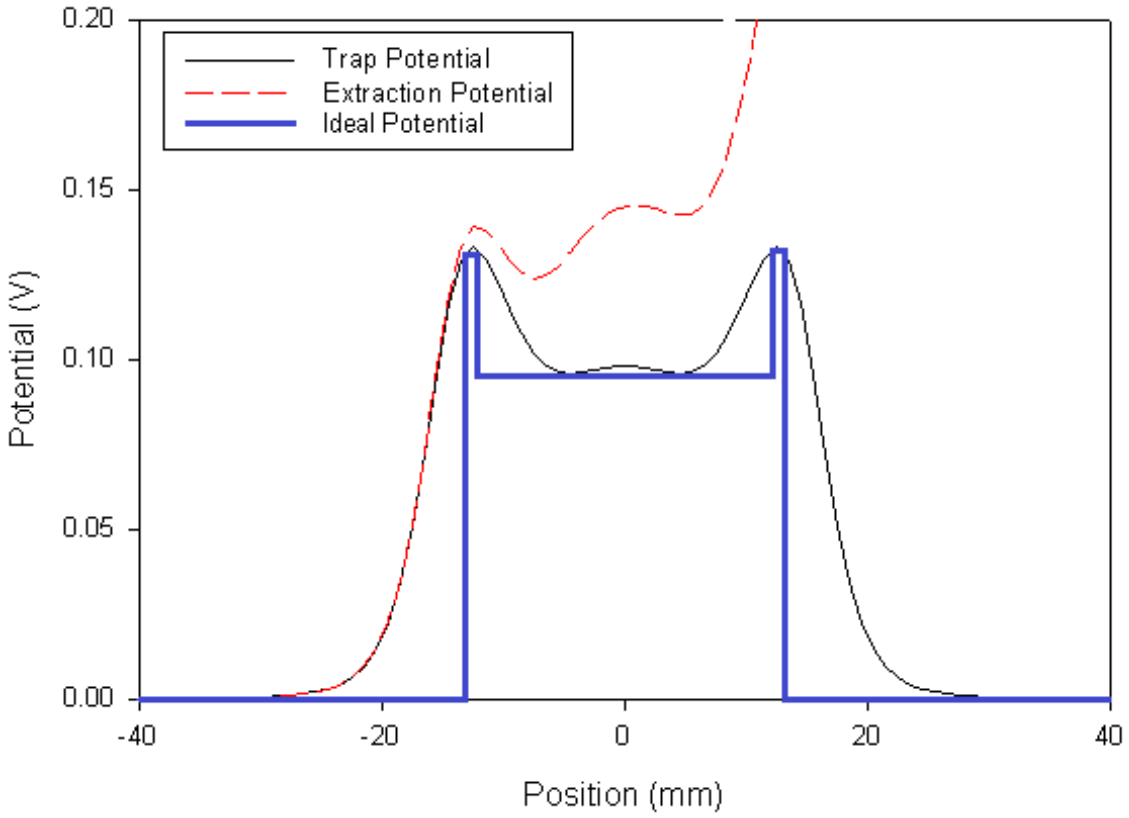


Figure 3.11: The on-axis potential of the Penning trap configuration from our electrodes (black line) and the ideal case (blue line). The red, dashed line shows the extraction potential to pull electrons toward the detector. The ion and electrons are confined to the center region of the potential in the axial direction by this field. Electrons will not spend much time in the wells created by the ion confining field as they accelerate quickly through this region. Any electrons that are thermalized in this region can be reintroduced into the trapping environment with small tipping pulses at the expense of heating. Radially, a strong magnetic field will cause any charged particles trying to escape to be confined around the magnetic field lines.

other experiments [17], it is essential that we achieve efficient collection of the electron signal. The rate of electron escape as measured by our detector is the main signal in all of our experiments. To achieve efficient collection of the electrons, several considerations need to be made. First, we need to ensure that none of the electrons can escape to the grounded surfaces of the vacuum chamber to be lost. To do this, we create the UCPs at a potential that is slightly above ground (0.35 V on the center electrode in our current setup) so that the electrons see a large potential hill near any grounded surfaces that they have insufficient energy to overcome. Second, we need to ensure that any electrons that do escape the UCP are directed towards our detector. To do this, we can apply a bias electric field which pulls the electrons toward the detector. This field is created by applying voltages to the electrodes on either side of the center electrode. One consideration that we had to make when choosing these electrode voltages was that higher positive potential will attract the electrons. So, when creating an electric field that would pull the electrons toward the MCP, we needed to ensure that the electrons would not be lost by their attraction to the electrodes that created these fields. To maximize our extraction efficiency, we grounded the inner-most electrode on the set of electrodes on the MCP side of the electrode assembly, meaning that no electron could approach closely to the electrode itself. To get the electrons through to the detector, the outer two electrodes were increased in voltage (4.7 V in our current setup) to create a strong electric field on the axis of the electrodes.

The ideal electric field environment for the UCPs in our system will be one that has the minimum electric field in the plasma region while maintaining efficient extraction of the electrons from the UCP to the detector. The electric field is minimum when the UCP lifetime (the amount of time it takes for the last electron to escape the UCP) is maximized. To minimize the field, we can experimentally tune the voltages on each of the electrodes individually while maintaining peak extraction efficiency until we maximize the UCP lifetime. For our experiments, we operate with effective electric field values between 1-10 V/m. Our method for determining these electric field values experimentally will be presented in Section 3.6.

Once the electrons are out of the plasma region and past the electrodes, we still need to get the electrons all the way to the detector. To do this, we installed a system of extraction grids that keeps the electrons moving toward the detectors as seen in Figure 3.1 and in Figure 3.12. The grids assembly consists of 5, 1 inch diameter (0.1 inches thick), 0.2 inches wide stainless steel rings

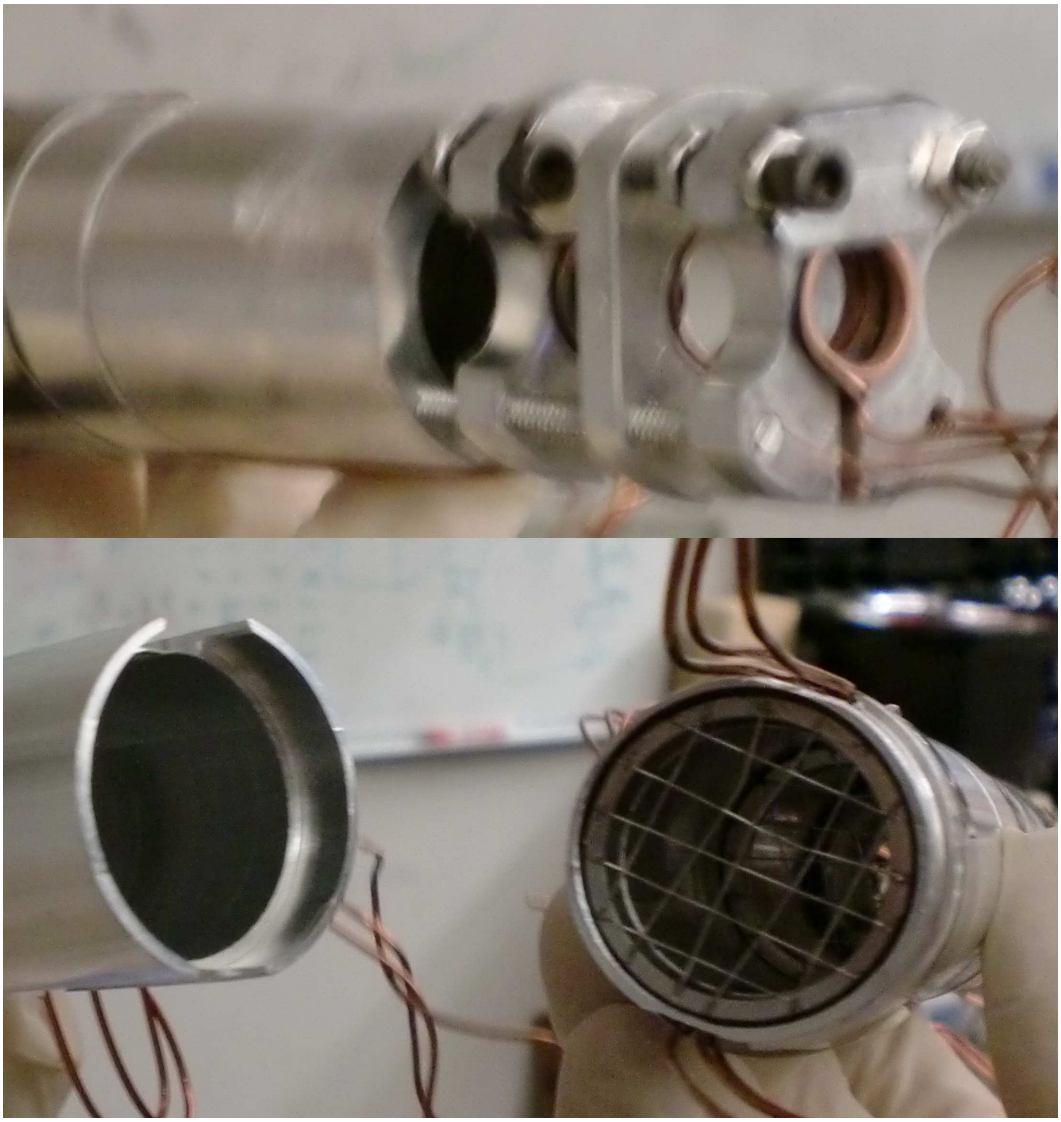

Figure 3.12: A picture of the electrodes and grids that are used in our system. The electrodes (top) are diagrammed in Figure 3.9. The grid assembly consists of 5 wire mesh, stainless steel grids that are spot welded stainless steel rings. They are mounted in a grounded, aluminum housing which is isolated from the grids by kapton.

with 99 % area free stainless steel wire mesh spot welded across the face of the rings. The 5 rings were evenly spaced at 2.25 inches apart in a cylindrical aluminum housing that was broken into 4 sections so that we could place the grids. The grids were separated from the housing by thin rings of kapton for electrical isolation. The rings were brought up to 120 V while the aluminum housing was kept at ground. These grids guided the electrons that escaped the UCP toward the MCP for our signal extraction. Simulations using SIMION have shown that the fast electron speed along the axis of the grids assembly should keep the electrons from approaching the rings that are held at 120 V. The grounded aluminum housing keeps the electrons near the center of the grids assembly as the electrons travel toward the detector.

The complex nature of our electric field environment required a complicated set of electrodes and grids to meet all of the needs of our experiment. As such, this created a number of difficulties in providing the proper voltages to all of the different electrodes and grids, which were individually wired. One of the main problems was to provide all of the necessary wiring while maintaining a clean vacuum system. Improper materials and connections made inside a vacuum system can produce spots with a large out-gassing rate, which can reduce the lifetime of the atoms in the magnetic trap. Because of this, we used specially made, vacuum compatible, kapton-coated copper wire. This wire could be welded directly to each of the copper rings used for our electrodes, and then connected to a set of vacuum compatible electrical feedthroughs to provide the proper voltages. To connect wires to the grids, special techniques had to be implemented because the copper wire could not be welded or soldered to the stainless steel rings (which were stainless steel so we could spot-weld the grids to them). To connect these wires, we simply hammered the ends of the wire flat and wedged them directly between the rings and the kapton insulation. The size of the rings were such that the wire was friction locked tightly between the ring and the kapton insulation, providing a good electrical connection.

Providing electrical connections to the separate grids and electrodes in the system was a challenge not only for the connections to the actual components, but also in getting the wires through the chamber without having adverse effects on the system. On the MOT side of the chamber, it is possible that wires that are not held to the bottom of the chamber will impede the transfer of the atoms in the magnetic trap by physically blocking the path of the transfer (this was, in fact, a problem that arose). To deal with this problem, we were able to hold the wires down to the bottom

of the chamber with a thick ring of kapton, which was cut and placed in the chamber about 5 inches away from the electrode assembly. On the other side of the electrodes assembly, the wires from the electrodes and grids that are connected to electrical feedthroughs near the MCP need to kept out of the region where the electrons travel toward the MCP. This is because wires in region can create image charges on the grounded surface of the vacuum chamber that change the electric field environment for the electrons. Also, the high voltage applied to the wires for the grids (120 V) will be attractive to the electrons and may divert them from their path to the detector. To avert this problem, these wires were directed through channels that were cut on the outside of the aluminum housing that holds the grids so that the wires can be shielded from the region of electron travel. To get the wires for the grids out of the region of electron travel, small holes were drilled through the aluminum housing near the location of the grids. This allowed for the wires to exit the region of electron travel and go into the channels cut on the outside of the aluminum housing.

When using vacuum compatible, kapton-coated wire, one must take care to keep the wires away from any moderately hard or sharp surface in order to ensure that the kapton coating is not removed during the installation of the electrodes and grids assembly. If the coating is removed, any contact with any surface in the vacuum chamber will cause a short to ground of the electrode or grid that the wire is connected to. Therefore, it is very important to make sure that the wires are not put under any stress during installation. Also, since there are various bends that are required through and around the channels in the grids housing, it is important to make sure that the corners are properly rounded and that the wires are not in contact with these corners. Shorts that occur in the vacuum system generally require the system to be reopened, which may require another system bake-out. Baking out the vacuum system can require up to 3 weeks of down time before the system is operational. If one chooses to forego a bake-out after opening the chamber, this can result in a significant decrease in the lifetime of the magnetic trap as we have observed. However, it is possible that a short can be fixed by applying a light impulse to the appropriate part of the vacuum chamber in an effort to move the wire slightly from the location of electrical contact with a grounded surface. This generally works best on a flange of the vacuum chamber, with the handle of a screwdriver being the tool of choice.

### 3.4.2 Magnetic Field Environment

The magnetic fields that are required for our experiments are much simpler than the electric fields as the Penning trap configuration requires only a strong, uniform magnetic field in the region where the UCP is created. So, besides the transfer shim magnetic coils that are placed near the plasma region to help us align the atoms with the electrodes, an axial magnetic coil is wrapped directly to the chamber as seen in Figure 3.1 and Figure 3.9. This magnetic coil is lined up with the center electrode in the plasma region. It consists of 100 turn, 2.3 cm radius coil wrapped in a plastic coil form which constrains its axial extent to 9 mm. This produces magnetic fields of 27 G/A at the center of the coils. Also, the magnetic field strength changes by only ∼1% over 2 RMS radii (∼2 mm) from the center of the coil region. This gives us an approximate uniform magnetic field in the plasma region.

The small non-uniformity to the magnetic field in the plasma region led to a question of whether there would be a significant magnetic anti-mirror effect, which results from a change in magnetic field strength as a particle travels through the field. As a particle travels from a region of higher magnetic field to a region of lower magnetic field, the particle's velocity parallel to the magnetic field will change as,

$$v_{\parallel}^2 = v_0^2 - v_{\perp 0}^2 \frac{B(z)}{B_0} \tag{3.19}$$

where $v_0$ is the total velocity and is a constant, $v_{\parallel}$ and $v_{\perp}$ are the particle velocities parallel and perpendicular to the magnetic field respectively ($v_{\parallel}^2 + v_{\perp}^2 = v_0^2$), $B_0$ is the magnetic field at the location of the particle's initial position, $B(z)$ is the magnetic field as a function of the axial position, and $v_{\perp 0}$ is the perpendicular component of the velocity at the point where $B(z) = B_0$. Here, $B(z)$ varies as $(R^2 + z^2)^{-3/2}$, where $R$ is the radius of the magnetic coil (2.3 cm for our system). As the particle moves through to a region of weaker magnetic field, the velocity perpendicular to the field lines will transfer to axial (parallel) motion. So, Equation 3.19 tells us how much the velocity parallel to the magnetic field lines will increase as the particle moves away from the center of the UCP parallel to the magnetic field. As discussed before, the magnetic field strength only changes by ∼1% over 2 RMS radii (along the axial direction) of the UCP. So, using this change in magnetic field in combination with Equation 3.19, the parallel velocity at the edge of the UCP becomes

$v_\parallel = \sqrt{v_0^2 - 0.99 v_{\perp 0}^2}$. One can already see here that the anti-mirror effect will only contribute a very small component to the axial velocity of the electron. If we assume an electron with a total velocity of $v_0 = 20,000$ m/s with $v_{\parallel 0} = v_{\perp 0} \sim 14,140$ m/s, moving to the edge of the UCP will increase $v_\parallel$ to ~14,210 m/s. From this change in velocity, we can calculate the effective electric field that would produce this amount of acceleration over the $2\sigma = 2$ mm distance we are considering to be $E = m_e(v_\parallel^2 - v_{\parallel 0}^2)/(4\sigma e) \sim 3$ mV/m. This effective electric field is much less than the few to several V/m electric fields that are produced by the electrodes and can induced by thermal motion inside the UCP. Thus, we can ignore the effect of the magnetic anti-mirror.

The Penning trap requires a large magnetic field which is on the order of 0.1 T, or 1000 G, which requires around 37 A of current to be run through our axial magnetic field coil. Switching on such a large amount of current in short amount of time is a difficult task using just commercial power supplies as discussed previously. It can require a large amount of time (10s of ms) to switch between current levels in this fashion, which is far too slow for the studying UCP physics on the 10s of $\mu$s timescale. Also, there is only ~3 ms between the release of the atoms from the trap to the point of photoionization which means that any switching of the magnetic field levels needs to happen in this time. Switching too early will push the atoms in the trap out of the ionization region before the atoms are released from the trap. Too late and any switching that occurs after photoionization will heat the electrons owing to the large electric fields that can be induced by a large $dB/dt$ term.

To switch quickly to high magnetic field levels, we developed a system in which a large inductor can be used force current through the axial coil in a short amount of time in conjunction with field-effect transistor (FET) switches as seen in Figure 3.13. In this configuration, we can set two paths for the current; one with through the axial magnetic coil (path 1) and one that serves as a dump for the high current when it is not desired (path 2). The large inductor is placed before the two paths are split. We place a FET in each path to serve as switches that regulate what path the current travels down. We start in a configuration with all the current flowing through path 2 by closing the FET switch in this path. In path 1, the FET switch is left open to prevent any current flow. To turn the current on through the axial magnetic coils, the states of the two FET switches are reversed. The large inductance of the inductor will produce large voltages that will tend to

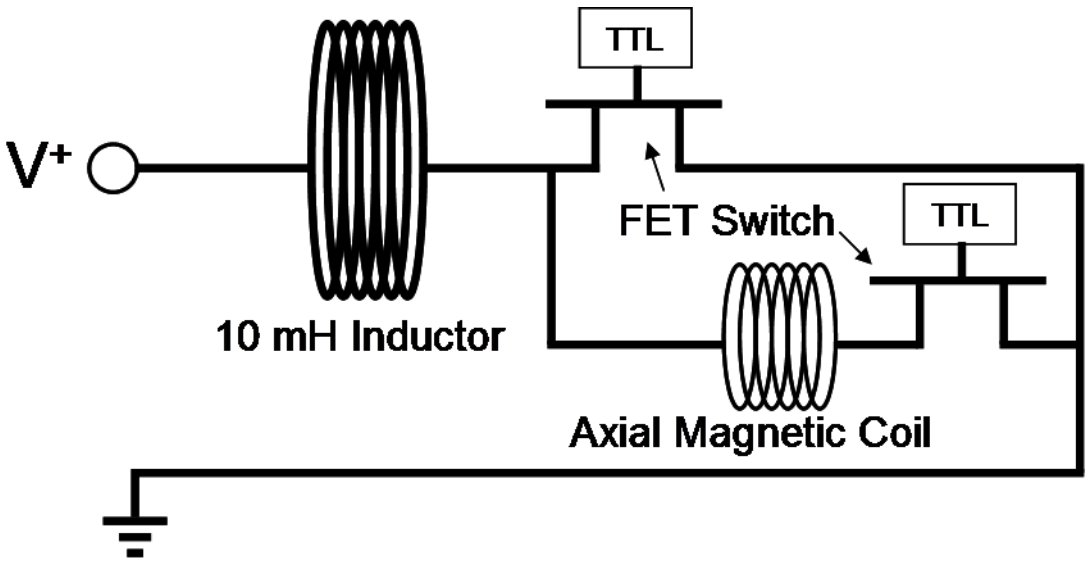


Figure 3.13: A diagram of the circuit we will use for switching to very high current levels on the axial magnetic field coil. A 10 mH inductor is placed in series with two current paths. One current path has the axial magnetic field coil and the other is a dump for the excess current when the magnetic field is not in use. Each current path has a FET switch that regulates when the current is going through each path. The current starts by going on the path without the axial magnetic field coil. When the FETs are switched, the 10 mH inductor keeps the current level through the circuit nearly constant, which forces a large amount of current through the axial magnetic field coil in $\sim$10 $\mu$s.

keep a constant current through the circuit, which forces a large amount of current through the axial magnetic field coil in a short amount of time. This method as produced switching times as fast as $\sim$10 $\mu$s, which greatly exceeds our requirements for this system.

The magnetic fields used for the work presented in this thesis only range between 0-14 G (0.5 A through the axial magnetic field coil), as the focus of my experiments for this thesis are on UCPs in weak magnetic fields (Chapter 6). Using higher magnetic fields in this experiment produces a significant reduction in the total ionization number owing to the Zeeman broadening of the $5S_{1/2} - 5P_{3/2}$ transition. When using a higher value of the magnetic field, additional lasers will have to be added to the system in order to excite transitions between particular states that have been shifted due to the Zeeman effect. The servo that controls the field levels for the current configuration have slower switching times on the order of 1 ms, which is sufficient when going between low current levels.

## 3.5 Dye Laser System

To produce the ultracold plasmas in our system, we photoionize the $^{85}$Rb atoms using a commercial pulsed-dye laser system produced by Spectra Physics. The dye laser produces $\sim$10 ns pulses with up to 10 mJ of energy. For our experiments, we operate the dye laser at wavelengths ranging from 471 nm to 480 nm. This represents a range of energy from just below the ionization threshold for atoms in the $5P_{3/2}$ state to $\Delta E/k_B$ $\sim$500 K above threshold. To optically pump the laser dye used for photoionization, we use a Quanta Ray INDI-40-10 Nd:YAG laser. Although the laser is commercially produced, it requires regular maintenance to keep our system running with the desired experimental parameters. So, it is necessary to understand the individual components of the system and their basic operation.

The Nd:YAG laser head consists of an optical cavity, Nd:YAG crystal in the shape of a cylindrical rod, flash lamps, and a Pockels cell used for Q-switching (Section 3.5.1) as seen in Figure 3.14. The flashlamps and laser rod are both enclosed in an elliptical gold reflector cavity (not the lasing cavity) to create the population inversion required for lasing. The flashlamps are water-cooled using a closed circulation system, where the cooling water flows through the reflector cavity. After the output of the lasing cavity, the laser light goes through a pair of crystals to produce the 3rd

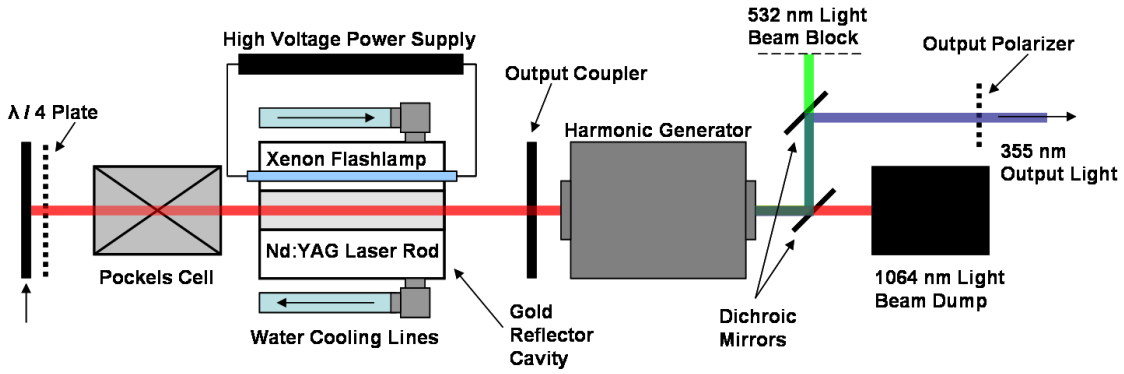


Figure 3.14: A diagram of the INDI-40-10 Nd:YAG laser setup. The xenon flashlamps pump the Nd:YAG laser rod which acts as the gain medium. The Pockels cell acts as the Q-switch which allows the production of high intensity laser pulses. The harmonic generator has two stages, one to produce second harmonic light at 532 nm and the other to mix the 532 nm light with the 1064 nm light to produce light at 355 nm. This light is separated by dichroic mirrors to output only the 355 nm light.

harmonic light at 355 nm, which is used to pump the laser dye for our system. The angle of the harmonic generating crystals can be adjusted to optimize the power output of the 3rd harmonic light, and are the only simple adjustments that can be made to the laser without taking the cover off of the laser head.

The dye laser system consists of a dye circulation system, dye cell, and resonator cavity in a Littrow configuration (as with our diode lasers) for frequency control. The dye that is used for our experiments is Coumarin-102, which produces light in the blue part of the visible spectrum. The wavelength of the laser is frequency controlled by a diffraction grating on the output of the resonator, which can be computer controlled to set the wavelength to within 0.005 nm.

The Nd:YAG laser operates in a 10 Hz pulsing configuration where the pulsing is produced using a Pockels cell for Q-switching. The laser system was engineered for the heat load introduced under this configuration, so the optimum power is achieved by running at 10 Hz. However, the experiment itself works on a timescale where we only need one laser pulse every 30 s - 1 min. As the 355 nm light pumps the laser dye, it actually begins to break down the molecules of the dye, which degrades the power slowly over time. So, to preserve the integrity of the dye in the system, we placed a shutter in between the Nd:YAG pump laser output and the dye laser system so that we can use dye laser pulses only when we need them while maintaining the optimum output of the pump laser as seen in Figure 3.15. The shutter system consists of a FW103 High Speed Motorized Filter Wheel controlled by an APT Precision Motion Controller, both of which are sold by ThorLabs. The filter wheel has one slot with a mirror that directs the 355 nm output towards a beam dump when the dye laser is on standby. When a pulse from the dye laser is desired, the filter wheel can be rotated rapidly to an empty slot in the filter wheel, passing a single 355 nm pulse to the pulsed dye amplifier before rotating back to the mirror. The output of the dye laser is sent to the plasma side of the vacuum chamber to photoionize the $^{85}$Rb atoms in the system.

### 3.5.1 The Nd:YAG Laser

The Nd:YAG laser rod is produced by doping a $Y_3Al_5O_{12}$ (Yttrium Aluminum Garnet) crystal with the rare earth element neodymium [18]. The Nd takes the place of the Y in the YAG crystal structure and acts as $Nd^{3+}$, which is used as the lasing medium for the Nd:YAG laser. The laser is pumped by Xenon flash lamps in the near infrared to a band of energy levels higher in energy

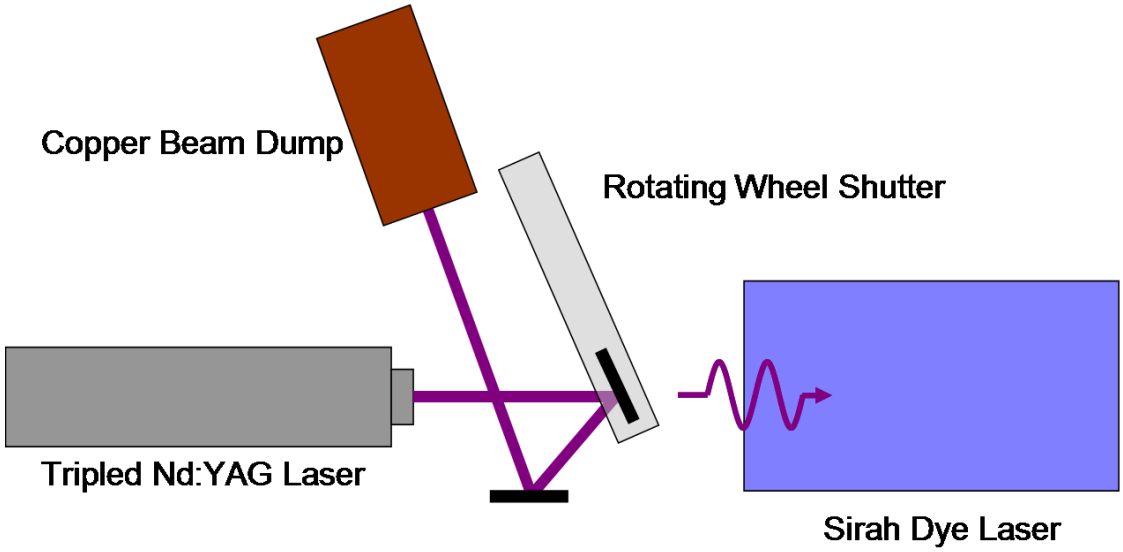


Figure 3.15: A diagram of the wheel shutter assembly for the pulsed, dye-laser system which consists of a FW103 High Speed Motorized Filter Wheel controlled by an APT Precision Motion Controller. The Nd:YAG laser pulses at 10 Hz for optimum performance. The overall system operates at a much lower repetition rate and doesn't require pulses at 10 Hz. Continuous pumping of the laser dye would degrade the output power of the system unnecessarily. When the laser pulses are not needed, the 355 nm output of the Nd:YAG laser is directed by a mirror placed in the wheel shutter towards a copper tube which serves as a beam dump. When the shutter is triggered, the wheel rotates to let a single laser pulse from the Nd:YAG laser into the resonator of Sirah Dye laser.

than the $^4F_{3/2}$ state, the upper level of the lasing transition. The population of this state decays quickly ($\tau$ <1 ns), populating the long lived ($\tau \sim 230\mu$s) $^4F_{3/2}$ state [19]. The laser transition with the highest gain is between the $^4I_{11/2}$ and the $^4F_{3/2}$ state at 1064 nm. The lower state of the lasing transition also decays in less than 1 ns, making it possible to produce a relatively large population inversion between the two states.

The production of the high intensity pulses needed to photoionize a large number of atoms quickly requires our Nd:YAG laser to operate in a Q-switch configuration. The Q-switch acts as an effective shutter, which keeps photons from feeding back into the cavity after they leave, preventing any lasing from occurring. This greatly reduces the amount of stimulated emission that can take place, as the number of photon passes through the gain medium is greatly reduced. So, population will accumulate in the $^4F_{3/2}$ state, and is only limited by the spontaneous emission lifetime ($\sim$ 230 $\mu$s). This will build up a large amount of energy in the $^4F_{3/2}$ state, which can be used in the laser pulse when the Q-switch is flipped.

The Q-switch itself is produced by a Pockels cell, which is an electro-optical device that controls the orientation of linearly polarized light that passes through it. By using the Pockels cell in conjunction with the proper polarizing optics, one can change the polarization state of the light to be blocked from feeding back through the cavity. When enough energy has been stored in the population inversion in the Nd:YAG crystal for the desired laser pulse, the Pockels cell can be switched to allow light to feedback through the cavity, depopulating the upper level of the lasing transition, which produces a short, high-intensity laser pulse.

The light produced by the Nd:YAG laser in our system is at 1064 nm. To produce light at the shorter wavelength required to pump the dye laser system, we rely on second harmonic and sum frequency generation to produce light at 355 nm. Second harmonic generation is special case of sum-frequency generation and occurs from the interaction of high-intensity light with a medium of non-linear electric susceptibility. In this case, the polarization of the medium from the impending light has a non-vanishing term that is proportional to the input electric field squared. This squared electric field term produces frequency components of the electric field at the sum and difference of the frequencies of the input light. In the case of second harmonic generation, there is only one frequency present in the input light. So, the non-linear output consists of light with double the frequency of the input light. To maximize the output of the higher harmonic components of the

light, the components of the light need to be properly phase-matched along the proper axis of the non-linear crystal. The harmonic generator for our Nd:YAG pump laser has external tuning knobs on the second and third harmonic crystals which can be adjusted to maximize the output of 355 nm light from the laser. These are the only external adjustments that can be made on this commercial system. There are two circular holes that are cut into the cover of the laser than allow for a 9/64 hex key to be inserted into the adjust these knobs. The 355 nm output will generally stay near its peak output for long periods of time without adjustment. However, if an adjustment is needed, then each of the harmonic knobs can adjusted in an alternating fashion to optimize the 355 nm output. If additional adjustment is needed, they laser cover can be removed and the input waveplate for the harmonic generator can be adjusted along with these knobs.

A few other problems have been encountered during the course of our experiments that have taken the laser power off of its optimum output. The flashlamps have an operational lifetime of that exceeds 10 million discharges. Over time, the output power of the flashlamps degrades, so they have to be replaced regularly. Another problem we encountered was with a breakdown of the water pump for the internal cooling of the flashlamps in our system. This water pump eventually required replacement. This breakdown of the water pump lead to insufficient cooling of the flashlamps, degrading their performance and lifetime. Also, when the pump broke down, it contaminated the cooling water, which coated the gold reflector cavity in a foreign substance. To clean the gold reflector cavity, we used 5% concentrated table vinegar and scrubbed the gold reflectors with Q-tips. The gold reflector cleaning was also combined with a flush of the system's cooling water. These situations need to be considered when doing maintenance on the Nd:YAG laser. Fortunately, the actual lasing cavity has not needed to be adjusted at this point, and should remain stable over a very long period of time.

For this system, we produce laser pulses with up to 100 mJ of energy at 355 nm with $\sim$10 ns widths. This light is then fed into the dye laser system as the pump light so that we can produce laser pulses that are near the ionization threshold for $^{85}$Rb.

### 3.5.2 Sirah Dye Laser System

The dye laser system used for our experiments is also commercially produced and distributed by Spectra Physics, and requires very little maintenance to operate at optimal conditions. The system

consists of a laser dye circulator and pump system, optical resonator, and a wavelength control diffraction grating. The gain medium for the dye laser is Coumarin-102 dye using methanol as a solvent. The dye is pumped into the dye cell, which is ∼2 cm in length, where it is optically pumped using the 355 nm output of the Nd:YAG laser. The energy levels of a dye laser gain medium are generally more complicated than those of other types of laser systems, as they tend to involve excitation between energy levels that also have closely-spaced molecular vibrational and rotational energy levels associated with them [20]. However, the principle of operation is that same as that of the general four-level laser system, where the gain medium is optically pumped to a rapidly decaying, highly excited state. This rapidly decaying excited state decays to a longer lived excited state such that a population inversion is produced.

The wavelength of the output of the dye laser is controlled by diffraction grating feedback as in the case of our diode laser systems. In this case, the angle of the diffraction grating is controlled with a high-precision motor that is computer controlled and factory calibrated. The wavelength can be controlled and reproduced to within 0.005 nm, which more than exceeds the needs for our applications. To avoid problems from backlash when changing the grating angle, the grating is turned all the way to the edge of its range before being tuned to the desired wavelength.

Using a dye as a laser medium has the advantage of having a tunable wavelength at high power. However, using the dye repeatedly causes its quality to breakdown as pumping with a high-powered laser can break the bonds in the dye molecules. The dye circulator system needs to be flushed and the dye replaced at regular intervals in order to maintain a high enough pulse power for our experiments. When replacing the dye, we see a rapid (but not detrimental) initial degradation of pulse power from its peak levels followed by a long (many months) period of stable output power from the dye laser. We attribute this long, stable period to our low duty cycle of operation when performing our experiments. For this system, we can achieve pulse energies of up to 10 mJ for 10 ns pulses.

### 3.5.3 Photoionization of Rubidium

The purpose of the Nd:YAG pump laser and dye laser in our system is for the photoionization of Rb atoms from the $5P_{3/2}$ state. When the atoms are transferred to the plasma region of the vacuum chamber, the atoms are released from the magnetic trap. After we release the atoms, we wait for

2.2 ms to allow any electrical noise associated with the magnetic field shutoff and track motion to dissipate. This time is also used to change the axial magnetic field to the desired levels for the experiments. Eddy currents associated with the magnetic field shutoff decay quickly, on the order of $\sim$100 $\mu$s. After this, we can pump the atoms out of the $F = 2$ ground state and into the $5P_{3/2}$ using pick-off beams from the cooling and repump diode lasers for 5 $\mu$s (we generally repump them from the $F = 2$ ground state a few hundred $\mu$s earlier, but the extra light has little effect because the atoms quickly become dark to the hyperfine repump light). The intensity of these pump beams is $\sim$2 $I_{sat}$, with beam diameters of $\sim$5 mm which pumps $\sim$ 33% of the atoms the excited state. The pickoff from the trap laser beam is coupled into an optical fiber which allows us to align the beam on the plasma side of the vacuum chamber (since little hyperfine repump light is needed, we allow this beam to travel in free space across the optical table).

From here, the Rb atoms are ionized with the light from the dye laser near the ionization threshold at $\sim$479 nm. The beam has waist sizes of $w_{0z} = 2$ mm and $w_{0x} = 1.3$ mm in the vertical and horizontal directions respectively. The beam from our dye laser is far from a $\mathrm{TEM}_{0,0}$ mode, and requires additional shaping of the laser which we do with cylindrical lenses. Even in this case there is a large "halo" of light that surrounds the main beam which can be problematic when trying to perform our experiments. If enough light reaches the chamber that impinges on any part of the electrode assembly, a large background signal of electrons can be ejected from the electrode assembly owing to multi-photon processes. Therefore, it is necessary to aperture the beam near the vacuum chamber to ensure that all of the high intensity light passes through the vacuum chamber unimpeded.

We can estimate the expected ionization fraction from our beam parameters combined with the density distribution of the atoms in the plasma region. The expected ionization fraction at a given point in the atomic distribution can be found by solving rate equations for photoionization from the $5P_{3/2}$ state given by,

$$\frac{dN(t)}{dt} = -RN(t) \tag{3.20}$$

where $N$ is the number of atoms and $R$ is the rate of ionization given by [10],

$$R = \frac{I\sigma\lambda}{hc} \tag{3.21}$$

where $\sigma$ is the photoionization cross section which is $1.88 \times 10^{-17}$ cm$^2$ for the $5P_{3/2}$ state in Rb [10], $\lambda$ is the wavelength of the ionization transition (479 nm), $h$ is Planck's constant, and $c$ is the speed of light. We can solve for the number of ions produced to be,

$$N_{ion} = N_0(1 - \exp(-R\Delta t)) \tag{3.22}$$

where $N_0$ is the original number of atoms, and $\Delta t$ is the length of the ionization pulse. We can perform this calculation at each position in space, taking into account the number of atoms and their spatial profile in ionization region using absorption imaging and the profile of the ionization laser beam. This calculation shows that we should expect an ionization fraction of ∼21% of the total number of atoms that are transferred to the plasma region. By comparing over 20 images of the atoms to our measured number of ions and electrons in the plasma (using the number calibration technique discussed in the next section), we find that we ionize ∼19% of the atoms in the plasma region. This gives us as many as $1.4\times10^6$ ions and electrons for our UCPs. Typically we use $\sim 5 \times 10^5$ ions for our experiments.

Upon ionization, most of the photon energy above the ionization threshold will be transferred to the electrons. If we consider the Rb atom and incoming photon system in the center of mass frame, the excess energy above the ionization threshold will have to be carried away by the $Rb^+$ ion and electron with equal and opposite momentum. So we have,

$$m_{ion}v_{ion} = m_e v_e \tag{3.23}$$

where $m_{ion}$ and $v_{ion}$ are the mass and velocity of $Rb^+$ and $m_e$ and $v_e$ are the mass and velocity of the electron. If we consider all of the energy going to kinetic energy of the two particles, we have,

$$\Delta E = E_{ion} + E_e = \frac{1}{2}m_{ion}v_{ion}^2 + \frac{1}{2}m_e v_e^2 \tag{3.24}$$

where $\Delta E$ is the photon energy above the ionization threshold. Substituting $v_{ion}^2 = m_e^2 v_e^2/m_{ion}^2$ from Equation 3.23 into Equation 3.24 yields,

$$\Delta E = \frac{1}{2}\frac{m_e^2 v_e^2}{m_{ion}} + \frac{1}{2}m_e v_e^2 = \frac{1}{2}m_e v_e^2\left(1 + \frac{m_e}{m_{ion}}\right) \tag{3.25}$$

So,

$$E_e = \frac{\Delta E}{1 + \frac{m_e}{m_{ion}}} \tag{3.26}$$

The mass ratio of an electron to $Rb^+$ is $6.4 \times 10^{-6}$, which means that the electron receives 99.9994% of the photon energy above the ionization threshold.

## 3.6 Micro-channel Plate Detector

As the electrons are extracted from the plasma region by an electric field provided by our electrodes, they are directed toward a BOS-40 model micro-channel plate detector (MCP) [21] from Beam Imaging Solutions, which provides the signal that is used in all of our experiments. The setup of the MCP and the detection electronics can be seen in Figure 3.16. The current from the MCP flows into a high voltage capacitor, where the equalizing charge on the opposite side of the capacitor produces a current over a load resistance which provides the voltage that is read on an oscilloscope. The signal voltage is proportional to the number of electrons escaping the plasma region in any given time, and the constant of proportionality is dependent on the voltage between the plates of the MCP.

The MCP works to amplify the electron signal from the UCP through secondary electron emission from electronic impacts on the surface of the channels of the MCP [21]. The long, narrow channels of the MCP act as continuous dynode structures which allow for many impacts of both the primary electrons and secondary electrons as they travel down the channel. The electrons from the channel surface are replenished by an external power supply. The channels from the two micro-channel plates in our system are oriented in a matched chevron configuration as seen in Figure 3.16, with the channels cut at an 8 degree bias. The two plates are resistance matched as seen in Figure 3.16, which means that the resistance across each individual plate is the same. This allows us to control only the outside voltage on each plate, with the voltage between the two plates being halfway in between the voltages applied on the outside of the plates.

The MCP can amplify the electron signal by as much as a factor of $10^7$. In practice, we use a gain of $\sim 3 \times 10^4$ with an additional gain of a factor of 20 using electronics after the MCP. In addition to the high signal gain, the MCP also has sub-ns time resolution. Also, since the channels

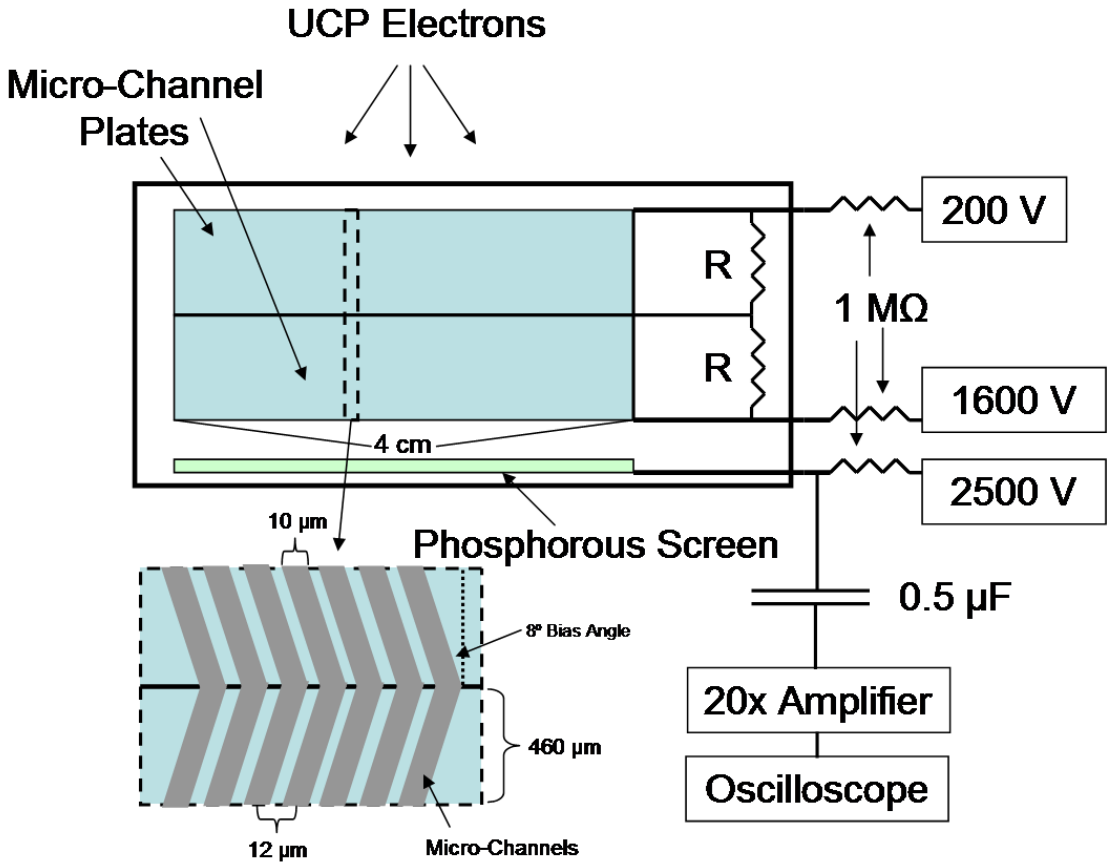


Figure 3.16: A diagram of the setup for our signal detection electronics. The MCP is a BOS-40 system purchased from Beam Imaging Solutions. The micro-channel plates are held at voltage by Stanford PS-325 power supplies. The internal resistance of the MCP ties the two plates together with a voltage divider, making the total gain of the system dependent only on the voltage difference between the two plates. The signal is read out at the phosphorous screen, where the current flows to the 0.5 $\mu$F capacitor, then to external amplifiers which separate the oscilloscope from the high voltage at the MCP. The 1 MΩ resistors limit the current from the high voltage power supplies to the micro-channel plates. The lower left-hand corner shows the orientation of the channels in each of the micro-channel plates in the chevron configuration.

are arranged in a two-dimensional array (4 cm diameter), it can be run in a high voltage mode that will allow for the imaging of the spatial distribution on a phosphorous screen. The spatial resolution is given by the center-to-center channel spacing, which is 12 $\mu$m. However, the time-resolved and spatially-resolved configurations cannot be run at the same time. In our experiments, we typically run in the time-resolved signal configuration and use the spatially-resolved signal infrequently. An example of an experimental signal obtained from our MCP is seen in Figure 3.17.

### 3.6.1 MCP Signal Calibration

The calibration of the MCP signal is critically important for providing an accurate measure of the number of ions in the system. This, combined with measurements of the peak density, allow us to determine the characteristic size of the UCP at any given point in the evolution using the technique described in Chapter 4. It also allows for the determination of the effective electric field strength in the region given a set of electrode conditions used for the calibration measurement. This calibration is crucial for making comparisons of our data to calculations of expected UCP evolution based on our initial conditions.

To calibrate the MCP signal, we can take advantage of the self-trapping nature of UCP systems. This self-trapping requires a minimum number of ions for a particular UCP distribution in order to provide a potential well barrier high enough to trap at least one electron with finite kinetic energy. In the presence of an externally applied extraction electric field (as in our system), this number increases in order to overcome the external field. By measuring the threshold ion number over a range of UCP conditions, we can compare these measurements to calculated values of the potential well depth in order to determine both the MCP signal calibration and the value of the external electric field as will be described below.

The threshold number of ions required to trap electrons in a UCP is defined as the number of ions sufficient to create a potential well with depth, $D$, that is as deep as the initial ionization energy [1]. This can be calculated from a spherically-symmetric Gaussian distribution of ions with a characteristic size, $\sigma$, in a constant external electric field, $F_0$. To simplify this calculation, I will consider the potential on-axis when calculating the depth.

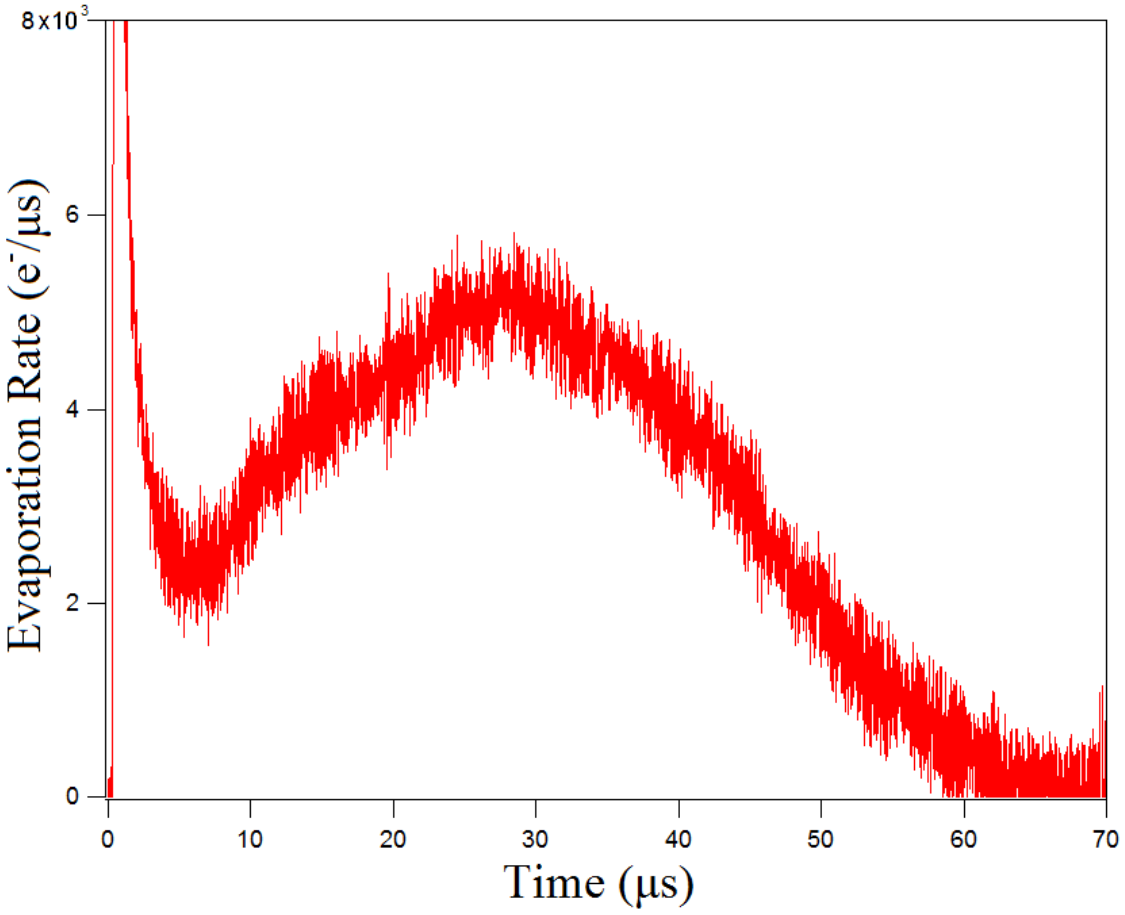


Figure 3.17: An example signal obtain from the MCP for our experimental data. In the first few $\mu$s, a large amount of electrons escape to create the confining potential. As the UCP expands, more electrons are able to escape the UCP and are extracted using an electric field towards our detector. This data shows evaporation from a UCP created at an initial ionization energy of $\Delta E/k_B = 50$ K, $2.5 \times 10^5$ total ions and a characteristic spatial extent $\sigma = 800$ $\mu$m.

I can start by considering spherically-symmetric Gaussian charge distribution given by,

$$n(r) = \frac{N_{tot}e}{(2\pi)^{3/2}\sigma^3}\exp\left(\frac{-r^2}{2\sigma^2}\right) \tag{3.27}$$

where $e$ is elementary charge, $N_{tot}$ is the total number of ions, and $\sigma$ is the characteristic size scale of the UCP. We can use Gauss' law to integrate this distribution in order to find the electric field owing to this charge distribution with an external field $F_0$ as a function of radial position on axis as,

$$\begin{aligned} E(r) &= \frac{1}{4\pi\epsilon_0 r^2}\int_0^r n(r')d^3r' && (3.28)\\ &= \frac{N_{tot}e}{4\pi\epsilon_0 r^2}\frac{\sqrt{2}}{2\sigma}\left(2\exp\left(\frac{-r^2}{2\sigma^2}\right) - \sqrt{2\pi}\sigma\cdot\mathrm{erf}\left(\frac{\sqrt{2}r}{2\sigma}\right)\right) - F_0 && (3.29)\end{aligned}$$

I can find the potential energy for an electron as a function radial position by integrating this field starting from the center of the charge distribution (setting the potential at the center to be 0) to be,

$$\begin{aligned} U(r) &= e\int_0^r E(r')dr && (3.30)\\ &= \frac{e}{4\pi^{5/2}\epsilon_0 k_B\sigma r}\left(\sqrt{2}\pi N_{tot}er - \pi^{3/2}N_{tot}e\sigma\cdot\mathrm{erf}\left(\frac{\sqrt{2}r}{2\sigma}\right) - 4\pi^{5/2}\epsilon_0\sigma F_0 r^2\right) && (3.31)\end{aligned}$$

where the potential here is scaled by $k_B$ to be in temperature-equivalent units. An example of the on-axis potential from this calculation can be seen in Figure 3.18. The desired quantity from this calculation is the total potential depth, $D$, seen by an electron on axis as it tries to escape from the UCP.

To perform the MCP signal calibration, we measure the threshold number of ions required to trap a single electron over a range of initial ionization energies, $\Delta E/k_B$, for a particular configuration of the electric field. To determine the threshold ion number, we measure the number of electrons that are trapped as a function of the total number of ions in units of the MCP signal as seen in Figure 3.19. We start by forming the UCP under a chosen electric field configuration denoted by $F_0$. The space charge that develops from the initial escaping electrons forms a potential well trapping any remaining electrons. After $\sim$3 $\mu$s, we apply an electric field pulse to extract any electrons trapped in the UCP. We can alter the power of the $5S_{1/2}-5P_{3/2}$ pump laser to control the

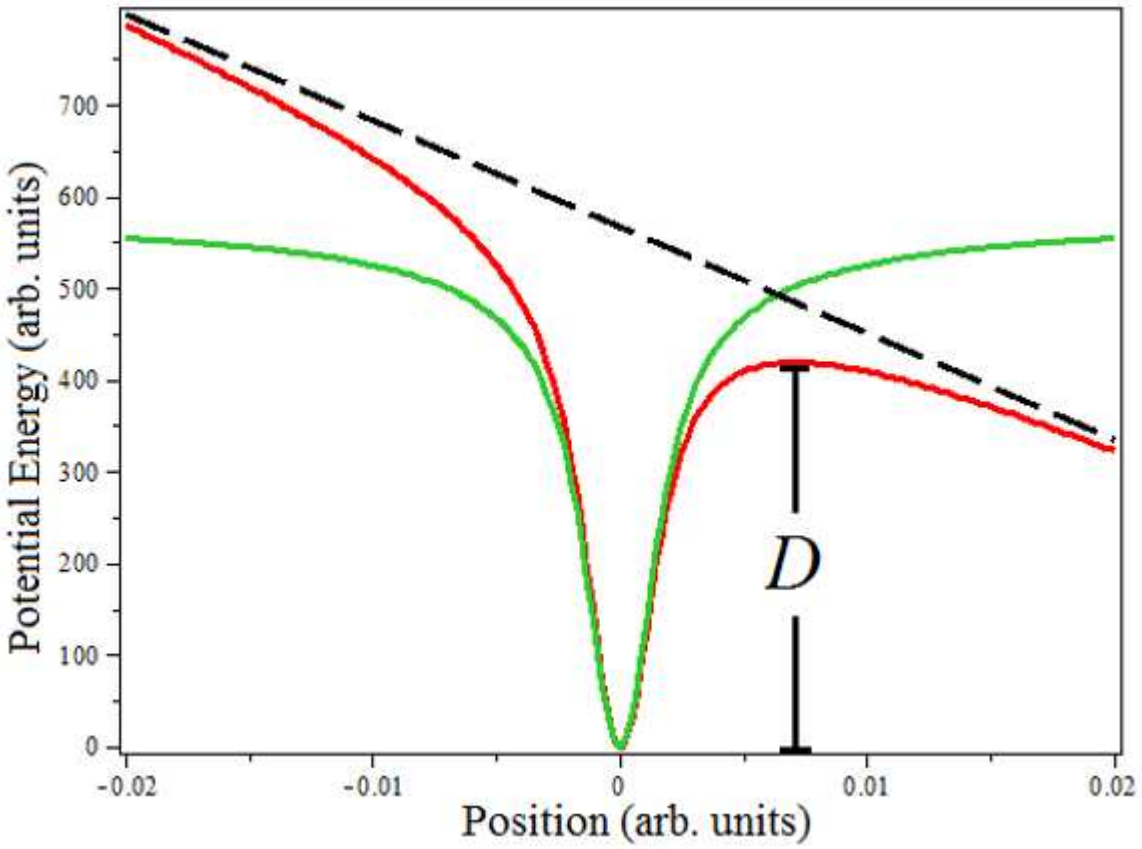


Figure 3.18: An example of the on-axis potential of an ion distribution in a uniform external electric field. The green curve shows the potential from the ion distribution alone. The red curve shows the addition of a uniform external electric field, $F_0$. The dashed, black line shows the slope of the potential owing to the external field. We define the potential well depth, $D$, as the difference between the minimum and maximum potential in the direction of extraction.

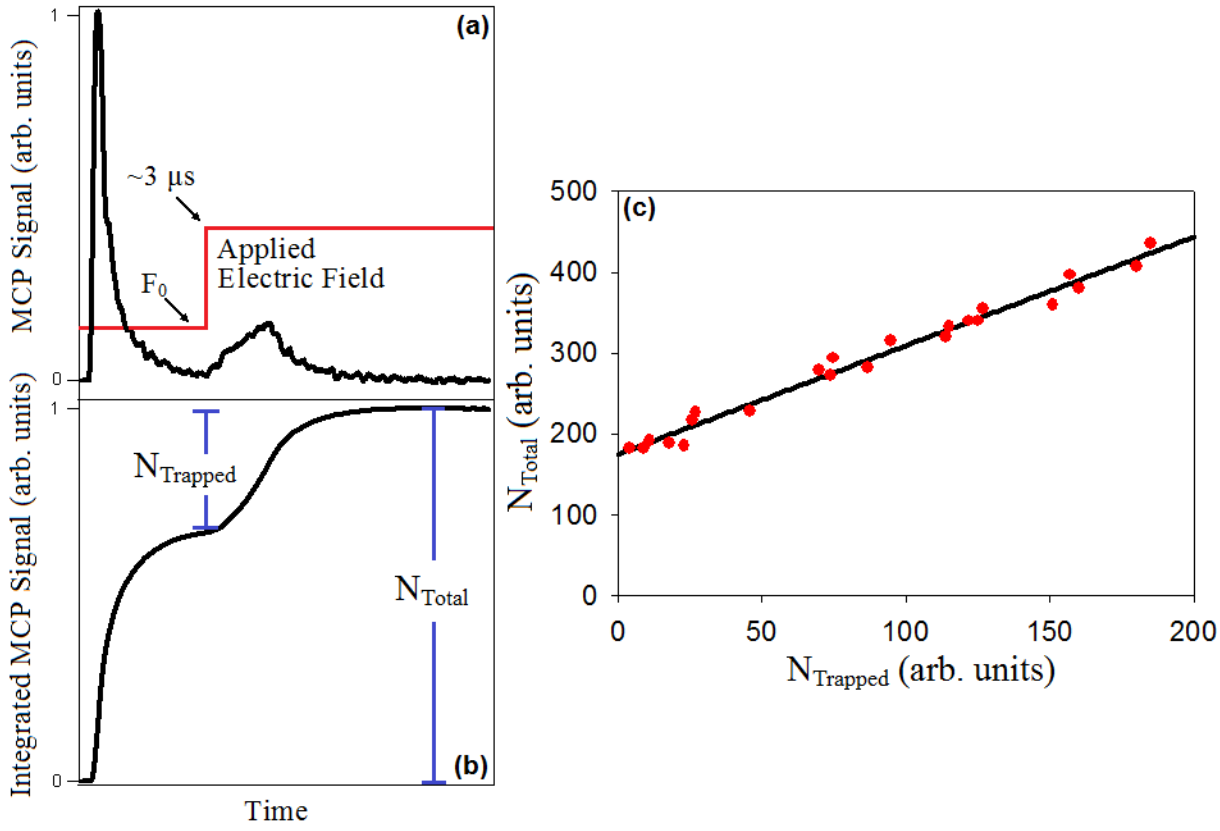


Figure 3.19: Example data for how the threshold ion number is determined. In (a), the MCP signal shows the rate of electron escape from the UCP in uncalibrated units. The UCP is formed in the presence of a chosen field of strength $F_0$. After formation (at ~3 $\mu$s), the electric field level is ramped to a higher level in order to extract all the electrons that are trapped by the UCP ions. In (b), the integrated MCP signal allows us to determine the total number of electrons trapped and the total number of ions and electrons that were created during photoionization in units of the MCP signal. We can alter the total number of ions by changing the power of the $5S - 5P$ pump laser power as described in the text. In (c), we plot the number of trapped electrons as a function of the number of total ions and electrons in the system. We can use a linear fit in order to extract the threshold ion number (where $N_{trapped}$ goes to 0) in units of the MCP signal for a given set of UCP conditions.

number of total ions in our UCPs. As the total number of ions decreases, the number of trapped electrons approaches zero. We can extrapolate our data to zero trapped electrons for a particular initial ionization energy and electric field ($F_0$) in order to find the threshold number of ions in units of the MCP signal. An example of our MCP calibration data for two different values of the electric field is shown in Figure 3.20.

To calibrate the MCP signal, we must compare our measurements of the threshold ion number over a range of initial ionization energies with calculations of the potential well depth taken from Equation 3.31. We can multiply the threshold ion number in units of the MCP signal by a number calibration factor, $\alpha$, to convert to the actual number of ions in the MCP, $N_{ion}$. By varying $\alpha$ and $F_0$, we can calculate the number of ions required to produce a potential well depth, $D$, that is equal to the initial ionization energy, $\Delta E/k_B$, for each of the data points in Figure 3.20 for a given value of $\sigma$. Note that the density in these measurements is extremely low because of the minimal photoionization. So, thermalizing collisions and three-body recombination heating should have no appreciable effect on the electron energy distribution. At this point, we perform a least squares fit to data to determine a best fit for the values of $\alpha$ and $F_0$. However, for any chosen value of the UCP size, $\sigma$, a different set of values for $\alpha$ and $F_0$ can be obtained. So, to constrain value of the number calibration parameter, $\alpha$, we measured the initial peak density of the UCP using the 2-cycle rf sweep technique described in Chapter 4 in order to link the value of the initial characteristic size of the ion distribution, $\sigma$, to the value of $\alpha$ ($\sigma = [N_{ion}/(2\pi)^{3/2} n_{peak}]^{1/3}$, and $N_{ion}$ is equal to $\alpha$ times the integrated MCP signal). This way the values of $\alpha$ and $F_0$ had to be consistent with both the measured threshold ion number data and with our measurements of the peak density, making the best fit a unique pair of values for $\alpha$ and $F_0$. We performed this calibration technique for several electric field configuration in order to determine the electric field as a function of the electrode voltage, and to check the reproducibility of the number calibration. We were able to determine the value of $\alpha$ with a statistical uncertainty of less than 5%. Systematic uncertainties associated with measurements of the characteristic size, $\sigma$, and MCP threshold signal are on the few percent level.

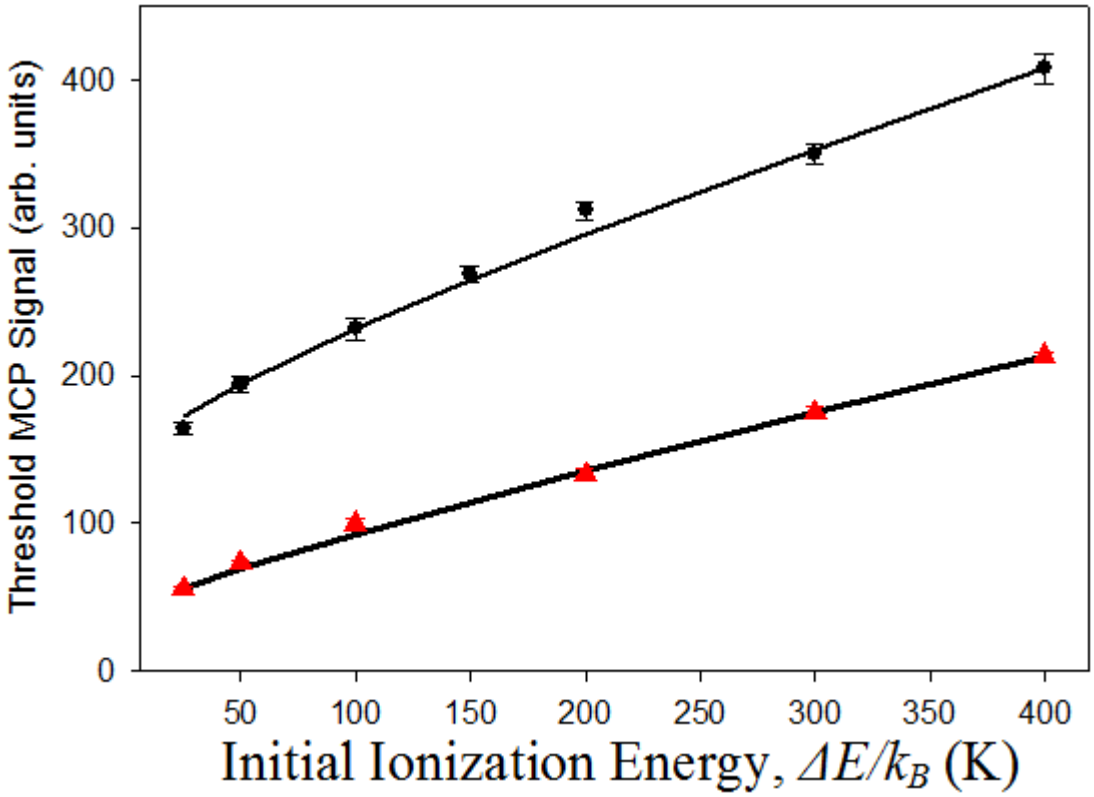


Figure 3.20: The MCP signal calibration measurement uses the MCP threshold signal over range of initial ionization energies for a particular electric field configuration. The red triangles show the threshold MCP signal for an electric field of 4 V/m, which was found using our calibration. The black circles show the threshold MCP signal for an electric field of 9 V/m. The lines through the data represent a best fit curve using the values obtained from our least squares fit of our parameters, $\alpha$ and $F_0$.

## 3.7 Computer Control of the Experiment

To get the experimental equipment synced to the proper timing sequence required to perform our experiments, we use a National Instruments Digital I/O control board to send the proper TTL signals to the equipment. The control board is produced by Viewpoint USA and consists of 64 individually controlled TTL terminals. The control board can be programmed to output an arbitrary sequence of TTL pulses by using LabView. These TTL pulses control nearly all of the aspects of the experiments including the translation stage motion, laser set points, optical switches, shutters and attenuators. To sync with the dye laser, the control sequence is triggered by the Q-switch of the Nd:YAG laser, ensuring that the timing of the experiment corresponds the 10 Hz output of the dye laser system.

The DIO board has an on-board 40 MHz clock that keeps the relative timing of the TTL pulses accurate to within 25 ns. Most of the experimental sequence used to produce UCPs only requires timing accuracy on the 10s of $\mu$s level or greater, so the 40 MHz clock is more than sufficient for these applications. However, during the UCP evolution, we require timing accuracy of $< 1$ ns for the electric field pulses that we apply (using Agilent 33250A function arbitrary waveform generators) for some portions of the experiment. Therefore, the DIO board is not sufficient for triggering devices that require this amount of precision in the timing of the trigger. So, to trigger devices with precise timing, we use a combination of the DIO board and the Q-switch sync to produce precise triggers. The Q-switch sync will output a TTL pulse at 10 Hz every time the Q-switch is engaged, which will occur far more often than when we need the trigger. So, to produce only one TTL signal that is precisely timed with the Q-switch sync, we can input the Q-switch sync and a TTL pulse from the DIO board into an AND gate. The TTL from the DIO board will switch to the high level first and serve to allow only the desired pulse from the Q-switch sync through to trigger the arbitrary waveform generators. The Q-switch sync occurs $\sim$180 $\mu$s before the laser pulse is fired. So, we require a delay between when the arbitrary waveform generator is triggered and when the waveform is sent to the electrodes. Even with this $\sim$180 $\mu$s delay, the timing of the electric field pulses will be preserved to $< 1$ ns.

The data that is produced from our experiments is seen in Figure 3.17, which is an MCP signal that is collected by a LeCroy WaveSurfer 104MXs-A, 1 GHz Digital Storage Oscilloscope. This

oscilloscope provides the ability to store each data trace and perform mathematical operations on the data (such as the integration of the signal to find the total electron number) in real time. The stored data can then be averaged together in order to reduce the statistical variation in the data. The data can also be smoothed using a box smoothing algorithm to further reduce the background noise in the data.

The ability to monitor the electron number for each data trace in real time provides us with a means to selectively store data that are nominally under the same initial conditions. At times, the total number of ions and electrons produced in the UCP can fluctuate dramatically (by as much as a factor of 2 under particularly bad operating conditions). So, to collect data under approximately the same initial conditions, we only save data that is within $\pm 10\%$ of our desired total ion and electron number. While this allows for us to produce a consistent data set from conditions that can vary by a large amount, at times it can force us to reject a large amount of the data that is produced. In the future, we will implement alternative data collection schemes that bin the data in certain number ranges. This will allow us to make use of previously rejected data to obtain measurements under a variety of total ion and electron number conditions.

## Conclusion

The experimental equipment described in this chapter was either bought commercially or built in-house starting in the spring of 2010. Before this time, only an empty optical table sat on that side of the lab. Some of the in-house produced equipment was modeled after designs used in the laser cooling and trapping experiment on the other side of the lab. These include the diode laser housings, frequency control, and temperature control. Other equipment was modeled after experimental equipment used at JILA in Boulder, Colorado, such as the magnetic trap and translation stage system. And others were new designs introduced solely for this experiment, such as the electrode assembly, the magnetic trap servo, and the designs for the vacuum chamber and mounts. The combination of all of these ideas is what brought us this new system for exploring the physics of ultracold plasmas

As a consequence of magnetically trapping and transferring the atoms to a separate region for plasma studies, the densities of the plasmas we produce are 1-2 orders of magnitude lower than those of other UCP experiments. This put us into a density regime where new physical phenomena

became important, and were therefore unobserved in previous experiments. Also, the low density allowed us to avoid problems with three-body recombination and disorder induced heating and put us into a regime where electron evaporative cooling became significant. This density therefore shows promise for achieving UCPs with high electron $\Gamma$ which may be limited in other experiments [22]. This also lead to the need to develop new techniques to characterize these low-density UCPs. These studies are the subject of the next three chapters of this thesis.

## References for Chapter 3


[1] T. C. Killian, S. Kulin, S. D. Bergeson, L. A. Orozco, C. Orzel, and S. L. Rolston, Phys. Rev. Lett. **83**, 4776 (1999).

[2] S. Ichimaru, Rev. Mod. Phys. **54**, 1017 (1982).

[3] J. H. Choi, B. Knuffman, X. H. Zhang, A. P. Povilus, and G. Raithel, Phys. Rev. Lett. **100**, 175002 (2008).

[4] L. Spitzer, Jr., *Physics of Fully Ionized Gases* (Dover, New York, 1962).

[5] D. A. Gurnett and A Bhattacharjee, *Introduction to Plasma Physics* (Cambridge University Press, 2005)

[6] P. M. Bellan, *Fundamentals of Plasma Physics* (Cambridge University Press, New York, 2006).

[7] H. J. Lewandowski, D. M. Harber, D. L. Whitaker, and E. A. Cornell, J. Low Temp. Phys. **132**, 309 (2003).

[8] H. J. Metcalf and P. van der Straten, *Laser Cooling and Trapping* (Springer-Verlag, New York, 1999).

[9] Daniel A. Steck, *Rubidium 85 D Line Data*, available online at http://steck.us/alkalidata (revision 0.1.1, 2 May 2008).

[10] A. Nadeem and S. U. Haq, Phys. Rev. A **83**, 063404 (2011).

[11] E. L. Raab, M. Prentiss, A. Cable, S. Chu, and D. E. Pritchard, Phys. Rev. Lett. **59**, 2631 (1987).

[12] D. W. Preston, Am. J. Phys. **64**, 1432 (1996).

[13] http://laser.physics.sunysb.edu/∼bazmoun/RbSpectroscopy/#The%20D2%20Transition

[14] K. L. Corwin, Z.-T. Lu, C. F. Hand, R. J. Epstein, and C. E. Wieman, Appl. Opt. **37**, 3295 (1998).

[15] W. Ketterle, D. S. Durfee, and D. M. Stamper-Kurn, "Making, probing, and understanding Bose-Einstein condensates," in *Bose-Einstein Condensation in Atomic Gases, Proceedings of the International School of Physics Enrico Fermi*, Course CXL, edited by M. Inguscio, S. Stringari, and C. E. Wieman (IOS Press, Amsterdam, 1999), pp. 67-176.

[16] G. Gabrielse, S.L. Rolston, L. Haarsma, and W. Kells, Phys. Lett. A **129**, 38 (1988).

[17] P. Gupta, S. Laha, C. E. Simien, H. Gao, J. Castro, T. C. Killian, and T. Pohl, Phys. Rev. Lett. **99**, 075005 (2007).

[18] J. E. Geusic, M. L. Hensel, and R. G. Smith, Appl. Phys. Lett. **6**, 175 (1965).

[19] J. A. Koningstein and J. E. Geusic, Phys. Rev. **136**, A 711 (1964).

[20] J. T. Verdeyen, *Laser Electronics*, (Prentice Hall, 1995).

[21] J. L. Wiza, Nuclear Instruments and Methods **162**, 587 (1979).

[22] S. Kulin, T. C. Killian, S. D. Bergeson, and S. L. Rolston, Phys. Rev. Lett. **85**, 318 (2000).

# Chapter 4

# Density-Dependent Response of an Ultracold Plasma to Few-Cycle RF Pulses

Collective oscillations are a fundamental feature in ultracold plasma systems (UCPs) and have been an invaluable tool for characterizing the density of UCPs as they freely expand. They were among the first reported experimental measurements in UCP systems [1], where the oscillations were excited by external rf electric fields in order to measure the expansion rate of the UCPs. Knowing the expansion rate allows one to infer the early time electron temperature and its subsequent evolution (discussed in Chapter 5) [2], which is important for studying energy transport in UCP systems.

The UCP expansion rate can be measured by exciting collective oscillations using externally applied rf fields because these oscillations are density dependent. The plasma frequency, $\omega_p$, is defined as the resonant frequency of oscillation in an infinite, uniform density plasma system. For cold electrons, the plasma frequency is $\omega_p = \sqrt{e^2 n_e / m_e \epsilon_0}$ [3], where $e$ is elementary charge, $n_e$ is the electron density, $m_e$ is the mass of the electron, and $\epsilon_0$ is the permittivity of free space. From this relationship, we can see that $\omega_p$ is proportional to one parameter that is not a fundamental constant, the density. Since UCPs are not infinite, uniform density plasmas, this relationship cannot be applied directly to our measurements. However, this relationship does indicate the resonant frequency is expected to scale with density, increasing with increasing density. So, it will serve as a reference for the calculations that are made which allow us to determine the densities of the UCPs in our system. Also, using this reference will come in handy when comparing the results of our calculations to studies of the resonant response of non-uniform UCPs from other theoretical studies [4, 5] and experiments [6].

The experiments and measurements in this chapter describe the response of the UCPs in our system to externally applied rf fields. In particular, I will focus on short pulses of rf, with as few as two cycles of a sine wave pulse. Continuous application of rf, which has been used to excite collective oscillations in other UCP systems [1, 6], causes significant heating of our UCPs, making an accurate determination of the UCP density by this method difficult. Despite using only two-cycles

of rf to excite plasma oscillations in our system, this method still produces a resonant response that is density-dependent. This will allow us to make accurate determinations of the UCP density.

In this chapter, I will discuss the results of previous measurements of plasma oscillations in other UCP systems to give a basis for comparisons to our results. I will then discuss the results of our measurements of the UCP response to a delayed application of rf and to short bursts of rf. I will show that the UCPs in our system have a resonant response to short bursts of rf. These results lead us to develop a model of the UCP response where the collective oscillations that are driven by our rf fields involve the motion of the entire electron cloud. This model allows us to relate the measured resonant frequencies from short bursts of rf to the peak density of the UCPs. I will then discuss the nature of the motion of the electron cloud. In this discussion, I will present measurements of the UCP response to sharp pairs of electric field pulses that shows that the motion of the electron cloud behaves as a damped oscillator. I will then show that the UCP expansion rate can be measured using this technique, and go on to discuss the value of this technique for future work.

## 4.1 Experimental Background

The creation of ultracold plasmas [7] has opened an avenue into studying a wide range of plasma phenomena at ultracold temperatures. After the initial report of the creation of these UCPs [7], the first measurement that was performed was the response to a continuously applied, external rf field [1]. In these measurements, it was first observed that the UCP has a density-dependent, resonant response to the externally applied rf which provided the first steps toward mapping the evolution of the UCP density as a function of time. It was recognized that knowing the density evolution of the UCP was important for studying the most interesting plasma phenomena at low temperatures, such as three-body recombination [2, 8–10] and the effects of strong-coupling physics [11].

The measurements presented in [1] showed a resonant response owing to the application of externally applied rf fields that was inferred from a large increase in the electron escape rate at the time of the resonance. In that work it was assumed that the applied rf was resonant only with regions of the plasma with densities that satisfy the resonance condition, $f_{app} = (1/2\pi)\sqrt{e^2 n_e/m_e\epsilon_0}$, where $f_{app}$ is the frequency of the applied rf. The peak in the electron escape rate was associated

with the most probable density in the plasma (having the most electrons in that density range) satisfying the resonance condition. It was further assumed that the energy imparted to the UCP from the rf was completely redistributed throughout the entire UCP through collisions on the order of the electron self equilibration timescale, which could be as short as 10s of ns. By applying different frequencies of rf, it was observed that the resonant response time scaled with applied frequency, which showed for the first time that these plasmas expand freely after formation. The effects of three-body recombination were also observed in this work for the first time at low initial ionization energies, where the expansion rate of the plasma no longer decreased with decreasing initial ionization energy which was later theoretically predicted in [9].

The response of the UCP to externally applied rf was further explored theoretically in [4]. In this work, the authors used cold plasma theory to show that although there are no normal modes associated with the response of a neutral UCP to applied rf, there is a damped quasi-mode that dominates the continuous spectrum of the free response of the UCP. In the case of a driven response, the UCP absorbs the most power from the applied rf through this damped, quasi-mode when frequency of the driving field, $\omega_{app} = 2\pi f_{app}$, is $\sim$0.2 times the frequency associated with the peak density of the UCP given by $\omega_{peak} = \sqrt{e^2 n_{peak}/m_e \epsilon_0}$ for Gaussian density distributions. This means that the estimates for the density of the UCPs in [1] were not correct, and from [4] were found to be off by a factor of $\sim$3.

The theoretical work from [4] only considered UCPs that were completely neutral. For experimentally created UCPs, electrons escape the plasma both during formation and during the subsequent expansion creating an imbalance of electrons and ions. The charge imbalance creates a potential well that traps any remaining electrons in the UCP. For low temperature electrons, the charge density of the UCP is nearly neutral. So, the charge density distribution can be approximated as a $T = 0$ distribution, in which the electron and ion densities match from the center of the UCP out to a cutoff radius. This cutoff radius is found theoretically by integrating the electron distribution to find the proper number of electrons remaining in the UCP. When this charge imbalance is taken into account, it was found in [5] that the sharp cutoff in the electron density distribution produced an eigenmode that could be excited in the presence of externally applied rf. This theoretical description of the plasma response showed that most of the energy absorption in the UCP occurred at the edge of the electron distribution, and is known commonly as the

"edge-mode". The "edge-mode" theory showed sharp features in the energy absorption spectrum at a particular resonant frequency that depends on the plasma conditions. Most importantly, this theory showed that resonant frequency has a significant dependence on the charge imbalance of the UCP, which complicates the results of the previous experiments [1].

The "edge-mode" was explored experimentally in the work in [6]. In this work, the resonant frequency as a function of the charge imbalance was measured over the evolution of the plasma and by deliberately altering the charge imbalance by applying electric field pulses. In both cases, the evolution of the plasma could be independently verified by extracting the ions and imaging the ion distribution on a phosphorous screen. In both cases, the results of the experiments were consistent with the presence of an "edge-mode" when an external rf field is applied.

In each of the experiments and theoretical models described above, the assumed mechanism for energy absorption and the subsequent electron escape is electron-electron collisions. At the densities in these experiments and considered in the models ($\sim 10^{10}$ cm$^{-3}$), the electron collision timescales could be as short as 10s of ns, which would produce a very fast response to the rf when the resonance condition is met. For the lower density UCPs in our system $\sim 10^{8}$ cm$^{-3}$, these timescales can become a significant fraction of the plasma lifetime (10s of $\mu$s), indicating that the response we should expect to observe will be very different. This is indeed the case for the UCP response to externally applied rf in our system. This led to the discovery of a new type of response in our UCPs, in which a collisionless mechanism is responsible for the increased electron escape signal that we observe. The results of our experiments and our theoretical interpretation of our observations are presented in the following sections of this chapter.

## 4.2 Continuous and Delayed Application of RF

The measured signal from the UCPs in our system comes from electron extraction from the UCP toward a microchannel plate detector (MCP) as described in Chapter 3. These were the first signals produced by our system, and by themselves do not characterize the most important properties of the UCPs that we have created. The most useful property of the UCP to have a measure of is the density, which will lend itself to revealing many other properties of the UCP system. When we first formed the UCPs in our system, we first followed the method which has been used in other

experiments to measure the UCP density, in which a continuous rf electric field is applied to excite plasma oscillations in the system. The rf in our system is applied by using the nearest MOT side electrode which is described in Chapter 3.

When applying continuous rf electric fields to the UCP, the resonant response is inferred from a dramatic increase in the electron escape signal as seen in Figure 4.1. As the UCP expands, the density decreases, which will put some part of the UCP density distribution at the resonance condition with the applied rf (if properly chosen). In previous work in other UCP systems [1, 6], it is implied that the increase in the electron escape signal comes from the collisional redistribution of energy gained during the application of the rf, which takes electrons from the lower part of the UCP energy and promotes them through collisions to energies that can escape the potential well of the UCP.

The collisional redistribution of energy will not happen instantaneously, but rather on timescales associated with the electron self-equilibration time [12] as discussed in Chapter 1. The electron self-equilibration time is approximately proportional to $T_e^{3/2}/n_e$ (the Coulomb logarithm varies slowly with both density and temperature). Since the densities of UCPs in our system can be $1-2$ orders of magnitude lower than those in other systems, our collision timescales can be relatively long compared to those other systems and can be as long as 10s of $\mu$s for our most extreme conditions. Our original plan was to use these long timescales as a way to study the collisional redistribution of energy. By delaying the application of rf to the UCP until after the initial formation, we could apply the rf near resonance at a particular time and measure the time delay associated with collisions in the electron component of the UCP. However, when the rf is applied, we observe a rapid response in the electron signal as seen in Figure 4.1. The delay between the application of the pulse and the observed electron signal is typically $\sim$175 ns, and has no dependence on the UCP density or temperature. This is far shorter than the collisional timescales associated with many of our conditions, which implies that there is a different mechanism associated with this rapid response to the applied rf. Also, Figure 4.1 shows that the delay of the application of the rf can shift the resonant response to later in time, complicating the use of continuous rf to determine the density of the UCP. This indicates that the continuous rf can cause significant heating to the UCP electrons, which in turn will cause the UCP to expand faster, so it comes into resonance at an earlier time in

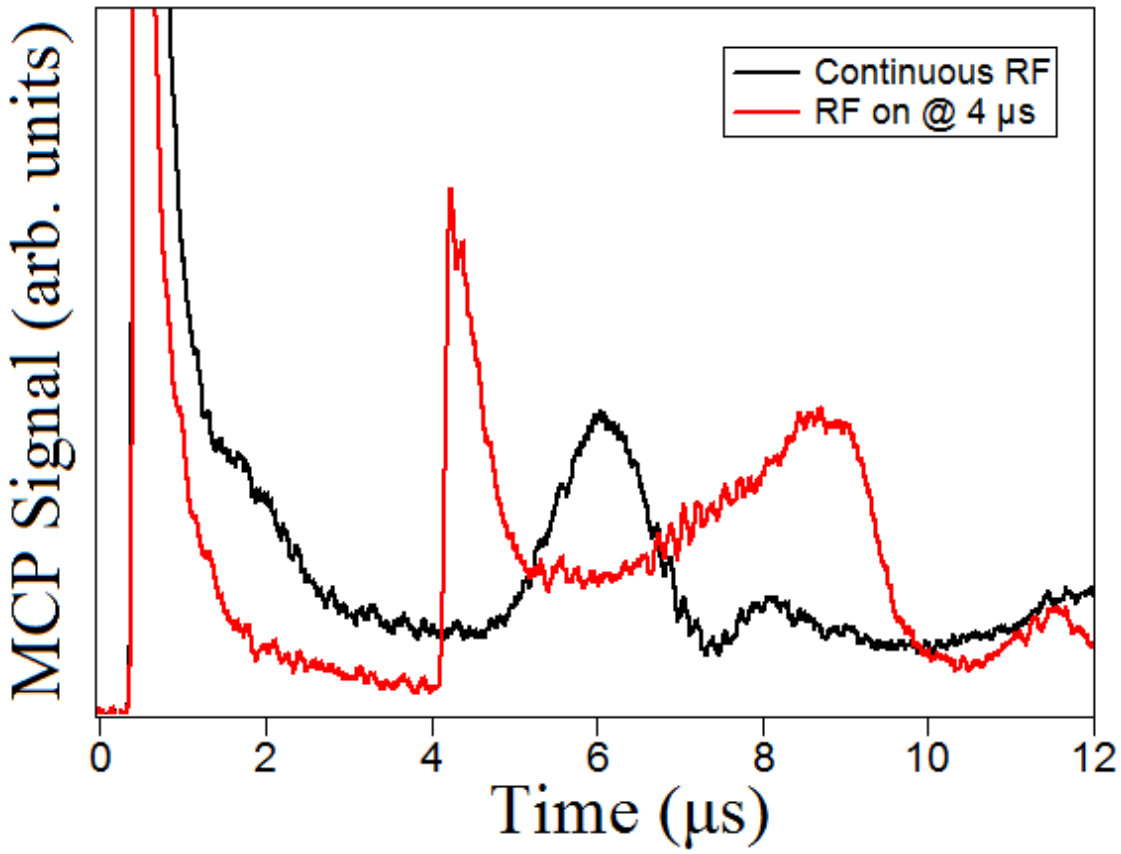


Figure 4.1: An example of our UCP's response to continuous rf throughout the UCP evolution and to a delayed turn-on of the rf for $\Delta E/k_B = 100$ K. The black curve shows the UCP response to continuously applied rf at 20 MHz (6 V/m p-p), with the resonant response of the UCP seen as an increase in the electron evaporation signal at $\sim$6 $\mu$s. The red curve shows the delayed application of rf at the same frequency and amplitude with the rf applied beginning at 4 $\mu$s and continuous thereafter. In this case, we see a sharp response to the initial application of the rf. Also, resonant response is moved to later in time, implying that heating occurs when rf is applied continuously. This is also inferred from the increased electron evaporation rate that is observed when the rf is applied away from resonance.

the evolution. Additional measurements of the UCP response to a delayed application of rf can be found at the end of this chapter in Section 4.5.

The initial peak changes in height as a function of frequency, with a maximum at a particular frequency. The rapid initial response implies that it can be excited using only a few cycles of the rf, with two cycles of rf used for most of the measurements discussed in these experiments. The UCP response to two cycles of rf can be seen in Figure 4.2. We can compare the signal of the two-cycle rf response to the MCP signal with no rf applied to see the effect on the UCP. The difference signal (seen in the inset of Figure 4.2) will allow us to determine precisely when the signal response occurs relative to the initial onset of the rf pulse. Also, integrating this difference signal gives us the total number of escaped electrons, which allows us to determine the magnitude of the response.

The response of the UCP to two cycles of applied rf also shows a peak in response as the frequency is changed through successive measurements at a particular time in the UCP evolution for the same experimental conditions as seen in Figure 4.3. The presence of this peak implies that there is a resonant response to the rf in the electron component of the UCP. The resonant frequency is found by fitting a Gaussian curve to the measured response seen in Figure 4.3. The frequency response is broad as would be expected based on the Fourier components present in just two cycles of an rf pulse. Although increasing the number of cycles can narrow this response to some degree, it does not narrow as much as would be expected based on the Fourier transform of the pulse alone. This lack of narrowing may be attributed to the fluid nature of the electron cloud and is discussed further in Section 4.4. In any case, the resonant frequency can be found reliably using the two-cycle rf method, and will be the experimental method used to measure the resonant frequency throughout the experiments described in this thesis.

The resonant frequency that we observe from applying two cycles of rf also shows a scaling with density as the UCP expands. Figure 4.3 shows a measurement of the resonant frequency at two different times during the UCP evolution for $\Delta E/k_B = 10$ K. For the earlier measurement ($t = 39\mu$s), the measured resonant frequency is higher than that of the later measurement ($t = 79\mu$s). This is a general trend that holds throughout the evolution of all the UCPs in our system. One can recall that $\omega_p \propto \sqrt{n_e}$. Since the scaling of our measured resonant frequency with density has the appropriate sign, this leads us to attempt to find a method that will allow us to measure the

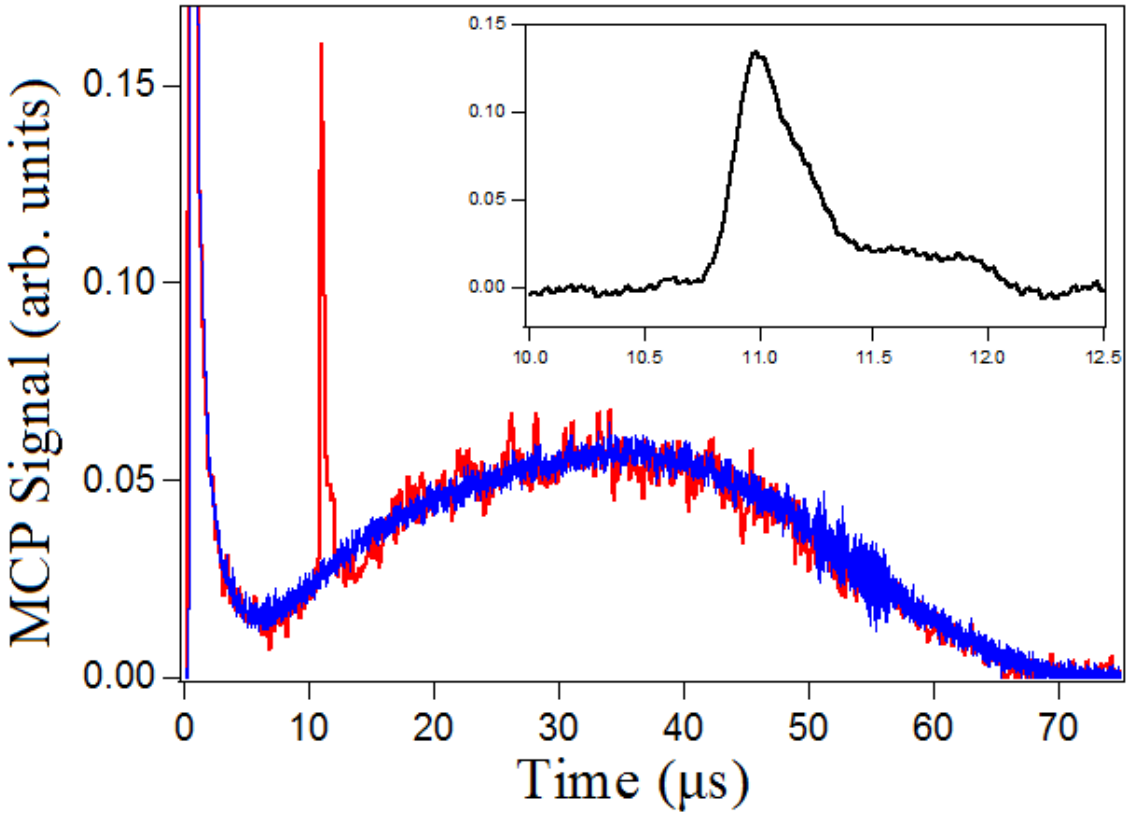


Figure 4.2: An example of the 2-cycle rf signal compared to a UCP electron escape signal without applied rf. The figure is scaled to better see the electron escape signal after the prompt peak. The inset figure shows the difference between the two signals, which we integrate in order to determine the response of the UCP to the rf pulse. The bottom axis is difference between the two signals from 10 to 12.5 $\mu$s, which is where there is a significant difference in the electron escape signal. The left axis is in units of the MCP signal, which are arbitrary for this figure.

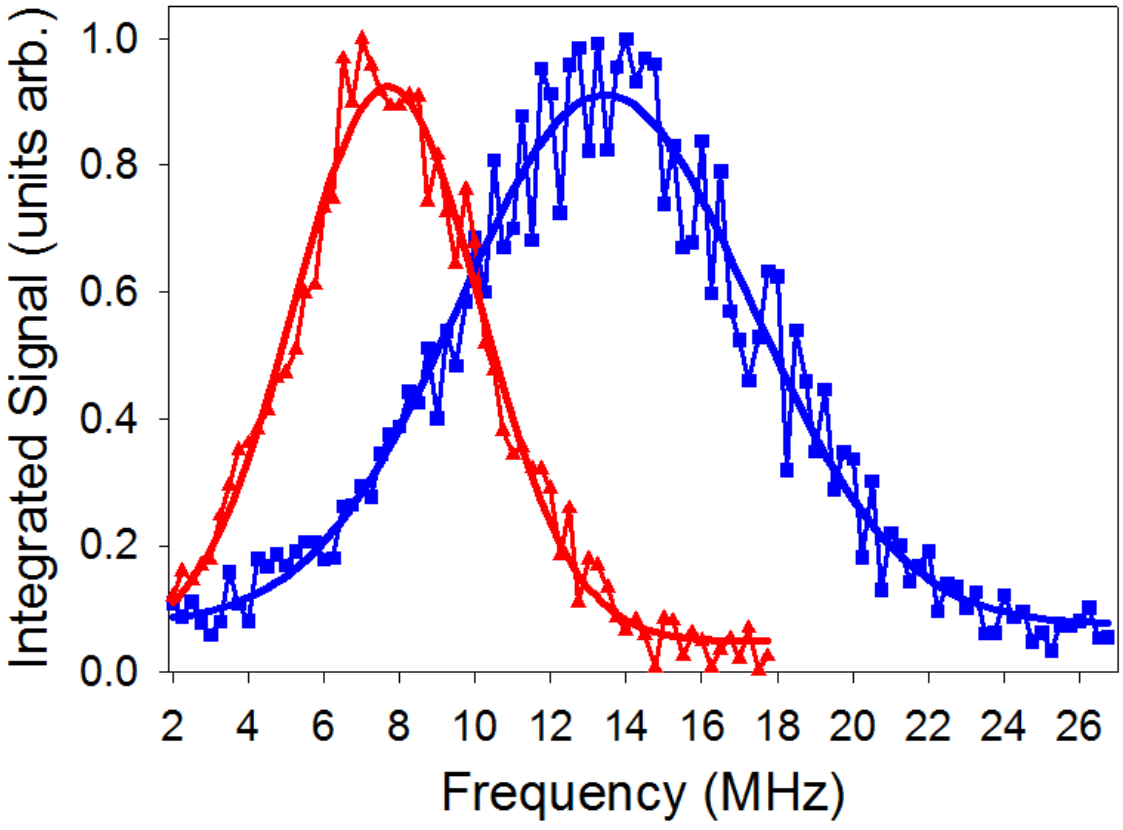


Figure 4.3: The integrated two-cycle response as a function of applied rf frequency for two different times in the plasma evolution ($\Delta E/k_B = 10$ K, $4.4 \times 10^5$ total ions, 5 V/m peak-to-peak applied rf field). The blue squares are at 39 $\mu$s in the UCP evolution and the red triangles are at 79 $\mu$s. These data are consistent with the proper scaling of frequency with the UCP density as the UCP expands. The data are shown with Gaussian fits curves, which are used to determine the peak rf response frequency.

density at a specific point in the UCP evolution as will be shown in the following sections. This technique is particularly useful for our experiments involving UCPs at low-densities compared to other UCP experiments as discussed in Section 4.4. Further, this technique will allow us to measure the UCP expansion and evolution as discussed in Section 4.7 and Chapter 5.

The measured timescale of the response of the UCP to the externally applied rf combined with estimates of the electron collisional timescales lead to a conclusion that the additional electron escape that is observed is not owing to a collisional redistribution of energy. To further characterize the response of the UCP to short bursts of rf, we also measured the change in the UCP response to the sign (0 or 180 degree phase) of our input 2-cycle burst. We saw a change in both the initial response time (for some conditions) and the peak time in the data as seen in Figure 4.4(a). For this particular measurement, there is a $\sim$50 ns shift in the peak response time owing to the initial direction of the rf pulse. The peak response when the phase was reversed was not always relatively later and seemed to change depending on the frequency of the applied rf. At lower frequencies, the time of the peak response was relatively close in the two cases. As the frequency was swept closer to resonance, the two responses began to deviate. One can notice in Figure 4.4(a) that the black curve has a small response at the same time as the opposite phase before the peak response that comes later. This type of response indicates that electron escape is directional, and that when the electrons gain enough energy to escape the UCP they must be traveling toward the MCP to escape at the earliest possible time. If the direction of oscillation is reversed, most of the escaping electrons will be traveling the wrong direction initially and will have to reverse direction in order to escape the UCP, hence the later peak response time. This later response time indicates that collisions from the low energy electrons that promote electrons above the escape energy required to leave the UCP is not the mechanism for this response, as binary collisions between electrons would randomize the direction of escaping electrons.

We also compared the response between 2- and many-cycle rf pulses. In Figure 4.4(b), a comparison of the response between 2- and 4-cycles is shown. In the 4-cycle data, we observed 2 additional peaks of electron escape when the frequency of the applied rf is near resonance. The frequency of the appearance of these peaks is at the frequency of the driving rf. As more cycles are applied to the UCP we see additional peaks that decay the longer the rf is applied. These data are further evidence that the local response does not fit well with our observations as collisionally

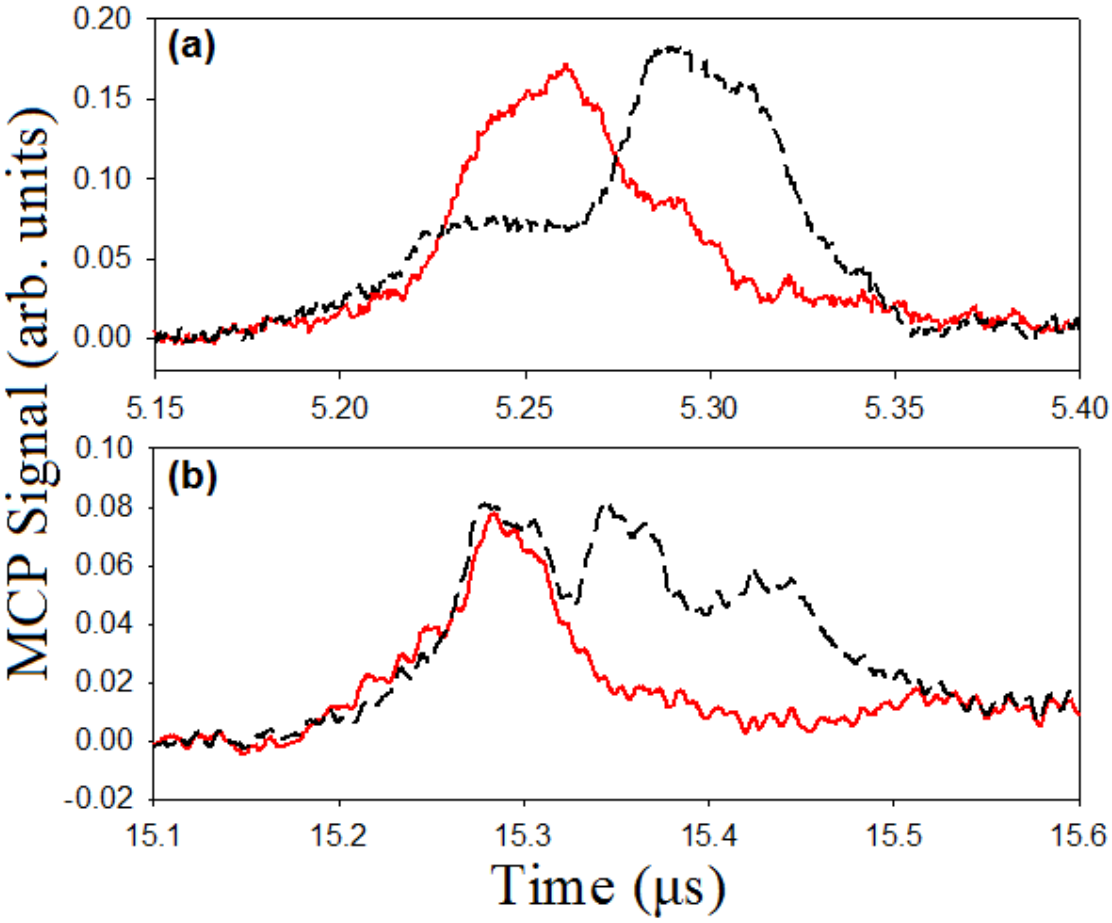


Figure 4.4: RF response under various conditions at $\Delta E/k_B = 10$ K. (a) shows the difference in the 2-cycle RF response with the initial phase (red/solid is 0 degrees, black/dashed is 180 degrees). (b) shows the difference between a 2- (red, solid) and 4-cycle (black, dashed) RF pulse. An increased electron escape signal resulting from the collisional redistribution of heat does not agree with the observations taken from this data.

based responses to the rf should be insensitive to the phase of the driving pulse and should have timescales longer than the features observed in the 4-cycle data.

While the response to a reversal of the rf phase and to additional cycles of the rf confirms the hypothesis that collisional heating is not the mechanism responsible for our UCP response, the nature of these responses does lead to a question of whether the additional electron escape that is observed is owing to an effective lowering of the confining potential barrier imposed on the electrons in the UCP. This question can be answered with a simple test of the electron response time relative to the driving rf. The electron signal as received by the MCP has a characteristic time-of-flight delay associated with the distance between the UCP region and the MCP. To measure this delay, we apply a sharp electric field ramp to quickly pull electrons out of the MCP toward the detector. This ramp will provide a sharp-edged electron signal at our detector that we can compare to the timing of the ramp to determine the time-of-flight, which for our system is 375 ns. We can then take this delay into account when comparing the timing of the electron signals with respect to our applied rf. The time delay between the initial application of the rf pulse and the initial response is $\sim$175 ns and does not have much variation under different UCP conditions. This delay would indicate that the peak response is after the end of the rf pulse near resonance when the frequency of the applied rf is $\sim$15 MHz, which is typical for our UCP conditions. This shows that the response that we observe is not from the lowering of the potential barrier for the electrons owing to the presence of the rf electric field, otherwise the peak electron response would occur when the applied electric field is at a maximum.

## 4.3 Model of the Electron Response to an Externally Applied RF Field

Since the frequency of the applied rf is on the order of $\omega_p$, the electron cloud will not have time to adjust itself to screen out the externally applied rf field [3]. So, the electrons in the UCP will feel a force in response to this external field. To model this response, we assume that the electron component of the UCP moves as a whole when subjected to an external rf pulse. When the electron component is offset from the ions, the excess space charge that is left behind will provide a linear restoring force (for small displacements of the electrons relative to the UCP size) that pulls the

electrons back toward the positive ions. The linear restoring force will allow us to treat the electron component of the UCP as being driven like a simple harmonic oscillator (SHO). The resonant frequency of oscillation is provided by this restoring force and is dependent on the density and the charge imbalance, $\delta$ (the number of electrons that have escaped in the UCP divided by the total number of ions created, $\Delta N_e/N_{ion}$), as will be shown. We will treat this problem in two different ways and compare the results of these calculations. First, we will calculate the resonant frequency of oscillation by assuming an infinitesimal displacement to the electron density distribution. Second, we will numerically calculate the restoring force by treating the electron cloud as a solid object, which is offset from the ion distribution. We relate these calculations to the measurements of the frequency in our experiment by assuming that the peak electron response will occur when the UCP electrons are driven by the external rf field at the resonant frequency.

The first calculation of the resonant frequency of the UCP starts by assuming spherically symmetric ion and electron density distributions, $n_{ion}(\vec{r})$ and $n_e(\vec{r})$. For cold ions and electrons, these density distributions should be approximately equal to a density distribution that I'll call $n(\vec{r})$. The electrostatic potential can be calculated to be

$$\Phi(\vec{r}) = \frac{e}{4\pi\epsilon_0}\int \frac{(n_{ion}(\vec{r'}) - n_e(\vec{r'}))}{|\vec{r} - \vec{r'}|} d^3r' \tag{4.1}$$

where $e$ is elementary charge and $\epsilon_0$ is the permittivity of free space. If the electron distribution is displaced from the ion distribution by an infinitesimal amount $\delta z$, then the electron distribution can be written in spherical coordinates to be $n_e(r,\theta,\phi) = n(r) + \frac{dn(r)}{dr}cos(\theta)\delta z$. The electrostatic energy becomes

$$\Phi(\vec{r}) = -\frac{e}{4\pi\epsilon_0}\int \frac{dn(r')}{dr'}\frac{cos(\theta')\delta z}{|\vec{r} - \vec{r'}|} d^3r' \tag{4.2}$$

From this, we can calculate the total electrostatic energy to be

$$\begin{aligned} W &= \frac{e}{2}\int (n_{ion}(\vec{r}) - n_e(\vec{r}))\Phi(\vec{r}) d^3r \qquad (4.3)\\ &= \frac{e^2}{8\pi\epsilon_0}\int\int \frac{dn(r)}{dr}cos(\theta)\delta z \frac{dn(r')}{dr'}\frac{cos(\theta')\delta z}{|\vec{r} - \vec{r'}|} r'^2 dr' d\Omega' r^2 dr d\Omega \\ &= \frac{e^2\delta z^2}{6\epsilon_0}\int\int \frac{dn(r)}{dr}\frac{dn(r')}{dr'}\frac{Y_1^0(\theta,\phi)Y_1^0(\theta',\phi')}{|\vec{r} - \vec{r'}|} r'^2 dr' d\Omega' r^2 dr d\Omega \end{aligned}$$

where $Y_L^m(\theta,\phi)$ are spherical harmonics. Next, the $1/|\vec{r}-\vec{r'}|$ term can be expanded into spherical harmonics as

$$\frac{1}{|\vec{r}-\vec{r'}|} = \sum_{L=0}^{\infty}\sum_{m=-L}^{L}\frac{4\pi}{2L+1}Y_L^m(\theta,\phi)Y_L^{m*}(\theta',\phi')\frac{r_<^L}{r_>^{L+1}} \tag{4.4}$$

where $r_<$ and $r_>$ represent the smaller or larger of $r$ and $r'$ respectively. This will allow me to take advantage of the orthogonality relationships among spherical harmonics and integrate this over $d\Omega$ and $d\Omega'$, yielding

$$W = \frac{2\pi e^2\delta z^2}{9\epsilon_0}\int_0^\infty r^2 dr\frac{dn(r)}{dr}\left(\int_0^r\frac{dn(r')}{dr'}\frac{r'^3}{r^2}dr' + \int_r^\infty\frac{dn(r')}{dr'}r dr'\right) \tag{4.5}$$

The term in the parentheses can be integrated by parts where we assume that the density at $r=\infty$ goes to zero. This yields

$$\begin{aligned} W &= \frac{2\pi e^2\delta z^2}{9\epsilon_0}\int_0^\infty r^2 dr\frac{dn(r)}{dr}\left(rn(r) - \int_0^r n(r')\frac{3r'^2}{r^2}dr' - rn(r)\right) \\ &= -\frac{2\pi e^2\delta z^2}{3\epsilon_0}\int_0^\infty r^2 dr\frac{dn(r)}{dr}\left(\int_0^r n(r')\frac{r'^2}{r^2}dr'\right) \end{aligned} \tag{4.6}$$

Reverse the order of integration to get

$$\begin{aligned} W &= -\frac{2\pi e^2\delta z^2}{3\epsilon_0}\int_0^\infty n(r')r'^2dr'\int_{r'}^\infty\frac{dn(r)}{dr}dr \\ &= \frac{2\pi e^2\delta z^2}{3\epsilon_0}\int_0^\infty n(r')^2r'^2dr' \\ &= \frac{e^2\delta z^2}{6\epsilon_0}\int_0^\infty n(r')^2 4\pi r'^2dr' \\ &= \frac{e^2\delta z^2}{2\epsilon_0}\frac{1}{3}\langle n\rangle N \end{aligned} \tag{4.7}$$

where $\langle n\rangle$ is the average density of the UCP electron distribution and $N$ is the number of electrons. This electrostatic energy can be compared to that of a simple harmonic oscillator, which will allow us to determine the resonant frequency. We set the mass of the oscillator to that of the total number of electrons, $N$, times the mass of an electron $m_e$. Again, we assume that the electron distribution moves as a fixed distribution in response to the external rf field and that the ions are heavy enough to be considered fixed at the origin. So,

$$W = \frac{1}{2}M\omega^2\delta z^2 = \frac{e^2\delta z^2}{2\epsilon_0}\frac{1}{3}\langle n\rangle N \tag{4.8}$$

which yields

$$\omega^2 = \frac{e^2}{m_e \epsilon_0} \frac{\langle n \rangle}{3} \tag{4.9}$$

This relationship shows that the resonant frequency is again dependent on the density of the plasma much like the case of the plasma frequency. It is useful to compare the results from this calculation to that of the frequency associated with the peak density, $n_{peak}$, given by $\omega_{peak} = \sqrt{e^2 n_{peak}/m_e \epsilon_0}$, because the peak density will be a much more useful characterization of the UCP than the average density. Since the resonant frequency depends on the average density of electrons in the UCP, the imbalance of electron and ion number results in the need for a correction to be applied to the resonant frequency measurements in order to accurately determine the peak density. This correction factor can be determined as a function of the charge imbalance of the UCP by integrating the electron distribution out from the center to a radius that produces the desired charge imbalance to find the average density. This method is valid because the outer ions will exert no force on the inner electrons owing to Gauss' law for spherically symmetric distributions. The results of these calculations for a spherical, Gaussian UCP are shown in Figure 4.5, where the ratio of the resonant frequency $\omega$ to the peak frequency $\omega_{peak}$ is given as a function of the charge imbalance of the UCP, $\delta$. For a neutral UCP, the average density is given by $\langle n \rangle = \sqrt{2} n_{peak}/4$ which can be substituted in the Equation 4.9 to show that $\omega/\omega_{peak}(0) = 0.343$. As the charge imbalance, $\delta$, increases, this ratio also increases. When $\delta \sim 1$, then $\langle n \rangle \sim n_{peak}$ which gives $\omega/\omega_{peak}(1) = 1/\sqrt{3}$.

The same restoring force and resonant frequency was calculated in a second and complimentary way by numerically calculating the restoring force on the electron component of the UCP from the ions when the electron cloud is offset in space from the ion distribution. This calculation will be useful as it will allow us to more easily determine various effects of the collective oscillation such as the effect of a non-spherical UCP charge distribution and the calculation of the internal fields produced by inducing such an oscillation. Also, this calculation will determine the displacement of the electron cloud where the application of the rf field is non-perturbative, as the electrons are predicted to be displaced by as much as $\sim$200 $\mu$m at the field strengths that we drive the collective oscillation. The electron cloud for this calculation is approximated as a rigid object. Although this would be poor model under many cycles of rf owing to the fluid nature of the UCP electrons, for only 2-cycles it is more applicable.

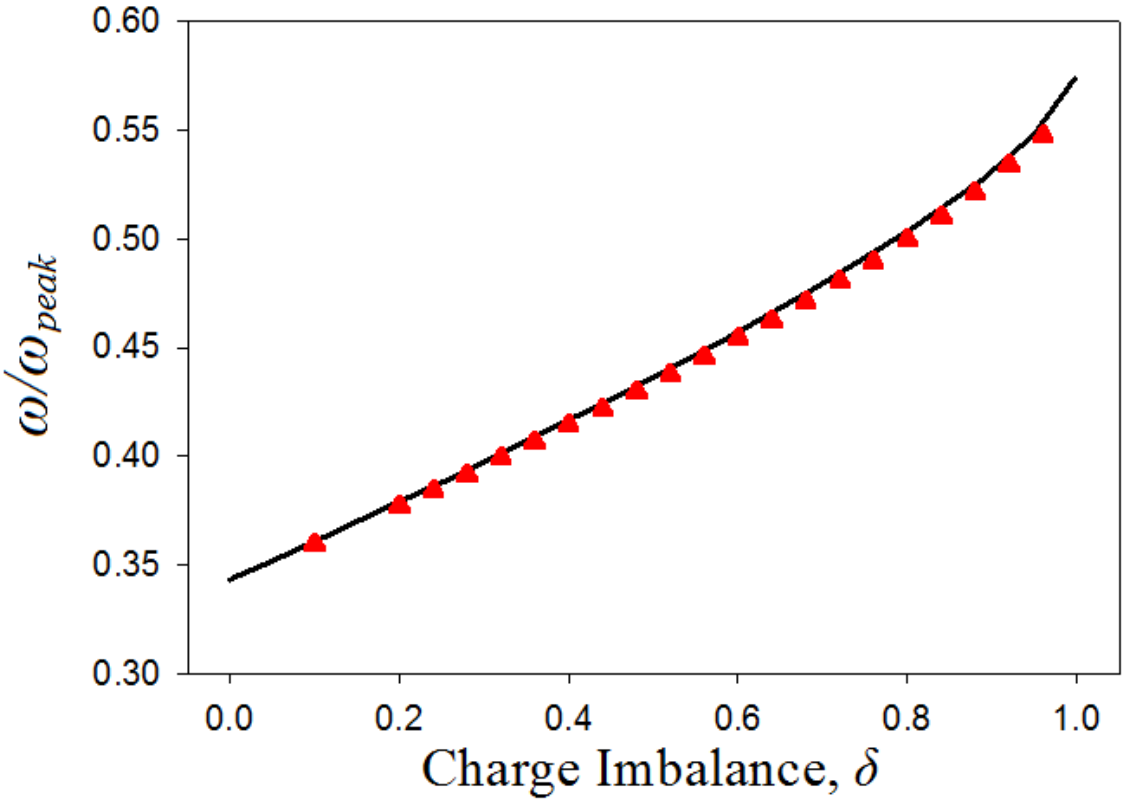


Figure 4.5: A plot of the ratio of the predicted resonant frequency to the plasma frequency associated with the peak density in the UCP as given by $\omega_{peak} = \sqrt{e^2 n_{peak}/m_e \epsilon_0}$. The black line shows the result of the average density calculation where a dipole perturbation is applied to the electron density distribution. The red triangles show the results from a numerical simulation in which the electron and ion distributions are offset from each other, and a restoring force is calculated.

The setup for this calculation is simple. Here we take our spherically symmetric electron and ion distributions and offset the centers of the distributions by a chosen amount, $\delta z$. We can then numerically calculate the force per electron resulting from this distribution. The restoring force from these calculations varies linearly as a function of $\delta z$ over the range of offsets we chose, allowing us to calculate the resonant frequency using a simple harmonic oscillator model, where

$$\omega = \sqrt{\frac{|F|}{N^2 m_e^2 \delta z}}. \tag{4.10}$$

Here $|F|$ and $\delta z$ are related by a constant owing to the linearity of the restoring force. To account for the charge imbalance, we can use a $T = 0$ electron distribution where the electron density matches the ion density. By integrating the electron density distribution in spherical coordinates from the center of the UCP, the number of electrons inside a radius $r_\delta$ from the center of the UCP can be calculated. To set the charge imbalance for this calculation, we set the electron density distribution equal to zero for $r > r_\delta$ for a properly chosen value of $r_\delta$. When we calculate the resonant frequency as it relates to the peak frequency, $\omega_{peak}$, over a range of charge imbalances, we find that there is good agreement (to within 2%) between this simple calculation and that of the perturbative calculation discussed above as seen in Figure 4.5. Corrections to $\omega/\omega_{peak}$ from a non-spherical aspect ratio from this calculation are less than 10%, even for extreme aspect ratios well beyond the 1:1.6:1.6 of UCPs in our system. This means that resonant frequency will depend mainly on the peak density of the ions in our system.

The ratio of the resonant frequency to the peak frequency, $\omega/\omega_{peak}$, as a function of the charge imbalance, $\delta$, implies that as the charge imbalance is increased for the same peak density, the resonant frequency will also increase. We measured this increase for the UCPs in our system over range of initial ionization energies and charge imbalances by applying electric field pulses (1.5 $\mu$s wide, up to 3 V/m amplitude) to the UCP to deliberately alter the charge imbalance at chosen points in the evolution of the UCP. For initial ionization energies from $\Delta E/k_B = 10 - 400$ K and initial $\delta = 0.15 - 0.65$, we measured the resonant frequency of the UCP at the same point in the evolution for the cases without and with and electric field pulse, 1 $\mu$s after the back edge of the pulse. The effect of the pulses was to increase the amount of charge imbalance by as much as $\Delta\delta = 0.2$. Since the time between the pulse and the measurement of the resonant frequency is

short, we can assume that the electric field pulse does not significantly alter the density. So, the peak frequency (density) should be the same between the cases with and without the pulse.

When we apply the electric field pulse, the frequency shifts in the direction (higher frequency) that is predicted by our model in all cases. The amount of shift in the frequency shows good matching between what we observe and the predictions in our model. However, there is an $\sim 2\%$ over-shift in the frequency over our range of typical conditions. This is mainly due to an over-shift in frequency at the earliest times in the UCP evolution for the lowest initial ionization energies ($\sim 10$ K). This could be due to the over-damped nature of the plasma oscillations that are induced by the external rf, which will be discussed further in Section 4.4. However, the over-shift in frequency is still relatively small, on the order $\sim 5\%$ for these conditions.

From this model, we were able to calculate the resonant frequency of a cloud of electrons displaced from the ion component in a UCP. However, we still need to evaluate whether this collective motion is a reasonable explanation for the observed electron signal in our measurements. To do this, we numerically evaluated whether the internal electric fields produced by the motion of the electrons could lead to additional electron escape. Since a full scale particle simulation of the response the external fields is computationally intensive (our talks with theorists had timescales of months on these types of simulations), we decided to sample individual electrons' motions as they were influenced by the externally applied rf fields and the overall motion of the UCP electron cloud. The goal of this calculation was to show that electrons could gain enough energy to escape the UCP without the need for binary collisions.

To setup this calculation, we started with a $T = 0$ electron and ion distribution with $5 \times 10^5$ ions, spatial extent $\sigma = 1$ mm, and charge imbalances in the range $\delta = 0.2 - 0.35$. The electron cloud will oscillate with an initial amplitude of $\sim$100 $\mu$m, which is based on typical predicted displacements based on our externally applied rf field. The oscillation is set to decay with exponential time constants that range from $\tau = 50 - 200$ ns (this is based on our observations from Section 4.4). The sample electron that we follow is placed in this distribution at a chosen position, trajectory, and kinetic energy. We vary these initial conditions to determine how likely it is for electrons to escape the UCP.

For these calculations, we sampled electrons with kinetic energies that ranged from $100 - 350$ K$k_B$. We also assumed potential depths of $400 - 750$ K$k_B$ of energy for our range of charge

distributions. The internal fields associated with the electron cloud motion could be as high as 10 V/m, which provided "kicks" to the electrons that gave them enough kinetic energy to escape the UCP under the proper conditions. This increase in energy occurs in just a few hundred nanoseconds without any collision processes.

Not all of the electrons that are subject to the internal fields associated with the collective electron motion escape the UCP. If the field is opposite the electrons motion, the particle may be slowed, which prevents it from being able to escape. The probability of an electron escape event is correlated mostly with the phase of the electrons motion relative to the internal field and also depends on the initial kinetic energy of the particle and the damping time of the collective oscillation. As the damping time is decreased from 200 to 50 ns, the electron can require up to six times the driving amplitude before escape is possible again. The damping time could be associated with both the density and the electron temperature which is discussed in the following section. While net 90 degree binary collisions (both electron-electron and electron-ion) will limit the transfer of energy for lower energy electrons, these collision timescales can be up to 10 times greater that the electron transit time across the UCP for higher-energy electrons [12], which makes this calculation reliable for higher-energy electrons.

### 4.3.1 Determining the UCP Size from Resonant Frequency Measurements

The calculations performed in the previous section allow us to determine the peak density of the UCPs created in our system from a measurement of the resonant frequency using the two-cycle rf sweep technique. While knowing the peak density can be useful, to compare our measurements to models of the UCP expansion, it is more convenient to determine the characteristic size of the UCP, $\sigma$. Therefore, it is important to describe how the value of $\sigma$ is determined in detail so that the reader can have a better understanding of the experiments presented in this thesis.

We start by measuring the resonant frequency of the UCP at a particular point in the UCP evolution using our two-cycle rf sweep technique described in Section 4.2 and seen in Figures 4.2 and 4.3. To determine the peak density, we need to determine the charge imbalance fraction, $\delta$, so that we can apply our model correction, $\omega/\omega_{peak}$, to our measured resonant frequency. Since the MCP signal (Figure 4.2) is proportional to the electron escape rate from the UCP, we can integrate the MCP signal in order to find the total number of electrons that escape the UCP as a function of

time (in conjunction with our MCP calibration factor, see Chapter 3). The integrated signal allows us to determine the charge imbalance fraction, $\delta$, at any point in the UCP evolution. In principle, the presence of three-body recombination can affect our determination of the charge imbalance as electrons recombine with the ions throughout the UCP evolution. However, for most of our UCP conditions, this effect is negligible. At our lowest initial ionization energies and highest densities, more care needs to be taken in order to accurately determine the value of the charge imbalance, $\delta$. With the value of $\delta$ at the time of the resonant frequency measurement, we can find the plasma frequency associated with the peak density of the UCP, $f_{peak}$, by multiplying the measured resonant frequency by the value of $\omega/\omega_{peak}$ taken from Figure 4.5. The peak density, $n_{peak}$, can be found by solving Equation 2.13 to be $n_{peak} = (f_{peak}/8980)^2$ in units of /cm$^3$.

To find $\sigma$, we use the fact that for a Gaussian ion distribution, $\sigma = [N_{ion}/(2\pi)^{3/2} n_{peak}]^{1/3}$, where $N_{ion}$ is the total number of ions in the UCP (this can be found from the integrated MCP signal by using the number calibration factor). There is one subtlety that needs to be considered when making this conversion. Although the electron distribution is not entirely Gaussian as electrons escape (the electrons closely match the ion density in the center, but there is a sharp cutoff in the outer part of the distribution), there is an underlying Gaussian shape to the ion distribution that we can characterize by the parameter $\sigma$. It is this value of $\sigma$ that we can compare to models of plasma expansion as will be discussed in Chapter 5.

## 4.4 UCP Response to Pairs of Sharp Electric Field Pulses

The model of the UCP response where the electrons act as a rigid object leads to a prediction that a collective oscillation can be excited by a sharp electric field pulse comparable to an impulse given to a simple harmonic oscillator system. To test this hypothesis, we applied a pair of sharp electric field pulses to the UCP and measured the response through the electron escape signal. The pulses we applied have a full-width half-max temporal profile of 12.5 ns. The first pulse served to excite the collective motion of the electrons in the axial direction. The second pulse was applied after a chosen time delay, and the resulting electron escape owing to the presence of the second pulse was measured as a function of this time delay. The result of this measurement was a clear oscillating behavior in electron escape signal as seen in Figure 4.6. The damped oscillation that was observed

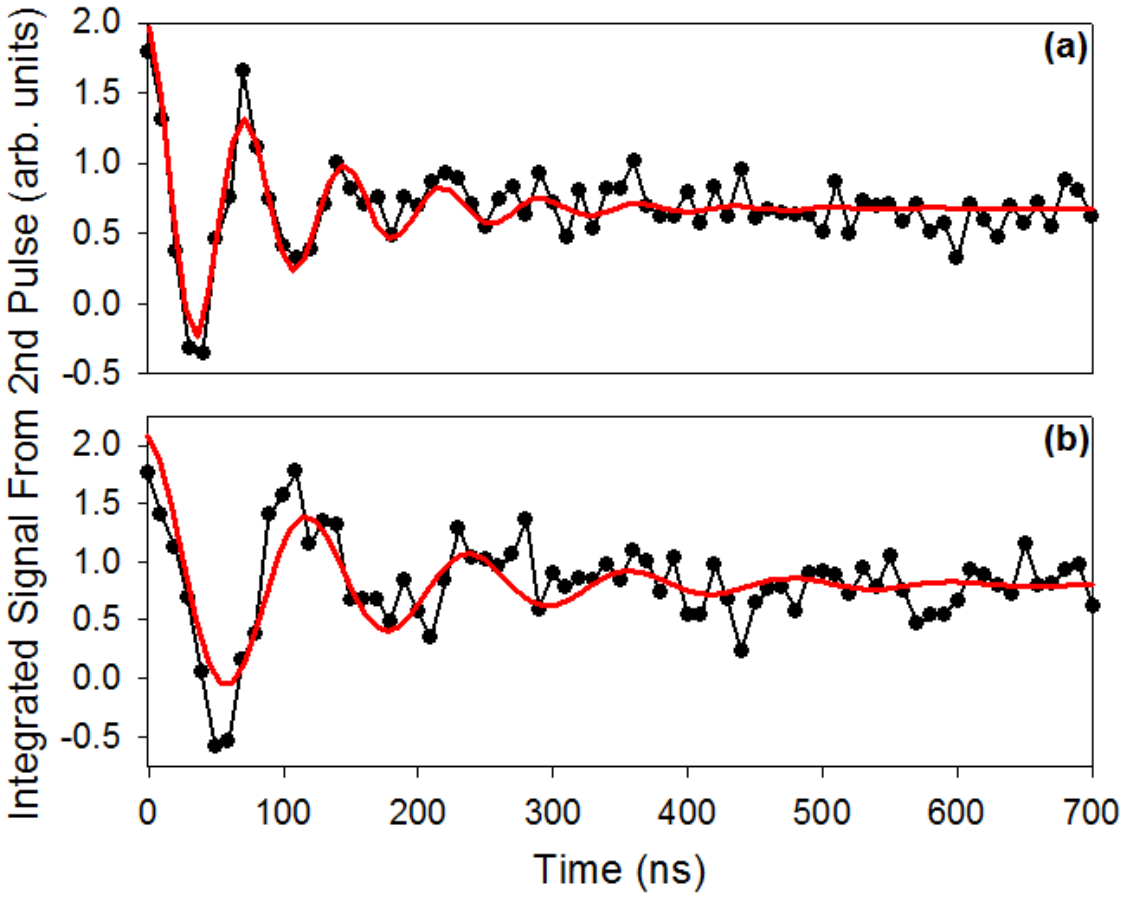


Figure 4.6: An example of the UCP response to two sharp electric field pulses. The left axis shows the additional electron escape owing to the presence of the second electric field pulse. The bottom axis is the pulse separation in ns. The two sets of data here show the response at $\Delta E/k_B = 10$ K for 55 (a) and 80 (b) $\mu$s after the initial UCP formation. We fit the response curves to decaying oscillating functions of the form $A\cos(2\pi ft)\exp(-t/\tau) + y_0$ where $f$ is the frequency of oscillation in Hz and $\tau$ is the decay time constant. In (a), the fits yielded a frequency of $13.61 \pm 0.23$ MHz ($13.31 \pm 0.12$ MHz from two-cycle rf). The time constant of decay was found to be $\tau = 103 \pm 14$ ns. In (b), the fit frequency was $8.33 \pm 0.14$ MHz ($8.05 \pm 0.1$ MHz from two-cycle rf). The time constant of decay was found to be $148 \pm 26$ ns

can be understood as a damped, harmonic oscillator system. The first pulse starts the motion, and the second pulse will either enhance or decrease the response based on the direction of the collective motion during the second pulse.

Figure 4.6 shows the results of this measurement for two different times in the UCP evolution (55 and 80 $\mu$s respectively) at $\Delta E/k_B = 10$ K. The frequency of oscillation decreases later in the UCP evolution, as would be expected from the density dependence of the resonant frequency as the UCP expands. The frequency of this response was compared to that of the peak response to a two-cycle rf sweep at the same time. To do this, it is easiest to compare the response of a two-cycle rf sweep to that of the fast-Fourier transform (FFT) from the oscillating signal to get the resonant frequency. The results of the FFT can be seen in Figure 4.7. Plotted with this is a scaled response curve from a two-cycle rf sweep at the time of the two-pulse measurement. From this, we can see a clear peak in the FFT signal in both cases at the same frequency of that from the sweep measurement. The response in both cases is relatively broad as would be expected since pulses of rf contain a range of frequencies around the principle frequency. This measurement shows that the nature of the response is the same in both cases, and further confirms that a collective motion of electrons is responsible for the response that is observed in our system.

The source of the decay of the oscillating signal from the two-pulse measurements could be due to dephasing of the motion of the electron component owing to its fluid nature or to electron-ion collisions which can also dephase the motion of electrons. The exact source of this decay is unknown at this time but is likely a combination of the two effects. Although this will be the subject of the thesis work for future students of this project, there are still some observations that can be made about the properties of this decay. The oscillating, decaying response was fit to a function of the form $A\cos(2\pi f t)\exp(-t/\tau) + y_0$, where $A$ is the amplitude of oscillation, $f$ is the frequency, $\tau$ is the time constant of the decay, and $y_0$ is the offset of the electron response. When the response curve from Figure 4.6 (a) was fit to this function, it yielded a decay constant of $\tau = 103 \pm 14$ ns. Later in time, in Figure 4.6 (b) the decay time increased to $\tau = 148 \pm 26$ ns. The error in the fit of the decay time was relatively large but shows the right trends for the expected collisional timescales associated with an expanding UCP. The electron-ion 90 degree deflection times for this data can range from 10s of ns up to several hundred ns depending on the temperature of the electrons in the UCP [12]. These types of measurements may lend themselves to estimating the

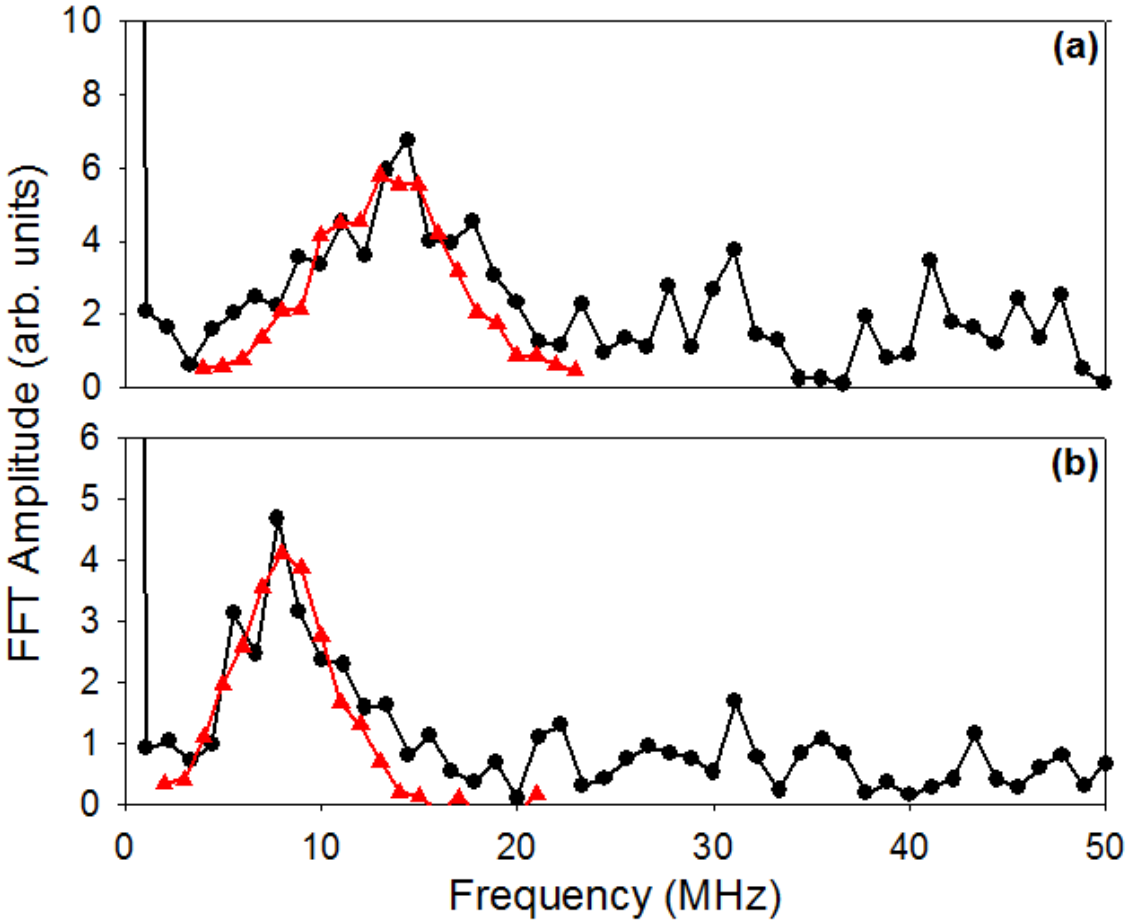


Figure 4.7: The Fast Fourier Transform of the two-pulse response data from Figure 4.6 (black). The red data that is superimposed on these plots is a scaled version of the two-cycle rf sweep data used to find the resonant frequency. Here we can see that the frequency response of the two cases is nearly the same, indicating that the response mechanism in both cases is the same.

electron temperature based on this decay time if the dephasing of the electron component of the UCP can be taken into account.

If we perform this measurement at very early times for $\Delta E/k_B = 10$ K, the response of the UCP can be very different. Here, we have observed over-damped behavior in which no oscillations in the electron component are present. The enhanced signal from these pulses decays in less than 40 ns, after which a relatively flat response is observed. At this point in the UCP evolution, the election-ion collision rate is significantly higher than at other points in the UCP evolution and a much higher damping rate owing to binary collisions is expected to occur. This could be the reason that the charge imbalance correction measured at this time in the UCP evolution is slightly different than what is predicted as discussed previously.

## 4.5 Scaling of the Two-Cycle Response with Density and Magnetic Field

The calculations from our model of the electron motion indicate that the magnitude of the restoring force on the electron cloud increases with increasing UCP density. This means that the amplitude of the oscillation of the electron cloud will decrease with increasing density when under the influence of the externally applied rf field, decreasing the overall response. This decrease in the response as a function of UCP density means that the energy transfer mechanism which is described by our model will not be as prevalent in other UCP experiments where the density is $1-2$ orders of magnitude higher [1, 6]. For our system, we were able to measure this response as a function of UCP density as seen in Figure 4.8. For these measurements, we measured the resonant frequency at a particular position in the UCP evolution using the two-cycle rf method. With the frequency, number of total ions, $N$, and the charge imbalance, $\delta$, we can find the peak density of the UCP at this time as described earlier. To determine the effective response size, we take the peak response size from the sweep measurements, and scale it by the number of electrons remaining in the UCP (we do this because near the end of the UCP lifetime where the density is lowest, there are not many electrons available to escape) to determine an effective response size.

These measurements show that as the density increases that the effective response size decreases. The data in Figure 4.8 was taken over a range of initial ionization energies ($\Delta E/k_B = 1 - 400$ K).

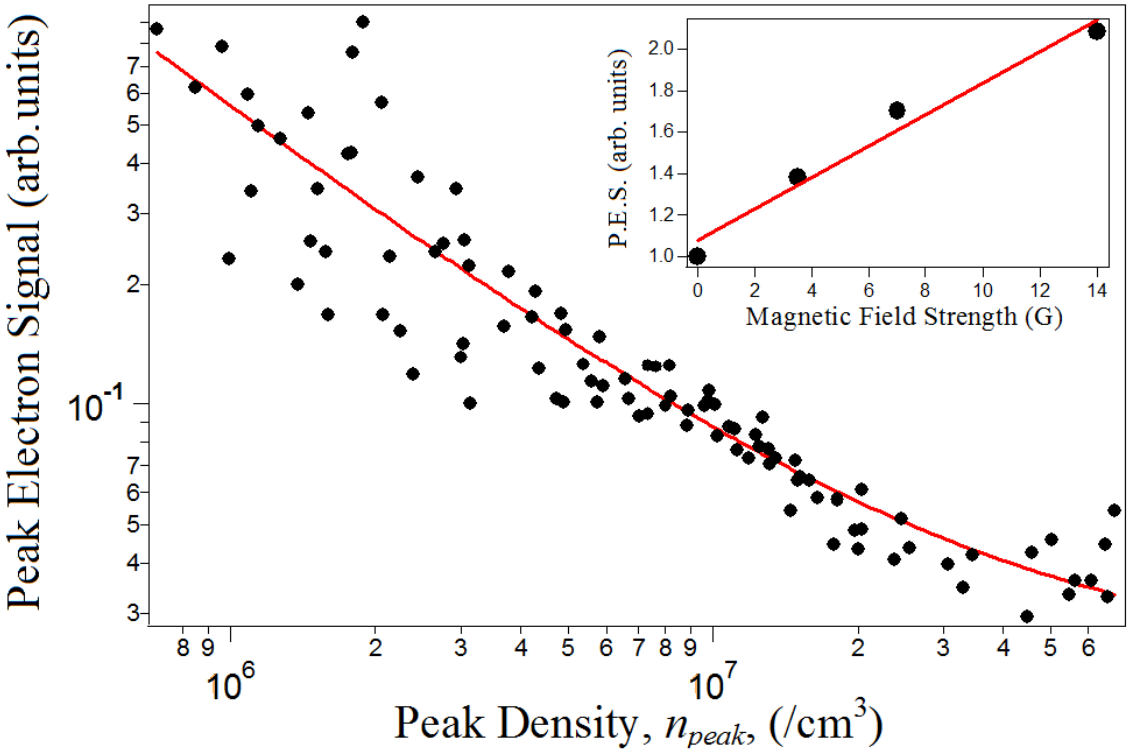


Figure 4.8: An example of the effective response size from a two-cycle rf measurement as a function of density. Each data point here represents the peak electron signal observed in a two-cycle rf sweep measurement, scaled by the number of electrons remaining in the UCP at the time of the rf application. The data here is a compilation of data sets over a wide range of temperatures ($\Delta E/k_B = 1 - 400$ K). This effect is attributed to the increase in the restoring force on the electrons from the ions as the density increases. Inset is the effective response size as a function of magnetic field for $\Delta E/k_B = 10$ K. The increase in the response size with magnetic field here is likely owing to better coupling between the driving rf and the dipole response mode of the oscillating electrons.

The effective response size shows no additional scaling as a function of the initial energy of the UCP.

We are also able to measure the effective response size as a function of the magnetic field between $0 - 14$ G. The results of these measurements show that there is a general increase in the effective response size as the magnetic field increases. This is likely due to the fact that the magnetic field is able to restrict the electron motion that is not along the axis of the driving force, which allows for better coupling to the dipole oscillation mode.

## 4.6 Additional Measurements of the Delayed RF Response

The application of delayed rf to our UCPs is what led us to the studies of the effects of short rf pulses in our system. The original motivation for the delayed rf measurements was to measure the collisional timescales that led to electron evaporation in UCPs by trying to heat the electrons at the lowest energies of the electron distribution. These electrons would occupy small radius orbits near the center of the UCP distribution. Our initial estimates of the density (which were ultimately consistent with our observations) of the UCP allowed us to estimate the electron-electron collision timescales early in the UCP evolution. Over our range of initial conditions, we expected collision timescales for the electrons that could be as long as many $\mu$s. Therefore, if energy is given to the electrons in the lower portion of the energy distribution, we should be able to measure how long it takes for energy to be redistributed to the top of the energy distribution where electrons can escape the UCP. Although we could not guarantee that the energy that we deposited into the UCP through the rf would be absorbed mainly in the lower part of the energy distribution, most of the electrons in the UCP exist at energies well below the potential well barrier. So, it was presumed that we would still see an effect owing to the heating of these lower energy electrons.

What we observed was quite different from our expectations given the results of other UCP experiments [1, 6]. As discussed earlier, there is a rapid response to the rf that has no dependence on the UCP temperature and therefore no dependence on electron-electron collision timescales. Also, the delayed application of rf also shifted the time of the observed resonant response to later in the UCP evolution. The discussion earlier in this chapter focused on the rapid response of the UCP to the applied rf. Here I will discuss the results of further measurements of the shift in the

resonant response. To see how much the application of the continuous rf affected the UCP evolution, we applied the delayed rf at many times throughout the UCP evolution for the same applied rf frequency. We performed this measurement at initial ionization energies of $\Delta E/k_B = 10$, 100, and 400 K. The results of these measurements can be seen in Figure 4.9. In these measurements, we continue to shift the time of the rf application until only the initial response to the applied rf is observed.

In Figure 4.9, we observe that as the rf is applied later in the UCP evolution, that the time of the resonant response that we observe can shift out to much later in the UCP evolution. This is particularly true at $\Delta E/k_B = 10$ K, where we can apply the rf as much as $\sim$20 $\mu$s later and still see a resonant response. As $\Delta E/k_B$ increases, the amount of time that the resonance shifts decreases. At $\Delta E/k_B = 400$ K, the resonant response does not shift significantly as the time of application of the rf is changed. Also, at the time of the observed resonance, the initial response here is at its greatest. These observations suggest that the application of the rf causes a significant amount of heating that can greatly alter the expansion rate of the UCP when the rf is applied. At $\Delta E/k_B = 400$ K, the expansion rate is fast enough compared to the additional energy received from the applied rf that there is no significant shift in the resonant response.

## 4.7 Comparison of the Two-Cycle and Continuous RF Response

Although the response of the UCP to continuous rf depends strongly on many UCP parameters besides density, the nature of this response can be compared to that of our two-cycle rf pulses under certain experimental conditions. To do this, we take advantage of the fact that the time of the UCP resonance with the continuously applied rf changes with the applied rf amplitude. The effect of the continuous rf on the time of the observed resonance was first noticed in the data in Figure 4.1, where a delay in the rf application shifted the resonance to later time. It was also noticed that as the rf amplitude was increased, the resonance shifted to earlier times in the UCP evolution as seen in Figure 4.10. This result lead us to the conclusion that the application of the continuous rf caused a significant amount of heating in the UCP which can drive a faster expansion in the ion component (this point will be discussed further in the following section). The faster expansion will cause the density to reach the resonance condition at an earlier point in the UCP evolution, which

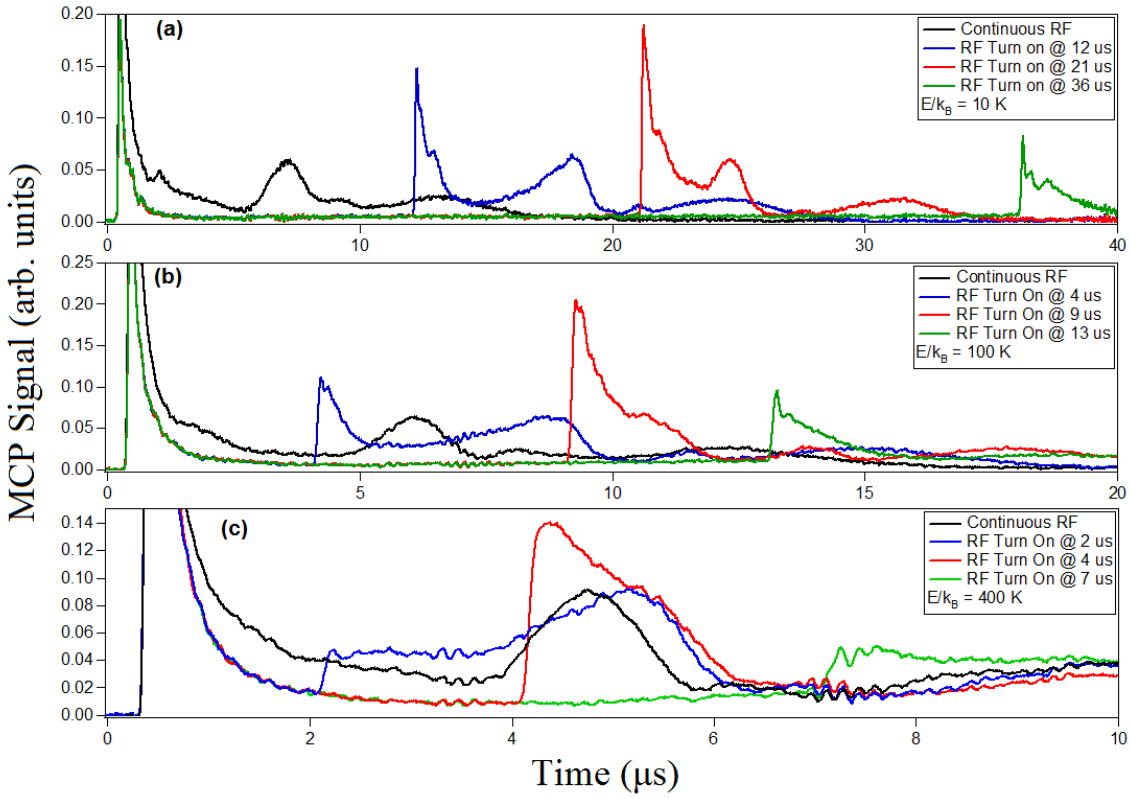


Figure 4.9: Further demonstration of the delayed application of the rf and the induced shift in the resonant frequency time for $\Delta E/k_B$ = 10, 100 and 400 K (applied frequencies of 20, 20 and 25 MHz respectively). We observed here that there is an initial ionization energy dependence on the magnitude of the shift in the resonant response as the rf is delayed. At $\Delta E/k_B = 10$ K, the shift is $< 20$ $\mu$s. At $\Delta E/k_B = 400$ K, there is no detectable shift in the time of the resonance. Our data suggests that the expansion rate of the UCP is altered by the application of the rf.

explains the shift in time that we observe. This effect is greater at lower initial ionization energies, $\Delta E/k_B$, as seen in Figure 4.10 (a). Here, at $\Delta E/k_B = 10$ K, the time of the observed resonance peak can be shifted by as much as 15 $\mu$s, which is a substantial fraction of the $\sim 110$ $\mu$s lifetime of the UCP (The lifetime of the UCP is defined by the time at which the last electron escapes from the UCP). At $\Delta E/k_B = 400$ K, the resonance time changes by less than 1 $\mu$s for a UCP lifetime of $\sim$25 $\mu$s. This relatively mild influence at higher initial ionization energies can be understood when considering that "natural" expansion rate of the higher initial energy UCP is higher than for lower energies. So, if a similar amount of energy is imparted to the UCP from the continuous rf, the relative effect will be greater for the lower energy UCP.

As a consequence of the more rapid expansion, the lifetime of the UCP can be greatly reduced, particularly for the lower initial energy case. For the $\Delta E/k_B = 10$ K data in Figure 4.10 (a), the life time was reduced to $\sim 20\%$ of the "natural" lifetime at the highest amplitude of the applied rf. At $\Delta E/k_B = 400$ K, this reduction is to only $\sim 90\%$ of the "natural" lifetime, which would be expected from the arguments made above.

To compare the response to the continuous rf to the two-cycle rf method, it is necessary to find a way to account for the shift in the resonance time owing to the heating of the UCP from the applied rf. To do this, we measure the observed time of the resonance as a function of the amplitude of the applied rf. If the resonance time can be extrapolated to zero applied rf power, we can take the extrapolated time to be where the resonance would occur in the absence of any heating effects. An example of this type of measurement can be seen in Figure 4.10(a) for $\Delta E/k_B = 10$ and 400 K. For the $\Delta E/k_B = 10$ K data, the peak time as a function of power is not linear, which makes the determination of the zero-power peak time difficult. In this case, the effect of the rf seems to saturate at higher power. At higher initial ionization energies, the extrapolation back to zero applied rf power is linear, which will allow us to make comparisons to the two-cycle rf method under these conditions.

We can use this method for finding the resonance time using continuous rf for multiple frequencies of the applied rf. By accounting for the charge imbalance, $\delta$, at the extrapolated time of the resonance, we can use our model to determine the value of $\omega_{peak}$, which can be converted to a measure of the peak density, $n_{peak}$. From the value of the peak density, and the total number of ions and electrons produced for our UCP, $N_{ion}$, we can calculate the rms size, $\sigma$ of a spherically

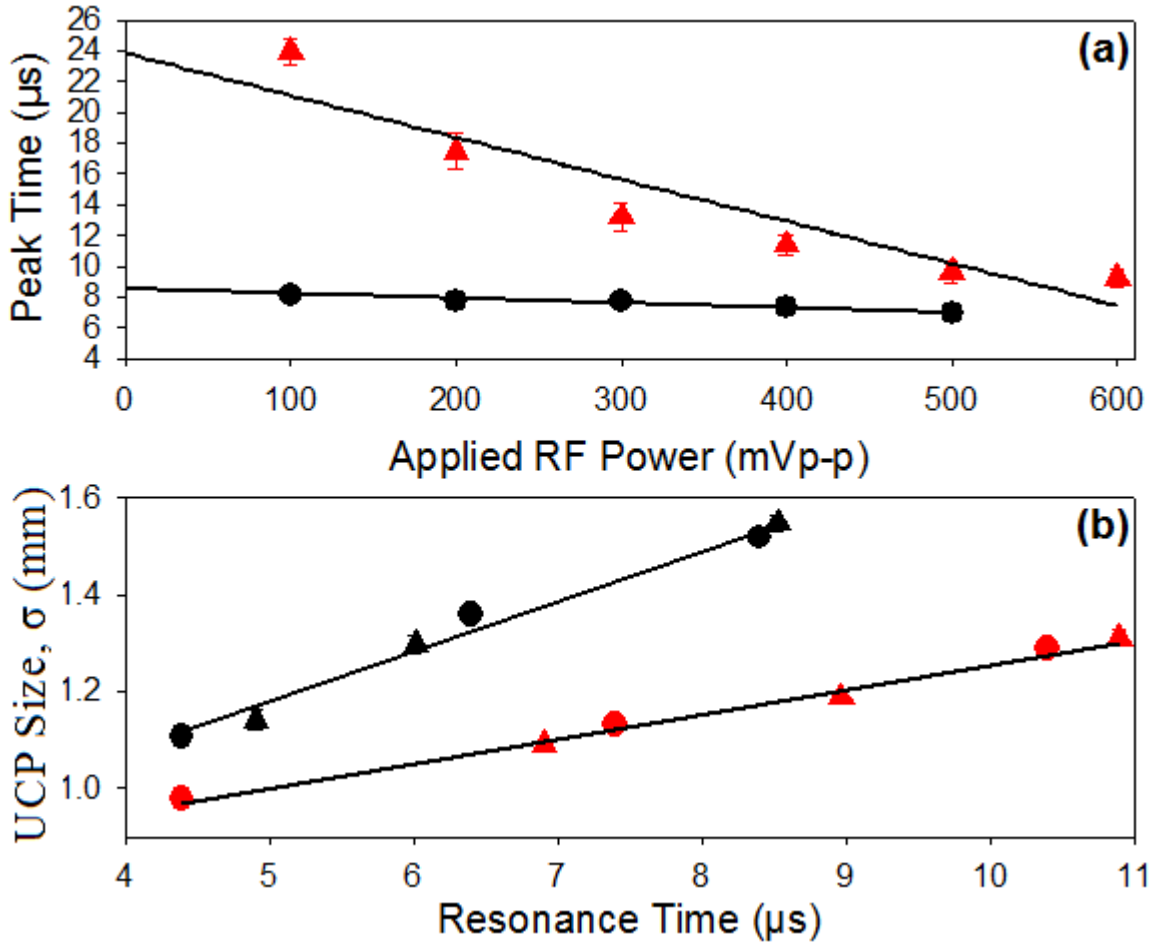


Figure 4.10: (a) An example of the shift in the resonance peak time as a function of the continuous rf amplitude. At $\Delta E/k_B = 10$ K (red triangles), one can see that the extrapolation is not linear, and the zero-power peak time can not be determined by a linear fit (12 MHz applied rf field). At higher initial ionization energies (shown here at $\Delta E/k_B = 400$ K as black circles) the extrapolation is linear, allowing the determination of the zero-power peak time (16 MHz applied rf field). In (b), we compare this extrapolation for a few different frequencies of continuous rf (triangles) with the measured frequencies at specific times with two two-cycle rf method (circles). These data, for $\Delta E/k_B = 100$ K (red) and 400 K (black) show a consistent trend in time.

symmetric Gaussian distribution as given by $\sigma = [N_{ion}/(2\pi)^{3/2} n_{peak}]^{1/3}$. The rms size can be used to measure the expansion of the UCP, which will be discussed in more detail in Section 4.8. We can measure the rms size, $\sigma$, using our two-cycle rf method and compare to the values that were measured using the extrapolation technique for continuous rf by plotting the values from both techniques together as seen in Figure 4.10(b). Here we have this comparison for $\Delta E/k_B = 100$ and 400 K, where we observe no significant (i.e. greater than 3%) difference between the two techniques. This degree of agreement implies that the mechanism for the resonant response is likely the same when using either technique. This further illustrates that our experimental parameters put us in a range where the theory from [5] does not apply because the charge imbalance correction from this model would produce corrections to the density that would be inconsistent with our data.

## 4.8 Using Two-Cycles of RF to Measure the UCP Expansion Rate

One of the most useful applications of the two-cycle rf sweep method is the ability to measure the expansion rate of the UCP. This was done in part as discussed in Section 4.7 to compare the response of the two-cycle rf sweeps to the continuous rf response. Mapping the full expansion and evolution of the UCP will be used to study the effects of evaporative cooling (Chapter 5) and influence of magnetic fields on the UCP formation (Chapter 6). To begin our studies of the UCP expansion for our system, we mapped out the expansion for UCPs ranging in initial ionization energy from $\Delta E/k_B = 1 - 400$ K as seen in Figure 4.11. Here, we can see that the expansion of the UCP increases with initial ionization energy. From the expansion curves, we can find the asymptotic expansion velocity as a function of initial ionization energy which is seen in Figure 4.11. There are a few things to notice from the asymptotic expansion velocity. The red line in the figure represents the expansion velocity of the UCP that would be expected if all of the energy of UCP is transferred to the ion expansion energy. For initial ionization energies below $\Delta E/k_B = 10K$, we observed an asymptotic expansion velocity that no longer decreased as the initial energy was lowered. This has been observed in other UCP experiments [1], and is attributed to three-body recombination heating effects on the UCP. Because of our lower densities, this effect occurs at lower initial energies for the UCPs in our system. For higher energies, the asymptotic expansion velocity falls below the expected full energy expansion velocity (red line). This lowering of the

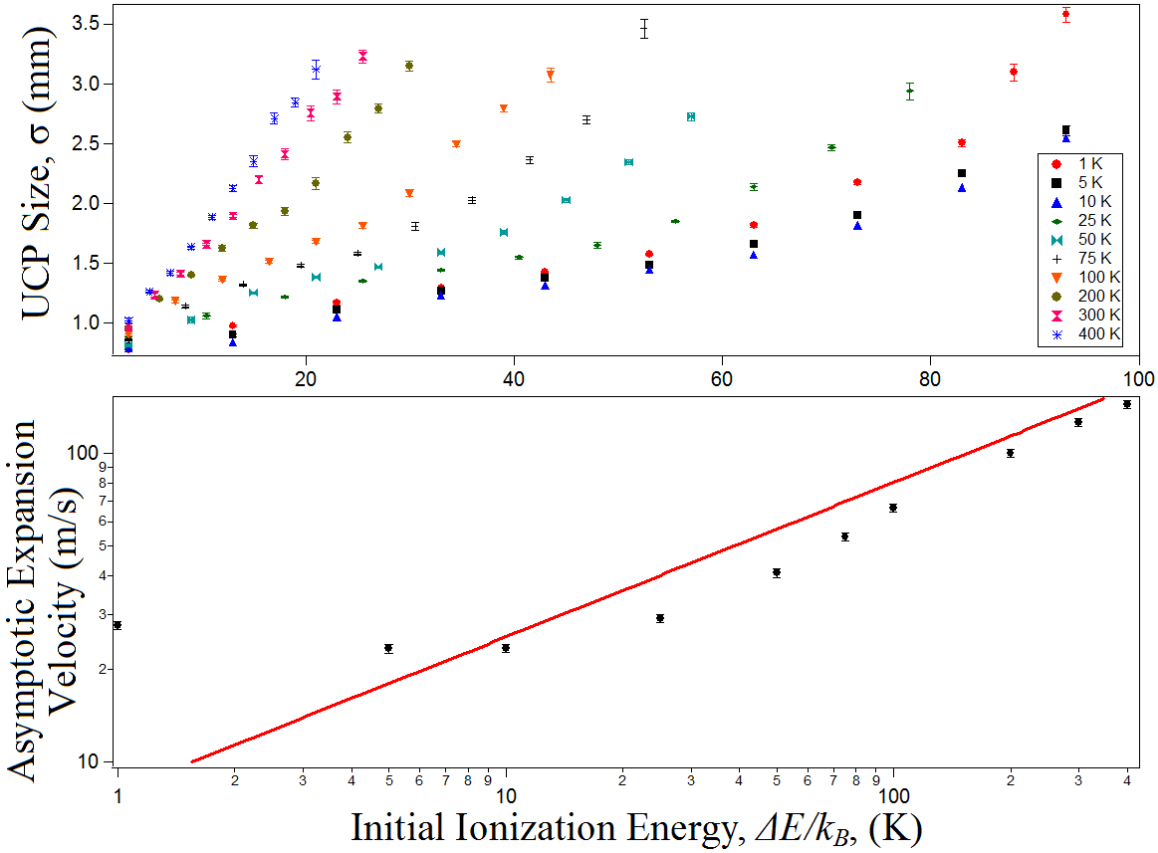


Figure 4.11: Using the two-cycle rf method for determining the density (and from that the rms size $\sigma$) of the UCP, we were able to measure the expansion of the UCP over an initial ionization energy range from $\Delta E/k_B = 1 - 400$ K. From these curves, we were able to find the asymptotic expansion velocity as a function of the initial ionization energy which is seen in the lower figure. The red line in this figure represents a full conversion of the initial energy to expansion energy. At low $\Delta E/k_B$, the expansion energy is above this line, which is attributable to three-body recombination heating which increases the expansion energy of the UCP [1, 9]. At higher $\Delta E/k_B$, it falls consistently below this line, which implies that there are effects from evaporative cooling on the expansion of the UCP.

expansion energy is what led us to our studies of the effects of electron evaporative cooling on the UCP expansion velocity that will be discussed in Chapter 5.

The expansion curves that were measured in Figure 4.11 were taken with a 7 G magnetic field, which at the time that this data was taken helped us to extract all of the electrons from the UCP (see Chapter 3). As a consequence of using a magnetic field during the UCP expansion, we observed unexpected expansion behavior that caused the expansion to deviate from the expected form of a self-similar expansion, where the rms size of the plasma scales in time as $\sigma(t) = \sqrt{\sigma_0^2 + v^2 t^2}$, and $v$ is the asymptotic expansion velocity. The initial expansion of the UCP is more rapid than is expected. Also, there appears to be a period of deceleration in the UCP expansion that was not expected and is also not observed under magnetic field free conditions of the UCP. These observations led to the studies of the effects of a magnetic field on the UCP formation and expansion that are discussed in detail in Chapter 6. At later times in the UCP evolution in some cases, a rapid acceleration of the ions can be observed. This occurs when there are typically less than 10% of the total number of electrons remaining in the UCP. At this point a breakdown the UCP screening can occur, which can cause a "coulomb explosion" of the ions [13].

## 4.9 Ultracold Plasma Heating from Short Bursts of RF

Although using the two-cycle rf technique for measuring the density of the UCP is ideal for our system because it does not add heat to the UCP before the application of the rf, short bursts of rf can be used to add heat that measurably alters the evolution of the UCP after the rf is applied. This was first observed in the form of subtle changes to the lifetime of the UCP when the rf was applied early the UCP evolution. This type of effect might be useful when trying to characterize electron-ion collisions which will be the subject of future work for this project. Also, it may prove useful to have a method for deliberately altering the electron temperature that does not involve changing the initial ionization energy. At this time, only preliminary measurements were made where it concerned the effects of short bursts of rf on the UCP. A summary of those results will be presented here.

For this measurement, we applied four cycles of rf near resonance early in the UCP evolution, and looked for changes in the subsequent evolution of the UCP compared to the case without the

applied rf. As seen in the measurements presented in this chapter, the application of a short burst of rf can cause a large increase in the amount of electron escape at the time of application. The electrons that escape carry away energy from the UCP, and if there is heating from the rf, some of the heat can be removed by the escaping electrons. To study the effects of heating from the rf, it will be necessary to prevent electrons from being able to carry this heat away. To do this, we can shut-off the electron escape entirely for a short period of time. By creating the UCP in a relatively large DC electric field, we can allow the UCP to form and apply a sharp electric field ramp to a lower electric field to increase the confinement of the electrons in the UCP. Figure 4.12(a) shows the total charge imbalance (fraction of electrons that have escaped) of the UCP as a function of time for $\Delta E/k_B = 100$ K ($2.5 \times 10^5$ ions), with and without a heating pulse. The UCP is formed in a relatively high DC electric field ($\sim$20 V/m), which extracts a large number of electrons in the "prompt" peak. After 2 $\mu$s the electric field is ramped quickly down to a lower DC field ($\sim$1 V/m). When the DC field is lowered, the excess of ions compared to the electrons and the lower DC field combine to create a potential well with a very high barrier relative to the temperature of the electrons. This prevents any electron escape from taking place for $\sim$8 $\mu$s, until the UCP expands enough to lower the potential barrier to a level where electron escape can resume. This provides a window in time where we can apply the four cycles of rf while minimizing the chance for electron escape. The rf that is applied is at 25 MHz, 5 V/m peak-to-peak, and at 3 $\mu$s (1 $\mu$s after the electric field ramp) after the formation of the UCP. To study the effects of the rf heating on the UCP, we can make comparisons of the UCP size using the two-cycle rf sweep method described in this chapter between the cases with and without the heating pulses.

The results of these measurements can be seen in Figure 4.12(b). Here, we measure the size of the UCP at four points in the UCP evolution between $14 - 29$ $\mu$s after the formation of the UCP. The figure shows that when the heating pulse is applied, the rms size, $\sigma$, of the UCP is larger at each time when compared to the case without the heating pulse. The difference is small, but we can take the ratio of the size increase at each point and perform a weighted average to find the size with the heating pulse is on average $3.5 \pm 0.7\%$ larger than the case without the heating pulse present. The fit lines in Figure 4.12(b) are shown extrapolated so that the small difference in slopes between the two sets of data can be seen, which is $\sim$ 7% increase for the data with the heating

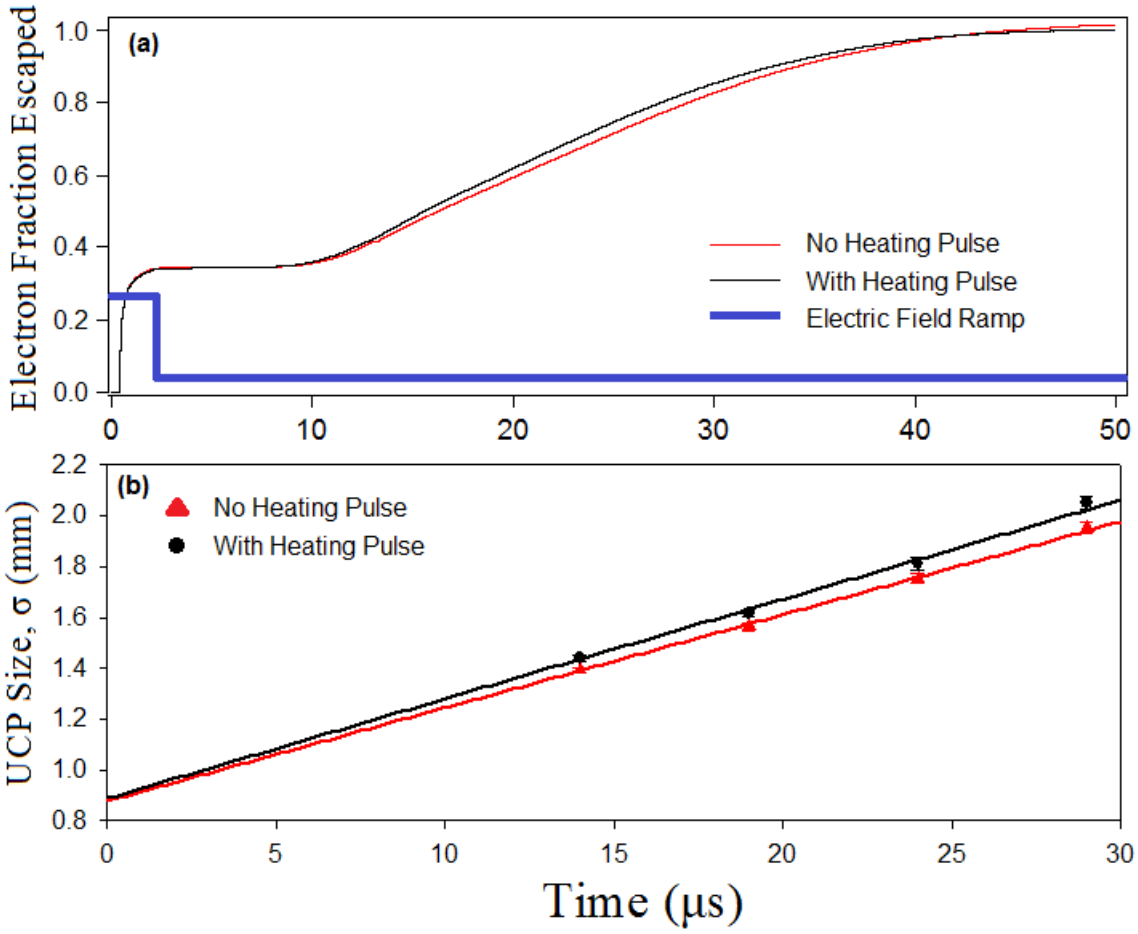


Figure 4.12: (a) The red and black curves show the electron escape fraction as a function of time without and with a four-cycle heating pulse respectively. The blue curve shows the electric field level in time. We ramp the field down at 2 $\mu$s to shut off the electron evaporation, 1 $\mu$s after which we apply a heating pulse to the UCP. (b) shows the results of the UCP size measurements and their comparisons with and without the heating pulses. We can see here that when the heating pulse is applied, the UCP is larger at the time of each size measurement.

pulse. However, for this data, the error in the ratios for the slopes is $\sim 5\%$ which would imply that there is not a statistically significant difference between the two cases.

Another indication that heating has taken place when the four-cycle rf pulse is applied is the increase in the electron evaporation rate seen in Figure 4.12(a). Here it can be seen that as the electrons begin to escape again after the application of the DC electric field ramp, that the slope in the electron escape fraction is greater when the heating pulse has been applied. At the point of the highest electron evaporation rate, the data with the heating pulse has a $9.1 \pm 0.1\%$ higher electron evaporation rate. While an increase in electron temperature generally lowers the electron-electron collision rate, the rate of electron evaporation is will be strongly influenced by the potential well depth created by the excess of ions to electron temperature ratio. So, an increase in electron temperature can produce an increase in the electron evaporation rate from the UCP. Also, increases in the UCP size can lower the potential barrier caused by the excess of ions, which will increase the rate of electron escape from the UCP. The influence of electron evaporation on the evolution of UCPs is the subject of the next chapter, and will be discussed in great detail.

## Conclusion

The nature of the response of the UCP to short bursts of rf in our system showed us that there is a collisionless energy transfer mechanism that is present for low-density UCPs within the range of our experimental conditions. The applied rf was shown to excite a collective motion of the electron component of the UCP with a resonant frequency. Modeling of a collective electron response to external fields showed that this frequency was determined by the peak ion density and the charge imbalance through the average electron density. The collective motion of the electrons was further confirmed by applying two sharp electric field pulses to the UCP separated in time. The pulses were able to excite motion that resembled a damped, driven harmonic oscillator system, whose frequency is the same as the resonant frequency from the two-cycle rf data.

The development of the two-cycle rf method for measuring the density of the UCP as a function of time will allow us to characterize many different properties of the UCP. It is the most important tool that we have developed for our system and it will serve as a the main measurement technique for the rest of the UCP experiments described in this thesis and for many future experiments beyond those discussed here. The main advantage of our technique is the ability to measure the

expansion rate of the UCP without the heating effects that are present in the continuous rf case. These expansion rate measurements will allow us to make comparisons to models of the effects of electron evaporative cooling on the ultimate UCP expansion as discussed in the next chapter.

## References for Chapter 4


[1] S. Kulin, T. C. Killian, S. D. Bergeson, and S. L. Rolston, Phys. Rev. Lett. **85**, 318 (2000).

[2] P. Gupta, S. Laha, C. E. Simien, H. Gao, J. Castro, T. C. Killian, and T. Pohl, Phys. Rev. Lett. **99**, 075005 (2007).

[3] D. A. Gurnett and A Bhattacharjee, *Introduction to Plasma Physics* (Cambridge University Press, 2005), 10-12.

[4] S. D. Bergesonand R. L. Spencer, Phys. Rev. E **67**, 026414 (2003).

[5] A. Lyubonko, T. Pohl, and J. M. Rost, New J. Phys. **14**, 053039 (2012).

[6] K. A. Twedt and S. L. Rolston, Phys. Rev. Lett. **108**, 065003 (2012).

[7] T. C. Killian, S. Kulin, S. D. Bergeson, L. A. Orozco, C. Orzel, and S. L. Rolston, Phys. Rev. Lett. **83**, 4776 (1999).

[8] T. C. Killian, M. J. Lim, S. Kulin, R. Dumke, S. D. Bergeson, and S. L. Rolston, Phys. Rev. Lett. **86**, 3759 (2001).

[9] F. Robicheaux, and J. D. Hanson, Phys. Rev. Lett. **88**, 055002 (2002).

[10] R. S. Fletcher, X. L. Zhang, and S. L. Rolston, Phys. Rev. Lett. **99**, 145001 (2007).

[11] S. Ichimaru, Rev. Mod. Phys. **54**, 1017 (1982).

[12] L. Spitzer, Jr., *Physics of Fully Ionized Gases* (Dover, New York, 1962).

[13] X. L. Zhang, R. S. Fletcher, S. L. Rolston, P. N. Guzdar, and M. Swisdak, Phys. Rev. Lett. **100**, 235002 (2008).

# Chapter 5

# Electron Evaporative Cooling in Expanding Ultracold Plasmas

With the development of techniques that can be used to measure the ultracold plasma (UCP) density at a chosen point in the UCP evolution as discussed in Chapter 4, we can now use measurements of the UCP expansion to characterize the electron temperature profile of the UCPs created in our system (see Equation 2.19). In particular, we want to study the effects of electron evaporative cooling on evolution of the UCP expansion and electron temperature for our UCPs. By demonstrating the importance of evaporative cooling for the UCPs created in our system, we can then begin to explore ideas such as forced evaporative cooling in attempts to push the electron component of our UCPs further towards the strong-coupling regime [1].

Measurements of the UCP expansion can be used to determine early-time properties of the plasma such as the electron temperature [2]. These measurements have been used to study the various heating effects that can occur during the UCP formation. These heating effects include three-body recombination [2, 3], disorder induced heating [4], threshold lowering [5], and Debye screening [6]. All of these effects lead to lower strong coupling than what can be theoretically achieved based solely on the initial ionization energy of the ionizing laser and the thermal temperature of the ultracold atoms used to create the UCP. This is particularly true for the electron component of the UCP, where three-body recombination has placed a theoretical limit on the amount of strong coupling that can be achieved of $\Gamma \sim 0.2$ [7], at least for some ranges of UCP parameters.

In this chapter, I will discuss predictions derived from a simple model of UCP evolution with the effects of electron evaporation taken into account that shows electron evaporation plays a significant role in the evolution of UCPs at *lower* densities. This result is counter-intuitive given the results of evaporative cooling experiments involving ultracold atoms, where higher densities drive higher evaporation rates from a sample of ultracold atoms [8]. Thus, in general effective evaporative cooling is associated with higher densities in ultracold atom systems. The counter-intuitive behavior in ultracold plasmas is due to the fact that the ultracold plasma systems are self-confining because of the space charge imbalance that develops as electrons leave the system. The excess positive charge

that is left behind will serve to help confine the electrons remaining in the UCP. As more electrons escape, this confining potential becomes stronger. At high densities, a little fractional electron loss increases the confinement enough to rapidly prevent a significant fraction of electrons from being lost, truncating evaporation. Therefore, it is expected that evaporation will have a more significant effect on the UCP evolution at low densities.

In addition to presenting the simple model predictions discussed in the previous paragraph, I will also discuss measurements of the expansion of the UCPs in our system that show an expansion rate that is less than what would be expected in the absence of evaporative cooling effects. From this data, we can use models that we developed that take the electron evaporation rate into account to show that evaporative cooling is a reasonable explanation for our observations. By using these models, it is possible to extract the electron temperature evolution in our UCPs in the absence of any heating effects. The temperature evolution of our UCPs shows that it may be possible to achieve strong-coupling parameters for the electron component that exceed the theoretically predicted value of $\Gamma_e \sim 0.2$ in the absence of strong three-body recombination effects. However, while our results are suggestive of a value of $\Gamma_e > 0.2$, measurements of the expansion rate of the UCP are insufficient to determine accurate values of $\Gamma_e$. Therefore, it will still be necessary to develop a local temperature probe that can measure the electron temperature at a specific time in the evolution of the UCP to get an accurate measure of the electron strong-coupling parameter, $\Gamma_e$. One such possible measurement of the electron temperature will be discussed in Chapter 8 of this thesis.

## 5.1 Experimental Background

Since the creation of ultracold plasmas [9], there has been a continual push towards creating UCPs with higher strong coupling parameters in both the ion and electron components. Although disorder-induced heating can initially reduce the amount of strong coupling in the ion component, the strong coupling parameter for the ion component, $\Gamma_i$, can be greater than 1 as the UCP evolves [10]. For one-component ion plasmas, laser cooling of the ions in a Penning trap configuration has produced very high values of the strong coupling parameter, to the point of producing ion crystals [1]. The addition of the electron component to the plasma complicates the physics of the system

through the addition of various heating [2, 3, 5] and screening [6] processes. The most important problem with regard to creating high $\Gamma_e$ UCPs is three-body recombination, which limits the achievable strong coupling for the electron component in UCP systems [7].

Although three-body recombination heating has been observed to have a significant effect on the electron temperature in other UCP systems [2, 3], it is expected to have a negligible effect on the electron temperature for the UCPs created in our system over a wide range of UCP density and temperature conditions. The classical three-body recombination rate per ion is given by [12]

$$K_{TBR}^{tot} \sim 3.8 \times 10^{-9} \cdot T_e^{-9/2} n_e^2 \quad \mathrm{s}^{-1} \tag{5.1}$$

where $T_e$ is the electron temperature in units of K and $n_e$ is the electron density in units of $\mathrm{cm}^{-3}$. One can note here that the three-body recombination rate has a very strong scaling with temperature as $T_e^{-9/2}$. For the range of conditions accessible by our system, we can have initial electron temperatures ranging from $T_e \sim 1 - 400$ K at densities from $n_e \sim 10^7 - 10^8$ $/\mathrm{cm}^3$. At the lowest initial electron temperatures ($T_e \sim 1$ K), the three-body recombination rate can be as high as $2.3{\times}10^8$ $\mathrm{s}^{-1}$, which would give recombination times as short as 25 ns. However, with an increase in the electron temperature to just $\sim$7 K ($\Delta E/k_B \sim 10$ K), the recombination time increases to greater than 150 $\mu$s, which is longer than the lifetime of the UCPs created by our system under all conditions. At higher initial ionization energies, this recombination time increases even further, meaning that we expect negligible contributions from three-body recombination at initial ionization energies above $\Delta E/k_B = 10$ K.

The very fast three-body recombination rate that is calculated for low temperatures would imply that the UCP ions would recombine almost completely into a Rydberg gas on the order of $\sim$1 $\mu$s. However, this is not what is observed in [3] or in our work at low electron temperatures. This can be understood from the $T_e^{-9/2}$ scaling of the three-body recombination rate. As the recombination event occurs, the extra electron will carry away the energy that comes from the binding of the other electron into a Rydberg state with the ion. This will heat the electron component of the UCP, which will increase the temperature. This in turn quickly decreases the three-body recombination rate. This was studied in molecular dynamic simulations in [7] which had good agreement with the results from [3], where the heating from three-body recombination keeps the value of $\Gamma_e \sim 0.2$.

So, even though the classical recombination theory is expected to break down for $\Gamma_e \sim 1$ [13], $\Gamma_e$ is predicted to be limited to below this value in some UCP systems.

The lack of three-body recombination will be very important when studying the effects of electron evaporation in our system. The model that we develop allows us to infer the electron temperature evolution as the UCP expands, which will allow us to calculate both the electron strong coupling parameter, $\Gamma_e$, and the three-body recombination rate as a function of time. Our model shows that electron evaporation may lead to values of $\Gamma_e$ that are greater than the 0.2 limit observed in [3, 7] before the three-body recombination rate become significant. This means that electron evaporative cooling is an excellent candidate for pushing the value of $\Gamma_e$ closer to the strong coupling regime.

Evaporative cooling has been studied extensively in ultracold atom systems [8], as it was the primary means of creating atom clouds with temperatures low enough to form Bose-Einstein condensates when they were first experimentally realized. To increase the influence of evaporation in ultracold atom experiments, it is desirable to have very high densities in the system to increase the collision rates in the ultracold gas. Through the increase in collisions, energy can be transferred to the high energy atoms that can allow them to escape the trap and carry away energy from the system, lowering the temperature of the sample.

While the collision rate of charged particles also increases with the density, it is actually not desirable to have large density plasmas to increase the influence of evaporation in the UCP systems. This is not only owing to the increased effect of three-body recombination in these systems, but also because the self-confining nature of UCP systems limits the amount of evaporation that can take place. As electrons escape the UCP through evaporation, the excess positive charge in the UCP creates a stronger confining potential for the electrons that remain. For higher density UCPs, a smaller fractional amount of charge is required to escape to create the same confining potential for the remaining electrons (i.e. 10 times the density requires 0.1 times the relative charge imbalance to create the same confining potential). This means that the larger fractional electron escape from a lower density UCP will lower the average thermal energy of the remaining electrons more than the higher density case. This implies that it is desirable to work at lower densities in the UCP case which is counter to what is expected from ultracold atom experiments. This increased influence of electron evaporation at lower densities will be shown in detail in this chapter.

The typical models for UCP expansion [2, 7, 14] do not take into account the loss of electrons from the UCP through evaporation and conserve the total energy of the UCP from formation throughout the expansion. They also assume that the electrons are in thermal equilibrium throughout the UCP expansion. The ions are treated as a $T = 0$ fluid, since they have a low thermal energy in comparison to the electrons, with a Gaussian density distribution given by

$$n(r) = \frac{N_{tot}\beta^{3/2}}{\pi^{3/2}} \exp\left(-\beta r^2\right) \tag{5.2}$$

where $N_{tot}$ is the total number of ions in the UCP and $\beta = 1/(2\sigma^2)$, which is defined this way for convenience. The electron distribution is determined self-consistently from a thermal distribution and has a density $n_e \propto \exp(-U/k_B T)$. Since the electrons have a much higher thermal temperature than the ions, the electron distribution will be slightly less dense than the ion distribution. However, the electron distribution will still follow the ion distribution closely, otherwise large electric fields will develop that are inconsistent with the electric field screening present in the UCP. This slight imbalance will create an excess of positive charge throughout space, which gives rise to a radial electric field which will drive the expansion of the ion component of the UCP. This leads to a system of equations that models the transfer of energy from the electron component of the UCP to the ion component as follows

$$\frac{3}{2}Nk_B\frac{dT_e}{dt} = -\frac{3}{4}Nm_{ion}\frac{d}{dt}\left(\frac{\gamma^2}{\beta}\right) \tag{5.3}$$

$$\frac{d\beta}{dt} = -2\beta\gamma \tag{5.4}$$

$$\frac{d\gamma}{dt} = -\gamma^2 + \frac{2\beta k_B T}{m_{ion}} \tag{5.5}$$

Here $\gamma$ is defined by $\vec{v} = \gamma\vec{r}$ which relates the ion velocity to position for a self-similar expansion. Equation 5.3 takes into account conservation of energy as the electrons cool during expansion and transfer all of their thermal energy to ion expansion energy (in the absence of evaporation). Equations 5.4 and 5.5 relate to the ion expansion itself, which will allow us to calculate the expected size of the UCP, $\sigma$, as a function of time for comparisons to our measurements. These equations are only approximate, but do an adequate job of modeling the UCP expansion for the parameters evaluated in [7]. To account for electron evaporation, these equations will need to be modified. This will be discussed in detail in the following section.

## 5.2 Determining the Influence of Electron Evaporation

To determine the effects of evaporative cooling of the electrons on UCP systems, we have to adapt the cold fluid ion models [2, 7, 14] discussed previously to take the evaporation into account. This will mainly affect the energy conservation term given by Equation 5.3, where the escaping electrons carry away energy that will no longer be conserved by the system. The first calculation that we will want to make determines under what conditions (specifically the density) the electron evaporation significantly reduces the amount of expansion energy that can be transferred to the ions.

To start, we need to model the rate of electron evaporation from the UCP for a given set of conditions, which we model after calculations related to the evaporation of antiprotons from a Penning trap configuration [15]. For charged particles in a trap with potential depth, $D$ (in units of temperature), the rate of evaporation is dependent on the number of particles in the trap, $N$, the Spitzer collision timescales, $\tau$ [16], and the ratio of the depth to the thermal temperature of the particles in the trap, $\eta = D/T$. For one dimensional evaporation, the rate of electron escape is proportional to $\frac{\exp(-D/T)}{(D/T)}$. For evaporation in more than one dimension, the power of $D/T$ in the denominator can be changed by 1/2 per dimension (i.e. in the case of three dimensional evaporation the rate is proportional to $\exp(-D/T)$). For the antiprotons in a Penning trap, the magnetic field is strong enough to confine the motion of the protons in one dimension. For UCPs with electrons extracted toward an MCP, the geometry is a bit more complicated. Although the electric field tends to extract electrons in a particular direction from the UCP, the electron escape is not truly one dimensional or three dimensional. So we chose to model the evaporation as being somewhere in between one and three dimensional to have an evaporation rate from the UCP given by

$$\frac{dN}{dt} = -\frac{N}{\tau}\frac{\exp(-D/T)}{\sqrt{D/T}} \tag{5.6}$$

Although precise modeling evaporation rate for our geometry is difficult, we can use our data to confirm that this form for the evaporation rate is reasonable in order to perform calculations under various UCP conditions. We compared the calculated evaporation rate to our evaporation data and observed agreement between our data and the evaporation rate on the 50% level. Using the one dimensional form for the evaporation rate produces worse agreement (factor of 3) between this

calculation and the data. In either case, the exponential term dominates the evaporation rate, which means that the depth will only have to change slightly to correct for differences in the pre-factors of Equation 5.6. This was confirmed by making changes to these pre-factors and observing that these changes produced little change in the results of our calculations of the influence of evaporation on the available expansion energy in the UCP. While Equation 5.6 is useful for making semi-quantitative model predictions on the relative influence of evaporation, when making comparisons to our data in the following sections we use our measured evaporation rate as detected by our MCP. This will help us to increase the accuracy of the model when making comparisons to our data.

The second part of our modifications to the expansion model determines how changes in the UCP electron number affect the potential well depth, $D$, of the UCP. To do this, we can calculate the how much $D$ changes per electron removed by using a $T = 0$ distribution in an external electric field. In a $T = 0$ distribution, the electron and ion densities match exactly in the central region of the UCP. For finite (but low) temperature electrons, there is a slight offset in the electron and ion densities that can be ignored for the purposes of this calculation. The electrons that leave the UCP are generally considered to escape from the outer part the electron distribution, with the remaining electrons being concentrated in the center of the ion distribution. This separates the UCP into two parts: the first part being ions and electrons in the inner part of the charge distribution and the second part being the unscreened ions in the outer part of the charge distribution. The inner part of the distribution is considered to be well screened from external fields and expands in a way that is governed by the equations that we developed for this model. The evolution of the outer part of the ion distribution is governed by the Coulomb force. The Coulomb force can produce large electric fields that can cause a rapid, outward expansion of the outer ions. This is known as the "Coulomb explosion" and has been observed in UCP systems in [17]. Owing to a combination of spherical symmetry and Debye screening, the "Coulomb explosion" of the outer ions should not have an effect on the inner part of the UCP.

As electrons escape the UCP, the inner part of the UCP distribution becomes smaller relative to the UCP as a whole. In general, this changes how one might characterize the size of the UCP. However, as discussed in Chapter 4, our measurements are of the peak density of the UCP. This peak density measurement can then be translated into a spatial extent of a Gaussian distribution through the relation $\sigma = [N_{ion}/(2\pi)^{3/2} n_{peak}]^{1/3}$.

For the conditions under which we used the model, we can approximate the change in $D$ per electron removed as a constant, $\alpha$, which allows us to write the following equation which relates the change in depth to the rate of evaporation as

$$\frac{dD}{dt} = -\alpha \frac{dN}{dt} \tag{5.7}$$

For our model conditions, the size of the UCP changes by less than 10% during the time that energy loss from evaporation is still significant, which makes the approximation of constant $\alpha$ reasonable. To calculate $\alpha$, we start with a $T = 0$ UCP distribution in an external electric field with a charge imbalance that creates a potential well depth, $D$, that is just deep enough to trap electrons with a kinetic energy that is equal to the initial ionization energy, $\Delta E$. From this initial distribution, we can calculate the change in depth after removing a single electron from the UCP to find $\alpha$. The value of $\alpha$ will depend on the UCP spatial extent, $\sigma$, and the strength of the external electric field. The value of $\alpha$ was computed for each condition for which we calculated the effect of evaporation.

The last modification to the expansion model that we make concerns the conservation of energy equation given by Equation 5.3. As electrons leave the UCP, they will carry away energy that can no longer be used to drive the expansion of the ions. The electrons that leave must carry away an energy that is at least as great as the potential well depth, $D$, that prevents other electrons from escaping. If the electrons leave with higher than the average thermal energy of the electrons remaining in the UCP, then the temperature of the electrons will decrease as the electrons escape. We can change Equation 5.3 as follows

$$\frac{3}{2} N k_B \frac{dT_e}{dt} = \left( k_B D - \frac{3}{2} k_B T_e \right) \frac{dN}{dt} - \frac{3}{4} N m_{ion} \frac{d}{dt} \left( \frac{\gamma^2}{\beta} \right) \tag{5.8}$$

Here, the evaporation term, $k_B D - 3k_B T_e/2$, takes into account the relative energy of the escaping electron as compared to the thermal average energy of the electron cloud. Since all of the escaping electrons come from the top of the electron energy distribution in order to have enough energy to escape from the confining potential, escaping electrons will always lower the average energy of the electron cloud for any reasonable value of $D$.

To evaluate the effect of evaporation on expansion, we can integrate our new system of equations given by Equations $5.4 - 5.8$ to calculate the energy loss as given by $\frac{dN}{dt}\left( D - \frac{3}{2} T_e \right)/N$. This calculation will allow us to evaluate the fraction of energy that is lost that can no longer be

transferred to ion expansion. The $3/2T_e$ factor in the energy loss equation is necessary in order to properly account for the fact that we are considering the expansion of the UCP in the presence of the loss of electrons. If the electrons escaped at a depth, $D$, equivalent to $3/2T_e$, then evaporative cooling would have no effect because the average energy of the UCP electrons are never affected by the evaporation. We integrate our system of equations in time until the loss owing to evaporation becomes small (less than 5%) as the integration time window is increased significantly. During this time, the UCP expands by less than 10%.

By integrating Equations $5.4 - 5.8$, we are able to determine under what UCP size and density conditions evaporation will have a significant effect on the expansion energy of the UCP. The results of these calculations under two different UCP size conditions for a range of densities can be seen in Figure 5.1. Here, we can see that our model has confirmed our general prediction that evaporation will have a more significant effect on the loss of available expansion energy at lower densities. However, we can note that the loss owing to evaporation is not strictly a function of the UCP density, as a change in the spatial extent, $\sigma$, from 0.8 to 0.3 mm shifts the curve to higher densities on the graph. The trend in density does hold qualitatively though, in that decreases in the UCP size at constant ion/electron number and increases in the ion/electron number at constant size *decrease* in the influence of evaporation on the UCP expansion energy.

From this model, we also confirmed that the amount of energy that leaves the UCP through evaporation is a slowly varying function of the density as can be noted by the logarithmic scaling of the density on the horizontal axis in Figure 5.1. We attribute this slow variation in the energy lost as a function of density to the exponential term in Equation 5.6. Although small changes in the density (e.g. factor of 2) will initially have a large effect on the evaporation rate of the UCP given by Equation 5.6, where the number, $N$, and Spitzer time, $\tau$, will work to increase the evaporation rate, the depth, $D$, will also increase faster which will work very quickly to lower the evaporation rate. This will, in effect, work to decrease the fractional energy loss as the UCP evolves, which lowers the effect of evaporation on the UCP expansion as the density increases.

In addition to comparing trends for different UCP sizes, we also were able to compare the calculated decrease in UCP expansion energy from our model to the UCP size and density conditions from other experiments [2, 18]. We performed these calculations to show that we expected evaporation to be more important for our conditions at low density and that it could be ignored for

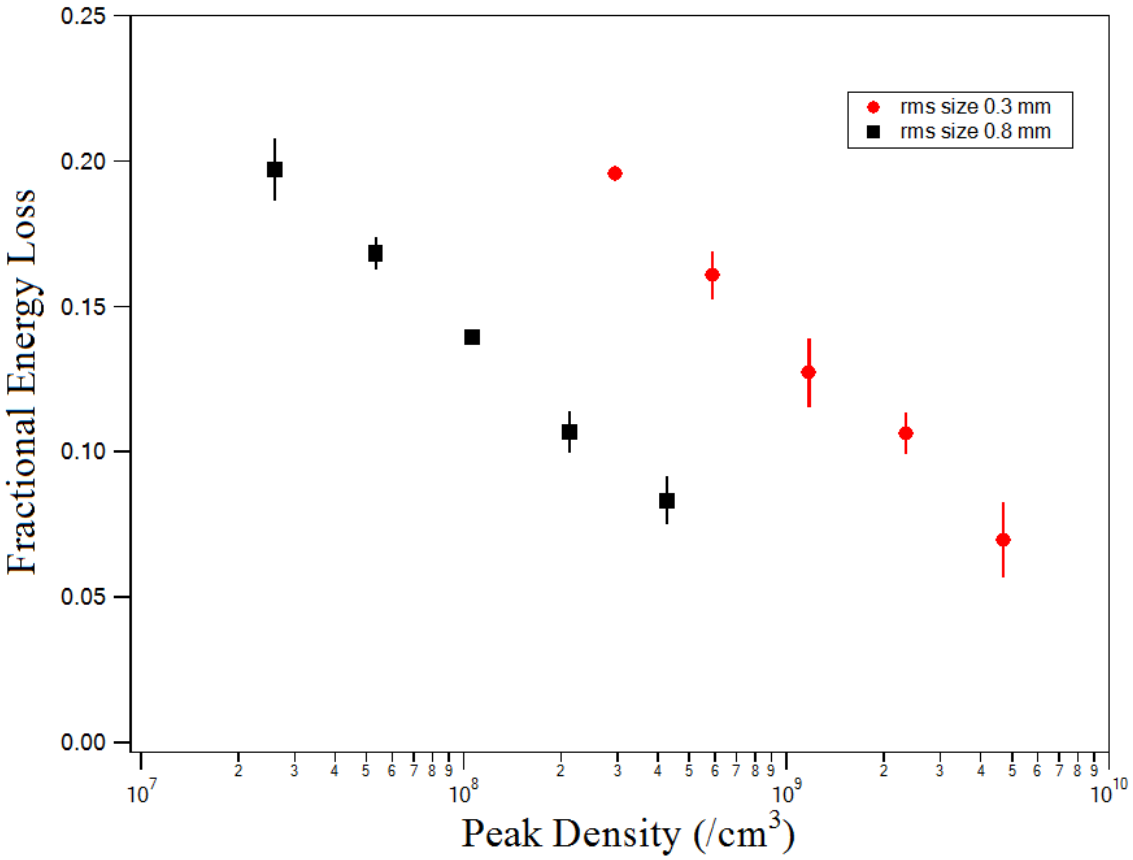


Figure 5.1: Calculations from our simple model that show the fractional amount of expansion energy that is lost owing to evaporation. The black squares show the density scaling at $\sigma = 0.8$ mm for the UCP. The red circles show the density scaling for 0.3 mm. The horizontal lines on each of the data points show the range of energy lost for the same initial density conditions for $\Delta E/k_B = 25 - 75$ K. The scaling of the energy lost as a function of density varies slowly, as can be seen from the log scale on the bottom axis of this graph. One can see however that the energy lost is not strictly a function of the density, as changes in the value of $\sigma$ at the same density can affect the influence of evaporation. However, it still shows the same decreasing trend in the influence of evaporation on the UCP as the density is increased at that size.

the analysis of the UCP expansion in their systems. This was indeed the case, where the expected decrease in expansion energy for our experimental conditions was twice that of [18] and nearly twenty times that of [2]. These model calculations strongly suggest that modeling our expansion with evaporation will be essential for properly accounting for the energy transfer to the ions to match our observed expansion data, as will be shown throughout this chapter.

## 5.3 Measuring the UCP Expansion Rate

To measure the effect of electron evaporation on the UCP, we used our UCP density determination technique discussed in Chapter 4 to measure the expansion rates of the UCPs in our system. Using this technique, we can measure the peak density over a range of chosen times in the UCP evolution. From the peak density, $n_{peak}$, and the total ion number, $N_{tot}$, we can determine the time variation of characteristic spatial extent of the UCP from $\sigma = (N_{tot}/(2\pi)^{3/2} n_{peak})^{1/3}$. This will allow us to make comparisons of our observed UCP expansion rate to what would be predicted without any effects from electron evaporative cooling.

If there was no significant effect on the electron temperature owing to electron evaporative cooling, then we would expect that nearly all of the electron thermal energy would be converted to ion expansion energy as the UCP evolves. In the absence of three-body recombination, the expected expansion rate of the UCP can be calculated easily by assuming a self-similar expansion of a spherical, Gaussian UCP with a density distribution given by

$$n(r,t) = \frac{N_{tot}}{(2\pi)^{3/2}\sigma(t)^3} \exp\left(-\frac{r^2}{2\sigma(t)^2}\right) \tag{5.9}$$

Here, $\sigma(t)$ is given by $\sigma(t) = \sqrt{\sigma_0^2 + v^2 t^2}$, where $\sigma_0$ is the initial size of the UCP and $v$ is the asymptotic expansion velocity. If all of the electron thermal energy is converted into ion expansion energy, the asymptotic expansion velocity can be found from the initial ionization energy as $v = \sqrt{2\Delta E/3m_i}$, where $m_i$ is the mass of an $^{85}$Rb ion.

To compare the predicted evaporation-free expansion to our observed UCP expansion, we measured the UCP expansion for $\Delta E/k_B = 25 - 75$ K as seen in Figure 5.2. Unfortunately, for the range of conditions accessible by our system, there was only a small range of initial ionization energies that could be explored while maintaining the validity of our models. For initial ionization

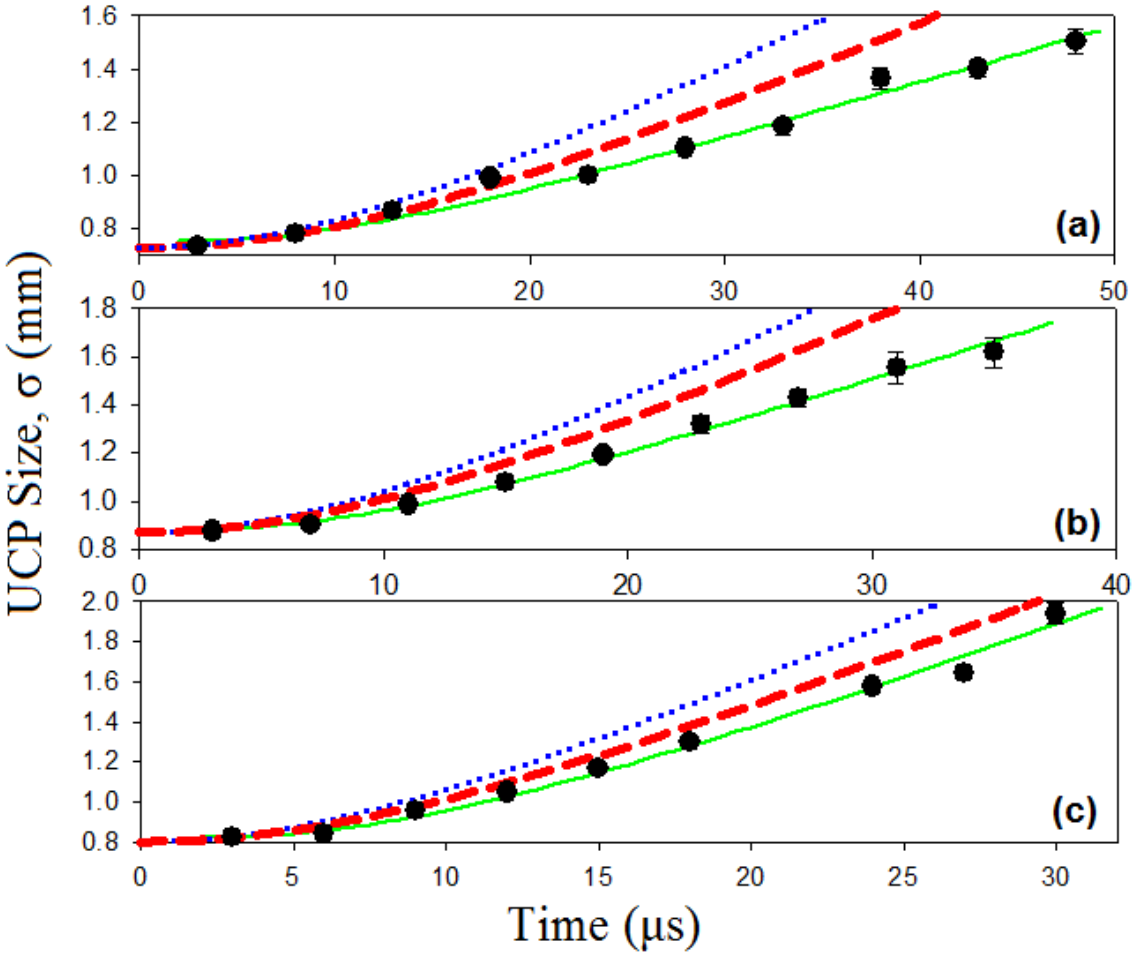


Figure 5.2: An example of the UCP expansion for $\Delta E/k_B = 25$, 50, and 75 K for (a), (b), and (c) respectively ($2.5\times10^5$ total ions). The black dots show the measured data, where the size of the data points has been increased for clarity. If error bars cannot be seen, then the error is on the order of or less than the symbol size. The blue, dotted lines show the predicted expansion for a full conversion of the initial ionization energy to UCP expansion energy. The red, dashed lines show this same prediction with 20% of the initial energy removed by evaporation during the formation of the UCP. The green, solid line shows a fit to our data using the model of UCP expansion with evaporation after expansion taken into account. We can see from these data that the actual expansion curves fit better when we model the expansion with evaporation both during and after formation.

energies higher than these values, the assumption of thermal equilibrium for the electrons in the UCP is questionable since the predicted electron self-equilibration times can be on the order of the UCP lifetime [16]. For lower initial ionization energies, the effects of three-body recombination can become significant, which would counteract the effects of evaporation that we are trying to study and add significant complications to the analysis of the data.

The results of our measurements of the expansion can be seen in Figure 5.2 for $\Delta E/k_B = 25$, 50, and 75 K. In each case, the measured expansion rate falls well below what is expected if all of the initial ionization energy is converted to ion expansion energy. This implies that electron evaporation does play a significant role in the UCP expansion and evolution. This leads to a question of whether most of the effect of evaporation occurs during the formation of the UCP, when a substantial fraction of the electrons can escape quickly, or if there is a larger influence from evaporation after the formation when the electrons escape during the later part of the UCP expansion. To explore this question, we developed a set of model calculations that can use our electron escape data from our MCP signal to calculate the amount of energy that leaves the UCP during formation and during the subsequent expansion. The results of this analysis are discussed in the following section.

## 5.4 Calculating the Effects of Electron Evaporation on the UCP Expansion

The measurements of the UCP expansion in the previous section show that expansion energy of the UCPs created in our system are less than what would be expected for the given photoionization energy. While this shows qualitatively that expansion energy is lost from the system, we performed further analysis on this expansion data using our simple model to show that electron evaporative cooling is a reasonable explanation for the observed expansion behavior. To do this, we can break up the model into two parts. The first part of the model examines the effects of evaporation during the formation of the UCP and the second part of the model examines the effects of evaporation during the expansion of the UCP. It is convenient to separate the model in this way because the UCP conditions during the formation stage are more straightforward to calculate, as there is not enough time for significant changes in the ion distribution to take place. This allows us to calculate

the depth of the potential well that is formed from the excess of ions that results from electrons escaping from the initial ion distribution in an external electric field as will be discussed shortly. As the UCP begins to evolve, space charge effects such as the "Coulomb explosion" can affect the potential depth in such a way that makes it difficult to calculate precisely. At this time in the UCP evolution, using an average potential well depth to temperature ratio allows us to extract the general behavior of the effects of evaporation on UCP expansion sufficiently. In both calculations, we use our actual UCP evaporation data seen in Figure 5.3 in the place of Equation 5.6 to more accurately model the UCP evolution.

### 5.4.1 Electron Evaporation During UCP Formation

The first part of our calculations examine the amount of energy that is removed from the electron component of the UCP owing to evaporation during the UCP formation. For the purposes of this calculation, we define the formation stage of the UCP as the first 2 $\mu$s after the initial ionization. During this time period, there is a large amount of electron escape during the prompt peak and subsequent evaporation as the UCP electrons thermalize. At the end of formation period, the electron evaporation rate is reduced to near the evaporation levels of the subsequent expansion.

Upon formation, the UCP electrons will have an energy that is approximately equal to the initial ionization energy, $\Delta E$ (see Chapter 3). In the presence of an extraction electric field, a minimum number of electrons are required to escape the UCP until there is a sufficient charge imbalance to create potential well that is able to confine the remaining electrons in the UCP. As this potential well is created, the electrons that escape the UCP must have an energy that is at least as high as the potential well barrier or else they will be confined inside the UCP. The potential well depth can become several times the initial ionization energy, meaning that as the electrons thermalize, they can reduce the average energy per electron remaining in the UCP, lowering the effective electron temperature.

The formation stage is unique in that there is not a significant amount of time for any ion dynamics to occur that may arise later in the UCP evolution. Therefore, we can approximate the potential well depths by directly integrating the electric fields that result from the initial ion distribution, which we approximate as a spherical Gaussian distribution given by $n(r) = n_0 \exp(-r^2/2\sigma^2)$. For this calculation, we have to take a different approach than what was used to calculate the number

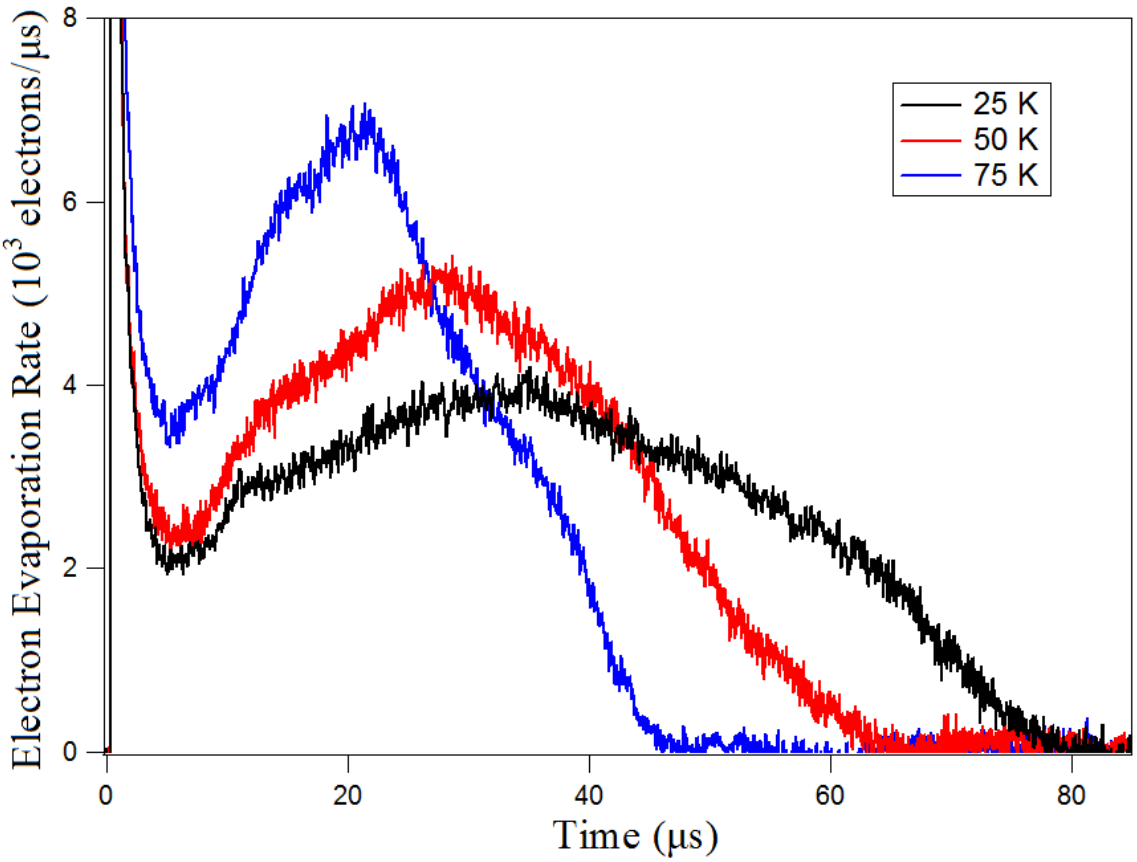


Figure 5.3: Example electron evaporation traces as detected at our MCP for $\Delta E/k_B = 25$ (black), 50 (red), and 75 (blue) K. One can see that as the initial ionization energy increases that the initial evaporation rate increases, reducing the overall lifetime of the UCP.

and electric field calibrations from Chapter 3. Here, we have to consider a UCP with a substantial fraction of the electron component remaining, which means that the effects of electron screening need to be taken into account. To do this, we use a $T = 0$ approximation where the electron and ion densities are equal from the center of the charge density distribution up to a cutoff radius that sets the charge imbalance. So, to find the cutoff radius, we can integrate the density distribution as follows

$$\delta = 1 - \int_0^{r_c} \frac{4\pi r^2}{(2\pi)^{3/2}\sigma^3} \exp\left(-\frac{r^2}{2\sigma^2}\right) dr \tag{5.10}$$

where $\delta$ is the charge imbalance, defined as the fraction of electrons that have escaped the UCP, and $r_c$ is the corresponding cutoff radius of the charge distribution. The cutoff radius, $r_c$, can be solved for numerically for a given value of the charge imbalance, $\delta$, and for a known size of the UCP, $\sigma$. To find the electric field resulting from this charge distribution, we can simply use Gauss' law, where only the unmasked ion charge contributes to the electric field from the UCP charge distribution. So, we can find an express for the total charge inside a radius $r$ for our charge distribution as

$$Q_{enc}(r) = \frac{4\pi N_{tot} e}{(2\pi)^{3/2}\sigma^3} \begin{cases} 0 & r \leq r_c \\ \displaystyle\int_{r_c}^{r} r^2 \exp\left(-\frac{r^2}{2\sigma^2}\right) & r > r_c \end{cases} \tag{5.11}$$

where $e$ is elementary charge, and $N_{tot}$ is the total number of ions in the UCP. This contribution to the field is from the unmasked ions alone. So, we need to take into account the effects of the external field on the UCP. Not only does this field contribute to the DC field outside the UCP, but it also alters the charge distribution of the electrons slightly as they move to screen this external field. Since the main effect of the external electric field is an offset of the electron and ion distributions, we can add a correction term to the net outside electric field in the form of an electric dipole to a lowest order approximation. To perform this approximation, we can consider a conducting sphere in an external electric field. This approximation of a conducting sphere stems from a $T = 0$ UCP, in which the external fields are perfectly screened inside the cutoff radius, $r_c$. This consideration produces a dipole electric field given by [19]

$$E_{dip} = \frac{2E_{ext} r_c^3}{r^3} \tag{5.12}$$

for the electric field on the axis of the dipole. This produces a total electric field that is given by

$$E_{tot}(r) = \begin{cases} 0 & r \leq r_c \\ \dfrac{Q_{enc}}{4\pi\epsilon_0 r^2} - E_{ext}\left(1 + \dfrac{2r_c^3}{r^3}\right) & r > r_c \end{cases} \tag{5.13}$$

To find the potential well depth in temperature-equivalent units we can integrate the electric field from the center of the UCP to get

$$U(r) = \frac{e}{k_B}\int_0^r E(r)dr \tag{5.14}$$

By finding the maximum potential we can calculate the total depth as a function of charge imbalance, $\delta$, for a set of UCP conditions. This will allow us to calculate how much energy is removed during the UCP formation stage.

To make the calculations for this model, we used our actual UCP electron escape signals, examples of which are seen in Figure 5.3. To calculate the energy removed from the UCP, we divided the calculation into discrete time steps of 400 ps, which was set by the sampling rate of our oscilloscope. During each time step, a certain number of electrons leave the UCP at a given potential well depth, $D$. As the electrons leave the UCP, they change the value of $D$, which is then recalculated for each time step with a new value of $\delta$ as seen in Figure 5.4. If $D < 0$, then no potential well is formed because there is not enough of a charge imbalance to overcome the external electric field. This part of the formation process typically lasts less than 100 ns, which is less than the electron-electron thermalization times for all of the UCP conditions that will be discussed in this chapter [16]. For this part of the formation process, we assume that the electrons escape the UCP with energy equal to $\Delta E/k_B$. For $D > 0$, the electrons must have an energy that is greater than $k_B D$ to escape the UCP. For this part of the formation process, we assume that the electrons escape the UCP with energies ranging between $k_B D$ and $k_B D + \Delta E$, which represents a reasonable range of likely electron escape energies.

To calculate the effective electron temperature after formation, we calculated the total amount of electron energy remaining in the UCP after formation and divided it by the number of electrons remaining in the UCP. We performed these calculations using data from UCPs with initial ionization energies ranging between $\Delta E/k_B = 25 - 400$ K and $(2.5 - 5) \times 10^5$ total ions. The results of these calculations showed that for the lower end of our total ion number ($\sim 2.5 \times 10^5$ ions), electron

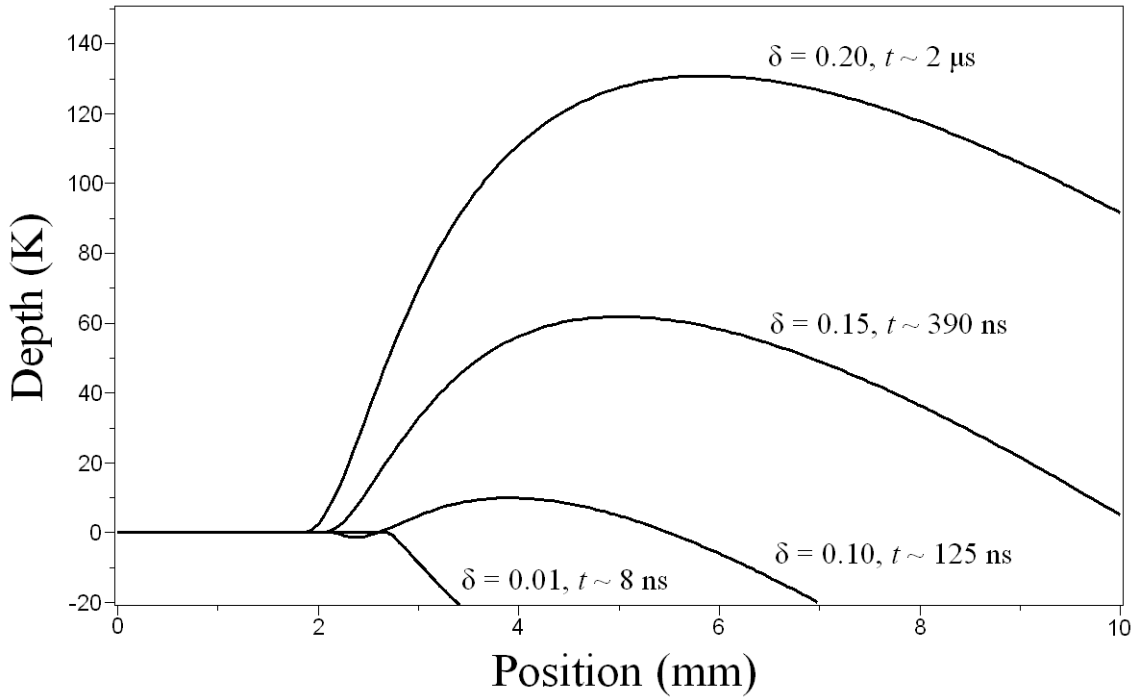


Figure 5.4: The evolution of the UCP potential depth during the UCP formation ($t \leq 2$ $\mu$s) on axis, parallel to the applied electric field (2 V/m) in units of temperature as calculated from a $T$=0 model of the electron and ion distributions. As electrons escape during the formation of the UCP, the increasing charge imbalance creates potential well depths that increase. The electrons that escape later must have a greater energy than the initial escaping electrons in order to overcome this potential well barrier. This process decreases the amount of energy that remains in the UCP that is available for expansion. The flat region at small distances from the center of the UCP is the region where the external field is assumed to be screened. These calculations included a dipole electric field term resulting from the offset of the electron cloud from the ions to screen the external field. These calculations were taken from data with $\Delta E/k_B = 50$ K, $2{\times}10^5$ total ions, and $\sigma = 850$ $\mu$m.

evaporation during UCP formation removed $13-25\%$ of the energy available for expansion as seen in Figure 5.5 (a). The vertical lines in Figure 5.5 show the range of fractional energy reduction over different data sets with electrons escape energies ranging from $k_B D$ to $k_B D + \Delta E$ as discussed above. At higher total ion number ($\sim 5\times10^5$ ions), a smaller fraction of electrons leave the UCP during formation. This also corresponded to a lower fractional energy loss from the UCP, in a range of $8-12\%$ as seen in Figure 5.5 (b).

To better understand the energy loss during formation, we can also use these calculations to determine the depth to temperature ratio, $D/T$, after the formation of the UCP as seen in Figure 5.6. These calculations show that as the initial ionization energy increases, $D/T$ decreases in value both for $2.5\times10^5$ and $5\times10^5$ ions. This means that energy removed per electron is fractionally higher for the low initial ionization energy case. We can also see that as the initial ionization energy increases, that the value of $D/T$ can become very low (less than 2). This trend is consistent with the expected increase in the thermalization times for the electrons in our UCPs as the initial ionization energy increases. These thermalization times can become on the order of the lifetime of the UCP, meaning that a true thermal equilibrium cannot be reached. This means that the UCP will not have a sufficient collision rate that can sustain electron evaporation to create large values of $D/T$ in these conditions.

### 5.4.2 Electron Evaporation After the UCP Formation

When comparing our measured expansion rate to the predicted expansion with a full conversion of the initial ionization energy to ion expansion energy, we observed significantly less expansion for our data as seen in Figure 5.2. This observation led to the development of a model for determining the energy reduction that takes place owing to evaporation during the UCP formation. This energy reduction was calculated to be between $13-25\%$ for a total ion number of $\sim 2.5\times10^5$ ions. When taking this loss of energy into account, the measured expansion rate was still lower than what was predicted by this calculation for each initial ionization energy that we were comparing between $\Delta E/k_B = 25-75$ K. This comparison implied that there was still more expansion energy that was lost owing to evaporation after the initial formation of the UCP. Since the dynamics of the outer ions are complicated after the formation of the UCP, we cannot easily calculate the amount of energy that leaves the UCP through evaporation explicitly even at the level of approximation

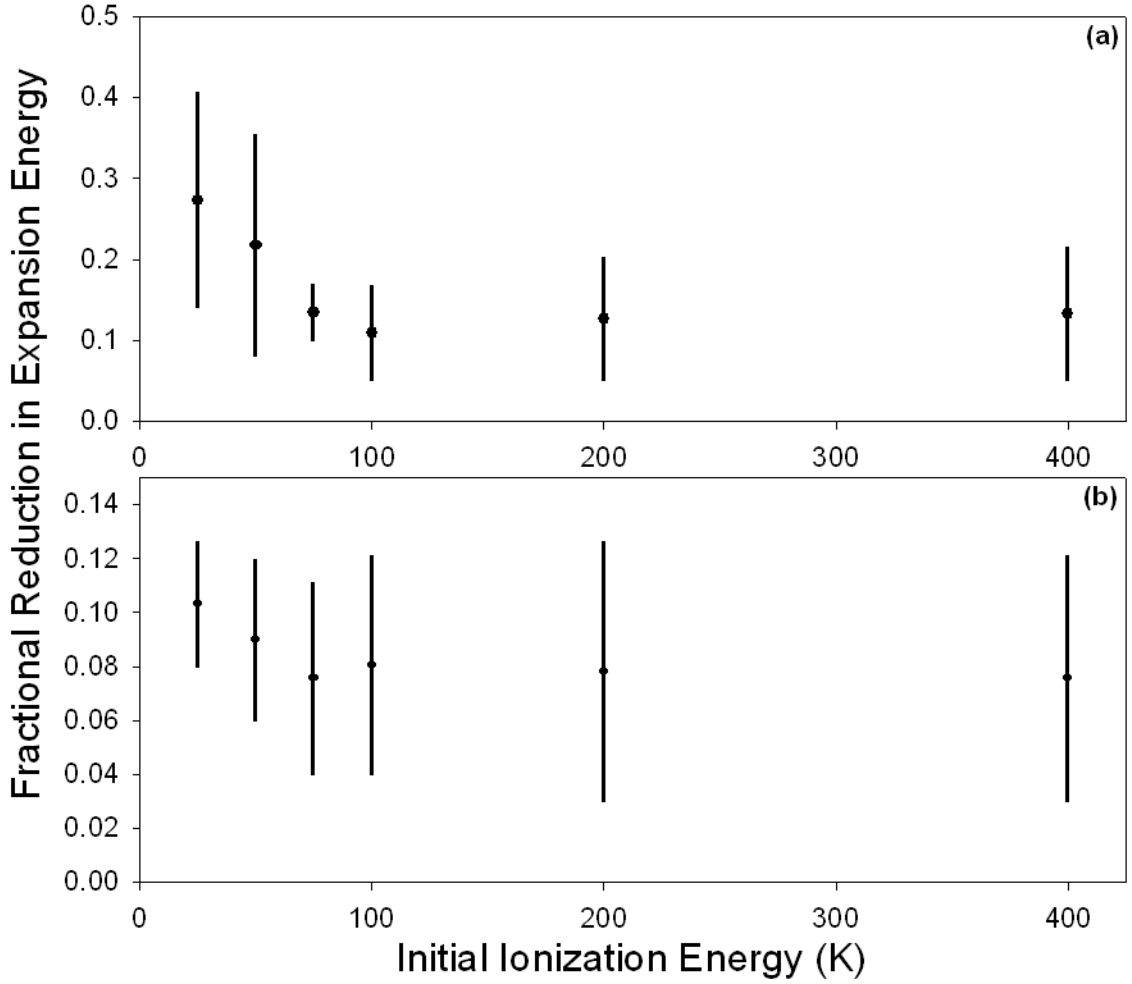


Figure 5.5: Fractional energy removed during UCP formation over a range of initial ionization energies ($\Delta E$) for (a) $2.5\times10^5$ ions and (b) $5\times10^5$ ions. The vertical lines represent the range of energy removed for electron escape energies from $k_BD$ to $k_BD + \Delta E$ as discussed in the text. At low initial ionization energies, there is a slight increase in the fractional energy removed, which is due to an increase in the depth to temperature ratio during formation at low initial ionization energy as seen in Figure 5.6.

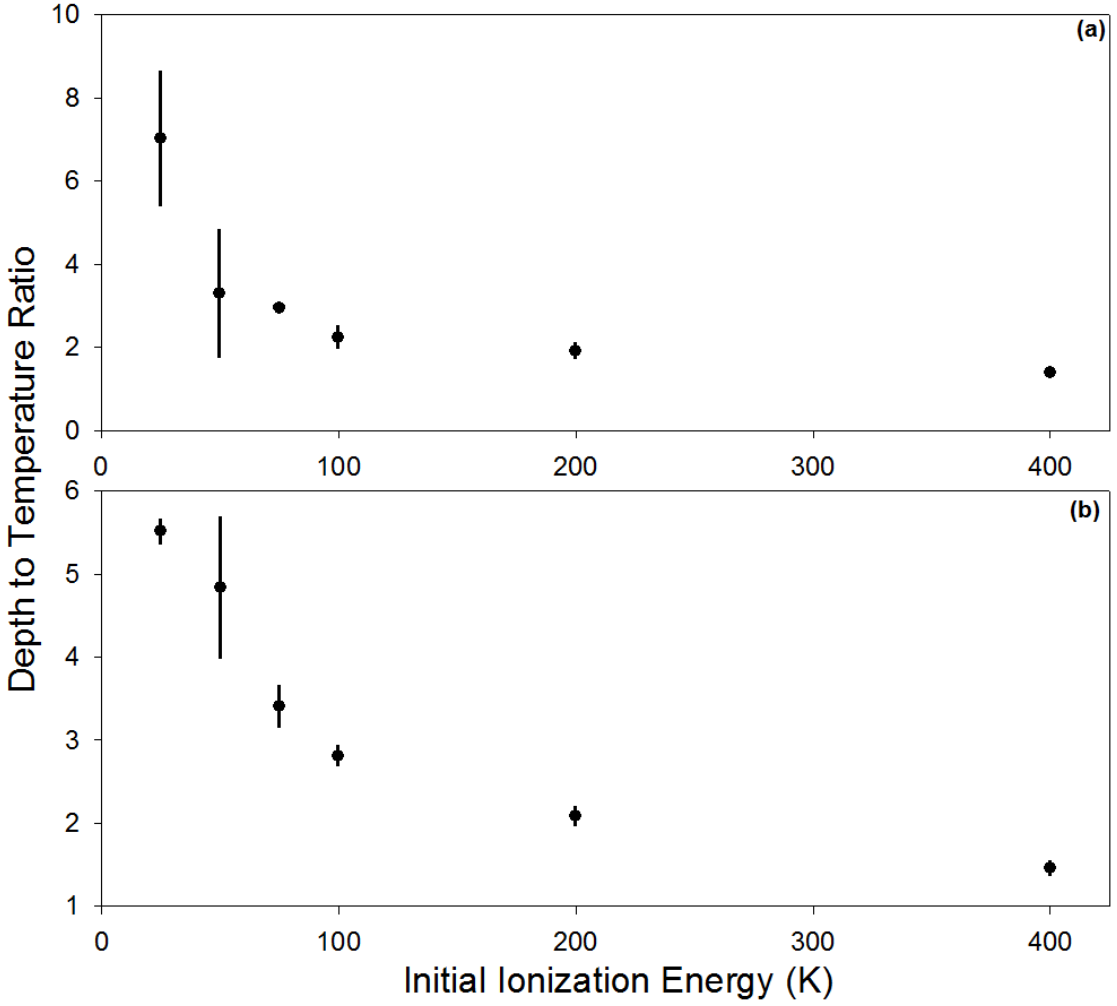


Figure 5.6: A plot of the calculated depth to temperature ratio, $D/T$, over a range of initial ionization energies for experimental data at (a) $2.5\times10^5$ ions and (b) $5\times10^5$ ions. The vertical lines represent the range of energy removed for electron escape energies from $k_BD$ to $k_BD + \Delta E$ as discussed in the text. These calculations show that the depth sharply decreases with increasing ionization energy at low initial ionization energy and then levels off at higher energies. The fractional energy removed during formation for these data is seen in Figure 5.5.

used in the previous section. The "Coulomb explosion" of the outer ions can alter the depth in ways that require much more sophisticated modeling. To model the evaporation after the formation stage, we can modify the model discussed in Section 5.2 to not only use our measured evaporation rate (Figure 5.3) in the place of Equation 5.6, but also an average depth to temperature ratio after formation in the place of the explicit depth calculation. By doing this, we can fit our data to this model by varying the value of this average depth to temperature ratio, which will allow us to understand the general behavior of evaporative cooling in our system.

The measured evaporation rate, $dN(t)/dt$, is fit to a polynomial for $t > 2$ $\mu$s before being input into the model equations. For the data shown in Figure 5.2 ($2.5\times10^5$ ions), we reduce the initial energy of the UCP by 20% to reflect the amount of energy that is lost through the UCP formation process. At this point we can begin to integrate Equations 5.4−5.8 to produce a predicted expansion curve for the UCP with the assumption of an average depth to temperature ratio which can be compared to our data. We can then compute the error of our fit to the data by using a $\chi^2$ fitting technique which takes into account the weighted error of each of the individual data points in Figure 5.2. To find the best fit to our data, we alter the initial size, $\sigma(0)$, and the average depth to temperature ratio, $D_{avg}/T$, until we minimize the value of $\chi^2$. The error in the fits can then be determined by calculating how changes in the UCP parameters change the value of $\chi^2$, where the error bar is typically set in this type of fitting by increasing the value $\chi^2$ by 1.

The results of these calculations found average potential well depth to temperature ratios of 5.4±0.4, 4.7±0.5, and 2.1±0.2 for $\Delta E/k_B = 25$, 50 and 75 K for the data seen in Figure 5.2. In Figure 5.2, these fits are represented by the green curves, which shows good agreement between our model and the data for reasonable values of $D_{avg}/T$. The values found for $D_{avg}/T$ over this range of $\Delta E/k_B$ also show a consistent trend when compared to the values of $D/T$ found from the UCP formation calculation, in that $D/T$ decreases with increasing $\Delta E/k_B$. Also, as noted earlier in this chapter, these values of $D_{avg}/T$ produce evaporation rates that are consistent with our measured evaporation on the 50% level. The exponential dependence of the evaporation rate on the value of $D_{avg}/T$ makes it difficult to match our observations to these calculated rates with more precision, but this degree of agreement does indicate that electron evaporative cooling is a reasonable explanation for our observed decrease in the UCP expansion rate.

For higher densities in our system ($\sim 5\times10^5$ ions, $\sigma \sim 750\mu$m), we do not observe a significant difference in the overall expansion rate of the UCP as seen in Figure 5.7. Our model calculations from Section 5.2 indicate that a factor of 2 change in the density would only change the fraction of energy removed through evaporation for our conditions by a few percent (see Figure 5.1). These observations indicate that larger changes in the UCP density are necessary to alter the effect of evaporation in our system, which requires significant changes to our experimental apparatus. Such studies were beyond the scope of this work.

## 5.5 Temperature Evolution of Expanding Ultracold Plasmas

When using our models to track the energy loss of the UCP through electron evaporation, we are able to track the electron temperature evolution as the UCP expands, under the assumption that the UCP maintains thermal equilibrium. For the lower initial ionization energy conditions that we measured, the Spitzer self-equilibration timescales for the electrons are on the order of 1 $\mu$s or less [16], which means that the UCP will come into thermal equilibrium early in the UCP evolution. So, by using our measurements of the UCP expansion under these conditions, we can calculate the evolution of the electron temperature for our UCPs. These calculations will allow us to determine other useful parameters of the UCP such as the strong-coupling parameter [1], and the predicted three-body recombination rate [12]. Since we use an average depth to temperature ratio when modeling our UCP expansion, these calculations will only produce estimates of the electron temperature evolution and therefore estimates of the other parameters of interest. To get an accurate measure of the electron temperature, we will still need to develop a measurement technique for the temperature of the UCP at a specific point in the evolution as in [20]. However, as our estimates will show, there is potential for producing UCPs with electron strong-coupling parameters that exceed the 0.2 theoretical limit shown in [7] before the three body recombination rate becomes significant for our UCP conditions.

The temperature evolution for the expansion data from Figure 5.2 at $\Delta E/k_B = 50$ K can be seen in Figure 5.8. Here the solid, red curve is the temperature evolution taken from our model where the dotted, black curve is the temperature evolution that would be expected without the effects of evaporation (adiabatic expansion only). It can be seen here that with evaporation included

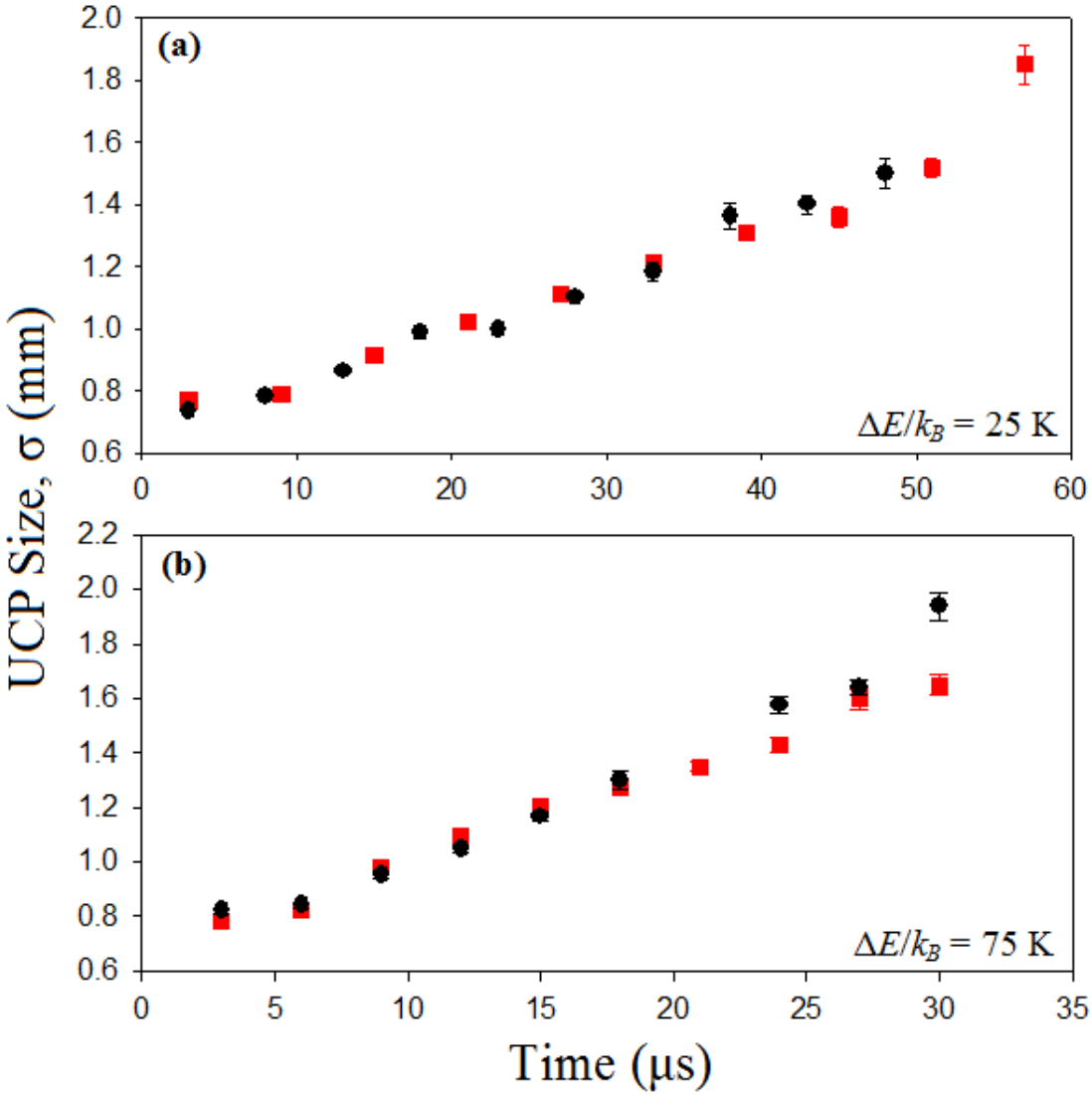


Figure 5.7: A comparison of the UCP expansion for $N_{tot} = 2.5\times10^5$ (black circles) and $N_{tot} = 5\times10^5$ (red squares) for (a) $\Delta E/k_B = 25$ K and (b) $\Delta E/k_B = 75$ K. One can see that the expansion curves do not differ significantly for the majority of the data. At late times, there is a slight deviation that is at this time unaccounted for in (b) but we observe good matching between the expansion curves at early times when the effect of evaporative cooling is still important. This implies that a larger change in the density is required to observe a significant change in the expansion behavior as predicted by the general trends of our simple model.

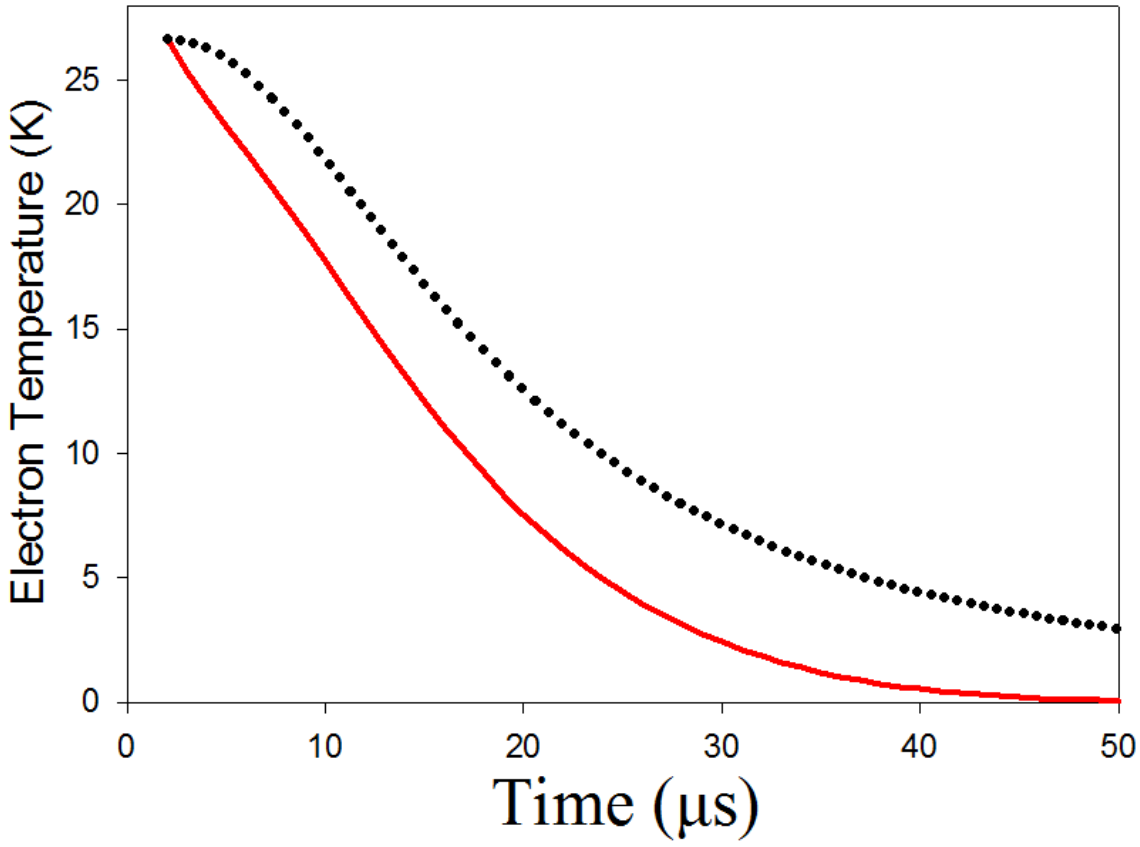


Figure 5.8: An example of the electron temperature evolution as the UCP expands for $\Delta E/k_B = 50$ K as seen in Figure 5.2 (b). The black, dotted curve shows the evolution of the electron temperature when only taking into account the reduction in temperature owing to adiabatic expansion. The solid, red line shows the temperature evolution when electron evaporative cooling is taken into account. It can be seen here that when electron evaporation is taken into account, that the temperature of the electrons in the UCP falls much more rapidly, and approaches zero near the end of the UCP evolution.

in the model for the expansion, that the temperature decreases much more rapidly than the case without evaporation. At late times in the evolution, the temperature of the electron in the UCP can approach very low values (close to 0 K), which is promising from the perspective of creating strongly coupled electrons. However, it should be noted that any small heating effects that would keep the electron temperature from falling too low would be difficult to observe in our expansion data. The expansion energy of the UCP at this point would be much higher than the small amount of energy that would be added from three-body recombination heating.

Although small heating rates would be difficult to measure by using the model that we developed, we can use the electron temperature evolution combined with our measurements of the UCP density to calculate the three-body recombination rate (Equation 5.1) and the electron strong coupling parameter as a function of time as seen in Figure 5.9. In this figure, we plot the inverse of the three-body recombination rate (recombination time) which shows how much time we expect to elapse for a recombination event to take place for a particular ion at the given density and temperature conditions. This plot shows that the electron strong coupling parameter can be as high as $\Gamma_e \sim 0.5$ before the three-body recombination time is on the order of $\sim 1\mu$s, where heating from three-body recombination is expected to be significant.

This potential increase in $\Gamma_e$ over the 0.2 limit discussed in [7] gives us exciting prospects for exploring ultracold plasma physics with $\Gamma_e$ near the strong-coupling regime. As $\Gamma_e$ approaches 1, many theoretical descriptions of processes in UCPs are expected to break down. For example, the three-body recombination rate scaling of $T^{-9/2}$ cannot hold for all temperatures down to zero temperature. As the temperature goes to zero, the motion of electrons decreases to the point of making recombination events unlikely.

## Conclusion

In this chapter, I discussed the importance of electron evaporative cooling when modeling the UCP expansion for our UCP size and density conditions. We developed a model of electron evaporation that tracked the energy loss of the UCP owing to electrons escaping with finite energy from a potential well caused by the excess of ions in the UCP. From this model, we were able to determine the UCP conditions under which we should expect a significant influence from electron evaporation on the UCP evolution. In each case, we determined that the effect of evaporation

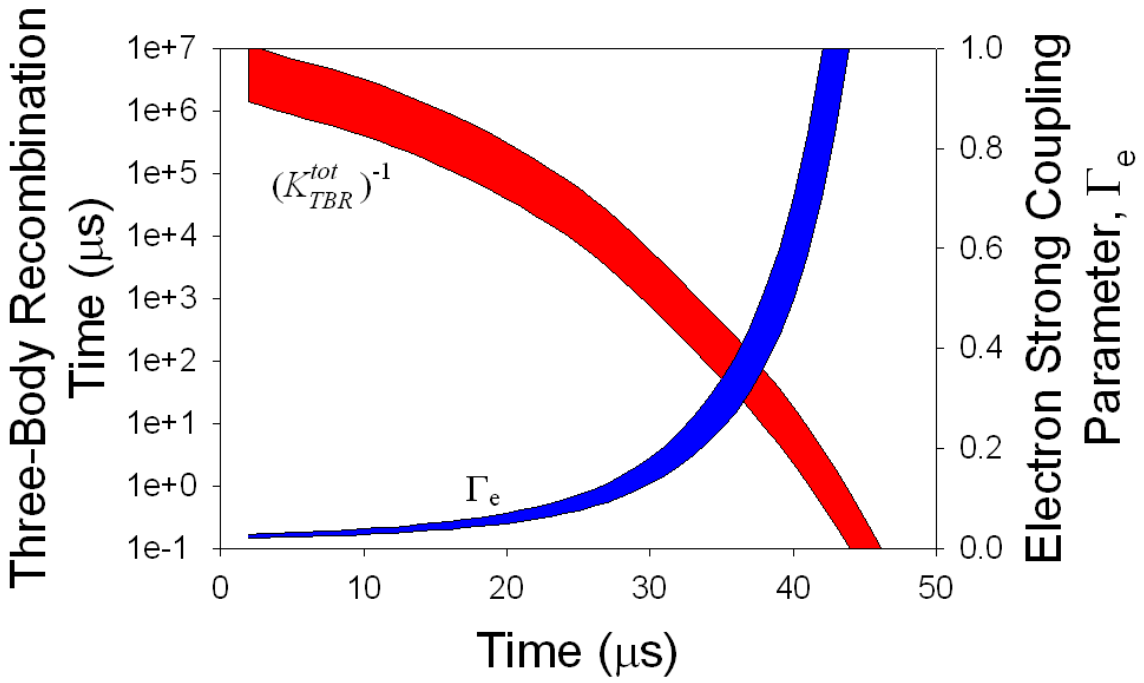


Figure 5.9: A plot of the three-body recombination time ($(K_{TBR}^{tot})^{-1}$, red, left axis) and the electron strong coupling parameter ($\Gamma_e$, blue, right axis) as a function of time. The data here uses the temperature evolution with evaporation from Figure 5.8. The range of values shown by the solid color for each calculation shows the possible range of these calculated parameters when using either the peak electron density ($n_{peak}$) or the average ion density ($n_{peak}/\sqrt{8}$) in these calculations. It can be seen here that when $\Gamma_e$ approaches the 0.2 limit [7], the three-body recombination time is still very long ($\sim$100$\mu$s), which means that heating from three-body recombination should be negligible.

should increase as the UCP density decreases, and should be significant for our UCP conditions. Our observations of the UCP expansion showed such a decrease in the UCP expansion energy. We were able to adapt our simple model to show that electron evaporation is a reasonable explanation for our observed behavior.

From our models, we were also able to extract the electron temperature evolution of the UCP as it expands. These calculations showed that it may be possible to increase the strong-coupling parameter, $\Gamma_e$, for the electrons beyond what has been observed in other UCP systems. By using electron evaporation, it may be possible to use forced evaporative cooling to lower the electron temperature before three-body recombination heating can take place. By increasing the value of $\Gamma_e$, we should be able to explore interesting physics in a region where classical plasma theory is expected to break down.

## References for Chapter 5


[1] S. Ichimaru, Rev. Mod. Phys. **54**, 1017 (1982).

[2] P. Gupta, S. Laha, C. E. Simien, H. Gao, J. Castro, T. C. Killian, and T. Pohl, Phys. Rev. Lett. **99**, 075005 (2007).

[3] T. C. Killian, M. J. Lim, S. Kulin, R. Dumke, S. D. Bergeson, and S. L. Rolston, Phys. Rev. Lett. **86**, 3759 (2001).

[4] A. Denning, S. D. Bergeson, and F. Robicheaux, Phys. Rev. A **80**, 033415 (2009).

[5] Y. Hahn, Phys. Rev. E **64**, 046409 (2001).

[6] M. Lyon, S. D. Bergeson, and M. S. Murillo, Phys. Rev. E **87**, 033101 (2013).

[7] F. Robicheaux, and J. D. Hanson, Phys. Rev. Lett. **88**, 055002 (2002).

[8] W. Ketterle and N. J. van Druten, Adv. At. Mol. Opt. Phys. **37**, 181 (1996).

[9] S. Kulin, T. C. Killian, S. D. Bergeson, and S. L. Rolston, Phys. Rev. Lett. **85**, 318 (2000).

[10] T. Pohl, T. Pattard, and J. M. Rost, Phys. Rev. Lett. **94**, 205003 (2005).

[11] J. J. Bollinger, J. M. Kriesel, T. B. Mitchell, L. B. King, M. J. Jensen, W.M. Itano, and D. H. E. Dubin, J. Phys. B: At. Mol. Opt. Phys. **36** (2003) 499510

[12] T.C. Killian, T. Pattard, T. Pohl, J.M. Rost, Phys. Reports **449**, 77-130 (2007).

[13] G. Bannasch and T. Pohl, Phys. Rev. A **84**, 052710 (2011).

[14] E. A. Cummings, J. E. Daily, D. S. Durfee, and S. D. Bergeson, Phys. Plasmas **12**, 123501 (2005).

[15] G. B. Andresen *et al.*, Phys. Rev. Lett. **105**, 013003 (2010).

[16] L. Spitzer, Jr., *Physics of Fully Ionized Gases* (Dover, New York, 1962).

[17] X. L. Zhang, R. S. Fletcher, S. L. Rolston, P. N. Guzdar, and M. Swisdak, Phys. Rev. Lett **100**, 235002 (2008).

[18] K. A. Twedt and S. L. Rolston, Phys. Plasmas **17**, 082101 (2010).

[19] J. D. Jackson, *Classical Electrodynamics, 3rd Ed.* (John Wiley and Sons, Inc., 1999), 62-64.

[20] J. L. Roberts, C. D. Fertig, M. J. Lim, and S. L. Rolston, Phys. Rev. Lett. **92**, 253003 (2004).

# Chapter 6

# Increased Ultracold Plasma Expansion Rate in a Weak Magnetic Field

The experiments presented in this chapter detail our observations of a dramatic increase in the ultracold plasma (UCP) expansion rate at early times in the UCP evolution in the presence of a relatively weak magnetic field, where the Larmor radius of the electrons in the UCP is greater than the Debye screening length. These experiments represent ongoing measurements which are in progress at the time of the writing of this thesis. The goal of this chapter will be to overview the status of our current understanding of our observations including the experimental results that we have obtained up to this point. Also, I will present some preliminary models and calculations that should help us to understand the nature of our UCP system when subjected to these external magnetic fields. I will then discuss additional modeling that may allow us to further our understanding of this phenomenon. Finally, I will briefly discuss future measurements that we will make in this line of investigation.

## 6.1 Experimental Background

The majority of plasma systems are subject to internal and external magnetic fields which can alter their behavior in interesting ways. These systems exhibit a wide range of phenomena that are discussed extensively in introductory textbooks [1, 2], such as Alfvén waves, Z-pinching, and various plasma instabilities among others. For ultracold plasma systems, the addition of an external magnetic field is interesting for several reasons. First, there is a predicted change in particle collision rate [3] as well as the three-body recombination rate [4] when magnetic fields are introduced to the UCP. Also, a variety of collective modes [5] and plasma instabilities [6] can be introduced. For our system, we are most interested the behavior of UCPs when confined in a Penning trap configuration [7], which requires a strong, uniform magnetic field in the trapping region. Understanding the behavior of our UCP system in the presence of a magnetic field will be essential for optimizing the loading of the Penning trap. Also, many of our future experiments, such as the two-pulse excitation of the UCP, electron temperature measurements, and electron evaporation measurements will be

conducted in a weak magnetic field. So, characterizing the expansion of the UCP in a magnetic field will be necessary in order to interpret these measurements.

The UCP expansion rate in a uniform magnetic field has been studied before in [8]. However, there are some key differences in the scope of the study in [8] compared to our experiments. First, the density of the UCPs in [8] are $\sim$2 orders of magnitude higher than those produced in our system. This difference in density could lead to a difference in observed behavior because many plasma parameters (collision rates, screening length, etc.) are very different for our UCPs. Second, our measurements focus on the early time expansion behavior whereas the work in [8] focuses on the asymptotic expansion of the UCPs. In [8], the early time expansion properties ($< 25$ $\mu$s) could not be measured because they used an ion extraction technique in order to determine the UCP size. This technique uses strong electric fields in order to extract all of the ions to a phosphorous screen to be imaged. These electric fields remove all of the electrons from the UCP which creates space-charge effects owing to the ion-ion interactions in the UCP, distorting the measurement of the initial expansion rate. Finally, our technique for measuring the density determines the peak density of the UCP and not just the two-dimensional spatial profile transverse to the magnetic field. This means that the UCP expansion parallel to the magnetic field should have some effect on our measured expansion rate.

The experiments in [8] showed an expansion rate transverse to the magnetic field lines that decreased as a function of the applied magnetic field. This effect was understood from a decrease in the ambipolar diffusion rate [2], where electrons and ions diffuse across the magnetic field lines at the same rate. This effect may be present in our later time data, as we observe a decrease in the expansion rate at late times as will be shown in the following section, but these measurements were only preliminary. The measurements that we have made at the time of writing this thesis show an increased expansion rate at early times in the UCP evolution that has not been reported in other UCP systems. While we have consistently observed an increase in the UCP expansion rate owing to the presence of an externally applied magnetic field, we have not yet obtained enough data to characterize the expansion's dependence on the strength of the magnetic field, initial ionization energy, density, and charge imbalance. Such measurements will be necessary in order to determine if our current explanation of the source of the increased expansion rate is correct.

## 6.2 UCP Expansion Measurements in a Weak Magnetic Field

One of our first observations of an effect of an externally applied magnetic field on the UCP was through measurements of the expansion rate. The expansion rate was measured using the same technique that was described in detail in Chapter 4. In our system, we were able to apply axially symmetric (with respect to the electrode assembly) magnetic fields using a 100-turn magnetic coil wrapped to the outside of the vacuum chamber (see Chapter 3). Using this coil, we can apply magnetic fields up to 14 G without adding additional lasers for optical pumping. At higher magnetic fields, the ionization fraction drops as Zeeman shifts detune the $5S - 5P$ resonances.

The simplest way to observe the effect of the magnetic field on the UCP expansion is through a direct comparison of the size of the UCP at chosen points early in the UCP evolution with and without the magnetic field present. We did this for $\Delta E/k_B = 50$ K and $\sim 2.5\times10^5$ total ions as seen in Figure 6.1(a). For this data, we measured the size of the UCP at 3 and 10 $\mu$s after the formation of the UCP with and without the presence of a 7 G magnetic field. In this data, it can be seen that in the presence of the magnetic field, the UCP expands more rapidly. At 3 $\mu$s, the size of the UCP, $\sigma$, is $\sim$3% larger with the magnetic field present. At 10 $\mu$s, this increases further to $\sim$15%. This continual increase in size of the UCP implies a different effective temperature for the UCP between the two cases with and without the magnetic field. To determine a reasonable effective temperature, we can fit the data points in Figure 6.1(a) to a self similar expansion of the form $\sigma(t) = \sqrt{\sigma(0)^2 + k_B T_{\text{eff}} t^2/m_i}$, where $T_{\text{eff}}$ is the effective electron temperature. Since the initial conditions are the same in both case, we constrain $\sigma(0)$ in our fits to be the same in both cases. For the data in Figure 6.1(a), the effective temperature, $T_{\text{eff}}$ was found to be $14 \pm 2$ and $39 \pm 4$ K for the case without and with the 7 G magnetic field respectively.

This data shows that the increase in the expansion rate with the magnetic field present is quite dramatic. This implies that the internal electric fields that drive the expansion are much higher than the thermal fields that would nominally be present (a calculation of these additional internal fields is presented in the following section). In fact, a conversion of the initial energy to the expected initial ionization energy from this case (multiply $T_{\text{eff}}$ by 3/2) is higher than the actual initial ionization energy of $\Delta E/k_B = 50$ K. However, this increased expansion rate does not continue throughout the full evolution of the UCP as seen in Figure 6.1(b). With the magnetic

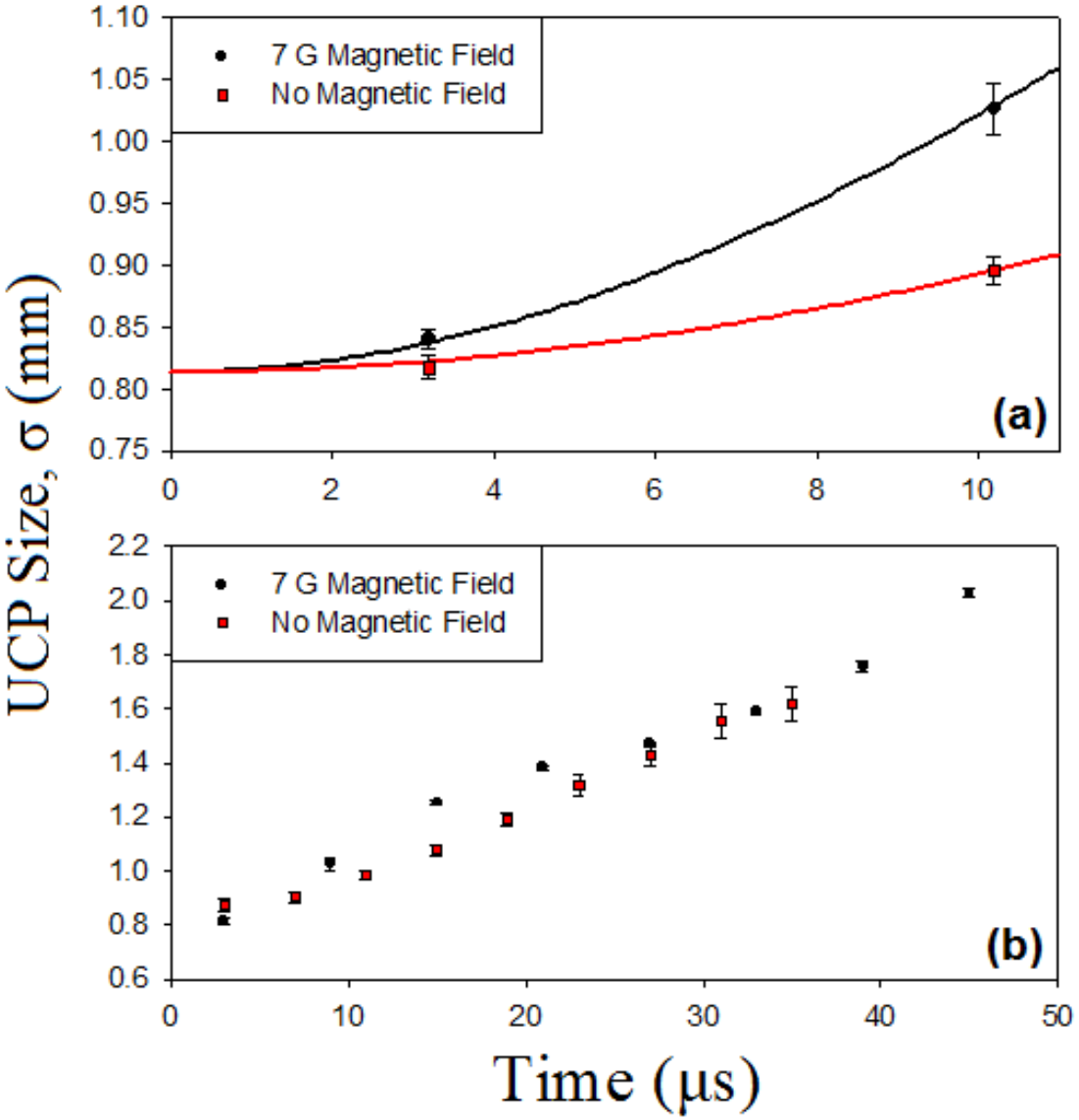


Figure 6.1: Comparisons of the measured UCP expansion rate at $\Delta E/k_B = 50$ K for an applied axial magnetic field of 0 G (red) and 7 G (black). In (a), we compare the initial expansion rate under the same initial conditions with $\sim 2.5\times10^5$ total ions and electrons. With the $B$-field present, the initial UCP expansion is much more rapid. The measured expansion rate from these two points fit to a self-similar expansion of the form $\sigma(t) = \sqrt{\sigma(0)^2 + v^2t^2}$ would imply an effective temperature that is $\sim$3 times greater with the magnetic field as compared to without the field. In (b), we compare the full expansion curves which shows odd behavior for the with $B$ field case at late times. At late times, there appears to be a deceleration of ion expansion that occurs after the rapid initial expansion.

field present, this data shows that although there is a rapid initial expansion as there is in Figure 6.1(a), there is deceleration of the ion expansion rate later in the UCP evolution that brings the two expansion curves closer together.

At the time of writing this thesis, the cause of this deceleration is unknown but there are several possibilities. In the following section, I discuss a model of UCP formation that shows that the additional acceleration at the beginning of the UCP evolution can come from confining the motion of the electrons in the UCP around the magnetic field lines. This confinement produces a higher ion density in the center of the UCP after formation that increases the internal electric fields that drive the additional expansion. It is possible that the deceleration results from a reversal of this effect as the UCP ions expand. If the electrons remain confined to the magnetic field lines as the ions expand, then the electron density would become higher in the center of the UCP than the ion density. Another possibility is that the initial increased expansion excites an ion acoustic wave [9], with a frequency that is expected to be much lower than the electron plasma frequency. Finally, it is possible that our measurements of the size of the UCP can break down at later times in the UCP evolution when the expansion greatly differs in the axial and radial directions. However, our calculations from Chapter 4 showed that even with a high aspect ratio UCP, the correction factor for our peak density measurements using the 2-cycle rf sweep should be less than 10%.

After we observed the increase in expansion, we collected data in a second set of measurements to determine how the expansion rate was influenced as a function of the magnetic field strength. To do this in a simple way, we compared the measured size of the UCP, $\sigma$, at 10 $\mu$s over a range of magnetic field strengths as seen in Figure 6.2. This figure shows that as the magnetic field increases in strength, the fractional increase in the size of the UCP also increases until it levels off at higher magnetic fields. Additional measurements of this effect at even higher magnetic fields have shown that the size at this time may actually have a downward trend as the magnetic field increases. However, these measurements are preliminary, and additional data is needed to confirm this trend.

The last measurement that was made prior to the writing of this thesis was a measurement of the prompt peak fraction as a function of the magnetic field as seen in Figure 6.3. The prompt peak fraction is defined as the fraction of electrons that escape the UCP during the UCP formation stage. Figure 6.3 shows that as the magnetic field increases, the prompt peak fraction also increases until it saturates at higher magnetic fields. The dramatic change in the prompt peak fraction also

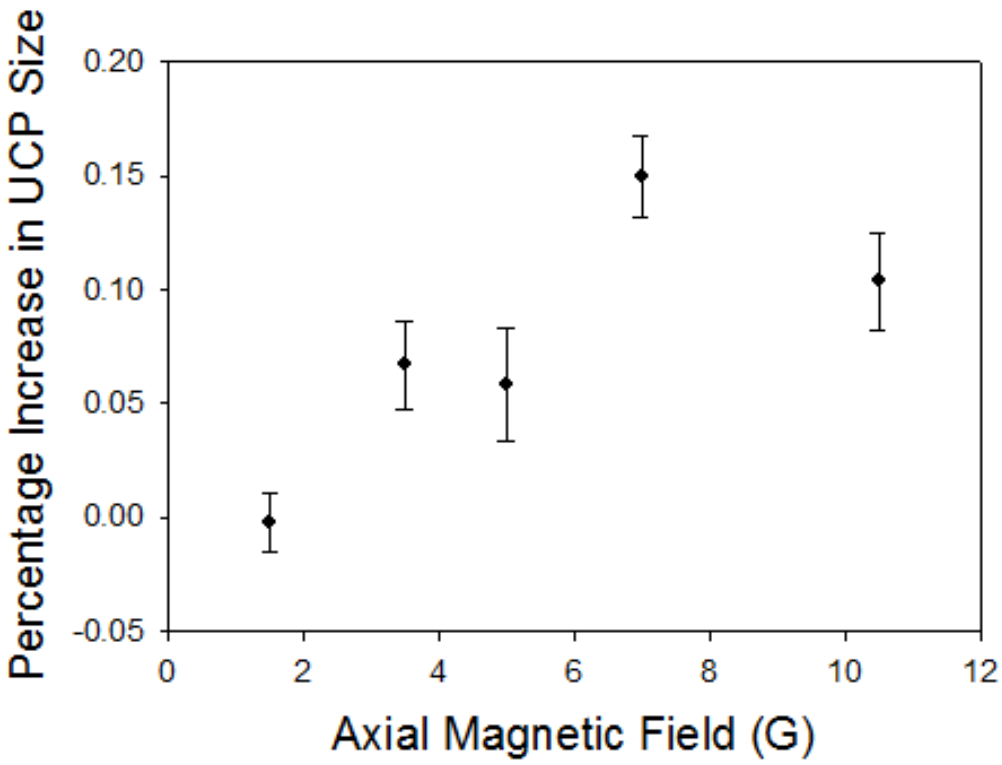


Figure 6.2: A plot of the relative size increase compared to without the magnetic field present at $t = 10$ $\mu$s as function of the applied magnetic field for $\Delta E/k_B = 50$ K. From this data, we observe an increase in the relative expansion rate as the magnetic field is increased up to $\sim 7$ G, where the increased expansion appears to saturate. Other data that we have obtained currently indicates a decrease in the relative expansion rate as the magnetic field is increased further. However, at this time, it is not known whether the effect of the magnetic field on the expansion rate is diminishing or if the deceleration of the ion expansion observed in Figure 6.1(b) is occurring earlier in the UCP evolution.

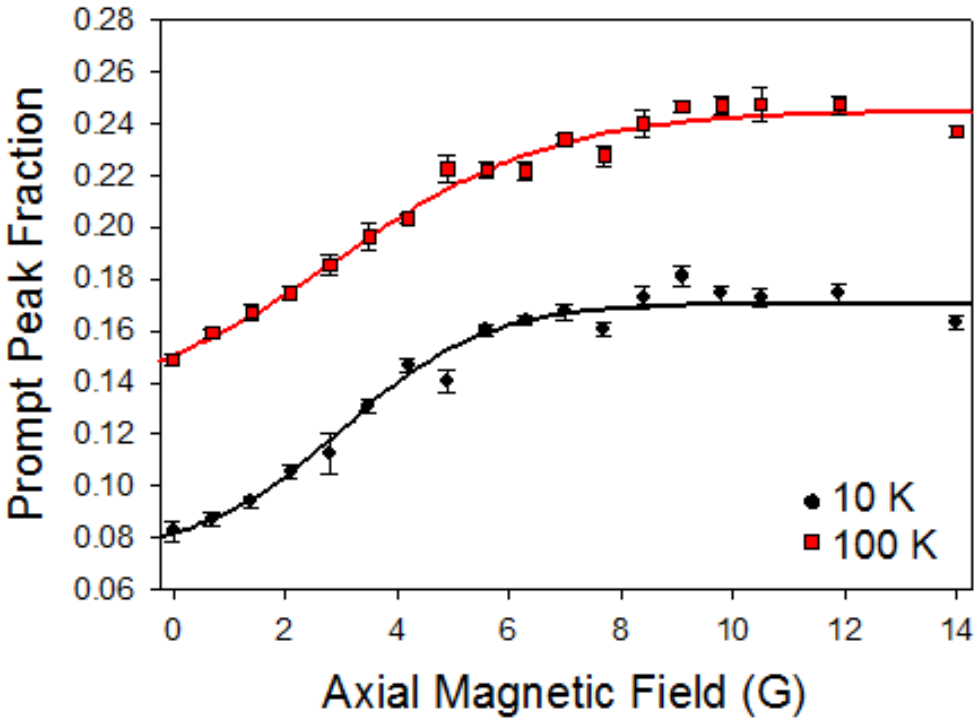


Figure 6.3: A plot of the increase in the prompt peak fraction as a function of the applied magnetic field for $\Delta E = 10$ (black) and 100 (red) K. This data shows that as the magnetic field increases, the number of electrons that escape during formation increases until it saturates. When fit to a saturating exponential function, the difference in the saturation field levels between 10 K and 100 K is a factor of $\sim$1.5, which is much less than the difference that would be expected if the saturation level was purely dependent on the level of magnetization of the electrons in the UCP.

calls for new models of UCP evaporation in the presence of a magnetic field. If we were to use our $T = 0$ models discussed in Chapter 5 to determine the depth of the UCP during the formation process, we would find that the depth is much greater that what we would expect given the rate of electron evaporation from the UCP. This means that the standard $T = 0$ treatment is inadequate for explaining the formation process of the UCP in the presence of a magnetic field.

One possible explanation for the increase in the prompt peak fraction in the presence of an externally applied magnetic field is that the trajectory of escaping electrons can change the number of electrons that can escape the UCP during formation. To evaluate this, I developed a simple model that determined the fraction of electrons that would be trapped in the UCP after formation as a function of the ion number. In the magnetic field free case, the electrons can escape the UCP in any direction. The fraction of electrons trapped after formation was calculated as a function of the ratio of the total number of ions to the threshold number of ions required to trapped the last electron from escaping the UCP with kinetic energy, $\Delta E$, as in [10]. This calculation can be easily reproduced and is seen as the black curve in Figure 6.4.

To simulate electron escape in a uniform magnetic field, I divided the UCP electron distribution (which was Gaussian) into a series of disks whose axes are concentric and considered to be aligned with the magnetic field. The ion distribution remained static. These disks were given a chosen kinetic energy and allowed escape only along the magnetic field lines (making this one-dimensional escape) from the UCP until the excess of ions trapped the remaining disks. To prevent numerical instabilities associated with disks approaching too close together after a given time step, the force on each disk approached a constant value associated with an infinite disk as the disk separation approached zero. We evaluated this over a range of total ion number in order to find the threshold number of ions, $N^*$, as well as the fraction of electrons trapped as a function of the total number.

The results of this calculation can be seen as the red curve in Figure 6.4. When compared to the results of the three-dimensional escape calculation, the one-dimensional escape traps more electrons when the total ion number is just above threshold. However, for higher total ion number, the trend reverses and the trapped fraction in the one-dimensional escape case becomes less than the three-dimensional case. While these calculations are simplistic, they do reveal a possible mechanism for the increase in the prompt peak fraction in the presence of a magnetic field.

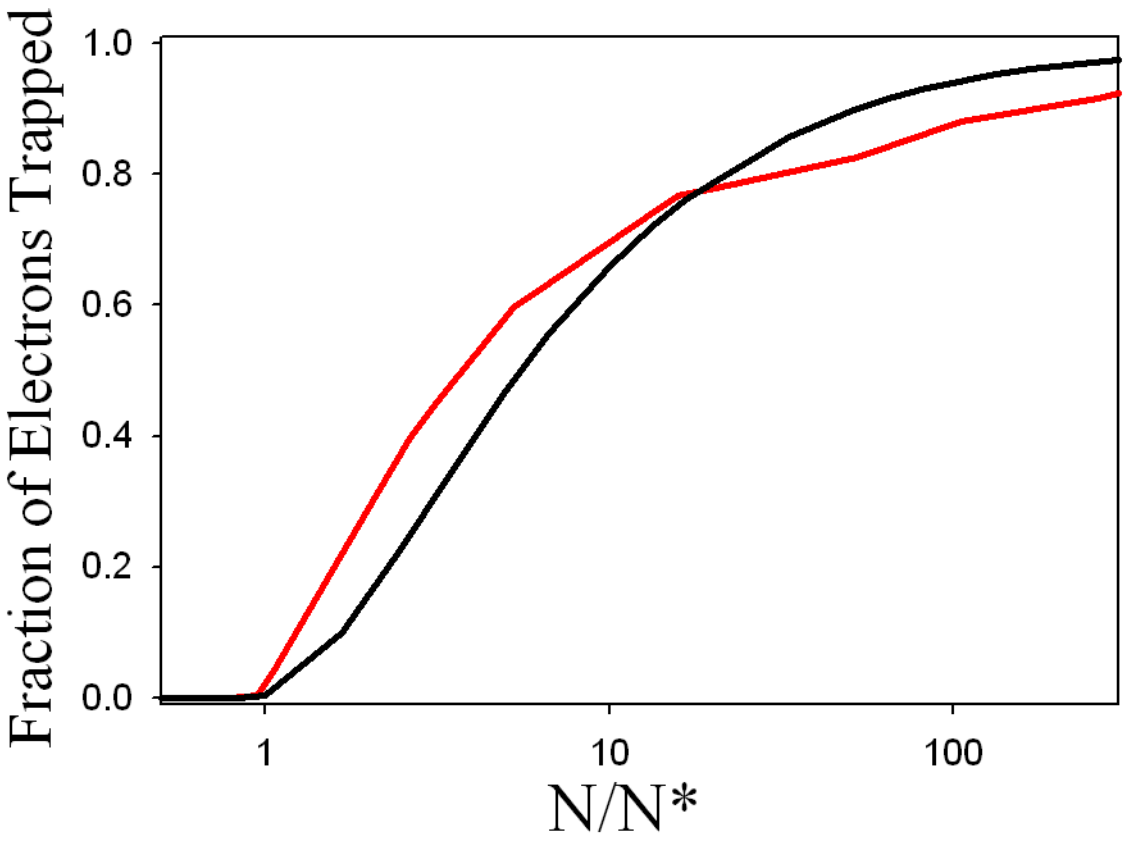


Figure 6.4: A plot comparing the fraction of trapped electrons for three-dimensional electron escape (black) to one-dimensional electron escape (red) as a function of the ratio of the total number of ions, $N$, to the threshold number of ions, $N^*$, as defined in the text. In this plot, we can see that the fraction of electrons trapped increases more rapidly in the one-dimensional case for ion numbers just above the threshold. As the ion number increases, the fraction trapped in the one-dimensional case becomes less than the three-dimensional case, which may contribute to the higher prompt peak fraction that is observed in the data in Figure 6.3.

At this point, we have encountered various systematic problems which have slowed the data collection rate for our system. The first problem was a slow breakdown of a commercial water-pump system which was used to cool the flashlamps of the Nd:YAG laser. This produced large fluctuations in the pump power for our dye laser system as well as a downward drift of the overall power. This pump failure greatly increased the variability in the system which made collecting data sets under a consistent set of conditions nearly impossible. After replacement of the water-pump, the Nd:YAG laser power improved greatly. The variability of our system was still present however, and was eventually traced to an electronics failure in an rf driver for an AOM that provided the $5S - 5P$ pump light in the plasma region of the vacuum chamber. Most recently, there has been an unexplained, sharp resonance $\sim$13-14 MHz which appears in our two-cycle rf sweeps. This resonance seems to depend of the position of the UCP relative to the electrodes. We attribute this resonance to patch charge effects which can create relatively strong, local electric fields which alter the behavior of the UCP. Over time, the strength of this resonance relative to the overall UCP response to the rf has decreased, which would be expected if patch charge effects were present. These issues have been addressed or are currently being addressed at the time of the writing this thesis, so the data collection is expected to resume shortly.

## 6.3 Modeling the Electron Distribution

Our observations of the increased UCP expansion rate in the presence of a magnetic field imply an increase in the internal electric fields that drive the UCP expansion. Therefore, it is necessary to evaluate how the electron distribution after formation differs from the magnetic field-free case. In the presence of a weak magnetic field, the Larmor radius for electrons in our UCPs is greater than the Debye screening length but for our data is still much less than the size of the UCP, $\sigma$. So, the motion of the electrons in the UCP transverse to the magnetic field will be restricted, which will change the nature of the formation process as discussed above. However, the Larmor radius of the ions is generally much larger than that of the electrons (and greater than the UCP extent) owing to the large mass difference. Therefore, for modeling these distributions, we will consider the electrons to be highly magnetized and the ions to be unmagnetized.

To begin the discussion of this model and to help evaluate its likely applicability, it is useful to review the properties of electron motion in a uniform magnetic field. The force on a charged particles in a uniform magnetic field is proportional to $|\vec{v} \times \vec{B}|$, which means that motion parallel to the magnetic field is unimpeded, whereas motion perpendicular to the field causes the particle to curve around the magnetic field lines as seen in Figure 6.5. For electrons, the radius of curvature around the field lines is given by $r_e = m_e v_\perp / |eB|$, $m_e$ is the electron mass, $v_\perp$ is the electron velocity perpendicular to the magnetic field, $e$ is elementary charge and $B$ is the magnitude of the magnetic field.

In the presence of radial electric fields owing to a thermal distribution of electrons, the electron motion transverse to the magnetic field lines is still restricted. We can compare the influence of the magnetic field on the electron motion to that of the radial electric field as follows. For a 50 K electron in a 10 G magnetic field, the Larmor radius is $\sim$200 $\mu$m ($\sigma \sim 850$ $\mu$m). The radial electric fields can be estimated from $E \sim k_B T_e / \sigma e$ which is $\sim$ 5 V/m [11]. The influence of the magnetic field can be estimated from $vB = \sqrt{2 k_B T_e / m_e} B$ which is $\sim$ 40 V/m. So, the influence of the magnetic field dominates, which will cause a $\vec{E} \times \vec{B}$ drift around the center of the plasma. The range of radial motion in the UCP of the electron will be on the order of the electron Larmor radius even with the radial electric field present.

To investigate the rapid increase in the UCP expansion rate in the presence of a weak magnetic field, we developed a simple model that determines the UCP electron distribution after the UCP formation if the electron motion is strictly confined to the magnetic field lines. In this model, we allow the electrons to redistribute themselves in order to screen out the component of the electric field along the magnetic field lines. Transverse to the field, the electrons are confined to a fixed radial distance away from the center of the ion distribution (an infinite $B$ approximation for the electrons). We can then calculate the total electric field inside the UCP owing to this new distribution of electrons. In this simulation, the ion dynamics are not modeled, and instead the electric fields are calculated from a particular assumed ion distribution. This approximation is valid early in the lifetime of the UCP as the ions do not have sufficient time to expand to alter their distribution.

While single particle motion is confined to magnetic field lines, for many particle systems the charged particles can undergo collisions which can change the trajectory of the particle motion.

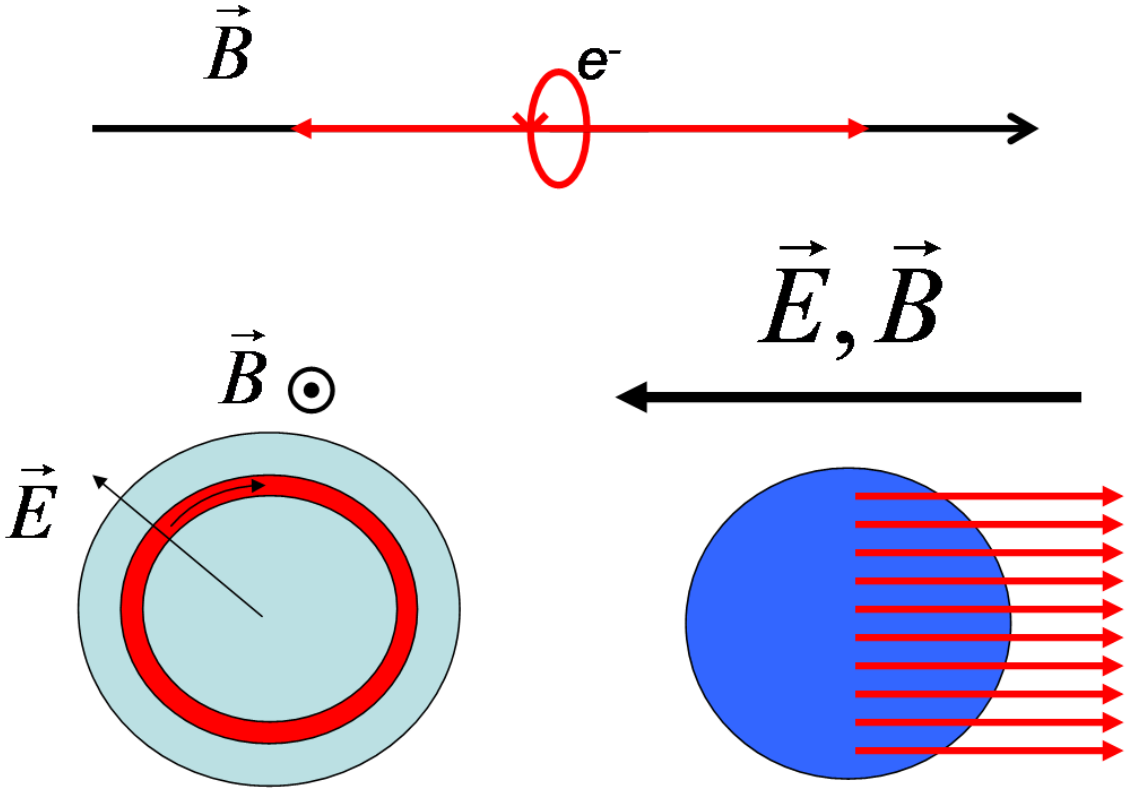


Figure 6.5: Diagrams of electron motion in a magnetic field. The top diagram shows the two types of motion of a single electron around a magnetic field line. Parallel to the field, the electron is free to move whereas the motion in the transverse direction curls the electron around the magnetic field line (thus the combined motion of the electron forms a helix). The lower left diagram shows the electron motion in a radial electric field (owing to the ion/electron charge imbalance caused by the finite temperature of the electrons) that is perpendicular to the magnetic field. In this case the $\vec{E} \times \vec{B}$ drift causes electron motion around the center of the plasma that maintains the radial position of the electron. The lower right diagram shows the motion of the electrons in the presence of an externally applied electric field parallel to the applied magnetic field. In this case, the electrons cannot move radially and have escape paths that are parallel to the magnetic field lines.

These collisions can allow for particles to diffuse across magnetic field lines. Textbook calculations for the diffusion rate of plasma particles across magnetic field lines only produce estimates that can differ by more than an order of magnitude. If we can determine the diffusion rate from our observations, it can help us identify the appropriate approximations to use when describing diffusion in our system. So, while our model will overestimate the impact of the magnetic field on the electron distribution, it will allow us to determine what type of effect we should expect to see if there are any restrictions to the electron motion transverse to the magnetic field.

### 6.3.1 Calculating the Electric Field

For the numerical calculation that we use to determine the equilibrium distribution of the electrons after the formation of the UCP, it is necessary to calculate the electric field at all points in space owing to the charge distribution. For this calculation, we can exploit the cylindrical symmetry of the situation. The most convenient way to calculate the electric fields from these distributions is to break up the distribution into an array of concentric rings with center axes that lie along the $z$-axis. Each ring's position will be defined by a position along the $z$-axis and a radial extent. The distribution can then be written by distributing the appropriate number of charges into these "ring bins" to match our desired initial charge distribution.

To start, we need to calculate the electric field from a ring of charge in the $z = 0$ plane of radius, $R$, at an arbitrary point in space defined by points in cylindrical coordinates ($\rho$,$\phi$=0,$z$), where $\phi = 0$ for simplicity. A diagram of this can be seen in Figure 6.6. I will first calculate the $z$-component of the field, which can be written as,

$$E_z = \int \frac{dq\ z}{4\pi\epsilon_0 r^3} \tag{6.1}$$

where $dq = \lambda R d\phi$, $\lambda$ is the linear charge density of the ring, $\epsilon_0$ is the permittivity of free space, and $r$ is the distance between the field point and the charge element on the ring, which is given by $r = \sqrt{(R\cos(\phi) - \rho)^2 + R^2\sin^2(\phi) + z^2}$. Writing this in a more convenient form, we have,

$$E_z = \frac{Nez'}{8\pi^2\epsilon_0 R^2}\int_0^{2\pi} \frac{d\phi}{(1 - 2\rho'\cos(\phi) + \rho'^{\,2} + z'^{\,2})^{3/2}} \tag{6.2}$$

where we have defined $\rho' = \rho/R$, $z' = z/R$, and substituted $\lambda = Ne/2\pi R$, where $N$ is the total number of electrons in the "ring bin" and $e$ is elementary charge. This integral can be solved to

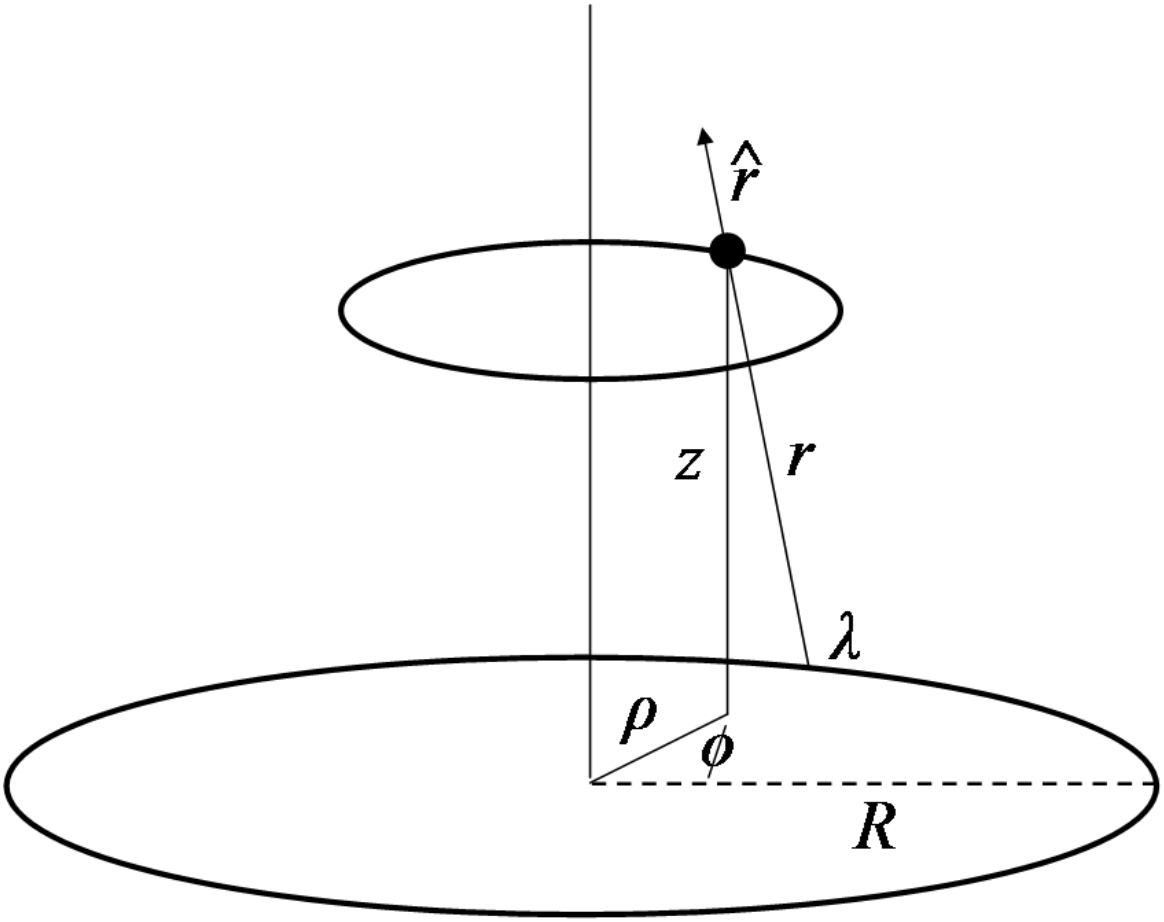


Figure 6.6: A diagram of the setup of the electric field calculation used in our model calculations. This calculation finds the electric field from a ring of radius, $R$, and uniform charge density, $\lambda$, off axis at an arbitrary point in space.

yield,

$$E_z = \frac{Nez'}{2\pi^2\epsilon_0 R^2} \cdot \frac{\mathrm{E}\left(2\sqrt{\rho'/\eta^+}\right)}{\eta^-(\eta^+)^{1/2}} \tag{6.3}$$

where $\eta^{\pm} = 1 \pm 2\rho' + \rho'^{\,2} + z'^{\,2}$ and $\mathrm{E}(k)$ is the elliptic integral of the second kind of argument $k$.

For the radial component of the electric field, we can replace the $z$ term in the numerator of Equation 6.1 with $(\rho - R\cos(\phi))$. Using the same notation, we obtain,

$$E_\rho = \frac{Ne}{4\pi^2\epsilon_0 R^2 \rho' \eta^-(\eta^+)^{1/2}} \left[\eta^- \mathrm{K}\left(2\sqrt{\rho'/\eta^+}\right) + (\rho'^{\,2} - z'^{\,2} - 1)\mathrm{E}\left(2\sqrt{\rho'/\eta^+}\right)\right] \tag{6.4}$$

where $\mathrm{K}(k)$ is the elliptic integral of the first kind of argument $k$. Using these forms of the electric field, we can calculate the total electric field owing to the charges that are in each of the rings that I define. The elliptic integral terms can be evaluated with high precision using the power series form of the integrals. In order to increase the computation speed of these calculations, we can evaluate each of the elliptic integrals only once, and store the values in a matrix associated with each of the interactions between two of the rings.

### 6.3.2 Results of the Model Calculations

For the calculations in this model, I began with an initially neutral, Gaussian distribution of ions and electrons which can be written in cylindrical coordinates as $n(\rho, z) = n_0 \exp(-(\rho^2 + z^2)/2\sigma^2)$, where $n_0$ is the peak density and $\sigma$ characterizes the spatial extent of the UCP. To make comparisons to our expansion data seen in Figure 6.1, the UCP consisted of $2.5 \times 10^5$ total ions and electrons and a size of $\sigma = 0.8$ mm. I divided this charge distribution in the $z$-direction into chosen number of equal-thickness segments over a total spatial range of $10\sigma$. Each of these segments in the $z$-direction are then further divided into equal thickness rings in the $\rho$-direction over a total spatial range of $5\sigma$. By dividing the charge distribution in this way, we can use the results of the calculation in the previous section to calculate the electric field over all space by simply taking into account the number of charges in each bin. The position and size of each of the bins remains fixed throughout the course of this calculation. Also, the total number of ions in each bin will also remain fixed as we are only concerned with the formation process of the UCP before the ions have a chance to move. Therefore, to perform this calculation, we only allow the electrons to transfer between bins.

It is important to note that this calculation is not dynamic, in that the electrons are not given a kinetic energy and allowed to travel throughout the UCP as governed by a set of equations of motion. That type of calculation requires very small timesteps, as numerical inefficiencies can present numerous problems, particularly the amount of computation time required to evaluate the effects we wish to study. Instead, our concern for this calculation is the equilibrium electron distribution after the formation of the UCP if the electrons are only allowed to move parallel to the magnetic field lines. To simulate the charge imbalance created from the escape of non-zero kinetic energy electrons, we added a uniform external electric field throughout all space. The electric field will require electrons to escape to neutralize the field and will serve as a way to control the charge imbalance to compare to our actual data.

To calculate the final electron distribution, I created a numerical routine that redistributes the electrons in each of the bins until the electric field in the $z$-direction is minimized. Each step of the calculation is simple. After calculating the electric field at the position of each bin, a fraction of the electrons proportional to the strength of the electric field can be transferred between adjacent bins in the $z$-direction to lower the absolute value of the electric field. After a sufficient number of steps, the electron distribution will screen the $z$-component of the electric field, reaching an equilibrium distribution.

The results of such a calculation can be seen in Figure 6.7, for both the axial ($z$) and radial ($\rho$) components of the electric field. It can be seen that the axial component of the electric field is completely screened as desired. For the radial component, the electric field is unscreened, producing a nearly linearly increasing field away from the center of the UCP in the radial direction. This unscreened field produces a radially outward force on the UCP ions, which will cause them to expand more rapidly.

We can compare the results of these simple model calculations to the expansion data shown in Figure 6.1. For the UCP conditions for this data, the calculations yielded an effective radial electric field of $\sim$1.7 V/m per ion, which was found by taking a weighted average of the electric field values over the UCP distribution. This electric field produces an additional acceleration that is $\sim$2 m/s/$\mu$s. This additional acceleration is not enough to explain the increased expansion rate that we observe in the UCP in the presence of the 7 G magnetic field that we applied. This means that while our model can show that there is an effect on the radial electric fields when electrons

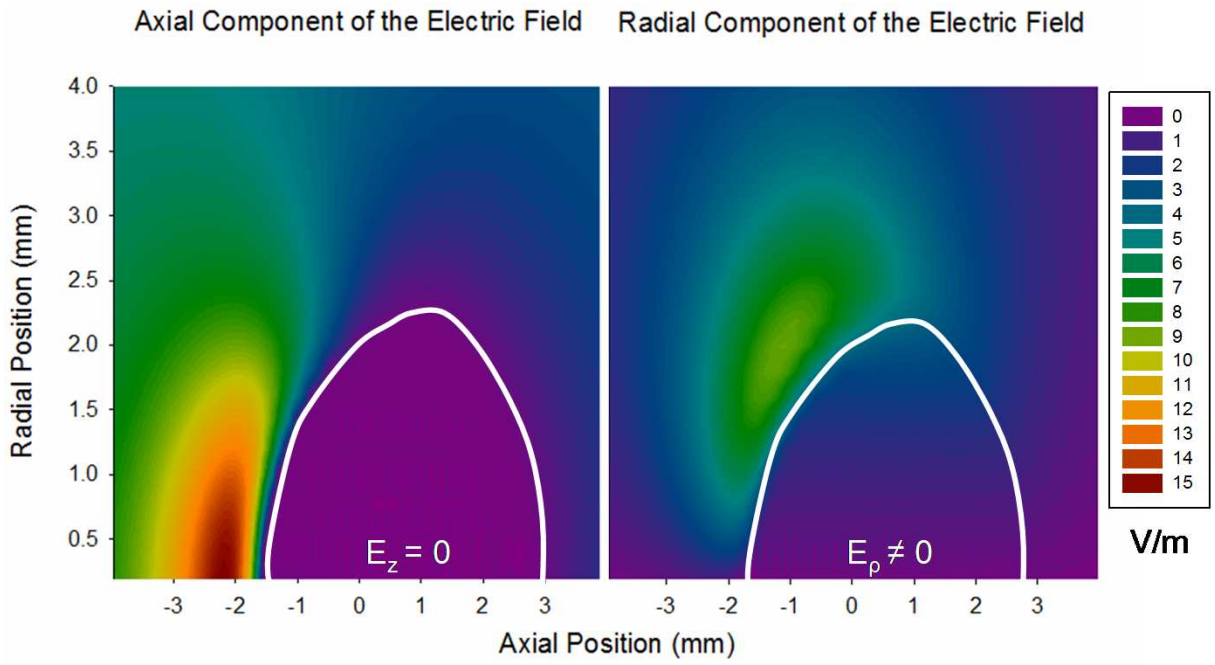


Figure 6.7: A plot of the axial (left) and radial (right) electric fields as a function of position after UCP formation as calculated from our model for $5\times10^5$ ions and a charge imbalance of $\delta = 0.14$ (14% of the electrons have escaped the UCP). One can see that as the electrons move to screen out the field in the axial direction, the radial electric fields are left unscreened. These unscreened fields result in additional ion expansion that can be measured for the UCPs in our system in relatively weak magnetic fields.

are confined radially but allow to escape the UCP axially, that the model cannot produce accurate quantitative predictions of the expansion rate of the UCP.

There are a few subtleties that will be quite difficult to model that I will discuss briefly here. First, from the difference in the initial charge imbalance with and without the magnetic field present, it is clear that we cannot treat evaporation in the same way between the two cases. This is because the greater charge imbalance with the magnetic field presence would produce a much greater potential will depth that would greatly decrease the evaporation rate. Therefore, accounting for the energy lost during evaporation with the magnetic field present will require more sophisticated modeling (beyond that which is discussed in Chapter 5).

### 6.3.3 Future Extensions to the Model

So, from these calculations, it is clear that either a more sophisticated approach is necessary to accurately determine the effect of the magnetic field on the UCP expansion in our system or there is a different mechanism that drives the increased expansion in the presence of a magnetic field. However, some simple modifications might allow us to better understand the dynamic processes of the UCP without using a full particle dynamics simulation. To start, we could model the electron distribution as a thermal distribution which will allow us to determine the thermal electric fields that contribute to driving the plasma expansion. In addition, we also want to formulate better models of the initial radial electron distribution after the UCP formation. This radial electron distribution plays a significant role in the UCP expansion behavior, and needs to be accurately modeled in order to calculate the magnitude of the radial electric fields that can be produced. By altering the ion distribution based on these internal electric fields, we can determine how the electron distribution needs to change in order to match our observed expansion rate. As an added feature of these calculations, we should be able to make estimates of the diffusion rate of the electron across magnetic field lines which will help us to understand how the electrons move in the UCP in the presence of a magnetic field.

## Conclusion

The measurements and models presented in this chapter, while incomplete, show that even a relatively weak magnetic field can have a significant influence on the expansion of our ultracold

plasma systems. Our measurements indicate that the initial expansion rate of the UCP increases with an increasing magnetic field up to ∼10 G, for our system. A simple model of the electron distribution after the formation of the UCP shows that confining the electron motion to be parallel to the magnetic field lines will create unscreened radial electric fields that drive additional ion expansion. While the simple estimates from our model do not account for all of the additional expansion energy, they do indicate that an effect should be present. These measurements and calculations show the need for more sophisticated modeling of UCP dynamics in the presence of a magnetic field, as concepts such as potential depth and electron evaporation become very complicated when the UCP can no longer be treated by a $T = 0$ distribution.

This effect will be very important for our future measurements of the UCP. Trapping the UCP in a nested Penning trap configuration requires a very high magnetic field, which should still have this type of effect present. When studying the dynamics of loading a UCP into this Penning trap, it will be important to understand these effects to optimize the loading configuration. Also, any experiment performed in the presence of a magnetic field will need to account for the faster expansion rate in order to properly model the UCP evolution.

## References for Chapter 6


[1] D. A. Gurnett and A Bhattacharjee, *Introduction to Plasma Physics* (Cambridge University Press, 2005)

[2] P. M. Bellan, *Fundamentals of Plasma Physics* (Cambridge University Press, New York, 2006).

[3] M. E. Glinsky, T. M. O'Neil, M. N. Rosenbluth, K. Tsuruta, and S. Ichimaru, Phys. Fluids B **4**, 1156 (1992).

[4] M. E. Glinsky and T. M. ONeil, Phys. Fluids B **3**, 1279 (1991).

[5] R. S. Fletcher, X. L. Zhang, and S. L. Rolston, Phys. Rev. Lett. **96**, 105003 (2006).

[6] X. L. Zhang, R. S. Fletcher, and S. L. Rolston, Phys. Rev. Lett. **101**, 195002 (2008).

[7] J. H. Choi, B. Knuffman, X. H. Zhang, A. P. Povilus, and G. Raithel, Phys. Rev. Lett. **100**, 175002 (2008).

[8] X. L. Zhang, R. S. Fletcher, S. L. Rolston, P. N. Guzdar, and M. Swisdak, Phys. Rev. Lett. **101**, 235002 (2008).

[9] J. Castro, P. McQuillen, and T. C. Killian, Phys. Rev. Lett. **105**, 065004 (2010).

[10] T. C. Killian, S. Kulin, S. D. Bergeson, L. A. Orozco, C. Orzel, and S. L. Rolston, Phys. Rev. Lett. **83**, 4776 (1999).

[11] F. Robicheaux, and J. D. Hanson, Phys. Rev. Lett. **88**, 055002 (2002).

# Chapter 7

# Increased Light-Assisted Collisional Loss via Excitation to the $5S-5D$ Molecular Potential in an $^{85}$Rb Magneto-Optical Trap

The experiment described in this chapter details the increased light-assisted collisional loss from an $^{85}$Rb magneto-optical trap (MOT) with the application of laser light resonant with the $5P_{3/2}-5D_{5/2}$ transition at 776 nm. This was the first experiment that I took part in upon entering the lab and was performed before the apparatus for ultracold plasma creation described in Chapter 3 was constructed. Although this experiment is not related to ultracold plasmas, its roots were related to creating an easy pathway to the production of Rb ions through auto-ionizing collisions, which has been observed through excitation to the $4D_{5/2}$ state in Rb in [1]. What we found in practice was a loss channel in Rb that did not have enough energy to produce Rb ions, so it would not prove to be useful for the creation of ultracold plasmas. However, there was interesting fundamental atomic physics present in this experiment. The characterization of the observed loss channel will be presented in this chapter.

## 7.1 Experimental Background

Since early in the development of laser cooling and trapping [2], it has been observed that light has a large influence on ultracold atomic collisions in magneto-optical traps (MOTs) [3]. Atom pairs that are excited resonantly onto molecular potential curves can accelerate along those curves and can spontaneously emit a red shifted photon (Figure 7.1) or approach to close internuclear distances where state changes can occur. In both cases, excess energy is converted to kinetic energy of the atom pair, and can lead to trap loss. These collisions have been extensively studied in one- and two-color experiments where the applied laser light is nearly resonant between a single pair of principal quantum states (e.g., the ground $S$ state and the first excited $P$ state in alkali metal atoms) [4–11]. The molecular states that are involved in these collisions have both attractive and repulsive potential curves associated with each pair of states [12]. Also, the addition of hyperfine structure will create a large number of interactions between every possible pair of states, which can produce more than 500 molecular curves for the interactions discussed in this chapter.

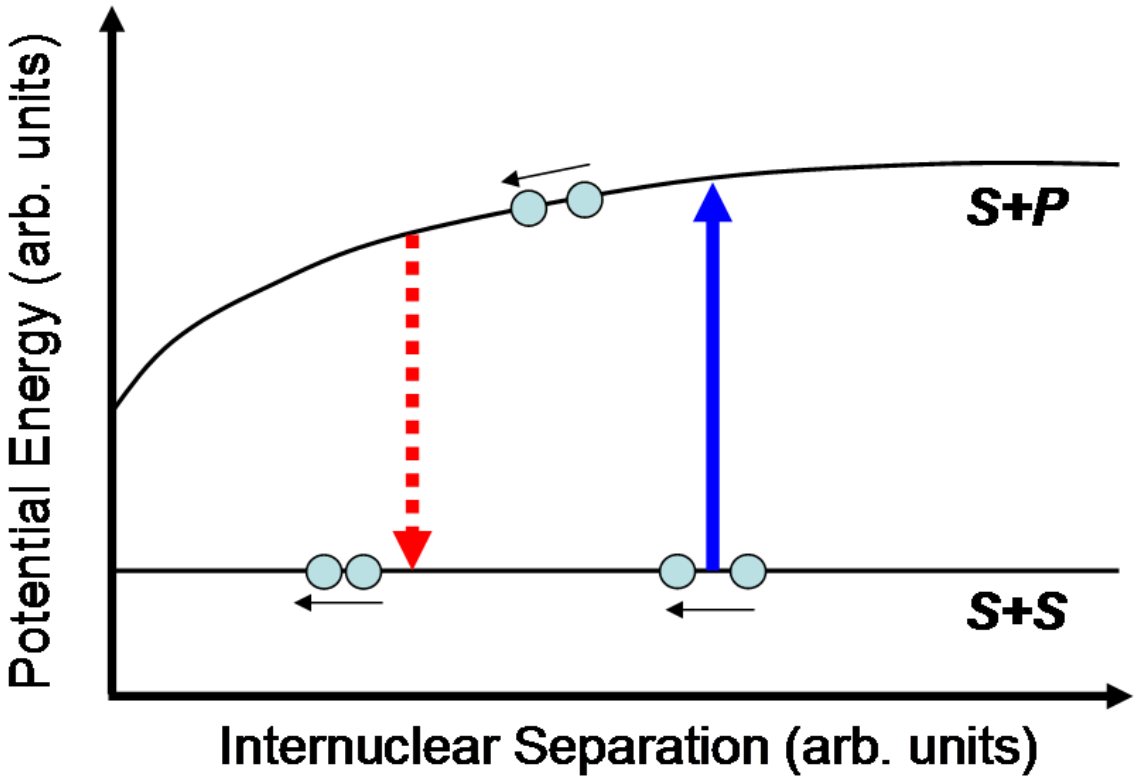


Figure 7.1: A diagram of a light-assisted collision. When two ground state atoms approach each other they can be excited up to an $S+P$ molecular state. The potential energy of this state decreases as the internuclear distance of the two atoms decreases. When the atom pair spontaneously emits a photon, it will be red-detuned relative to the incoming photon. The excess of energy is given to the atom pair as kinetic energy and can lead to a loss of atoms from the MOT. The repulsive curve for the $S + P$ state is not shown in this diagram.

These light-assisted collisions are not limited to just a single pair of states however. Collision channels involving more highly excited states are also associated with molecular potentials that can lead to loss in a light-assisted collision. Owing to larger energy splittings and smaller matrix elements, the molecular potential at long range for states combinations that do not couple by an electric dipole tend to be "flat" (i.e., constant) as compared to states that do couple by an electric dipole. The corresponding atom acceleration is then much smaller for these relatively "flat" states. In this work, we study light-assisted collisions that involve an excitation to one such "flat" molecular potential. This is done by applying $5S_{1/2} - 5P_{3/2}$ and $5P_{3/2} - 5D_{5/2}$ resonant light simultaneously to atoms in an $^{85}$Rb MOT [13]. We find that the light-assisted collision loss rate is increased by over an order of magnitude from the addition of the $5P_{3/2} - 5D_{5/2}$ resonant light, even though the molecular potential is flat and the overall light intensity is only increased by a factor of 2. By characterizing the behavior of these light-induced losses, we identify the likely loss mechanism as owing to a combination of the long lifetime of the $5D_{5/2}$ and a radiative cascade decay through steeper intermolecular potentials at closer internuclear separations.

Investigations of multi-excited-state photoassociative ionizing collisions (as opposed to light-assisted trap loss collisions in this work) have been reported in Rb for both quasicontinuous wave [1] and ultrashort pulsed configurations [14] when both $5S_{1/2} - 5P_{3/2}$ and $5P_{3/2} - 4D_{5/2}$ light was present. We find that the collision channel producing our observed trap loss is different that the collision channel responsible for ion production in Refs. [1, 14].

The ability to use multiple excited states in a light-assisted collision is potentially useful for deliberate control of ultracold collisions [15] and ion formation during the ultracold collisions [1, 14], as long-lived molecular excited states also allow for the transport of atom pairs to close internuclear separations along an excited state. Conversely, light-assisted collisions are often problematic in experiments where they are not the main focus of study. For instance, they limit the density in MOTs and optical traps [8]. Light-assisted collisions involving multiple transitions to various excited states could be a limitation in experiments with ultracold gases where excited-state atoms and molecules are created, such as Rydberg atom formation [16–18]. It could also impose limitations on extensions of laser cooling involving higher-energy excited states than the first excited state [19–21], if the excitation pathway involves similar states. Currently, techniques involving cooling to excited states beyond the first excited state to improve optical trap loading are being used in other

experiments [22, 23]. In at least one case [23], trap losses on the order of $10^{10}$ cm$^{-3}$ are observed, which are on the same order as our observations. Given the convenience of obtaining diode lasers resonant with the $5P_{3/2} - 5D_{5/2}$ transition in Rb at 776 nm, the $5D_{5/2}$ state would appear to be an excellent candidate for beyond-first-excite-state laser cooling studies. However, the presence of large light-assisted collision losses presents a potentially serious complication.

In this chapter, I will detail our measurements of the increased light-assisted collision losses in an $^{85}$Rb MOT owing to the addition of light resonant with the $5P_{3/2} - 5D_{5/2}$ transition at 776 nm. To characterize the loss rate, we measured the loss coefficient in steady state. Under different density and light intensity conditions we were able to determine that the loss was two body in nature, and we determined the probable loss channel for the atoms in the MOT.

## 7.2 Experimental Setup

As noted above, the experiments described in this chapter were performed before the apparatus used in the experiments for Chapters $4-6$ was constructed. Since this setup is different that what was described in detail in Chapter 3, I will describe the apparatus that was used for the experiments in this chapter here. This experiment involved the use of the same type of laser cooled atoms ($^{85}$Rb) as those described in Chapters $4-6$. However, the setup for this experiment is simplified as the creation of a magneto-optical trap (MOT) is the only requirement from this vacuum chamber setup. For this experiment, I was able to use the vacuum chamber and experimental setup used for the laser cooling experiments in the same laboratory [24] with a few modifications. These modifications included adding a laser at 776 nm to the MOT beam path and the addition of a CCD camera and imaging software to image the MOT atoms during the experiment. More details of the experimental setup are described below.

### 7.2.1 Magneto-Optical Trapping and the Addition of 776 nm Light

The MOT was created using standard techniques [25]. It consisted of three orthogonal beams from the primary trapping laser (which we will refer to as L1, at 780 nm) which were retroreflected to create a six-beam configuration with a total intensity between 23 and 42.5 mW/cm$^2$ for different experimental conditions as seen in Figure 7.2. The MOT was loaded from a background vapor of Rb, which was provided by a set of Rb getters in our vacuum chamber. The beams from L1

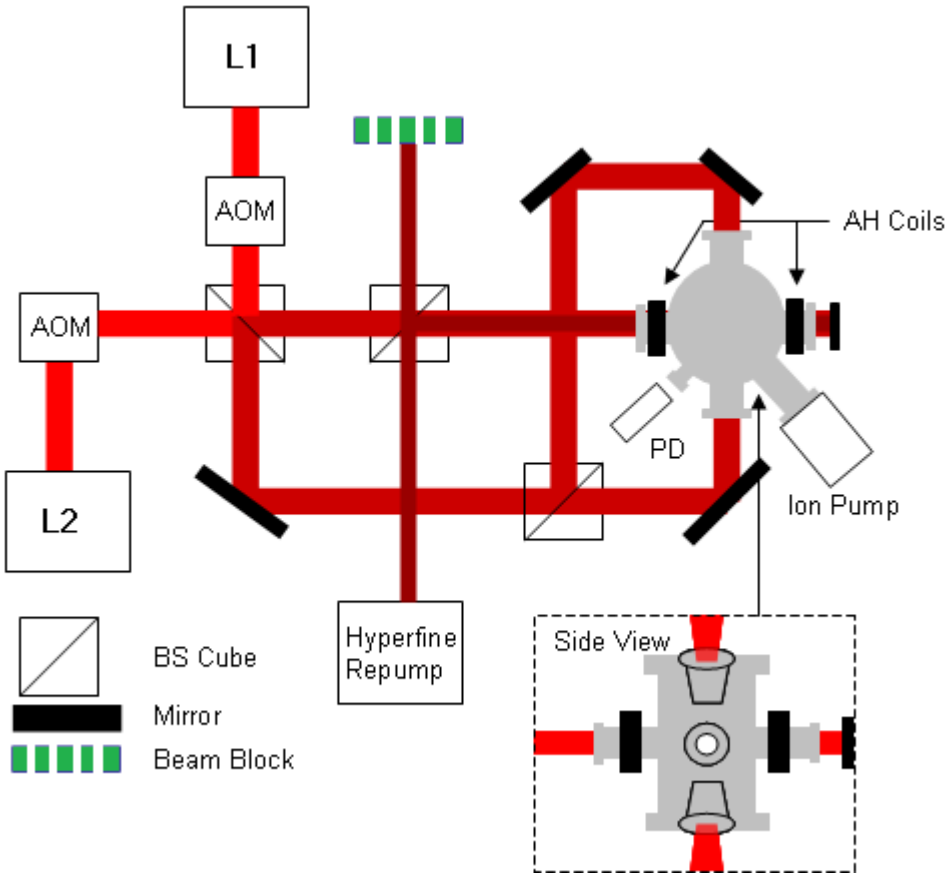


Figure 7.2: A diagram of the experimental setup for the measurements discussed in this chapter. Here, we have a standard magneto-optical trap (MOT) setup in a stainless steel vacuum chamber with L1 (780 nm) serving as the main trapping laser for $^{85}$Rb. Here, L2 (776 nm) is aligned along the same path as L1. (AOM: acousto-optic modulator; AH: anti-Helmholtz; PD: photodiode; BS: beam splitting.

were detuned between 6 and 18 MHz to the red of the $5S_{1/2}$ ($F = 3$) to $5P_{3/2}$ ($F = 4$) cycling transition in $^{85}$Rb as desired. In addition to L1, we used light from a hyperfine repump laser (at 795 nm tuned to the $F = 2$ ground state to $F = 3$ excited state D1 transition). The number of atoms trapped in the MOT was determined through a calibrated fluorescence measurement. The fluorescence of the MOT was captured in a lens and focused down onto a large-area photodiode, which provided the primary signal for these measurements. To calibrate the fluorescence signal, a standard probe absorption measurement was made (Chapter 3). The optical depth of the atom cloud was measured by a resonant laser probe image at a specific detuning for L1, and the atom number extracted from this absorption measurement was related to the reading measured by the photodiode (Chapter 3). We related the calibration measurement to other detunings of L1 that we used by using the fact that the fraction of atoms in the MOT in the $5P_{3/2}$ excited state was experimentally determined to be [26]

$$f = \frac{I/2I_{sat}}{(1 + I/I_{sat} + 4(\delta/\Gamma)^2)} \tag{7.1}$$

where $\delta$ is the detuning of the laser and $\Gamma$ is the natural line width of the transition ($2\pi\cdot 6$ MHz for Rb) [27].

To this standard MOT configuration, we added additional light from a second laser (which we will call L2, at 776 nm) to provide a second excitation up to the $5D_{5/2}$ level. Initially, we aligned a single beam from L2 with the atoms in order to provide excitation. In this configuration, we noticed that excitation from L2 resulted in a strong force on the MOT, which deformed the shape of the MOT and pushed atoms out of the trap. In order to suppress these effects, we aligned L2 along the same three-beam path as L1 to create a balance of forces as seen in Figure 7.2. When in this configuration, there was no noticeable net force on the MOT. Along this path, L2 was also expanded to a diameter $\sim$1.5 cm, giving a total six-beam intensity of 25 mW/cm$^2$ at the location of the atoms. At this intensity, the loss due to direct photoionizing transitions ($5D_{5/2}$ to the continuum via either L1 or L2) was negligible in our subsequent measurements based on measured ionization cross-sections found in [28].

The frequency of L2 was controlled by monitoring a fluorescence signal in a Rb vapor cell. A pickoff beam from L2 was counterpropagated through a cell with a beam on resonance with the $5S_{1/2}$-to-$5P_{3/2}$ transition (called L1a) as seen in Figure 7.3. When L2 was resonant with the

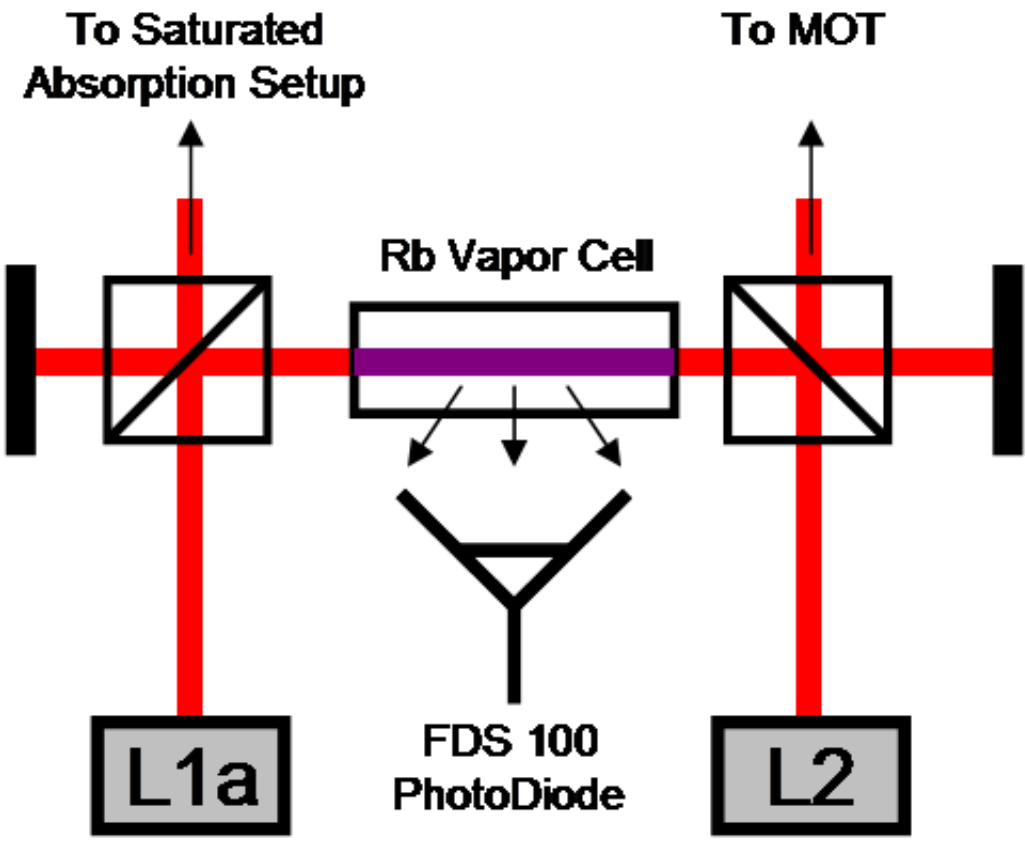


Figure 7.3: A diagram of the setup for tuning L2 to the resonant frequency. An additional laser tuned to the $5S_{1/2} - 5P_{3/2}$ transition (L1a) is send through a Rb vapor cell. A pickoff from L2 is counter-propagated through this cell and is put onto resonance by observing the 421-nm fluorescence owing to a cascade decay through the $6P_{3/2}$ state. This is accompanied by a reduction in the 780 nm fluorescence which is detected by an FDS100 photodiode, which is more sensitive to infrared light.

$5P_{3/2}$-to-$5D_{5/2}$ transition, a fraction of the atoms decayed to the ground state through the $6P_{3/2}$ state, fluorescing at 421 nm as seen in Figure 7.4. This 421-nm fluorescence could be observed by eye in the cell. This was accompanied by a slight but measurable reduction in the amount of infrared fluorescence observed in the cell. The second excitation produces a reduction in infrared fluorescence by preventing atoms from decaying back to the ground state from the $5P_{3/2}$ state at 780 nm, as the atoms can decay through different paths to the ground state as seen in Figure 7.4. By measuring the infrared fluorescence, we monitored the detuning of L2 with respect to the $5P_{3/2}$-to-$5D_{5/2}$ transition during the course of our measurements. The frequency of L2 was calibrated by altering the frequency of L1a by a known amount and measuring the change in piezoelectric transducer (PZT) voltage of L2 at the minimum of infrared fluorescence. For control of the frequency of L2 during measurements, the PZT voltage was adjusted in order to achieve the maximum loss (i.e., the minimum fluorescence) from the MOT.

The number of atoms in the MOT as a function of time is governed by the rate equation [10]

$$\dot{N} = R - \frac{N}{\tau} - \beta\bar{n}N - kN \tag{7.2}$$

where $N$ is the number of atoms in the trap, $R$ is the load rate, $\tau$ is the load lifetime, $\beta$ is the two-body loss coefficient, $k$ is an additional one-body loss coefficient due to the presence of L2, and $\bar{n}$ is the average density. $R$ and $\tau$ are found by loading from an empty trap without L2 light present, so that $\beta = k = 0$. The load curve $N(t)$ fits very well to an exponential curve, which implies a negligible amount of background two-body losses in the absence of L2 for our conditions. When the MOT filled completely, we determined $R$ by solving the rate equation in steady state: $R = N_{max}/\tau$. With L2 light present, a large reduction of the number of atoms in the MOT was observed (approximately a factor of 5 reduction in the steady-state MOT number, seen in Figure 7.5). When the light from L2 is applied, the equilibration time of the MOT is also shortened significantly. This implies that the loss was not from a simple reduction in the load rate ($R$) into the MOT, and suggests a need for additional loss terms ($k$,$\beta$) in the load rate equation. This conclusion was also supported by a measurement of the initial slope of the fill from an empty MOT, where $R$ dominates the load process. The observed initial slope did not change with the addition of the 776-nm light on the 10% level. This small (<10%) dependence, if any, is not unreasonable. In Ref. [13], only a small effect was observed for $^{85}$Rb, albeit for very different conditions. For the majority of our

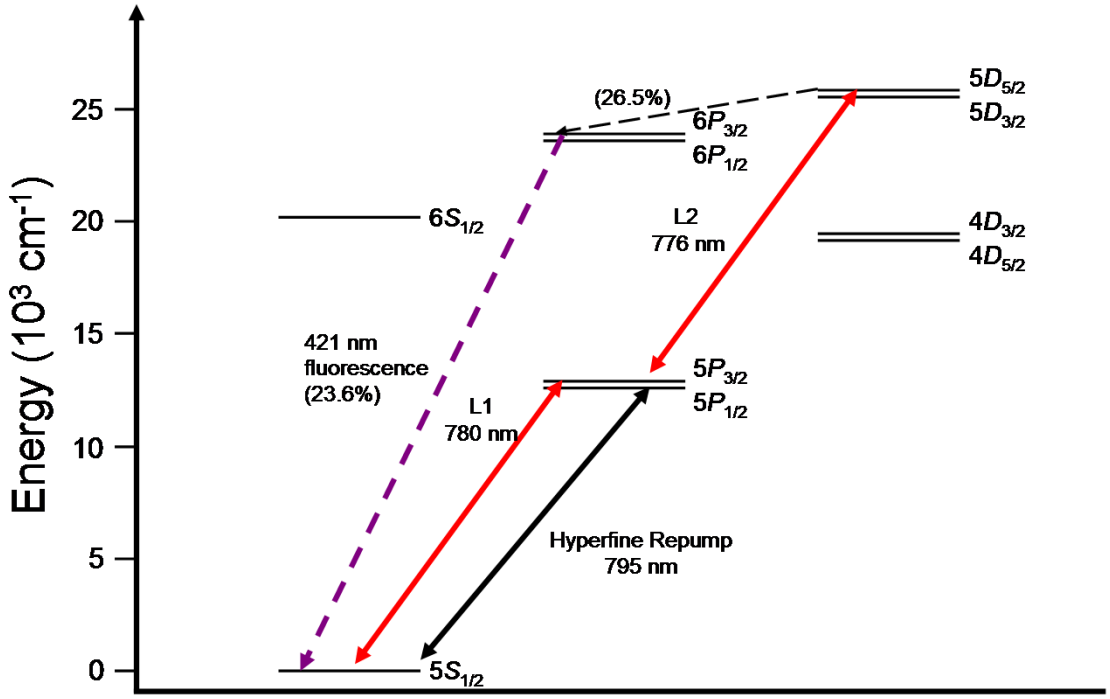


Figure 7.4: A diagram of the low-lying energy levels in $^{85}$Rb. The hyperfine structure of these levels is not shown. The relevant laser transitions are shown as solid, double-headed arrows between the relevant states. Spontaneous emission is shown as dashed arrows pointing from the upper state to the lower state. Only the relevant spontaneous emission decay channels are shown for clarity. L1 drives transitions between the $5S_{1/2}$ and $5P_{3/2}$ state at 780 nm using the main MOT trapping laser. A hyperfine repump laser at 795 nm is used to pump atoms out of the lower hyperfine state and back onto the cycling transition. L2 drives transitions between the $5P_{3/2}$ to $5D_{5/2}$ state at 776 nm. From the $5D_{5/2}$ state, 26.5% of the atoms will decay to the $6P_{3/2}$ state. 23.6% of the atoms in the $6P_{3/2}$ state will decay back to the ground state, fluorescing at 421 nm. We maximize this 421 nm fluorescence in the Rb vapor cell (Figure 7.3) to put L2 on transition.

experimental conditions, the L1 and L2 light is resonant with only a very narrow velocity class of atoms, resulting in a muted impact for the total Doppler cooling.

### 7.2.2 Measuring the Two-Body Loss Coefficient

One possible way to determine the value of the additional loss coefficients would be to fit Equation 7.2 to the type of data presented in Figure 7.5. However, we did not use this technique and decided to measure the loss coefficient in steady state for the following reasons. When the 776-nm light is applied (at $t = 0$ in Figure 7.5), the volume changes significantly. The time-dependent nature of this would have significantly complicated both the data collection and analysis. With the L2 frequency characterization technique we used, drifts during data collection would have adversely affected the data in a time-dependent measurement.

In order to solve for the two loss coefficients ($k$ and $\beta$), we first determined whether a one- or a two-body loss mechanism was dominant over the other. When loading the MOT, the number and density of the atoms trapped drifts slowly over time and successive measurements because the background Rb vapor is slowly pumped out of the system after getter flashes. For measurements at both low and high density, we solved Eq. (2) for the loss coefficients individually, assuming that the other coefficient is zero (Figure 7.6). This measurement showed that our observations were more consistent with a dominant two-body loss process. Additional measurements presented later in this chapter further and better confirmed the two-body nature of this loss.

We can solve for the two-body loss coefficient $\beta$ in steady state as

$$\beta = \frac{V}{N\tau}\left(\frac{N_{max}}{N} - k\tau - 1\right) \tag{7.3}$$

where $V$ is the volume of the MOT, and $\mathrm{N}_{max}$ is the full MOT number without L2 light. To determine the volume, an image of the fluorescing MOT in steady state is recorded through an optical access port as seen in Figure 7.7. The image is fit to a two-dimensional Gaussian distribution in order to determine the rms widths of the MOT. In the image, the features of the vacuum chamber of known dimensions are visible, allowing a calibration of the distance scale in the image. The volume is extrapolated from this two-dimensional profile by observing that the third dimension, as seen through a different view port, is approximately the size of the others.

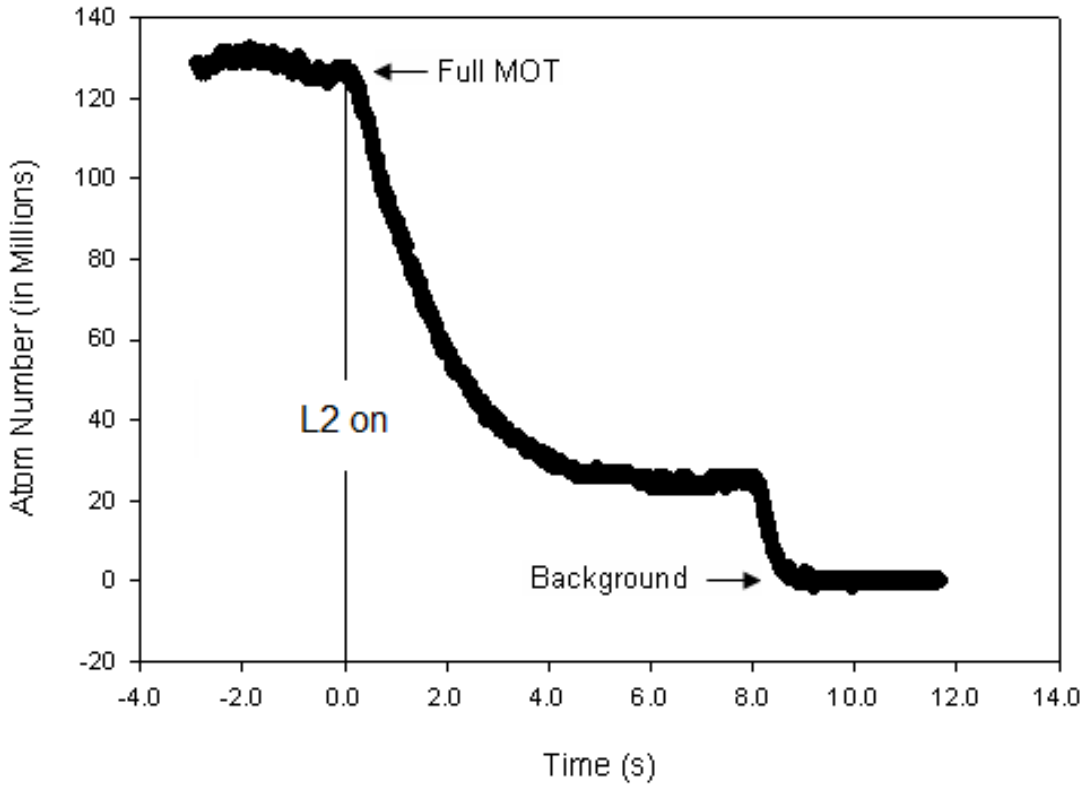


Figure 7.5: This is a typical fluorescence signal from the MOT before and during the application of the light from L2 at 776 nm. The MOT is filled to equilibrium without the L2 light present. At $t = 0$, the light from L2 is applied, and the MOT fluorescence can be observed to decrease on a time scale much faster than the $\sim$20 s MOT fill time, indicating the presence of additional losses.

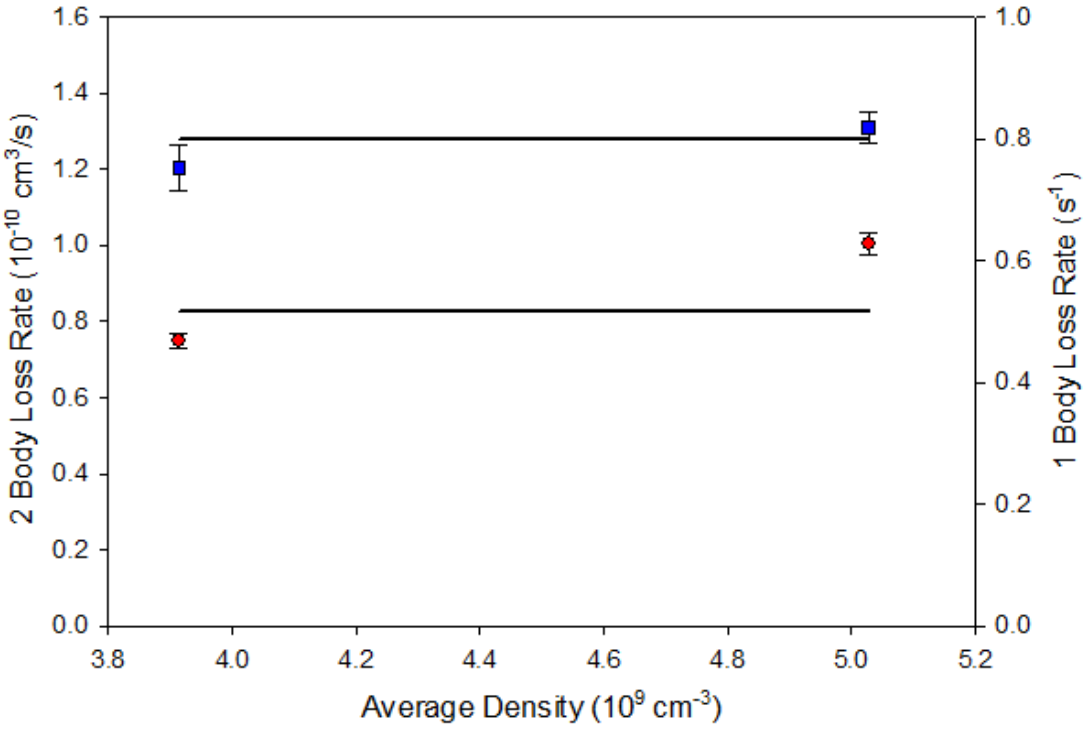


Figure 7.6: Density dependence of the one- and two- body loss calculations. The one-body loss calculation is represented by the red circles and the two-body loss calculation is represented by the blue squares. The one-body loss calculations show a significant statistical difference at different densities whereas the two-body loss calculations are consistent within statistical uncertainty. A simultaneous one- and two-body calculation produced a value for the one-body loss coefficient consistent with zero.

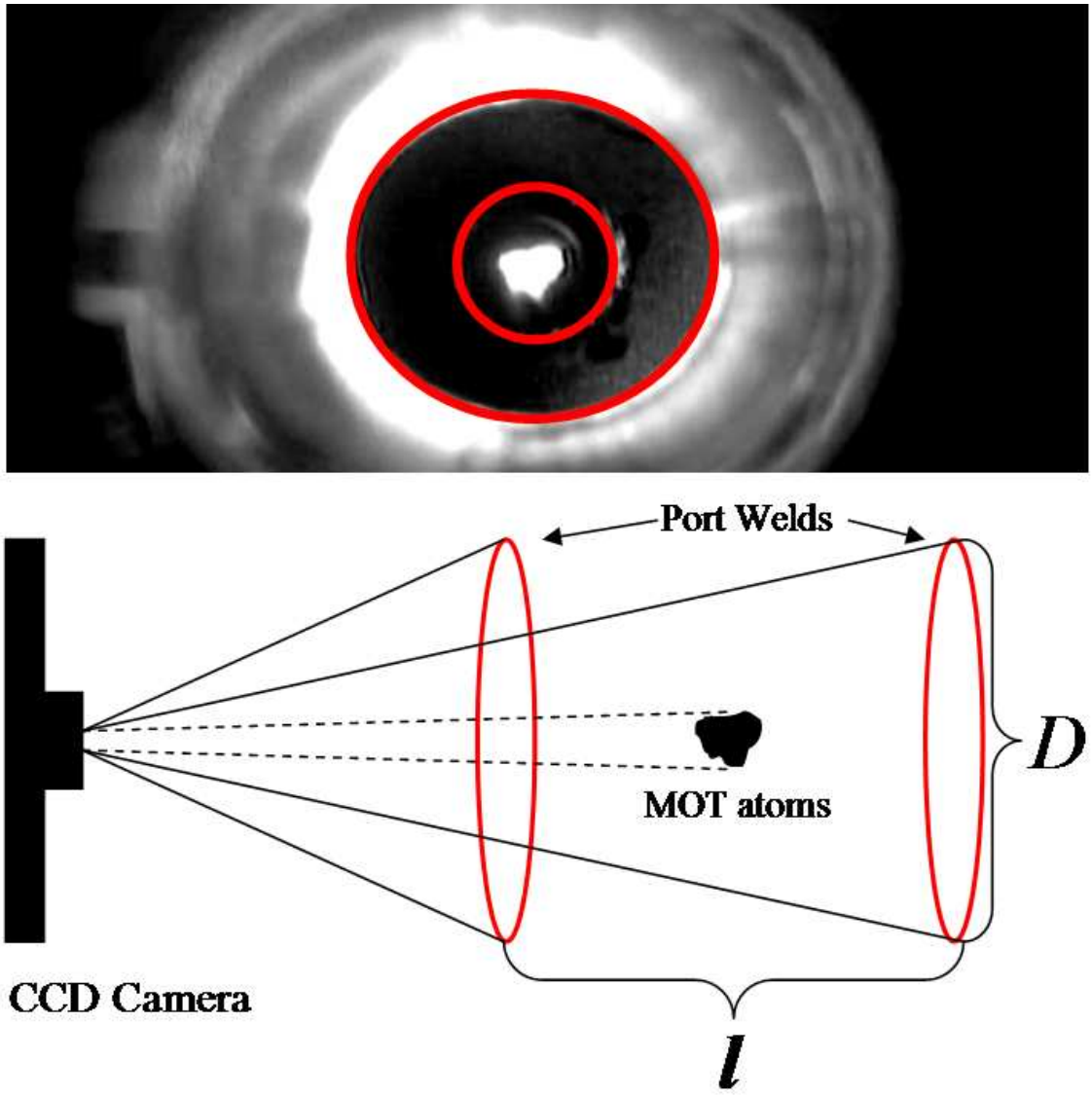


Figure 7.7: (Top) An image taken from our CCD camera of the MOT through a view-port into the vacuum chamber. The welds of the view-ports are highlighted by red circles. Their size and relative distance are known from the design specifications of our vacuum chamber. (Bottom) A diagram of our camera position. The port welds are a distance $l = 10.4$ cm apart and have diameter $D = 1.9$ cm. If we assume that the MOT atoms are halfway between the two ports then we can calculate the 2-D size of the MOT based on the apparent size of the port welds on our camera.

## 7.3 Identifying the Loss Mechanism

For our standard conditions (12 MHz detuned on L1 at 42.5 mW/cm$^2$, L2 at 25.0 mW/cm$^2$), we observed a peak loss coefficient of $\beta = (2.05 \pm 0.06$ (statistical) $\pm$ 1.0 (systematic))$\times 10^{-10}$ cm$^3$/s, which is more than an order of magnitude larger than the two-body loss coefficient for L1 light alone at the detunings used in our experiment ($\sim 10^{-11}$ cm$^3$/s for our intensities) [9]. This increase occurs with less than a factor of 2 change in overall light intensity.

To identify the loss channel involved in this process, we investigated how changes in the intensity of L1 and L2 changed the value of the loss coefficient $\beta$. From a maximum intensity of 42.5 mW/cm$^2$ for L1 and 25.0 mW/cm$^2$ for L2, we reduced the intensity of one of the lasers while keeping the other laser intensity constant . The scaling of $\beta$ with intensity indicates the number of photons involved in the loss process, and thus gives insight into the collision channels to which the atom pairs are excited. In the absence of saturation, the intensity scales directly with the number of photons involved in the collision channel. Saturation can complicate the picture, and may lead to a reduction in the intensity scaling.

To perform these intensity variation measurements, L1 was detuned to several chosen frequencies between 6 and 18 MHz to the red of the $5S_{1/2}$ - $5P_{3/2}$ transition, and L2 was then set to the frequency that produced the maximum reduction of the MOT number for a given frequency of L1. For $\delta$ = -12 MHz for L1, this was 20 MHz to the blue of the $5P_{3/2}$ - $5D_{5/2}$ transition for L2. For a -$\Delta$ change in detuning of L1, the frequency of maximum loss in L2 had a corresponding shift of approximately $\Delta$. There was no measurable change in the frequency of L2 at maximum loss for different intensities of L2.

To measure the loss rate variation with L2, the intensity of L2 was varied with constant L1 intensity in a pulsed configuration in two ways. The pulse sequences were performed by using an AOM for the L2 light. Both sequences had a 10-ms duty cycle. The first way kept the average power of the laser constant, meaning that as the pulse length was shortened, the intensity of the laser was increased to compensate. This was done with intensities at their full (25 mW/cm$^2$), half, quarter, and one-eighth levels. In this configuration, the overall loss rates under each of the different conditions yielded values that were equal to within statistical uncertainty as seen in Figure

7.8. This measurement implies a linear scaling of $\beta$ with the intensity of L2, with no indication of saturation. Additional measurements at even lower intensities of L2 gave no indication of saturation of a multi-photon process due to L2. The second pulse configuration kept the intensity of the beam constant (at 12 mW/cm$^2$), while altering the length of the pulse. In this configuration, the scaling of the loss rate was linear with pulse length as seen in Figure 7.9.

The data in Figures 7.8 and 7.9 strongly confirm the two-body nature of the loss because the atom density varies substantially in this data when the intensity and detuning of L2 are held constant. A one-body loss fits the data poorly. In addition, assuming that the number variation is owing solely to a variation in the load rate, $R$, fits the data even more poorly. This is because a change in $R$ is effectively "zero-body" loss that implies a particular scaling of the steady-state number with pulse length that is not the same as what we observed. Taking this further, data such as that in Figures 7.8 and 7.9 can be used to constrain the range of possible variation of $R$ by allowing such a variation as a fit parameter in a addition to the two-body loss coefficient. In doing so, we find that these data constrain $R$ to vary by less than 10% given the statistical uncertainty of the measurements. In this analysis we assumed that any change in $R$ would be proportional to the pulse length of the L2 light.

To find the dependence on the intensity of L1, we varied both L1 and L2 in a pulsed configuration (2-ms pulse out of a 10-ms duty cycle), but with the pulses for the two lasers in phase and 180° out of phase. L1 was pulsed for 2 ms at reduced intensity and was at full intensity for the rest of the duty cycle, whereas L2 was on for 2 ms and off for the rest of the duty cycle. The experiment was done in this configuration so as to not change the loading parameters for the MOT significantly while varying the intensity of L1 as L2 was applied. For one such measurement, we measured the loss rate with an L1 intensity of 30 and 22.5 mW/cm$^2$, a ratio of 0.75. We calculated the ratio of the loss coefficient $\beta$ measured under the two different intensity conditions and found a ratio of 0.75 $\pm$ 0.01 for $\delta$ = - 12 MHz for L1. This measurement would suggest linear dependence of $\beta$ on L1. Additional measurements at larger detunings also showed linear behavior.

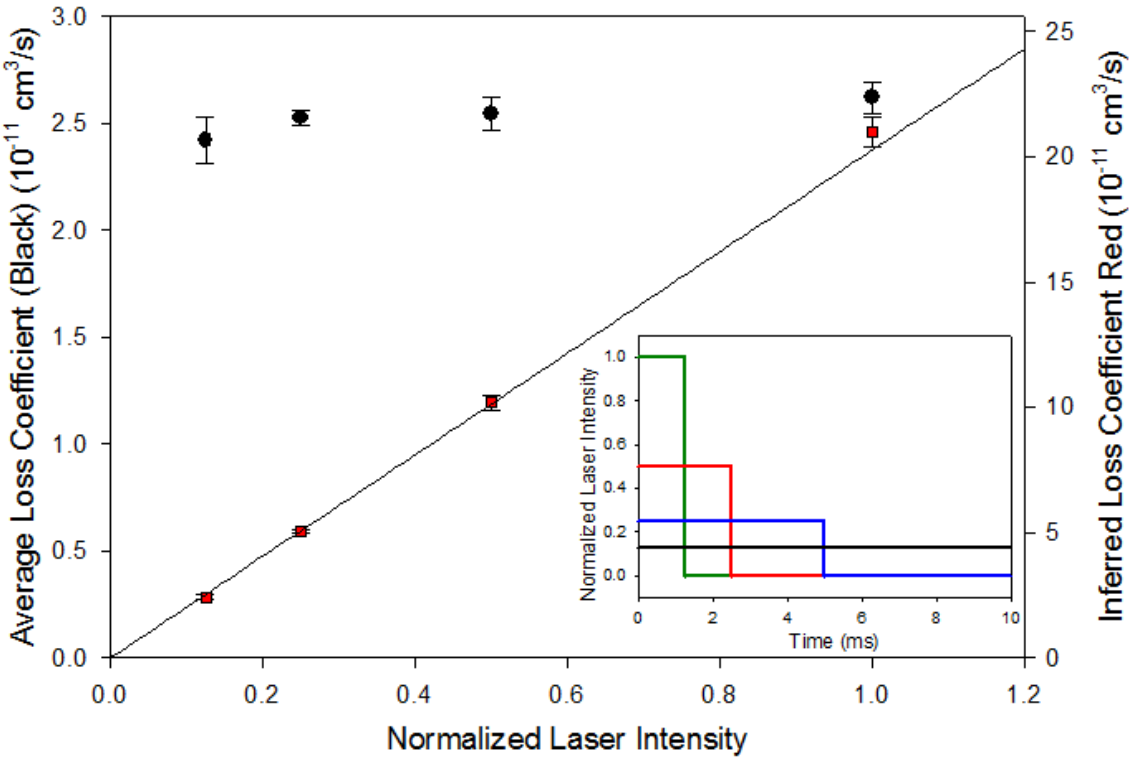


Figure 7.8: A plot of the two-body loss rate under different pulse timing configurations with constant average power. Here, the shorter pulses have higher intensities for L2 light. The black circles show the loss rate from the pulsed data and the red squares show the inferred loss rate where it is assumed that the pulse is on for the full duty cycle (10 ms) for the different intensities. Inset is a diagram of the different pulse configurations over the 10 ms duty cycle of the pulse. The integrated area of each pulse is equal in each of the different pulse configurations.

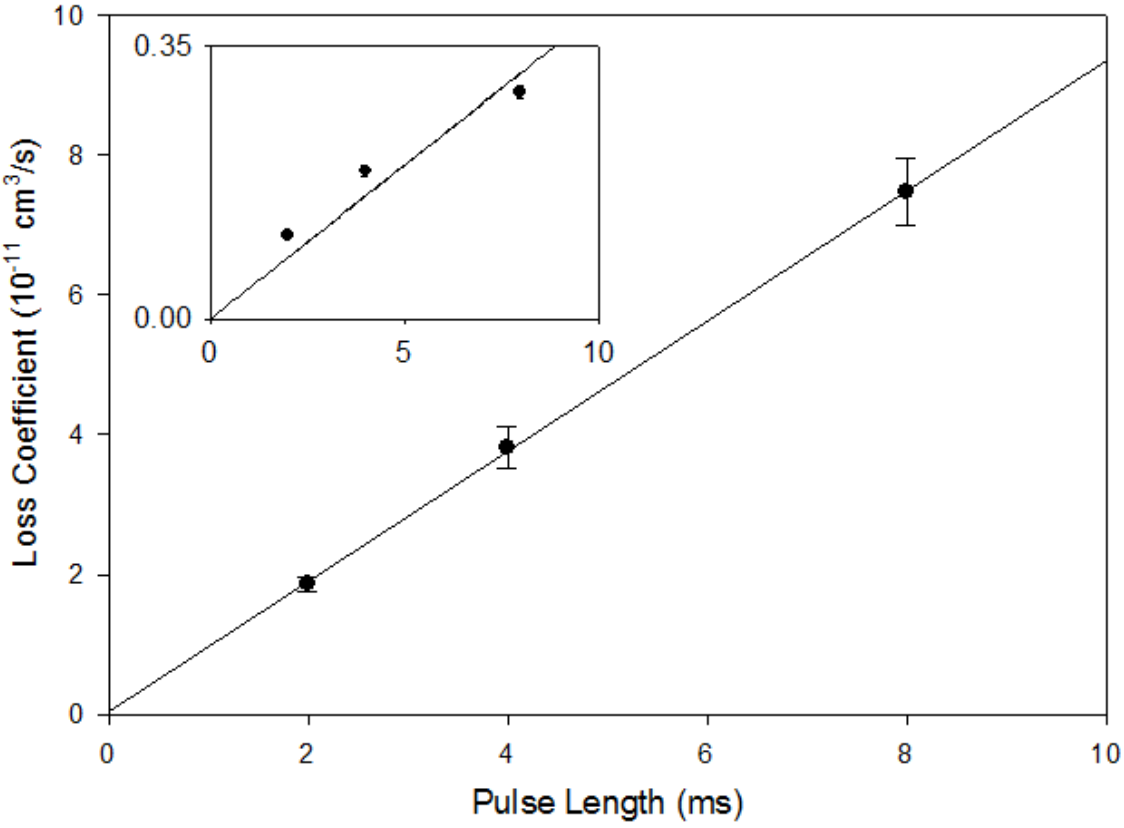


Figure 7.9: A plot of the two-body loss rate as a function of the pulse length. Here the intensity of each pulse is constant (12 mW/cm$^2$). Inset shows a one-body fit to the data from the main figure. The vertical axis is the one-body loss rate in units of s$^{-1}$, and the horizontal axis is the pulse length in ms. It can be seen here that two-body analysis fits much better to the observed data.

## 7.4 Models of Atom Motion

Given the observed two-body nature of the loss rate, and the intensity dependences of L1 and L2 on the loss coefficient, we can attempt to identify the loss channel of the collision. The collision dynamics will be determined by molecular potential curves formed by long range dipole-dipole interactions between an atom pair. In order to get an insight into these dynamics, we used a simplified model of the molecular potentials in which we modeled the atom motion classically along the potential curves. For the range of internuclear separations relevant to this work, these molecular potentials can be calculated with sufficient precision using perturbation theory [29]. We did not take into account the hyperfine structure in this simple model. Interactions between atoms with even total electron angular momentum (e.g. $5S-5S$, $5S-5D$) will have relatively flat potentials at long range due to a lack of a resonant dipole-dipole interaction. When L1 is detuned to 12 MHz to the red of the $5S_{1/2}$ - $5P_{3/2}$ cycling transition, the light drives transitions resonantly from the ground state to the $5S_{1/2}$-$5P_{3/2}$ molecular potential at ∼90 nm internuclear separation. We modeled the $5S-5P$ potential curve with a $-C_3/\mathrm{r}^3$ potential ($C_3 = 18.4$, in atomic units) and the 5S-5D potential with a - ($C_5/r^5 + C_6/r^6$) potential ($C_5 = 0.5079$ and $C_6 = 11.32{\cdot}10^4$, in atomic units) [29] (Figure 7.10). The $5S-5D$ potential is approximately flat for the internuclear separations of interest for this discussion. The maximum loss in the MOT was seen when L2 was detuned by 20 MHz to the blue of the natural transition, which is 8 MHz blue detuned of a coherent transition from the $5S$ to the $5D$ state. This implies that when an atom pair is excited up to the $5S-5P$ state, it accelerates along the potential curve for some amount of time before it is in resonance with L2. When excited up to the $5S-5D$ molecular potential, the relatively long lifetime of the $5D$ state (∼200 ns [30], compared to ∼26 ns for the $5S-5P$ state) allows the atom pair to travel along this curve to a much closer internuclear separation. If the atom pair decays back down to the $5S-5P$ molecular potential within ∼40 nm internuclear separation, the atoms will begin to have a significant probability of accelerating along the curve to the escape velocity of the trap (∼10 m/s). This radiative escape probability increases sharply as the atoms approach to even closer separations along the $5S-5P$ potential. Also, state changing collisions can occur if the atom pair reaches close internuclear separations. While the atom pair can reach the $5S-5P$ potential at a close separation through off resonant transitions from the ground state, the probability for this is

very low, meaning decay from an upper state is the more likely mechanism. Our observations are consistent with mechanism being responsible for the increased loss in the trap observed through the application of L2 light.

In our initial examination of the possible collision channels, there appeared to be a puzzle. At particular internuclear separations, both L1 and L2 are resonant with particular transitions. The polarization averaged incoherent single-atom saturation intensities for the $5S_{1/2} - 5P_{3/2}$ transition and the $5P_{3/2} - 5D_{5/2}$ are 4.97 and 14.7 mW/cm$^2$, respectively. Despite the fact that the L1 and L2 intensities exceed these values, we observed no evidence of saturation in the loss rate coefficients on either transition. Initial estimates using our simple model indicated that strong saturation should be observed for our conditions, particularly for L1.

However, by incorporating additional effects in our model, the amount of expected saturation is significantly decreased. One change was incorporating the fact that in general there are two broad classes of $5S - 5P$ excited states, strongly radiating (with the pair of atoms in a symmetric superposition of the ground and excited state [31]) and weakly radiating (the pair of atoms in an antisymmetric superposition). The strongly radiating states (whose lifetime is $\sim$13 ns) require excitation close to the $5P_{3/2} - 5D_{5/2}$ resonant internuclear separation or they will decay back to the ground state. Because at this internuclear separation the $5S_{1/2} - 5P_{3/2}$ light is detuned by approximately a natural linewidth for the conditions measured, the degree of saturation is reduced. The weakly radiating states are by their nature only weakly coupled to the ground state as only retardation effects make the excitation probability to these states nonzero.

To further evaluate the reduction in saturation for the weakly coupled states, we constructed a model consisting of modified Landau-Zener avoided crossings [32, 33] at the internuclear separations where L1 and L2 coupled different states to one another. The goal was to see how the fraction of atoms delivered into a region of 40-50 nm internuclear separation depended on L1 and L2 intensity for the parameters relevant to our measurements. Note that these weakly radiating states are only weakly radiating on the 5S-5P to 5S-5S molecular transition and decay normally from the 5S-5D state.

In these calculations, the atoms' motion was modeled semi-classically along dressed state potential curves. The transformation of the potential curves into the dressed states can be seen in Figure 7.11. Here the potentials are constructed from the molecular potential curves taking into account

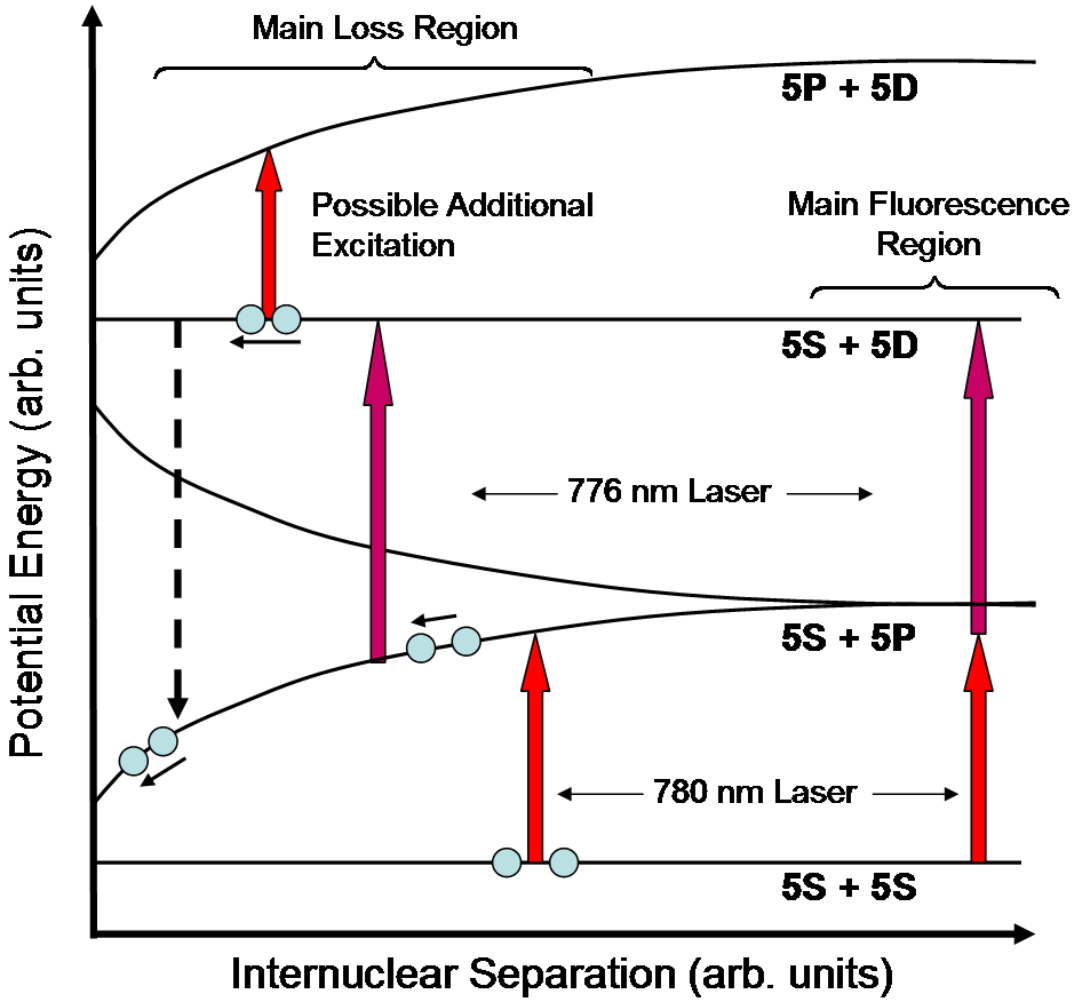


Figure 7.10: A diagram of the loss channel that is identified in the main text of this chapter. Pairs of atoms are excited to the $5S - 5P$ molecular potential by L1 (780 nm) and accelerate until they are excited by L2 (776 nm) up to the $5S - 5D$ state. The long lifetime of the $5S - 5D$ state allows the atom pair to travel into a region where they can be lost from the trap upon their decay to the $5S - 5P$ state, due to increased acceleration along the slope of the $5S - 5P$ molecular potential curve.

the photon energy from the lasers that excite the transitions between the states. For example, the $5S-5S$ potential is a flat potential at zero energy. If we were to excite a $5S_{1/2}-5P_{3/2}$ transition on resonance, then at large internuclear separations (before there is any structure to the $5S-5P$ potential) the dressed state potentials would have the same energy. Since we use photons that are 12 MHz detuned to the red of resonance, the $5S-5P$ potential is shifted up in energy by 12 MHz as seen in Figure 7.11. The same is true for the $5S-5D$ potential, where the excitation laser is tuned 20 MHz to the blue of resonance.

To transform the molecular potentials into their respective dressed states, we can setup a potential energy matrix of the following form

$$U = \begin{pmatrix} U_{5S-5D} & \hbar\Omega_{P,D} & 0 \\ \hbar\Omega_{P,D} & U_{5S-5P} & \hbar\Omega_{S,P} \\ 0 & \hbar\Omega_{S,P} & 0 \end{pmatrix} \tag{7.4}$$

where $U_{5S-5P}$ and $U_{5S-5D}$ are the molecular potentials associated with the $5S_{1/2}-5P_{3/2}$ and $5S_{1/2}-5D_{5/2}$ states respectively with the $5S_{1/2}-5S_{1/2}$ potential set to 0. The molecular potentials for the excited states are described above. The off-diagonal terms $\hbar\Omega_{S,P}$ and $\hbar\Omega_{P,D}$ are the coupling strengths between the different molecular energy levels, which are given by

$$\Omega = \sqrt{\frac{3I\lambda^3}{4\pi^2\hbar\tau c}} \tag{7.5}$$

where $I$ is the intensity of the laser on the respective transition at wavelength $\lambda$, $\tau$ is the lifetime of the excited state, and $c$ is the speed of light in a vacuum. To find the dressed state potential curves, we take the eigenvalues of Equation 7.4. The dressed state potential curves can be seen in Figure 7.11. Here, we can see the avoided crossings that result from transforming the potential curves into the dressed state. We can now consider modeling the atomic motion along these dressed state potential curves. If we choose the center curve (labeled in Figure 7.11 with a pair of atoms), motion of the atoms along that curve represents likely transitions between the molecular states at the avoided crossings. We can now construct a rate equation model to determine the probability that an atom pair will make it to 40-50 nm internuclear separation in the $5S_{1/2}-5D_{5/2}$ state given the parameters of our system.

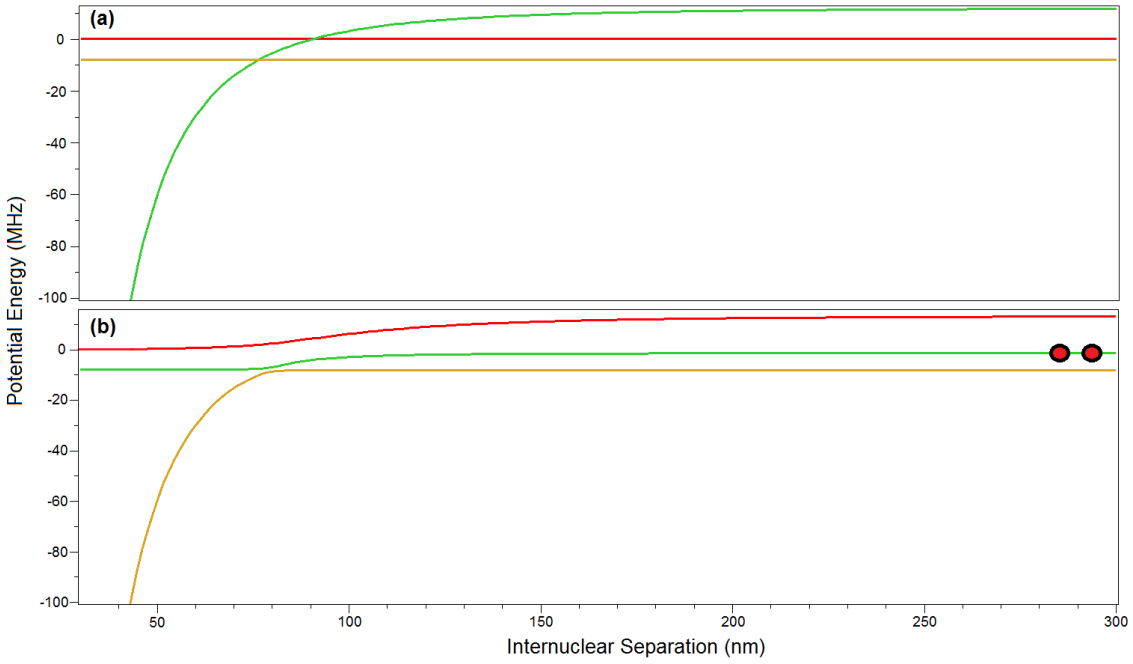


Figure 7.11: (a) Potential energy curves for the $5S_{1/2} - 5S_{1/2}$ (red), $5S_{1/2} - 5P_{3/2}$ (green), and $5S_{1/2} - 5D_{5/2}$ (gold) for L1 and L2 detunings of -12 MHz and 20 MHz respectively. (b) shows the curves transformed to the dressed state potentials, showing the avoided crossings of the potential energy curves. For our model, we model the acceleration of the atom pair along the green dressed state potential curve, which will take into account the accelerations of the atoms pair toward each other while undergoing transitions between the different molecular states owing to the presence of L1 and L2.

We can setup a system of differential equations that couple all of the relevant molecular states together as

$$\frac{1}{2\pi}\dot{c_1}(t) = i\hbar\Omega_{S,P}\cdot c_2(t) \tag{7.6}$$

$$\frac{1}{2\pi}\dot{c_2}(t) = iU_{5S-5P}(r(t))\cdot c_2(t) + i\hbar\Omega_{S,P}\cdot c_1(t) + i\hbar\Omega_{P,D}c_3(t) \tag{7.7}$$

$$\frac{1}{2\pi}\dot{c_3}(t) = iU_{5S-5D}(r(t))\cdot c_3(t) + i\hbar\Omega_{P,D}\cdot c_2(t) \tag{7.8}$$

$$\frac{d}{dt}r(t) = -\sqrt{v_i + 2\frac{U_D(r_i) - U_D(r(t))}{\mu}} \tag{7.9}$$

where $|c_1(t)|^2$, $|c_2(t)|^2$, and $|c_3(t)|^2$ are the probabilities of the atom pair to be in the $5S-5S$, $5S-5P$, and $5S-5D$ molecular states respectively, $U_D$ is the dressed state potential curve along which we model the motion of the atom pairs, $r(t)$ is the internuclear separation as a function of time ($r_i$ is the initial position in which we begin our modeling), $v_i$ is the initial relative velocity which that pair of atoms are moving with respect to each other (based on the thermal temperature of the MOT), and $\mu$ is the reduced mass of the atom pair which in this case is 1/2 of the mass of $^{85}$Rb. To model the dependence of the loss, we accelerate the atoms along the dressed state potential curves and calculate the probability that an atom will be in the $5S-5D$ state ($|c_3(t)|^2$ at internuclear separations between 40-50 nm, indicating loss.

For typical collision velocities in our gas, we observed that a factor of 2 reduction in L1 intensity reduced the net probability to be on the $5S-5D$ asymptote at close internuclear separation to ∼60%-65% of its initial value. For L2, a factor of 2 reduction reduced the probability to ∼55% of its initial value. Similar degrees of reduction were observed due to the off-resonant transitions of the strongly-radiating states.

While this degree of saturation is large enough that had it been present we would have detected it in our data, it is significantly less than what we naively expected. More quantitative calculations are complicated by the fact that there are ∼500 long-range molecular states associated with different combinations of spin and electronic states for the colliding pair. Also, many of these states have a complicated (i.e., not solely attractive) structure [12] and the two-photon nature and variable polarization of the light fields in space add more complications. We note that our data cannot rule out combinations where saturation is balanced by other loss effects (e.g., intensity-dependent

collisional flux enhancement [34], but such balancing would have to be just right to produce the linear scaling that we observe.

As an additional characterization, we also measured the nature of the 421-nm fluorescence from the MOT that is due to the $5D_{5/2}$ cascade decay to the ground state via the $6P_{3/2}$ state. This was done to give us a better insight into the single-atom transitions taking place inside the MOT. In this measurement, we ramped the frequency of L2 over the transition to the $5D_{5/2}$ state at our maximum intensity (25 mW/cm$^2$) and at half intensity and measured the fluorescence at 421 nm by using a filter to block out any infrared light. When the intensity of L2 was reduced by a factor of 2, the peak fluorescence was only reduced by $\sim$25%, suggesting that this particular single-atom transition is saturated. This observation is consistent with an optical Bloch equation model of a four-level atom consisting of the $5S$, $5P$, $5D$, and $6P$ states with averaged Clebsch-Gordan coefficients and coherent driving fields for the transitions. The full width at half maximum of the fluorescence peak was measured to be $\sim$3 MHz, which implies that the transition is coherent on the time scale of several tens of nanoseconds even though the transition is driven from two sources, L1 and L2. This width is much less than the width of the loss coefficient with detuning (see Fig. 7.12). It was also observed that the peak of the fluorescence was not at the same detuning for L2 as the point where we observed the maximum loss from the MOT. The maximum loss is $\sim$10 MHz to the blue of the point of the maximum 421-nm fluorescence for $\delta = -12$ MHz on L1. This indicates that the point of maximum 421-nm fluorescence corresponded to a coherent two-photon transition from the ground state to the $5D$ excited state, and the point of maximum loss in the MOT corresponds to some acceleration along the 5S-5P molecular potential in order to carry atom pairs into closer separation along the $5S - 5D$ potential.

The simplified models we have used do not take into account the hyperfine structure of the various states, particularly the $5D_{5/2}$ state. The $5D_{5/2}$ state in $^{85}$Rb has an inverted hyperfine structure, meaning that the highest angular momentum value of $F$ lies at the lowest energy. When observing the maximum fluorescence in the MOT, the most probable excitation from the $5P_{3/2}$ ($F = 4$) level is to the $5D_{5/2}$ ($F = 5$) level. From the $5D_{5/2}$ ($F = 5$) level, it is highly likely (more than 80%) that the atom will experience a spontaneous decay route that ultimately results in the atom returning to the $5S_{1/2}$ ($F = 3$) ground state. In contrast, when we observed the maximum loss in the MOT, we were tuned nearly on resonance with the $5D_{5/2}$ ($F = 4$) state, whose spontaneous

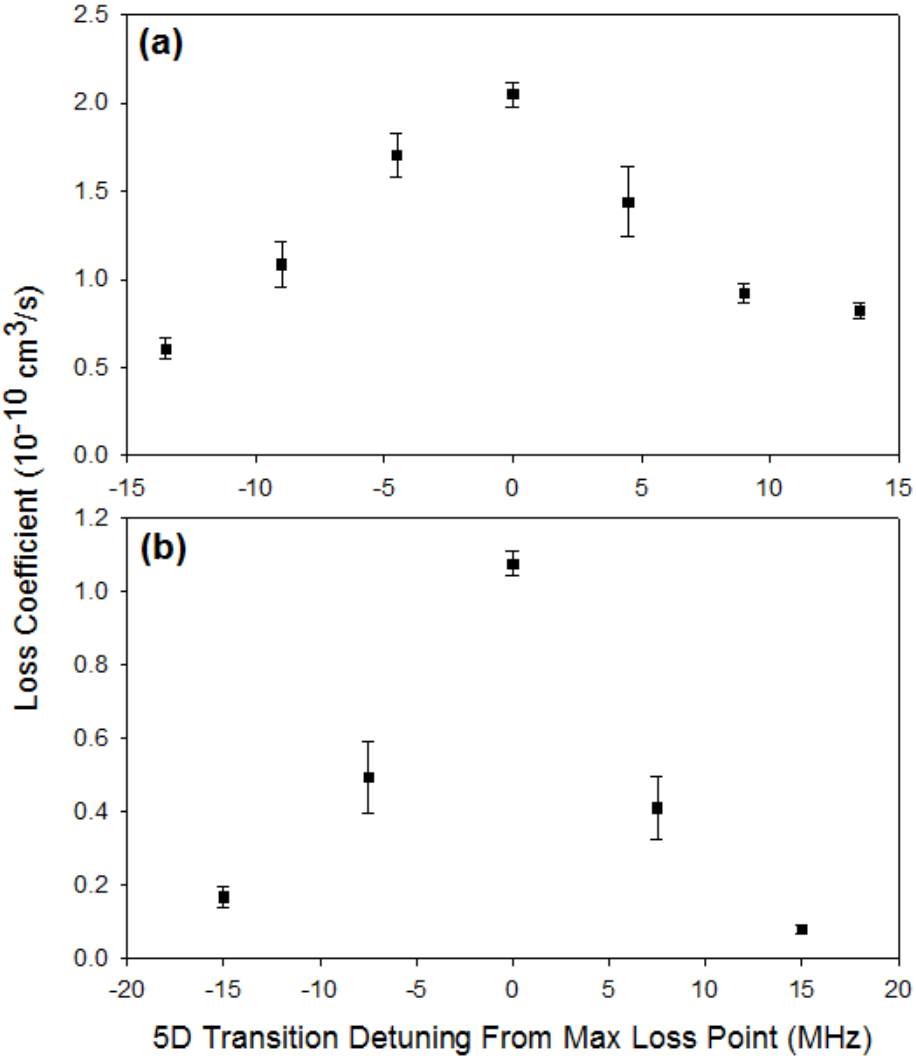


Figure 7.12: Two-body loss rate as a function of L2 detuning from the point of maximum loss. (a) shows the loss rate with a 12-MHz red detuning for L1. (b) shows the loss rate for 18-MHz detuning for L1. The widths of these curves is $\sim 15 - 20$ MHz, which is much wider than that of the 421-nm fluorescence, which is only $\sim$3 MHz.

decay channels have reasonable probability to put atoms out of resonance with both L1 and L2, leaving the atom in a "dark" state until repumped from the $F = 2$ ground state by the hyperfine repump laser. In principle, this process could lead to losses from the trap owing to loss of cooling efficiency, which would change the steady-state number in the MOT. We observe no such effect, which in any case would be a one-body loss instead of a two-body loss. This can be explained by the fact that we have a strong repump laser to pump atoms back to the $F = 3$ ground state from the $F = 2$ ground state quickly. In addition, the Clebsch-Gordan coefficients for the $5P_{3/2}$ $F = 4$ to the $5D_{5/2}$ $F = 4$ are 1/2 of those of the $F = 5$ transition, which would reduce the transition rates by a factor of 4 (the Clebsch-Gordan coefficients for the transition to the $5D_{5/2}$ $F = 3$ state are lower by a factor of 17). So the transition to the $5D_{5/2}$ $F = 5$ state will be the dominant transition.

## Conclusion

In summary, we have investigated the increased two-body loss rate produced by the addition of laser light that excites atoms in a MOT up to the $5S-5D$ molecular potential curve. We confirmed that the dominant loss was two-body in nature. Our measurements showed that the two-body loss rate was increased by over an order of magnitude with only a factor of 2 change in the overall light intensity. Using intensity variation measurements, we have been able to conclude that the loss channel likely involves a single photon transition from our main trapping laser and a single photon transition from a second laser tuned to excite to the $5D_{5/2}$ level. Finally we measured the width of the loss coefficient as a function of L2 frequency for two frequencies of L1. While this work was performed with the excitation to a particular long-lived excited state, we expect that this class of losses induced are not unique to the $^{85}$Rb $5S_{1/2} - 5D_{5/2}$ state and could possibly be observed in other experiments involving excitations to similarly long-lived states.

## References for Chapter 7


[1] M. L. Trachy, G. Veshapidze, M. H. Shah, H. U. Jang, and B. D. DePaola, Phys. Rev. Lett. **99**, 043003 (2007).

[2] S. Chu, Rev. Mod. Phys. **70**, 685 (1998); C. N. Cohen-Tannoudji, *ibid.* **70**, 707 (1998); W. D. Phillips, *ibid.* **70**, 721 (1998).

[3] P. S. Julienne and Jacques Vigué, Phys. Rev. A **44**, 4464 (1991).

[4] P. L. Gould, P. D. Lett, P. S. Julienne, W. D. Phillips, H. R. Thorsheim, and J. Weiner, Phys. Rev. Lett. **60**, 788 (1988).

[5] L.Marcassa, V. Bagnato, Y.Wang,C.Tsao, J.Weiner,O.Dulieu, Y. B. Band, and P. S. Julienne, Phys. Rev. A **47**, R4563 (1993).

[6] D. Sesko, T. Walker, C. Monroe, A. Gallagher, and C. Wieman, Phys. Rev. Lett. **63**, 961 (1989).

[7] M. Prentiss, A. Cable, J. E. Bjorkholm, E. L. Raab, D. E. Pritchard, and S. Chu, Opt. Lett. **13**, 452 (1988).

[8] J. Weiner, V. S. Bagnato, S. Zilio, and P. S. Julienne, Rev. Mod. Phys. **71**, 1 (1999).

[9] S. D. Gensemer, V. Sanchez-Villicana, K. Y. N. Tan, T. T. Grove, and P. L. Gould, Phys. Rev. A **56**, 4055 (1997).

[10] C. D. Wallace, T. P. Dinneen, Kit-Yan N. Tan, T. T. Grove, and P. L. Gould, Phys. Rev. Lett. **69**, 897 (1992).

[11] C. D. Wallace, V. Sanchez-Villicana, T. P. Dinneen, and P. L. Gould, Phys. Rev. Lett. **74**, 1087 (1995).

[12] A. R. Gorges, N. S. Bingham, M. K. DeAngelo,M. S. Hamilton, and J. L. Roberts, Phys. Rev. A **78**, 033420 (2008).

[13] T. T. Grove, V. Sanchez-Villicana, B. C. Duncan, S.Maleki, and P. L. Gould, Phys. Scr. **52**, 271 (1995).

[14] G. Veshapidze, M. L. Trachy, H. U. Jang, C. W. Fehrenbach, and B. D. DePaola, Phys. Rev. A **76**, 051401(R) (2007).

[15] M. J. Wright, J. A. Pechkis, J. L. Carini, S. Kallush, R. Kosloff, and P. L. Gould, Phys. Rev. A **75**, 051401(R) (2007).

[16] D. Jaksch, J. I. Cirac, P. Zoller, S. L. Rolston, R. Côté, and M. D. Lukin, Phys. Rev. Lett. **85**, 2208 (2000).

[17] W. R. Anderson, J. R. Veale, and T. F. Gallagher, Phys. Rev. Lett. **80**, 249 (1998).

[18] I. Mourachko, D. Comparat, F. deTomasi, A. Fioretti, P. Nosbaum, V. M. Akulin, and P. Pillet, Phys. Rev. Lett. **80**, 253 (1998).

[19] T. E. Mehlstäubler, K.Moldenhauer, M. Riedmann, N. Rehbein, J. Friebe, E. M. Rasel, and W. Ertmer, Phys. Rev. A **77**, 021402(R) (2008).

[20] G. Morigi and E.Arimondo,Phys. Rev. A **75**, 051404(R) (2007).

[21] S. Wu, T. Plisson, R. C. Brown, W. D. Phillips, and J. V. Porto, Phys. Rev. Lett. **103**, 173003 (2009).

[22] P. M. Duarte, R. A. Hart, J. M. Hitchcock, T. A. Corcovilos, T. L. Yang, A. Reed, and R. G. Hulet, Phys. Rev. A **84**, 061406(R) (2011).

[23] D. C. McKay, D. Jervis, D. J. Fine, J. W. Simpson-Porco, G. J. A. Edge, and J. H. Thywissen, Phys. Rev. A **84**, 063420 (2011).

[24] A. R. Gorges, *Simultaneous Trapping of* $^{85}$*Rb &* $^{87}$*Rb in a Far Off Resonant Trap*, Ph. D. Thesis, Colorado State University (2011).

[25] E. L. Raab, M. Prentiss, A. Cable, S. Chu, and D. E. Pritchard, Phys. Rev. Lett. **59**, 2631 (1987).

[26] M. H. Shah, H. A. Camp, M. L. Trachy, G. Veshapidze, M. A. Gearba, and B. D. DePaola, Phys. Rev. A **75**, 053418 (2007).

[27] U. Volz and H. Schmoranzer, Phys. Scr., T **65**, 48 (1996).

[28] B. C. Duncan, V. Sanchez-Villicana, P. L. Gould, and H. R. Sadeghpour, Phys. Rev. A **63**, 043411 (2001).

[29] M. Marinescu and A. Dalgarno, Phys. Rev. **A** 52, 311 (1995).

[30] M. S. Safronova, C. J. Williams, and C. W. Clark, Phys. Rev. A **69**, 022509 (2004).

[31] G. Lenz and P. Meystre, Phys. Rev. A **48**, 3365 (1993).

[32] L. Landau, Phys. Z. **2**, 46 (1932).

[33] C. Zener, Proc. R. Soc. London, Ser. A **137**, 696 (1932).

[34] V. Sanchez-Villicana, S. D. Gensemer, and P. L. Gould, Phys. Rev. A **54**, R3730 (1996).

# Chapter 8

# Future Work

The work presented in the previous chapters of this thesis represent the first investigations in a long line of planned experiments using our ultracold plasma apparatus here at Colorado State University. While we are now able to characterize the UCPs created in our system through measurements of the UCP size and expansion rate, there are still several diagnostic tools that would be very useful to develop in order to be able to better characterize the UCP. Most importantly, it would be good to develop methods for determining the UCP electron temperature that are independent of our model calculations. This will help us to confirm our predictions that low-density UCPs should allow us to achieve higher values of $\Gamma_e$ than in previous experiments [1, 2]. The development of these characterization tools will be necessary for performing experiments involving UCPs in the Penning trap. Without being able to characterize properties such as the electron temperature and ion/electron density, we will not be able to perform any measurements that will allow us to make comparisons to the appropriate theoretical predictions.

Although there is a long list of planned measurements and many lines of investigation that we could pursue, I will only briefly discuss three such planned experiments in this chapter. The first planned measurement involves revisiting the excitation of the UCP with two, sharp electric field pulses (Chapter 4). The decay time of the response to the excitation should be related at least in part to the electron-ion 90-degree deflection time (see Chapter 2), and thus the electron temperature. Another planned measurement is to develop a technique for measuring the electron temperature at early times in the UCP evolution using electric field ramps. Similar techniques have been developed in [3]. Using these measurement techniques, we should be able to compare the measured temperature by using this method to the calculations of the energy removed by electron evaporation during the UCP formation in Chapter 5. The last planned experiment that I will discuss in this chapter will be concerned with trapping the UCP in the Penning trap. The first measurements of the UCP in the Penning trap will be concerned with loading efficiency and loading dynamics, so that we can optimize the number of ions and electrons, the UCP density, and the ion and electron temperature in the initial trapped UCP.

## 8.1 Two-Pulse Excitation Measurement

As discussed in Chapter 4, a collective oscillation of the electron cloud can be excited by applied sharp electric field pulses using our electrode assembly. By applying two such pulses separated by a chosen amount of time, the oscillatory nature of the electron cloud response can be inferred from the additional electron escape signal as a function of the pulse separation. Examples of this data are seen in Figure 4.6, and show a damped oscillation in the electron response. This oscillation has a characteristic decay time on the order of a few hundred nanoseconds and could potentially be useful in determining new properties of the UCP that have not been directly measured at this time.

The source of the decay of the oscillation in Figure 4.6 will be one focus of our investigation into this response. There are several possibilities that we need to consider. First, we must consider the fluid nature of the electron cloud. For short electric field pulses, we have modeled the electron cloud to respond to the external field as a rigid object for convenience. Over many oscillations, this assumption will break down, because the anharmonicity in the potential from the offset of the electron cloud will cause electrons to oscillate at slightly different frequencies. This dephasing of the electron cloud will cause a decay in the response to the two-pulse excitation measurement as the motion of more electrons goes out of phase with the driving pulse. To determine the characteristic dephasing time of the electron cloud, there are a few different experiments that we can perform. First, we will want to determine the dephasing time as a function of the initial ionization energy of the UCP. At high initial ionization energies early in the UCP lifetime, the electrons should have a relatively high temperature which lowers the electrons' collision rate with the ions and other electrons in the system. If we can eliminate collisions between particles from the dephasing process then it should be possible to determine how much of the damping in the electron response is owing to the fluid nature of the electron cloud.

If the dephasing of the electron cloud can be taken into account, then it should be possible to relate the rest of the damping of the response to electron-ion 90-degree deflections (electron-electron collisions should not affect the center of mass motion of the electron cloud). By doing so, it should allow us to make better estimates of the electron temperature at late times in the UCP evolution when the potential well depth owing to the excess of ions is no longer well defined. By using the

two-pulse excitation data presented in Chapter 4, we can infer electron temperatures by using our measurement of the peak density and substituting the damping time for the 90 degree deflection in Equation 2.17. By naively using this formula, we obtain electron temperatures of ∼8 and 4 K for the data in Figure 4.6 (a) and (b) respectively ($\Delta E/k_B = 10$ K). This is at least on the order of what we might expect for the electron temperature given the presence of three-body recombination at this initial ionization energies. To better understand the relationship of the damping time to the 90-degree deflection time, we'll want to compare the damping measurements to other independent estimates of the electron temperature, such as those presented in Chapter 5 from the formation of the UCP. A second method for estimating the electron temperature will be discussed in the following section.

## 8.2 Electron Temperature Measurements

For our future experiments, it will be useful to develop many tools that allow us to independently estimate the temperature of the electrons in our UCPs. These estimates will allow us to determine what degree of strong-coupling we achieve in the electron component of the UCPs in our system which is essential for comparison to the relevant theories on how strong-coupling alters the behavior of UCP processes. So far, we have developed methods to estimate the temperature using models that take into account the energy lost owing to electrons evaporating from our UCP. To confirm these models, we can make an additional measurement of the number of electrons that escape the UCP when the external electric field is ramped up to a higher level. Similar measurements have been made in [3], but can be simplified and improved if the potential well depth can be estimated. Therefore, the measurement that we intend to make will be most useful at early times, before the ions outside of the electron distribution have a chance to expand under the influence of the Coulomb force.

To make these measurements, we form the UCP in a chosen external electric field strength. After formation, we ramp the external electric field to a higher value of the electric field, lowering the overall depth of the UCP. At this time, many electrons will escape in order to raise the value of the depth to increase the confinement of the electrons in the UCP. The electrons that escape during this time are from the high end of the energy distribution, which will lower the overall temperature

of the UCP electrons that remain. If we assume that the new depth to temperature ratio that is established after the escape of the electrons is equal to the value before the electric field ramp, a new electron temperature can be inferred from the number of electrons that escape the UCP during the electric field ramp. Our model of UCP formation discussed in Chapter 5 will be used in order to estimate the depth of the UCP.

In the past, we attempted this type of measurement with limited success. We have since determined that our estimates of the electric fields in the UCP region were not accurate based on calculations of the expected fields using estimates of the electrode spacings and their proper voltages. Even small deviations in the spacing of the electrodes can cause large changes in the expected electric field values. This deviation produced results that indicated electron temperatures that were too high given our UCP expansion rates. However, we have now developed techniques to accurately determine the effective electric field strength in the UCP region as discussed in Chapter 3. Also, we will have to take into account the effects of electron screening on the potential well depth in the UCP as was discussed in Chapter 5. We plan to improve this calculation to produce an even more accurate determination of the UCP depth. We will revisit these measurements using our more accurate determinations of the electric field values, the effects of electron screening, and our new estimates of the potential well depth to temperature ratio.

Although this measurement will be most accurate at early times in the UCP evolution, we hope to be able to combine this measurement with measurements of the damping rate discussed in the previous section to calibrate the damping rate as it relates to electron temperature. We hope that this will allow us to make better estimates of the electron temperature at late times in the UCP evolution.

## 8.3 Loading the UCP into a Penning Trap

Although we have discovered interesting new physics associated with the relatively low-density UCPs that we create in our system, our experimental apparatus was designed to trap two-component UCPs in a nested Penning trap configuration. This will extend the UCP lifetimes from the current $\sim$100 $\mu$s values to many hundreds of $\mu$s up to more than 1 ms so that it will be possible to study long-timescale thermalization processes between the electrons and ions and to better explore the

possibilities of forced evaporative cooling of the electrons. Also, there have been no studies up to this point of UCPs at the 0.1 T magnetic fields that we plan on employing in our Penning trap. However, it will first be necessary to optimize the loading of the Penning trap, and to explore any new physics associated with trapping our UCPs.

To trap the UCPs, there are several system upgrades that we need to implement. First, we will need to integrate the fast current switch for the axial magnetic field into the system as discussed in Chapter 3. This fast current switching will occur in between the time of the magnetic trap shutoff and photoionization. If we tried to switch the magnetic field after photoionization occurred, then there would be large induced electric fields from the changing magnetic field that could heat the UCP. Since this magnetic field will be on during the photoionization process, we require additional lasers to optically pump the atoms up to the $5P_{3/2}$ state because the Zeeman shift can alter the energy levels of the atoms significantly at high magnetic field levels. Also, we will need to add the proper function generators to the electrodes assembly to produce the proper electric fields that we need not only to confine the UCP, but also to extract electrons to the MCP at the proper time. Finally, we will need to better calibrate the electric fields in the UCP region. Currently, there is ongoing work to provide both calculational and experiment improvements to this calibration.

## Conclusion

The experiments that were briefly discussed in this chapter represent just a small fraction of the number of planned measurements that will be performed using our ultracold plasma apparatus here at Colorado State University. Each of the future measurements that will be performed will require the knowledge of UCP physics that has been acquired from the experiments performed in this thesis. In addition to the new physics that was discovered, essential diagnostic tools were developed that help us characterize the key properties of the UCPs created in our system. We hope that the experiments presented in this thesis and all of our future experiments help to further our knowledge of fundamental plasma physics and the effects of strong-coupling on a variety plasma dynamical processes.

## References for Chapter 8

[1] S. Kulin, T. C. Killian, S. D. Bergeson, and S. L. Rolston, Phys. Rev. Lett. **85**, 318 (2000).

[2] F. Robicheaux, and J. D. Hanson, Phys. Rev. Lett. **88**, 055002 (2002).

[3] J. L. Roberts, C. D. Fertig, M. J. Lim, and S. L. Rolston, Phys. Rev. Lett. **92**, 253003 (2004).